

NASA-CR135342
LMSC-D564116



(NASA-CR-135342) EVACUATED LOAD-BEARING
HIGH PERFORMANCE INSULATION STUDY - Final
Report, May 1974 - Aug. 1977 (Lockheed
Missiles and Space Co.) 204 p. DTIC A12/EF 401
GPO: 22-63/31

77-10201

Mac135
00502

FINAL REPORT

**EVACUATED LOAD-BEARING
HIGH-PERFORMANCE INSULATION STUDY**

By

R. T. PARMLEY and G. R. CUNNINGTON JR.

**PALO ALTO RESEARCH LABORATORY
LOCKHEED MISSILES & SPACE COMPANY, INC.**



**PREPARED FOR
NATIONAL AERONAUTICS AND SPACE ADMINISTRATION
NASA Lewis Research Center
Contract NAS3-17817**

ERRATA SHEET
FOR
EVACUATED LOAD-BEARING HIGH PERFORMANCE
INSULATION STUDY, NASA-CR 135342

Page

- 2-1 3rd Para, 2nd line: change "Ref 1-3" to "Ref. 1-4".
2-5 Change table as shown.

192.2 424
Weight Goal = 180.8 kg (398.8 lb)

Item	Weight, kg (lb)	Performance Partial	Pro-rated Burnout Weight kg (lb)
Fuel Tank Insulation	39.0 (86.0)	1	39.0 (86.0)
Oxidizer Tank Insulation	18.6 (41.0)	1	18.6 (41.0)
Purge System (Tug)	92.1 (203)	1	92.1 (203)
Purge System (Shuttle Bay)			
He	2.9 (6.4)	0.15	0.4 (0.9)
Bottles	35.7 (78.7)	0.15	5.4 (11.9)
Boiloff (163-hr Mission)			
LO ₂	27.0 (59.4)	0.39	11.3 (24.9)
LH ₂	65.1 (143.5)	0.39	25.4 (56.0)
			192.2 (424)
			180.8 (398.8)

- 4-37 Fifth bullet - change "spring/wire" to "spring/Kevlar".
- 4-57 2nd para, replace 4th line with - "slope of the hemisphere double curvature horizontal wedge stress-strain curve is about 10 percent higher than the other".
- 6-31 change $k_g = \dots$ to $k_g = k_{g0} / (1+2XL/\delta_a)$
- 6-45 line 6 change "10" to "12"; line 7 change "19" to "22" and change "28" to "26"; line 8 change "10" to "12".
- 6-39 For Figs. 6-18 and 6-19, change "13 cycles" to "7 cycles".
- 7-2 Table 7-1 change Length of Welded Joints from "393(1290)" to "364(1198)"
- 7-9 1st para, 7th line -- change "cover" to "cylinder".
- 7-21 Change length of LH₂ jacket welded joints
 from: 393(1290) 250(821) 49(160)
 to: 364(1198) 221(729) 20 (68)

1. Report No. NASA-CR 135342		2. Government Accession No.		3. Recipient's Catalog No.	
4. Title and Subtitle EVACUATED LOAD-BEARING HIGH PERFORMANCE INSULATION STUDY			5. Report Date DECEMBER 1977		
			6. Performing Organization Code LMSC		
7. Author(s) R. T. Parmley and G. R. Cunnington			8. Performing Organization Report No. LMSC-D564116		
9. Performing Organization Name and Address Lockheed Palo Alto Research Laboratory 3251 Hanover Street Palo Alto, California 94304			10. Work Unit No.		
			11. Contract or Grant No. NAS 3-17817		
12. Sponsoring Agency Name and Address National Aeronautics & Space Administration Lewis Research Center Cleveland, Ohio 44135			13. Type of Report and Period Covered Final Report (May 74 - Aug 77)		
			14. Sponsoring Agency Code		
15. Supplementary Notes Project Manager: J. R. Barber, Space Experiments Integration Office, NASA Lewis Research Center, Cleveland, Ohio 44135					
16. Abstract The next generation of reusable space vehicles, such as the LO ₂ /LH ₂ Space Tug must perform both within and outside the atmosphere. To prevent condensation of atmospheric gases within the insulation when the tanks are cooled to cryogen temperature, noncondensable gases such as helium must be substituted for air (helium-purged system) or the air must be removed (vacuum-jacketed system). The major problems associated with a vacuum-jacketed insulation system are: (1) maintaining an adequate vacuum level throughout the life of the system and (2) reducing the system weight so it is competitive with the gas-purged system. A new hollow-glass microsphere load-bearing insulation and light-weight flexible stainless steel jacket concept developed on this program demonstrates suitable vacuum levels can be maintained and system weights are competitive with the gas-purged system. The program consisted of a design and development phase where the vacuum jacket and microsphere insulation properties were characterized. A 1.17-m (46-in.) diameter test tank was insulated with the system and tests were performed to demonstrate: <ul style="list-style-type: none"> • Elastic flexure of the jacket • Vacuum levels and integrity • Microsphere shifting or packing, if any • Thermal performance as a function of warm boundary temperature, compressive load, insulation pressure, and 13 simulated flight cycles The test data were then scaled to the Space Tug LO ₂ and LH ₂ tanks, and weight, thermal performance, payload performance, and costs were compared with a helium-purged multilayer insulation system.					
17. Key Words (Suggested by Author(s)) Microsphere insulation Flexible metal vacuum jacket 1.17 m test tank Design, development, fabrication, thermal tests Space Tug			18. Distribution Statement		
19. Security Classification of this report UNCLASSIFIED		20. Security Classification of this page		21. Number of Pages 253	22. Price

For sale by the National Technical Information Service, Springfield, Virginia 22161

NASA CR 135342-1

FOREWORD

This is the final report of contract NAS 3-17817 entitled "Evacuated Load-Bearing High Performance Insulation Study." The work was conducted for the National Aeronautics and Space Administration through the NASA/Lewis Research Center, Cleveland, Ohio, Mr. James R. Barber, Program Manager.

The Lockheed Palo Alto Research Laboratory conducted the program within the Thermophysics Group of the Materials Sciences Laboratory. Key individuals who contributed to the success of this program and their contributions are as follows:

- | | | |
|-------------------------------|---|---|
| Mr. George R. Cunningham, Jr. | - | Provided technical consultation plus test program direction and analysis (Tasks V and VI) |
| Mr. Ed Cavey | - | Analyzed and laid out the forming dies, test article and Space Tug designs |
| Mr. Al Lindahn Jr. | - | Performed the development tests, test article assembly, test setup, and testing |
| Mr. Carl Jernberg | - | Aided in the test setup |
| Mr. Tom Bechdoldt | - | Fabricated the forming dies |
| Mr. William A. Bailey | - | Directed the stretch and hydropress forming |
| Mr. Charles L. Hovey | - | Supervised the jacket welding |
| Mr. Charles R. Arnold | - | Gold coated the tank and jacket |

Some of the technical data on the microsphere insulation performance and jacket design concept were developed under Lockheed Independent Technology Programs prior to and concurrent with this program. These data include:

- Flat plate conductivity tests of microspheres as a function of temperature, gas pressure, and compressive load with up to a hundred 1-atmosphere load cycles
- Development of the microsphere insulation thermal model
- Microsphere gas flow conductance data

- Gas fluidization method of microsphere transfer (that was demonstrated on this program)
- Development of and demonstration of the jacket design concept in a flat panel configuration (which was repeated on this program with a larger panel)

The results of this program and a complete description of the lightweight, high-performance microsphere insulation/flexible vacuum jacket system are provided in this report.

Richard T. Parmley
Principal Investigator

CONTENTS

Section		Page
	FOREWORD	iii
	ILLUSTRATIONS	ix
	TABLES	xiii
1	SUMMARY AND INTRODUCTION	1-1
	1.1 Summary	1-1
	1.2 Introduction	1-2
2	GOALS AND ENVIRONMENTS	2-1
	2.1 Goals	2-1
	2.2 Environments	2-6
3	SUBSCALE TEST ARTICLE DESIGN	3-1
4	SYSTEM CONCEPT DEVELOPMENT	4-1
	4.1 Vacuum-Jacket Development	4-1
	4.1.1 Flat Panel Vacuum-Jacket Flexure Tests	4-1
	4.1.2 Minimum Wedge Angle Tests	4-7
	4.1.3 Resistance Seam Weld Development	4-8
	4.1.4 Jacket Final Closure Development	4-12
	4.1.5 Jacket Repair Methods	4-18
	4.1.6 Preliminary Insulation Thickness Optimization	4-19
	4.1.7 Deflection Requirements of the Test Tank Vacuum Jacket	4-19
	4.1.8 Contoured Forming Dies	4-21
	4.1.9 Vacuum-Jacket Fabrication	4-30
	4.1.10 Test of the Hemispherical Vacuum Jacket	4-48
	4.1.11 Spring Assembly Development	4-63
	4.1.12 Tests of Gold Coatings	4-72

Section	Page	
4.2	Microsphere Insulation Processing Development	4-74
4.2.1	Sizing	4-74
4.2.2	Compression	4-75
4.2.3	Separation of Unbroken Spheres	4-75
4.2.4	Microsphere Vacuum Bakeout and Transfer	4-78
4.3	Microsphere Insulation Properties	4-85
5	SUBSCALE TEST ARTICLE FABRICATION	5-1
6	ENVIRONMENTAL AND OPERATIONAL TESTS	6-1
6.1	Test Article	6-1
6.2	Instrumentation	6-3
6.2.1	Temperature	6-3
6.2.2	Pressure	6-8
6.2.3	Tank Boiloff	6-10
6.2.4	Jacket Deflection	6-10
6.3	Test Setup	6-12
6.4	Test Procedure	6-12
6.4.1	Ground-Hold Thermal Performance	6-14
6.4.2	Space-Hold Thermal Performance	6-14
6.4.3	Thermal Performance as a Function of Jacket Compressive Load	6-15
6.4.4	Thermal Performance as a Function of Insulation Pressure	6-15
6.4.5	Thermal Performance Following Simulated Flight Cycles	6-16
6.5	Test Results	6-17
6.5.1	Thermal Performance	6-17
6.5.2	Mechanical Stability and Packing of Microsphere Insulation Under Load Cycling	6-24
6.5.3	Post-Test Emittance Measurements	6-25
6.5.4	Microsphere Self-Weight Contact Force	6-26
6.5.5	Vacuum Integrity and Evacuation Rate	6-28

Section		Page
6.6	Discussion of Test Results	6-30
6.6.1	Insulation Thermal Model	6-30
6.6.2	Effect of Compressive Loading on Thermal Performance	6-38
6.6.3	Effect of Insulation Gas Pressure on Thermal Performance	6-40
6.6.4	Space-Hold Thermal Performance	6-43
6.6.5	Ground-Hold Thermal Performance	6-44
6.6.6	Comparison of Calculated and Experimental Test Article Heat Inputs	6-45
6.6.7	Experimental Uncertainties	6-47
7	DESIGN AND ANALYSIS OF SPACE TUG INSULATION SYSTEM	7-1
7.1	Insulation System Preliminary Design	7-1
7.2	Insulation Thickness Optimization	7-10
7.3	Weight and Thermal Performance	7-13
7.4	Manufacturing Plan	7-13
7.4.1	Facilities and Tooling	7-16
7.4.2	Vacuum-Jacket Forming	7-16
7.4.3	Vacuum-Jacket Joining	7-20
7.4.4	Gold Coating	7-20
7.4.5	Spring Assembly Fabrication	7-22
7.4.6	Microsphere Insulation Processing	7-22
7.4.7	Final Assembly	7-23
7.5	Operational Requirements	7-23
7.6	Schedule and Costs	7-25
7.7	Performance Comparison With Goals	7-26
7.8	Payload Sensitivity Analyses	7-38
8	CONCLUSIONS	8-1
9	REFERENCES	9-1
10	DISTRIBUTION LIST	10-1

PRECEDING PAGE BLANK NOT FILMED

ILLUSTRATIONS

Figure		Page
1-1	Test Article	1-4
2-1	Reference Cryogenic Space Tug Vehicle	2-3
2-2	Orbiter Payload Bay Vibration Environment	2-7
2-3	Orbiter Payload Bay Acoustic Environment	2-7
2-4	Temperature and Pressure Environments	2-8
2-5	Acceleration Environment	2-9
3-1	Test Article Drawing Tree	3-1
3-2	Vacuum-Jacket Assembly	3-3
3-3	Spring/Kevlar Attachment Assembly	3-7
3-4	Strut Installation	3-11
3-5	Upper Dome Assembly	3-17
3-6	Lower Dome Assembly	3-21
4-1	Flat Male Metal Die for Vacuum-Jacket Forming	4-2
4-2	Biaxial Stretch Test Appartus	4-4
4-3	Biaxial Expansion Test Panel	4-4
4-4	Elastic-Plastic Range Definition of Flat Test Panels	4-6
4-5	Elastic-Plastic Range Definition of Larger Joint Flat Areas in the Flat Test Panels	4-6
4-6	Joint Designs	4-7
4-7	Wedge Angle Test Apparatus	4-9
4-8	Net Change in Wedge Base Dimension as a Function of Thermal Cycles	4-10
4-9	50-kVA Sciaky Seam Welder	4-11
4-10	Leak Check Test Panel	4-11
4-11	Soldered Final Closure Design	4-13
4-12	Overlap Joint Soldering Tool	4-15
4-13	Wooden Support Ring	4-15

Figure		Page
4-14	Flange Joint Soldering Tool	4-16
4-15	Flange Tool Installed	4-16
4-16	Welded Final Closure Joint Design	4-17
4-17	Wedge Design Procedure	4-25
4-18	Expansion Pattern Relationship	4-26
4-19	Stretch Form Block	4-27
4-20	Gore Forming Die	4-31
4-21	Polar Cap Die	4-33
4-22	Setup for Milling Wedge Slots	4-35
4-23	Closetup of End Mill Operation	4-35
4-24	Stretch Form Block	4-36
4-25	Gore Forming Die (Minus Stiffening Beads)	4-36
4-26	Polar Cap Die	4-36
4-27	Stretch Forming Sequence of Stainless Steel Panels	4-38
4-28	Gore Panel Forming Sequence for the Test Article	4-45
4-29	Jacket-Hemisphere Assembly Sequence (Does Not Include Final Closure Joint)	4-47
4-30	Jacket Pressure Expansion Test Setup	4-49
4-31	Measuring Wedge Expansion	4-51
4-32	Vertical Wedge Expansion in the Elastic Range	4-54
4-33	Horizontal Wedge Expansion in the Elastic Range	4-54
4-34	Elastic to Plastic Transition Point of Wedges	4-55
4-35	Elastic Range Tested for Polar Cap Transition Wedges	4-55
4-36	Elastic-Plastic Transition Points Versus Wedge Height	4-56
4-37	Comparison of Flat Panel and Hemisphere Expansion Data	4-58
4-38	Potential Out-of-Plane Movement of the Vacuum Jacket	4-58
4-39	Point Load Expansion Test (as Viewed From Inside the Plexiglas Hemisphere)	4-60
4-40	Radial Expansion Measurements	4-60
4-41	Point Load Expansion Increase in Jacket Radius for Unstiffened Panels	4-62
4-42	Point Load Expansion Increase in Jacket Radius for Stiffened Panels (0.21%)	4-62

Figure		Page
4-43	Point Load Expansion Increase in Jacket Radius for Unstiffened Panels (0.43%)	4-64
4-44	Point Load Expansion Increase in Jacket Radius for Stiffened Panels (0.43%)	4-64
4-45	Spring Assembly	4-67
4-46	Kevlar 49 Thermal Conductivity	4-67
4-47	Tensile Tests of the Spring Assembly	4-69
4-48	Inspection Method for Spring/Jacket Solder Joint	4-71
4-49	Effect of Thermal Cycling in Gold-Coated Samples	4-73
4-50	Microsphere Size Distribution	4-73
4-51	Microsphere Compression Apparatus	4-76
4-52	Microsphere Flotation Apparatus	4-76
4-53	The Effect of Water Immersion on the Microspheres Compressive Strength Capability	4-77
4-54	Microsphere Vacuum Bakeout and Transfer Container	4-79
4-55	Temperature-Pressure History of the Vacuum Bakeout Apparatus	4-80
4-56	Effect of Vacuum Bakeout on Microsphere Compressive Strength	4-81
4-57	Pressure Decay of Microspheres as a Function of Bakeout Time	4-84
4-58	Microsphere Transfer Apparatus	4-84
4-59	Microsphere Insulation Physical Properties	4-85
4-60	Microsphere Evacuation Characteristics	4-86
5-1	Test Article Assembly Sequence	5-3
6-1	Test Article Mounted on Vacuum Chamber Door	6-2
6-2	Warm Boundary Temperature Control	6-2
6-3	Test Article Instrumentation	6-5
6-4	Vacuum-Jacket Pressure Measurement and Control	6-9
6-5	Test Tank Fill, Dump, Vent, and Boiloff Instrumentation	6-11
6-6	Chamber Test Setup	6-13
6-7	Data Processor Terminal	6-13
6-8	Ground-Hold Heat Rates	6-19
6-9	Space-Hold Heat Rates	6-19

Figure		Page
6-10	Strut Temperature Profiles	6-21
6-11	Effect of Insulation Gas Pressure on Heat Rates	6-22
6-12	Effect of Compressive Load on Heat Rates	6-23
6-13	Microsphere Packing as a Function of Load Cycles	6-24
6-14	Damaged Vacuum Jacket Caused by Accidental Overpressurization	6-26
6-15	Microsphere Self-Weight Test Apparatus	6-28
6-16	Microsphere Self-Weight [$\delta = 1.69$ cm (0.66 in.)]	6-29
6-17	Microsphere Self-Weight [$\delta = 0.98$ cm (0.39 in.)]	6-29
6-18	Dimensionless Solid-Phase Thermal Conductivity as a Function of Compressive Pressure	6-39
6-19	Comparison of Flat Plate and Test Tank Solid-Phase Thermal Conductivity Under a Compressive Load	6-39
6-20	Variation in Solid Conductivity With Packing Geometry	6-40
6-21	Apparent Thermal Conductivity of Microsphere Insulation as a Function of Gas Species and Pressure at Two Average Temperatures	6-42
6-22	Predicted Versus Experimental Values of Gas-Phase Thermal Conductivity	6-42
6-23	Space-Hold Thermal Conductivity	6-43
6-24	Ground-Hold Thermal Conductivity	6-45
7-1	Space Tug Insulation System Design	7-3
7-2	Space Tug Insulation System Design (Cont.)	7-5
7-3	Space Tug Insulation System Design (Cont.)	7-7
7-4	Relief Valve Design	7-11
7-5	Relief Valve Control System Schematic	7-11
7-6	Space Tug Ground-Hold Conductivity	7-12
7-7	Space Tug Space-Hold Conductivity	7-12
7-8	Optimum Insulation Thickness	7-13
7-9	Comparison of Jacket Forming Methods	7-18
7-10	Electroless Nickel Jacket Fabrication Method	7-19
7-11	LH ₂ Tank Final Assembly Sequence	7-24
7-12	Microsphere Insulation System DDT&E Schedule	7-27
7-13	Payload Performance Sensitivity to Microsphere Bulk Density	7-40
7-14	Payload Performance Sensitivity to Microsphere Thermal Conductivity	7-40

TABLES

Table		Page
2-1	Design Data for the Reference Cryogenic Space Tug (Taken From Ref. 1-3)	2-2
2-2	Performance Goals	2-5
4-1	Summary of Gore-Forming Development to Eliminate Tearing	4-40
4-2	Effect of Vacuum-Anneal on Jacket Properties	4-41
4-3	Summary of Gore-Forming Development to Eliminate Wrinkling	4-42
4-4	Wedge Expansion Test Data (Pressure Test)	4-52
4-5	Wedge Dimensions	4-53
4-6	Spring Force Required for Vacuum-Jacket Expansion	4-65
5-1	Weight and Thickness of Test Article Insulation System	5-11
6-1	Instrumentation and Data Acquisition Equipment	6-4
6-2	Summary of Test Results	6-18
6-3	Emittance Measurements of Jacket and Tank After 13 Thermal/ Pressure Cycles	6-27
6-4	Clearance Between Strut Boxes and the Tank	6-27
6-5	Calculated Versus Measured Heat Rates	6-40
7-1	Space Tug Vacuum Jacket Characteristics	7-2
7-2	Weight Statement for the Space Tug Microsphere Insulation System	7-14
7-3	Heat Transfer Summary for the Space Tug Microsphere Insulation System	7-15
7-4	Major Facilities and Tooling Requirements (Hydropress Forming)	7-17
7-5	Comparison of Forming Methods	7-21
7-6	Comparison of Final Closure Joint Locations for the LH ₂ Jacket	7-22
7-7	Microsphere Insulation System Inspection and Refurbishment Requirements	7-25

Table		Page
7-8	DDT&E Cost Breakdown for Microsphere Processing Equipment (Hours and 1973 Dollars in Thousands)	7-29
7-9	DDT&E Cost Breakdown for Spring Assembly Development (Hours and 1973 Dollars in Thousands)	7-29
7-10	DDT&E Cost Breakdown for Jacket Tooling and Fixtures (Hours and 1973 Dollars in Thousands)	7-30
7-11	DDT&E Engineering Model Cost Breakdown (LO ₂ Insulation System) (Hours and 1973 Dollars in Thousands)	7-31
7-12	DDT&E Engineering Model Cost Breakdown (LH ₂ Insulation System) (Hours and 1973 Dollars in Thousands)	7-32
7-13	DDT&E Qualification Model Cost Breakdown (LO ₂ Insulation System) (Hours and 1973 Dollars in Thousands)	7-33
7-14	DDT&E Qualification Model Cost Breakdown (LH ₂ Insulation System) (Hours and 1973 Dollars in Thousands)	7-34
7-15	Insulation Systems Cost Breakdown Comparison (Hours and 1973 Dollars in Thousands)	7-35
7-16	Insulation Systems Cost Comparison Summary (Millions of 1973 Dollars)	7-36
7-17	Helium-Purged Superfloc Insulation System Weight	7-37
7-18	Insulation System Weight Comparison	7-37
7-19	Insulation System Thermal Performance Comparison	7-39
7-20	Insulation System Syn-Eq. Payload Performance Comparison	7-39

Section 1
SUMMARY AND INTRODUCTION

1.1 SUMMARY

A new type of light-weight, vacuum-jacketed, load-bearing cryogenic insulation system was developed and tested on a 1.17-m (46-in.) spherical test tank. The vacuum jacket consists of 0.08 mm (0.003 in.) thick 321 stainless steel formed into a wedge design that allows elastic jacket movements as the tank shrinks (cools) or expands (warms up or is pressurized). Hollow glass spheres, approximately 80 μm in diameter with a bulk density of 0.069 g/cc (4.3 lb/ft³), provide the insulating qualities and one-atmosphere load bearing capability required. This design, fabrication, and test effort developed the manufacturing methods and engineering data needed to scale the system to other tank sizes, shapes, and applications.

Specifically, the program demonstrated that thin-wall jackets can be formed and welded to maintain the required vacuum level of .013 Pa yet flex elastically for multiple reuses. No significant shifting or breakage of the microspheres occurred after 13 simulated Space Tug flight cycles on the test tank and a hundred 1-atmosphere load cycles in a flat plate calorimeter. The test data were then scaled to the Space Tug LO₂ and LH₂ tanks, and weight, thermal performance, payload performance, and costs were compared with a helium-purged multilayer insulation system.

The Space Tug thermal performance of the insulation under 1-atmosphere load is outstanding with a conductivity of 3.8×10^{-3} W/m²°K (2.2×10^{-3} Btu/hr ft²°R), 280 to 20°K. Under no load, the measured thermal conductivity drops to 2.7×10^{-4} W/m²°K (1.6×10^{-4} Btu/hr ft²°R), 222 to 20°K. Since approximately 80 percent of the no-load heat transfer is by radiation, significant reductions in conductivity appear reasonable with design improvements in the insulation.

Applications where the low-weight and good thermal performance under varying external loads make this system attractive include the Space Tug, Single-Stage-to-Orbit Shuttle, LH_2 fueled aircraft, and LNG storage and transportation.

1.2 INTRODUCTION

The next generation of reusable space vehicles, such as the LO_2/LH_2 Space Tug, must perform both within and outside the atmosphere. To prevent condensation of atmospheric gases within the insulation when the tanks are cooled to cryogen temperature, noncondensable gases such as helium must be substituted for air (helium-purged system) or the air must be removed (vacuum-jacketed system).

From an operational simplicity and cost effectiveness viewpoint, vacuum-jacketed insulation systems are more desirable than gas-purged systems, since the latter must be purged on the ground, vented during ascent, and repurged during reentry and on landing for a specified period.

In addition, results of a test program (Ref. 1-1) have shown multilayer systems must initially be baked out in vacuum and must then be kept in either a dry gas or a vacuum environment at all times to achieve repeatable thermal performance. This requirement increases the cost, as well as the manufacturing and operational complexity of a gas-purged system, whereas the preconditioning treatment is required only once for a vacuum-jacketed system.

On the other hand, the major problems associated with a vacuum-jacketed insulation system are: (1) maintenance of an adequate vacuum level throughout the life of the system and (2) reducing the system weight so it is competitive with the gas-purged system.

Prior attempts at developing a flexible, load-bearing insulation vacuum jacket system (Refs. 1-2, 1-3) have not been entirely successful because jacket materials, constructed

of plastic/metal foil laminates, were allowed to expand and contract in an uncontrolled fashion as the tank dimensions change during cryogen fill or tank warmup. The resulting three-corner folds and pinhole leaks prevented obtaining the required low pressure of .0013 Pa. In addition, the insulation compressed under load requiring greater flexure capability of the jacket and the multilayer thermal performance degraded with load cycling. The high use of plastic materials, both in the jacket, and in the multilayer insulation system also presents an out-gassing problem. Use of inorganic powders does not solve the problem because they pack under load due to their irregular shape, causing the heat rates to increase.

A new hollow-glass microsphere load-bearing insulation and flexible stainless-steel jacket concept developed on this program overcomes the deficiencies noted for the previously tested plastic/metal laminate vacuum-jacketed, multilayer-insulation system concepts. The stainless-steel jacket, formed with a controlled elastic biaxial flex design as shown in Fig. 1-1, permits maintenance of a low insulation pressure for long periods of time. Use of organic materials in the insulation system is kept to a bare minimum and the nature of the glass microsphere insulation allows it to be thoroughly vacuum baked out at considerably higher temperatures than is possible if it were installed on the aluminum tank first. In addition, the required insulation pressure of .013 Pa under no load and 1.3 Pa under 1-atmosphere load is one to three orders of magnitude above that required of multilayers (.0013 Pa). The weight of the system is three times lighter than the most advanced vacuum-jacketed design demonstrated to date, a free-standing honeycomb hard shell with a multilayer insulation system, and is competitive with a helium-purged, multilayer insulation system. Its outstanding thermal performance under load, low- and high-temperature capability up to 480°C (900°F), nonflammability, nontoxic products in case of a fire, multiple thermal cycling capability without jacket leakage or change in thermal performance, and low weight makes the system concept a leading candidate for other reusable applications.

REPRODUCTION OF THIS PAGE FROM
ORIGINAL PAGE IS POOR

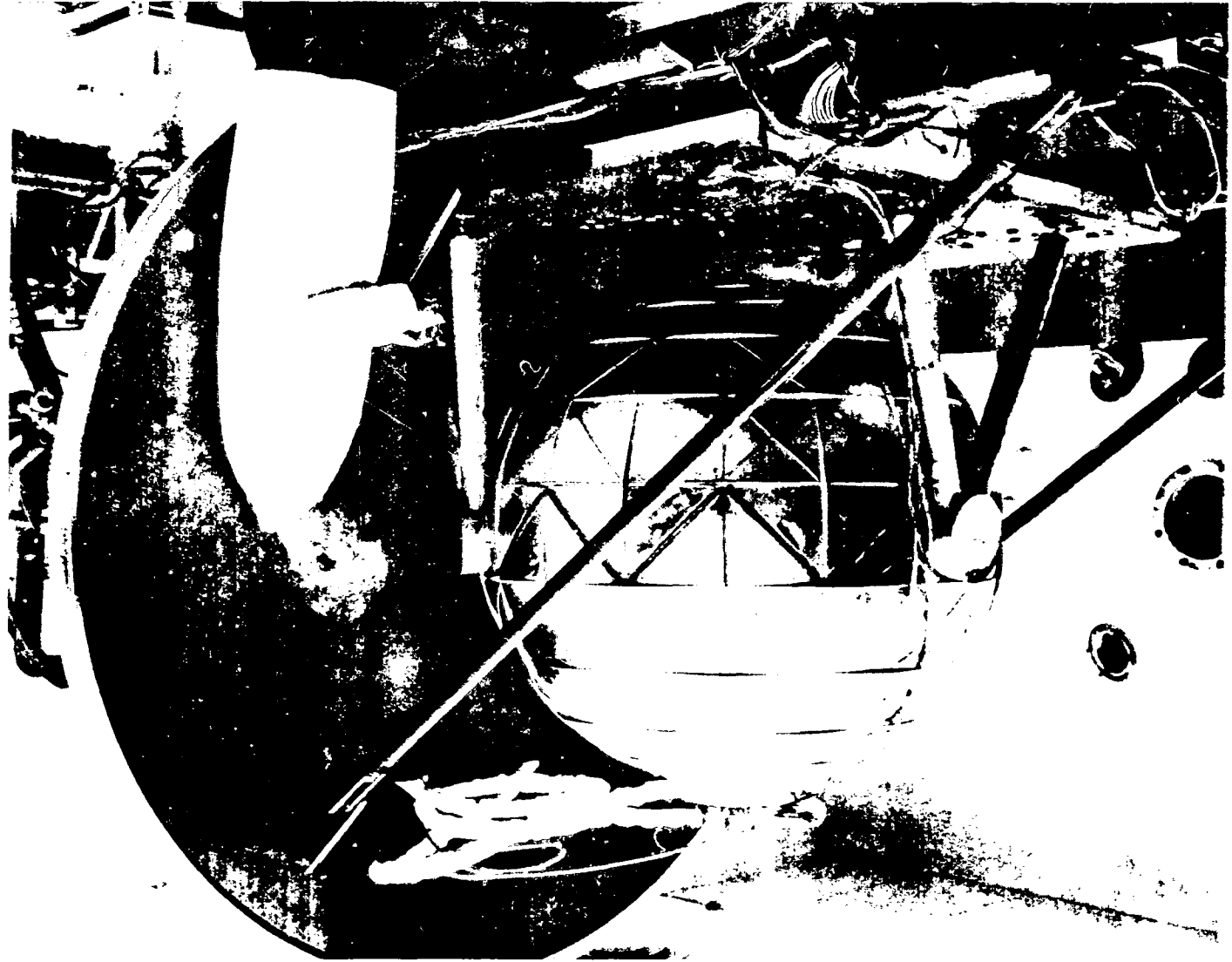


Fig. 1-1 Test Article

LOCKHEED PALO ALTO RESEARCH LABORATORY
LOCKHEED MISSILES & SPACE COMPANY, INC.
A SUBSIDIARY OF LOCKHEED AIRCRAFT CORPORATION

The major objective of this program is to provide the necessary technology advancements required to demonstrate the design characteristics and thermal performance of the microsphere insulation/flexible metal vacuum jacket system on a subscale tank (for reusable space vehicle applications such as the Space Tug).

This major objective can be subdivided into the following secondary objectives:

- Define the optimum design approach and associated analytical techniques
- Demonstrate the manufacturing techniques necessary to fabricate, assemble, inspect, and repair a subscale system
- Demonstrate the installed thermal performance of the subscale system as a function of boundary temperatures, compressive load, insulation gas pressure, and multiple reuse cycles
- Demonstrate the ability of the subscale system to maintain an adequate vacuum level, structural integrity, and minimal shifting of the insulation after multiple reuse cycles
- Provide sufficient data to scale the thermal, weight, payload performance, manufacturing, and cost results to full-scale LO_2 and LH_2 tanks of the Space Tug for direct comparison with a helium-purged multilayer insulation system defined in Ref. 1-4.

To achieve these objectives, the program was subdivided into seven tasks which were performed chronologically.

However, to prevent repetition and provide a logical flow of information from one section to another in this report, the Task descriptions are partially rearranged. For example, the full-scale Space Tug system design and performance numbers developed in Task I and updated in Task VII (based on the program results) is shown only in its updated form in Section 7. The goals and environments developed in Task I form Section 2 of this report.

The Task III subscale test article design (Section 3) was moved ahead of the Task II development work that led to the design (Section 4) in order, first, to acquaint the

reader with the basic insulation system concept and, second, to provide insight into why certain types of development work were performed. Tasks V and VI were combined into Section 6 covering all testing of the test article.

Summaries of each task and the section in which they are described in the report follow:

- Task I: Analysis and Requirements Definition (Sections 2 and 7)
Weight, thermal performance, payload performance, and inspection and refurbishment goals are defined for the microsphere/jacket system using a helium-purged multilayer insulation Space Tug system as the baseline reference. Operational environments are also established. A preliminary design of the microsphere/jacket system is then performed for the Space Tug LH₂ tank from which information relating to the established goals can be calculated.
- Task II: System Concept Development (Section 4)
Using the design information developed in Task I, experimental evaluations with supporting analyses are performed to substantiate key design features. Some of these major evaluations are:
 - Confirmation of the jacket expansion adequacy for compound contoured surfaces
 - Demonstration of adequate insulation thickness control
 - Development of jacket joining and inspection procedures
 - Development of localized jacket repair procedures
 - Demonstration of jacket and tank low-emittance coating procedures and properties
 - Demonstration of microsphere insulation processing procedures
 - Demonstration of a vacuum bakeout and transfer container for the microspheres
 - Overall demonstration of the system on a Plexiglas hemisphere assembly (simulating the tank surface), including jacket expansion, microsphere fill techniques, microsphere settling characteristics under vibration, and demonstration of localized repair procedures

- Task III: Subscale Test Article Design (Section 3)

Using the results of Tasks I and II, a complete test article design is performed on the microsphere/jacket system using an available spherical flight-weight, 1.17 m (46-in.) diameter, 2219 aluminum test tank and six filament-wound, epoxy-fiberglass support struts.

- Task IV: Subscale Test Article Fabrication (Section 5)

The test article designed in Task III is fabricated, leak checked, and functionally checked out prior to start of the testing in Task IV. The fabrication includes minor modifications to the test tank and installation of test instrumentation as the Task proceeds.

- Task V: Environmental Tests (Section 6)

Using the test article fabricated and instrumented in Task IV and a Test Plan prepared in this Task, 19 flight cycles are performed, each cycle simulating cryogen loading on the ground, ascent (chamber evacuation), orbit (boiloff plus propellant drain), reentry (chamber backfill with GN₂), and landing and storage (warmup to ambient temperatures). Thermal performance under both ground-hold and space-hold conditions are performed periodically to determine the effect of the flight cycles on thermal performance. Because of accidental jacket damage due to operator error, the test program was terminated following 13 flight cycles.

- Task VI: Operational Tests (Section 6)

A series of tests define (1) the effect of low nitrogen gas pressure (simulating air in-leakage) and (2) the effects of increasing compressive load on overall heat-transfer rates.

- Task VII: Analysis and Design of Full-Scale System (Section 7)

After reviewing the results of Tasks I through VI, the preliminary insulation design prepared in Task I for the full-scale LH₂ tank is updated and a design is also prepared for the full-scale LO₂ tank. Sufficient weight, costs, and payload performance numbers are calculated to allow a direct comparison with the Space Tug helium-purged multilayer insulation system. A manufacturing plan is provided.

Section 2
GOALS AND ENVIRONMENTS

A helium-purged multilayer insulation system is currently defined as the baseline choice for the cryogenic Space Tug. Since the vacuum jacketed microsphere insulation system developed on this program is a candidate to replace the purge system, a series of goals was established using the purge system design given in Ref. 1-4 as a baseline reference. The performance numbers for the vacuum jacketed microsphere insulation system are compared later in Section 7 with the goals established at the beginning of the program. In addition, the environments in which the insulation system must operate were established for use as design criteria.

2.1 GOALS

Using the Option 2 Cryogenic Space Tug design (Ref. 1-4) shown in Fig. 2-1 and defined in Table 2-1, a series of weight, thermal, payload, and inspection and refurbishment goals were established.

The weight goal is shown in Table 2-2. The fuel and oxidizer insulation weights, purge system weights, and helium weights were taken directly from Ref. 1-3. The helium bottle weights were obtained by ratioing the helium required for purge to the total helium onboard the Shuttle and multiplying this ratio times the bottle weight listed in Ref. 1-4. Gaseous oxygen is vented during ascent, but no venting occurs during orbit. The vented LH_2 was calculated by integrating a transient heat flux curve in Ref. 1-4. from liftoff to orbit equilibrium and adding on the orbit equilibrium heat-flux values for the remainder of the 163-hour mission.

The integrated propellant heating goal from liftoff to 163 hours shown in Table 2-2 was calculated using the technique described above for LH_2 boiloff. The Syn.-Eq. payload capability goals shown in the Table were taken directly from Ref. 1-4.

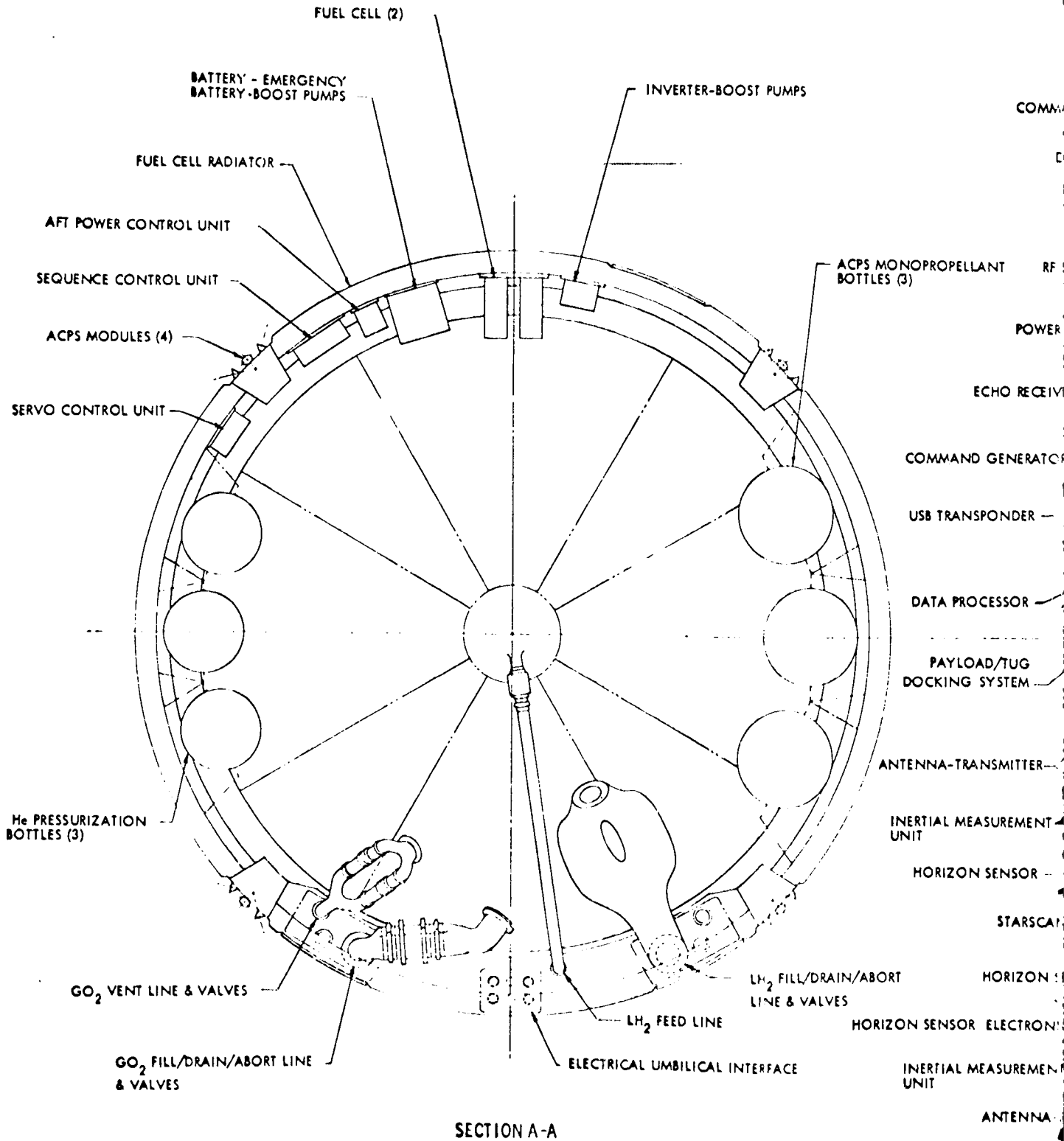
Table 2-1
 DESIGN DATA FOR THE REFERENCE
 CRYOGENIC SPACE TUG (TAKEN FROM REF. 1-4)

Tankage	LO ₂ Tank	LH ₂ Tank
Material	2219-T87 Al	2219-T87 Al
Dimensions		
● Diameter, m (ft)	3.683 (12.08)	4.166 (13.67)
● Length, m (ft)	3.094 (10.15)	5.464 (17.93)
● Cylinder Length, m (ft)	0.053 (0.17)	2.445 (8.02)
● Bulkhead Ratio	1.38	1.38
Capacity, m ³ (ft ³)	19.81 (699.6)	60.75 (2145.5)
Surface Area, m ² (ft ²)	36.05 (388.0)	76.84 (827.1)
Upper Access Cover Diameter ^(a) , m (ft)		0.91 (2.99)
Lower Access Cover Diameter ^(a) , m (ft)	0.91 (2.99)	0.64 (2.10)
Stainless Steel Plumbing ID, m(in.)	LO ₂ Tank	LH ₂ Tank
Pressurization ^(a)	0.01 (0.4)	0.01 (0.4)
Fill/Drain/Abort	0.13 (5.1)	0.15 (5.9)
Feed ^(a)	0.06 (2.4)	0.06 (2.4)
Ground Vent	0.08 (3.2)	0.08 (3.2)
Zero-g Vent ^(a)	0.01 (0.4)	0.01 (0.4)
Fiberglass Strut Data	LO ₂ Tank	LH ₂ Tank
Number	24	6 upper 12 lower
Effective length x Diameter ^(b) , m (ft)	0.38 x 0.038 (1.25 x 0.12)	0.23 x 0.025 (0.75 x 0.08)
Wall ^(b) , m (in.)	6 x 10 ⁻⁴ (0.024)	6 x 10 ⁻⁴ (0.024)

- a. Scaled from drawings.
 b. Estimated values.

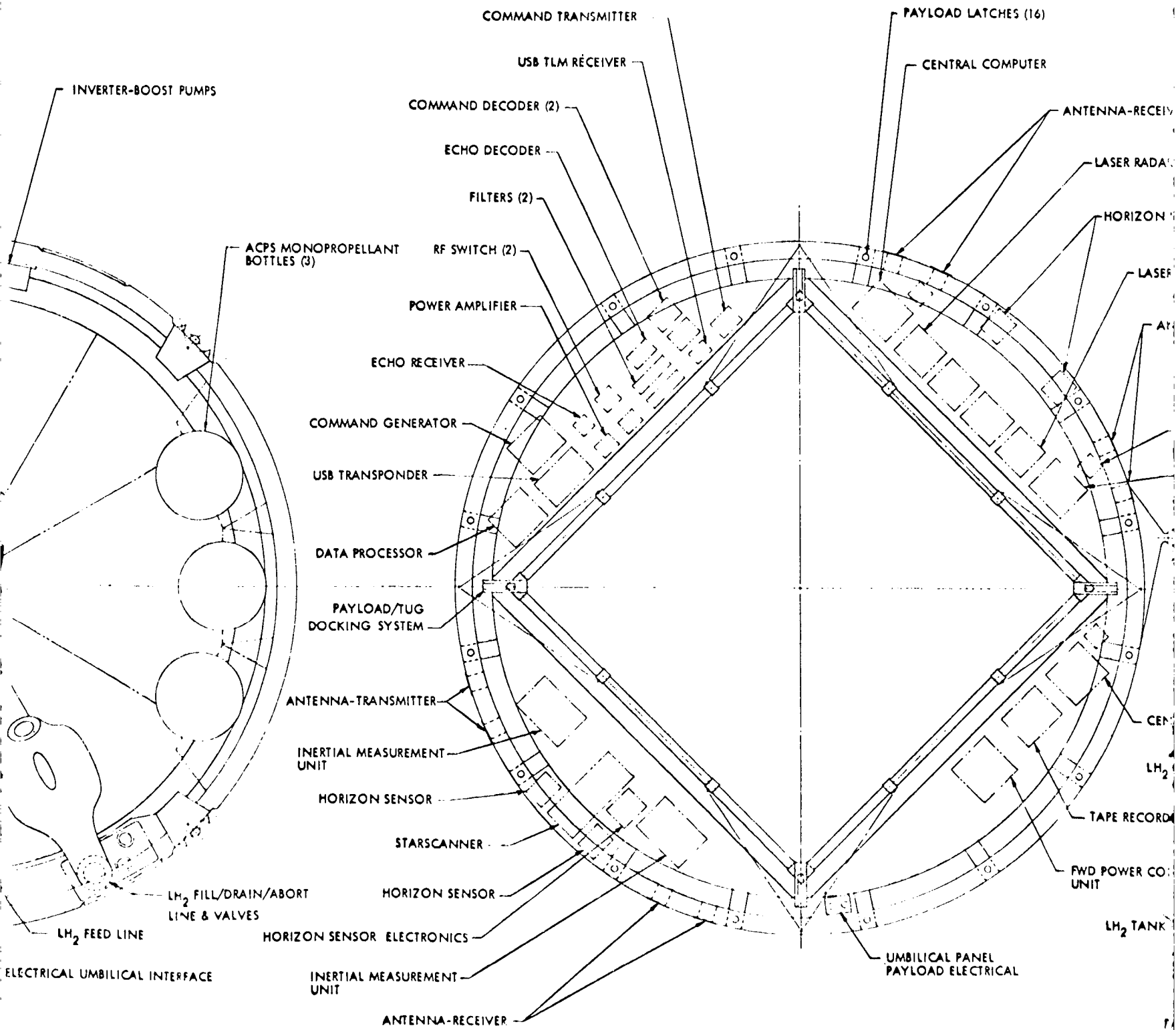
FOLDOUT FRAME

REPRODUCIBILITY
PAGE

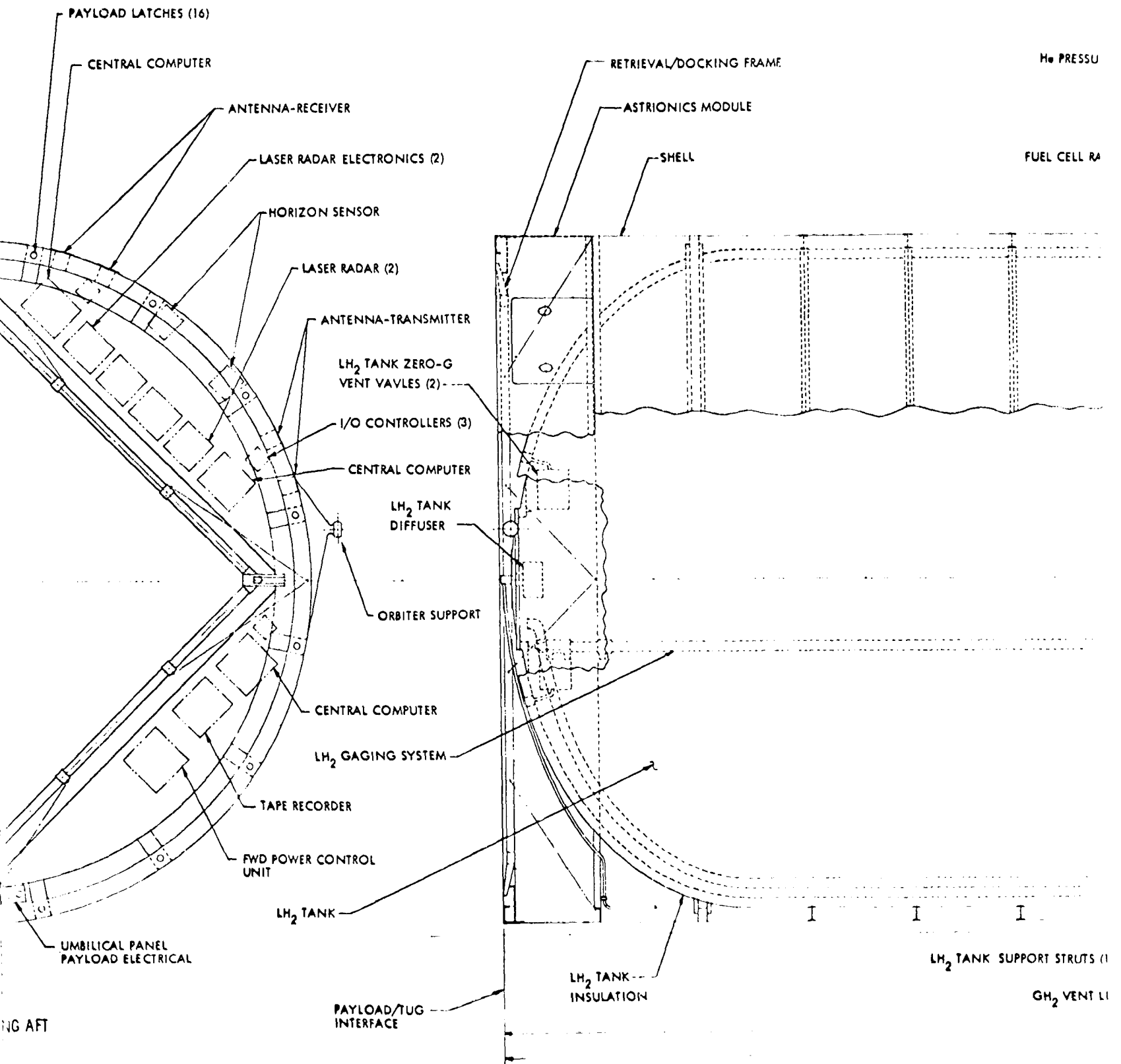


FOLDOUT FRAME 2

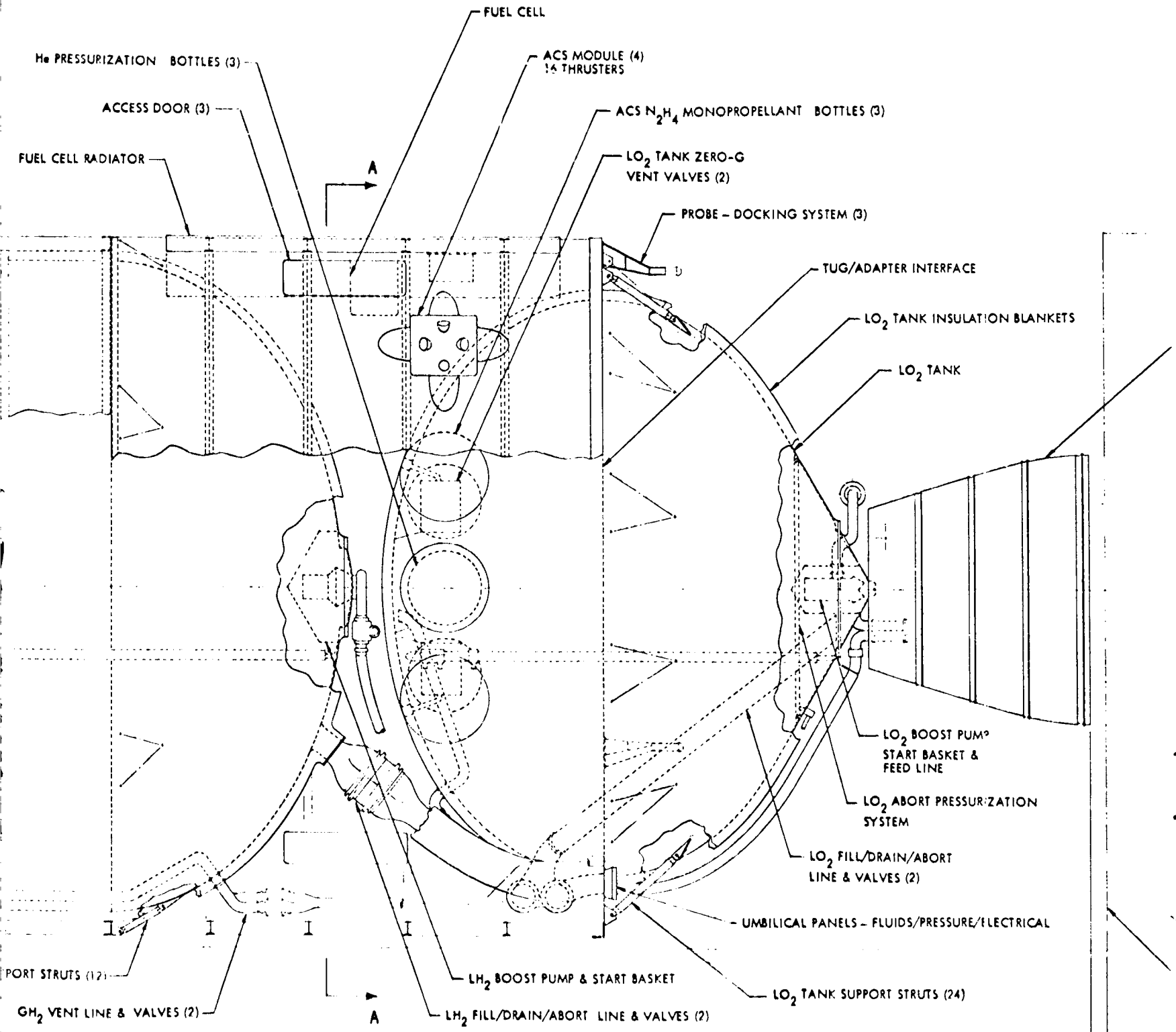
REPRODUCIBILITY OF THE
ORIGINAL PAGE IS POOR



VIEW LOOKING AFT



FOLDOUT FRAME 4

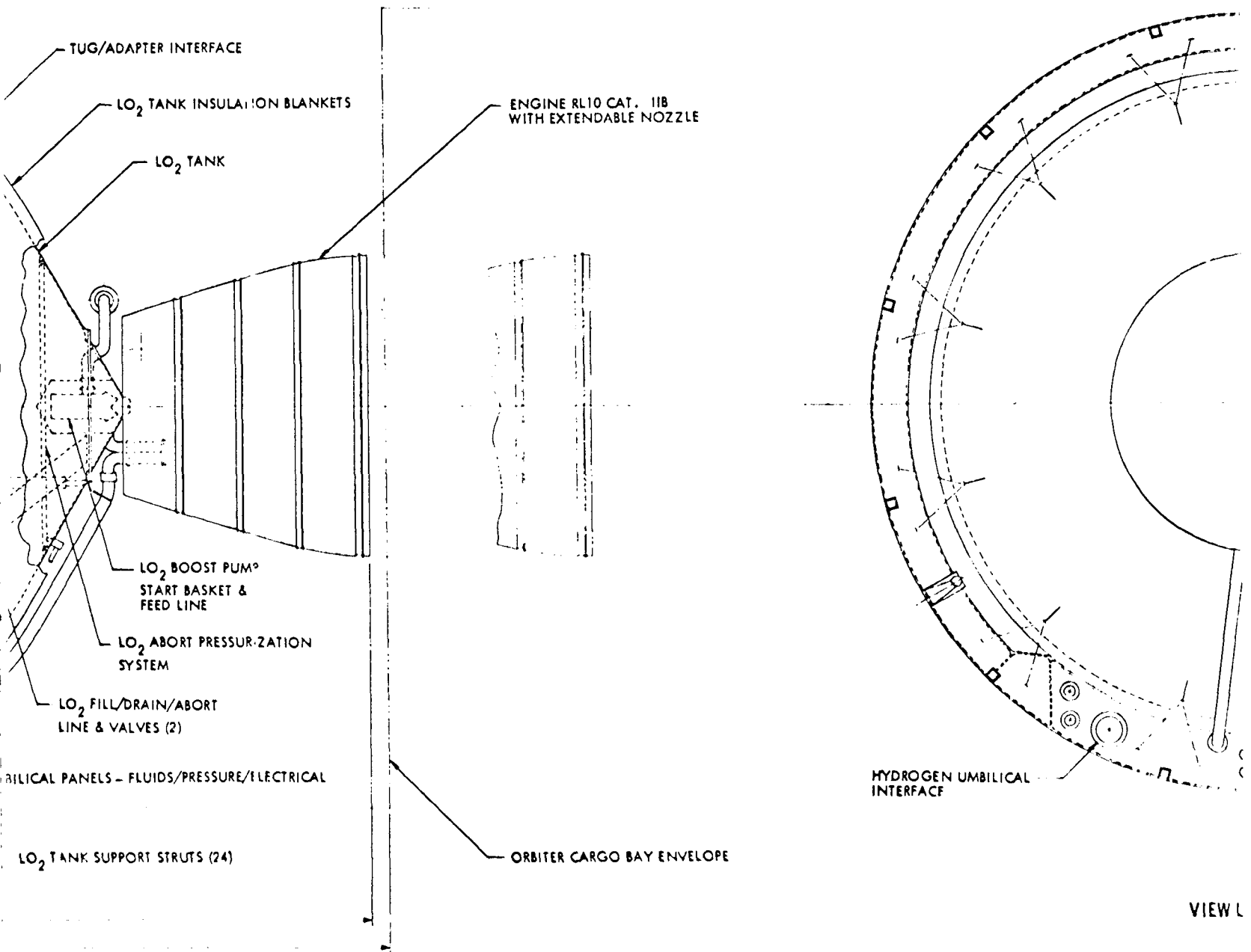


408.93 (10.39m)
412.93 (10.49m)

FOLDOUT FRAME 5

LLANT BOTTLES (3)

KING SYSTEM (3)

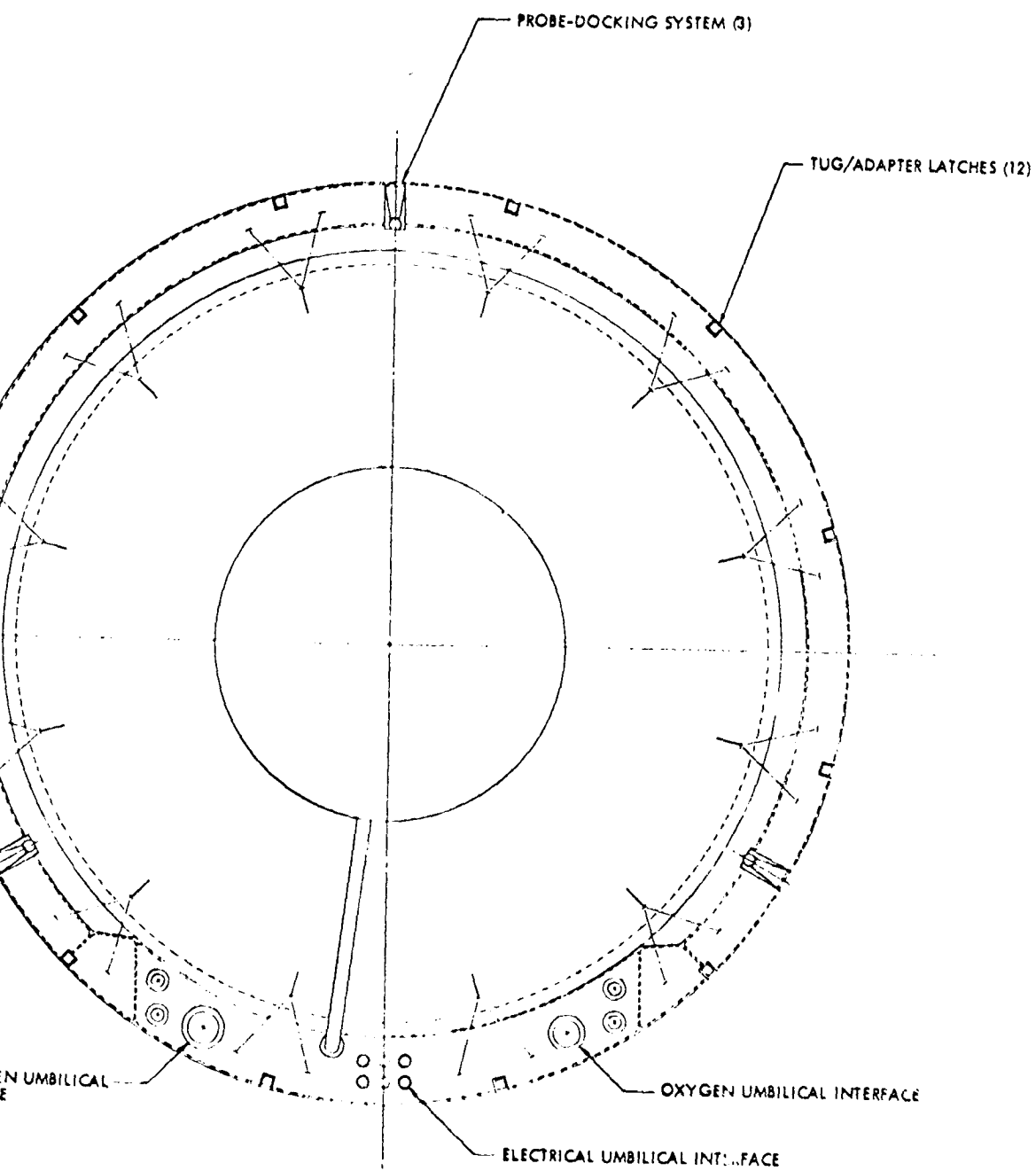


REVISIONS TO THE ORIGINAL

OUT FRAME 5

FOLDOUT FRAME 6

REPRODUCIBILITY OF THE ORIGINAL PAGE IS POOR



VIEW LOOKING FWD

NOTES:

1. ENGINE - RL10 CAT IIB
MR. 5.4:1
HEIGHT - 55.00 IN.
EXIT DIA - 57.50 IN.
2. PROPELLANT TANKS -
LH₂ CAPACITY - 2145.5 FT³
DIA. - 164.00 IN.
LENGTH - 215.12 IN.
BULKHEAD RATIO - 1.38
MTL-AL ALLOY (CRYO. ALLOWABLES)
LO₂ CAPACITY - 699.6 FT³
DIA. - 145.00 IN.
LENGTH - 121.80 (INCL. CONICAL SECT
& 2.10 IN CYL. SEC)
BULKHEAD RATIO - 1.38
MTL-AL ALLOY (CYRO. ALLOWABLES)
3. A.C.S. -
N₂H₄ MONOPROPELLANT
4. STRUCTURE -
COMPOSITE GRAPHITE/EPOXY
SANDWICH SHELL

Fig. 2-1 Reference Cryogenic Space Tug Vehicle

Table 2-2
PERFORMANCE GOALS

Weight Goal \approx 180.9 kg (398.8 lb)

Item	Weight, kg (lb)	Performance Partial	Prorated Burnout Weight kg (lb)
Fuel Tank Insulation	39.0 (86.0)	1	39.0 (86.0)
Oxidizer Tank Insulation	18.6 (41.0)	1	18.6 (41.0)
Purge System (Tug)	92.1 (203)	1	92.1 (203)
Purge System (Shuttle Bay)			
He	2.9 (6.4)	0.15	0.4 (0.9)
Bottles	35.7 (78.7)	0.15	5.4 (11.9)
Boiloff (163-hr Mission)			
LO ₂	0		0
LH ₂	65.1 (143.5)	0.39	<u>25.4 (56.0)</u>
			180.9 (398.8)

Propellant Heating Goal (163-hr mission)

Item	Integrated Propellant Heating	
	(W · hr)	(Btu)
LO ₂ Tank	\leq 4,440	(\leq 15,154)
	\leq 11,559 Before Venting	(\leq 39,450)
LH ₂ Tank	\leq 8,014	(\leq 27,352)

Payload Goal

Item	Syn.-Eq. Payload Capability, kg (lb)
Deployment	\geq 3,597 (\geq 7,930)
Retrieval	\geq 2,260 (\geq 4,982)
Round Trip	\geq 1,370 (\geq 3,020)

The inspection and refurbishment goals that follow were also taken from Ref. 1-4.

- Monitor boiloff during ground hold and pressure rise during orbit
- Visually inspect system after each flight
- Leak test system after each flight
- Functionally test system after each flight
- No scheduled replacements for 19 flights

2.2 ENVIRONMENTS

The induced environments the Space Tug vacuum jacket/microsphere system will experience both within the Shuttle bay and deployed in orbit include vibration, acoustic exposure, shock, thermal and pressure transients, and acceleration. These environments affect the vacuum jacket/microsphere system design in different ways.

For example, vibrations (Fig. 2-2) cause the microspheres to settle and approach their maximum solid packing fraction, $\delta_s = 0.7$, when accelerated with essentially no atmospheric pressure load on the vacuum jacket. (The microspheres are vibrated during the initial fill to control this settling.) Vibration, acoustic, and shock environments could conceivably break the glass microspheres. (Prior tests show no breakage occurred when the microspheres were exposed to an overall sound pressure level of 144 dB. The shuttle cargo bay level is 145 dB as shown in Fig. 2-3.

The temperature and pressure environments (Fig. 2-4) and acceleration environments (Fig. 2-5) affect the structural design of the vacuum jacket and the jacket support as well as the thermal performance of the microspheres.

The atmospheric pressure in the cargo bay shown in Fig. 2-4 initially compresses (supports) the jacket during the early portion of flight (~110 s); other means of jacket support are required for the last 350 s of ascent flight plus the first 700 s of reentry flight.

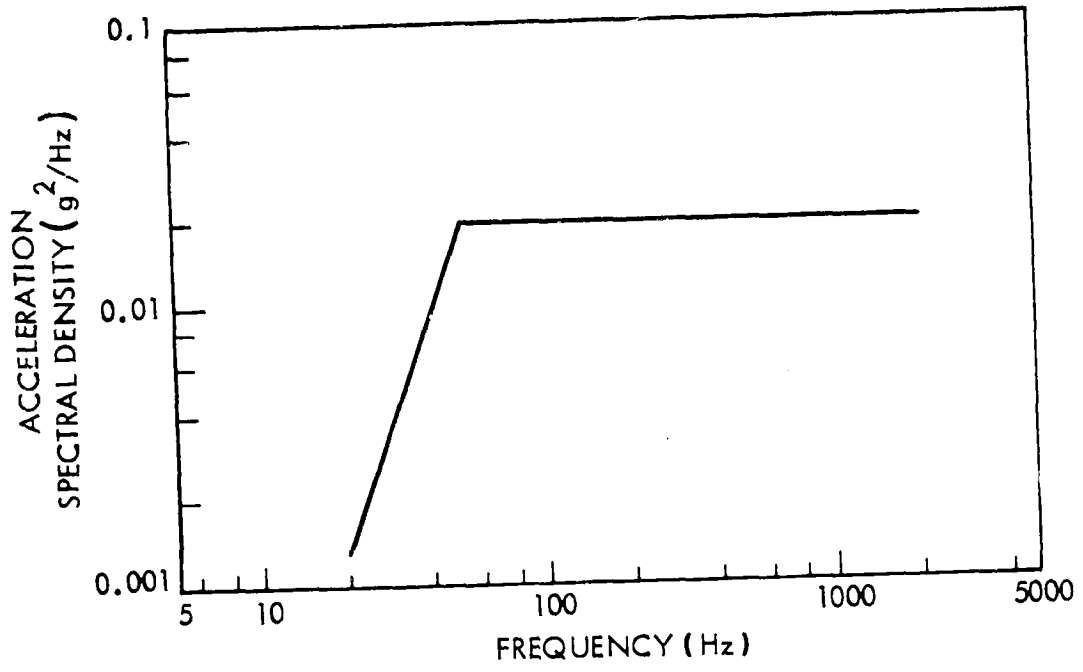


Fig. 2-2 Orbiter Payload Bay Vibration Environment

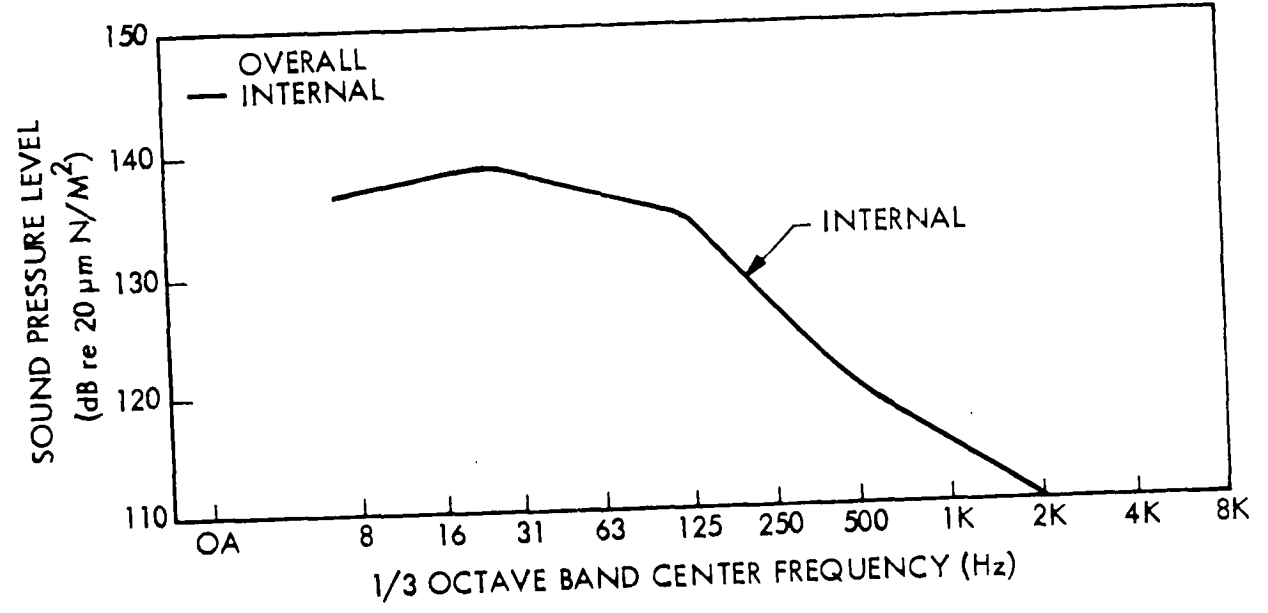
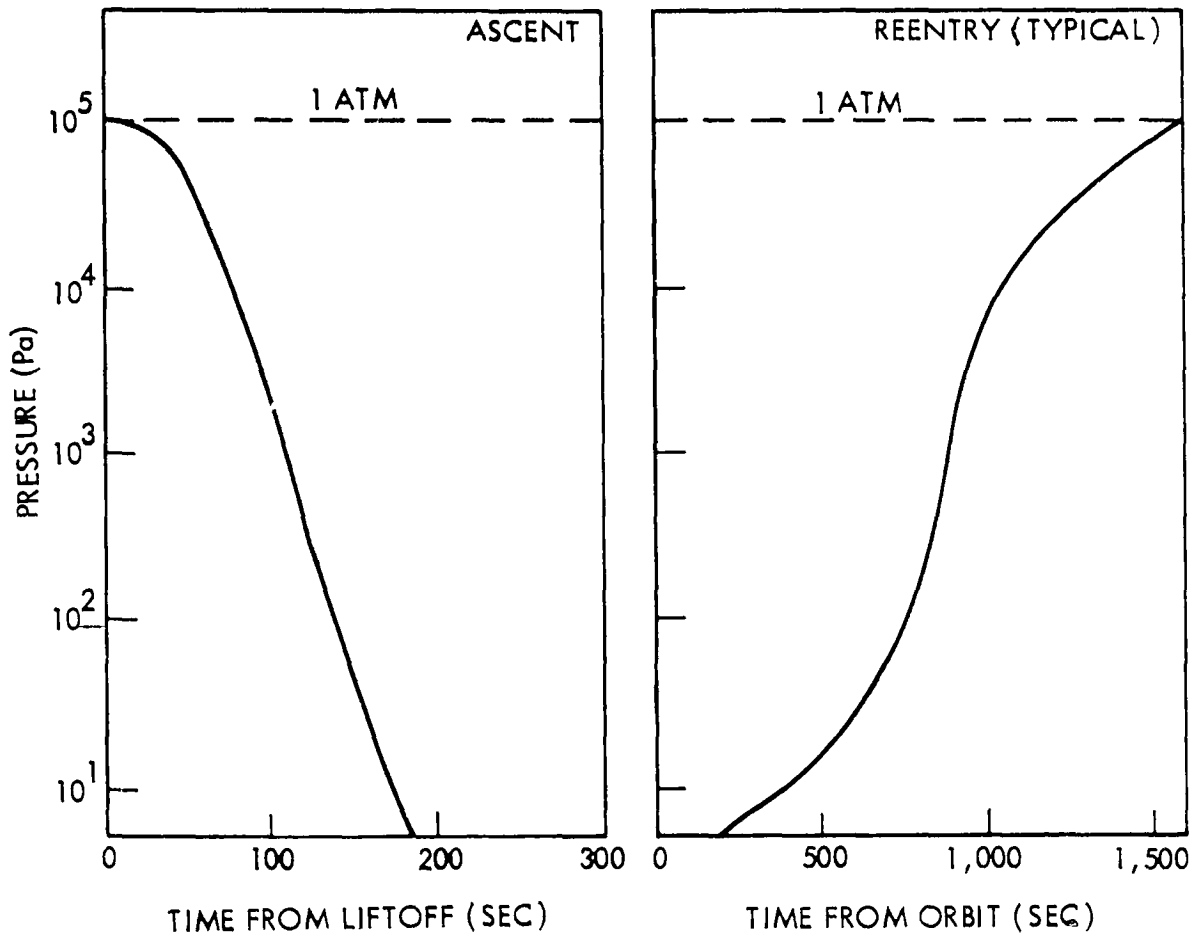


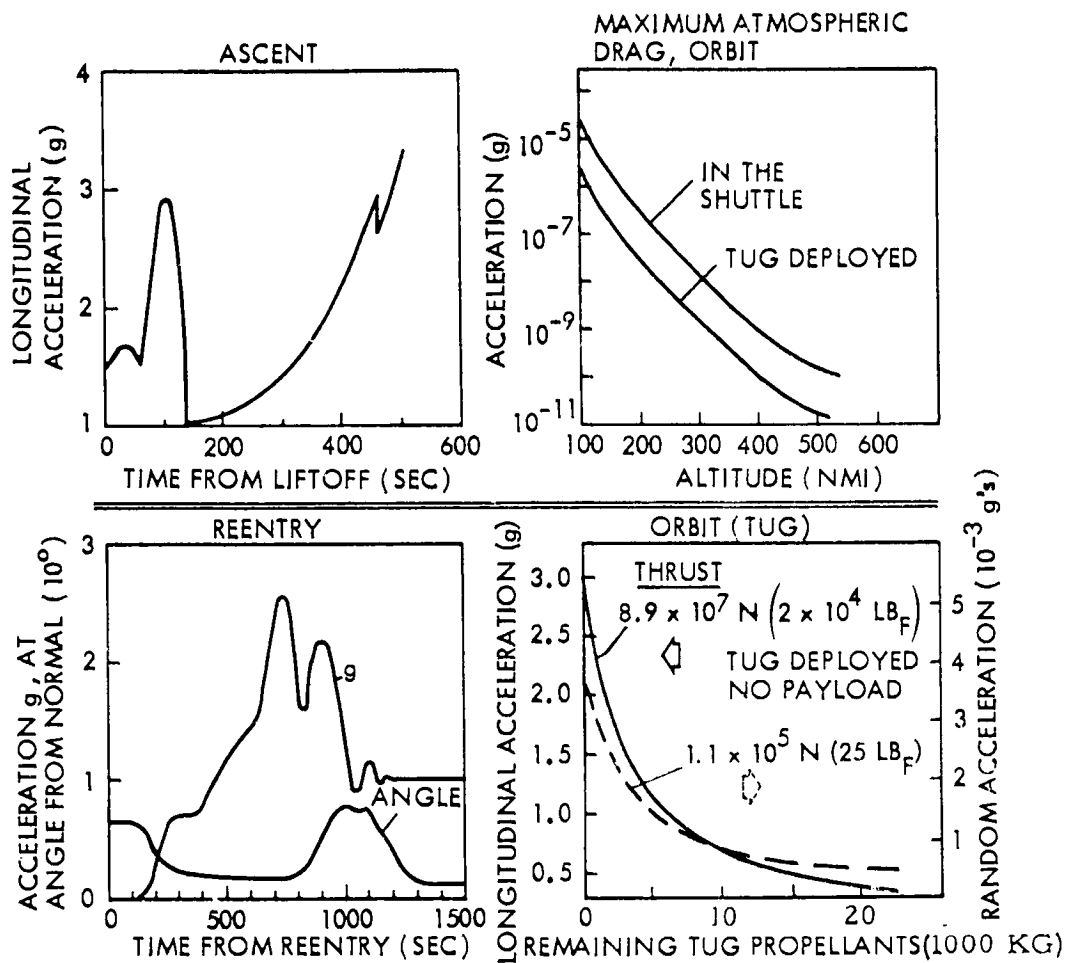
Fig. 2-3 Orbiter Payload Bay Acoustic Environment



VACUUM JACKET TEMPERATURE, °K (°R)

	MIN	MAX
• PRELAUNCH	278 (500)	322 (580)
• LAUNCH	278 (500)	339 (610)
• ORBIT (DEPLOYED FROM SHUTTLE)	167 (300)	261 (470)
• ENTRY AND POST-LANDING	199 (358)	367 (660)

Fig. 2-4 Temperature and Pressure Environments



MAX ACCELERATION VALUES

	X_o	Y_o	Z_o
BOOSTER END BURN	-3.0 ± 0.3	± 0.2	-0.4
ORBITAL END BURN	-3.0 ± 0.3	± 0.2	-0.5
SHUTTLE SPACE OPERATIONS	$-0.2, +0.1$	± 0.1	± 0.1
ENTRY	± 0.25	± 0.5	+3.0, -1.0
LANDING AND BRAKING	± 1.5	± 1.5	+2.5
CRASH	+9.0, -1.5	± 1.5	+4.5, -2.0

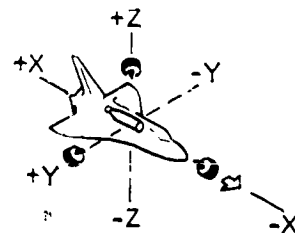


Fig. 2-5 Acceleration Environment

The 367°K (660°R) upper limit during post-landing shown in Fig. 2-4 affects material selection and the preconditioning temperatures required to outgas the system.

Note the maximum Tug acceleration level in orbit of 3.17 g due to main engine firings (Fig. 2-5) does not exceed the maximum acceleration level of the Shuttle, 3.0 ± 0.3 g. ACS thruster firings have such short pulse duration as to be negligible from a heat-transfer point of view. The higher acceleration levels associated with the Tug main engine firings have a negligible effect on the microsphere heat inputs to the propellant tanks due to (1) the relatively short time durations and (2) the higher acceleration levels that occur only when the propellants are nearly depleted.

The requirements of the type listed above (resulting from the induced-environments) have been accounted for in the jacket/microsphere design developed in this program.

Section 3
SUBSCALE TEST ARTICLE DESIGN

The design of the biaxial flex, stainless-steel vacuum jacket, and load-bearing microsphere insulation system was based on the environmental requirements provided in Section 2 and the system concept development results described in Section 4.

The finished test article that was built to the design drawings in Fig. 3-1 was shown previously in Fig. 1-1. It consists of an aluminum tank, six fiberglass tank supports, pallet, stainless-steel vacuum jacket, vacuum jacket spring/Kevlar standoffs, microsphere insulation, associated plumbing, and test instrumentation.

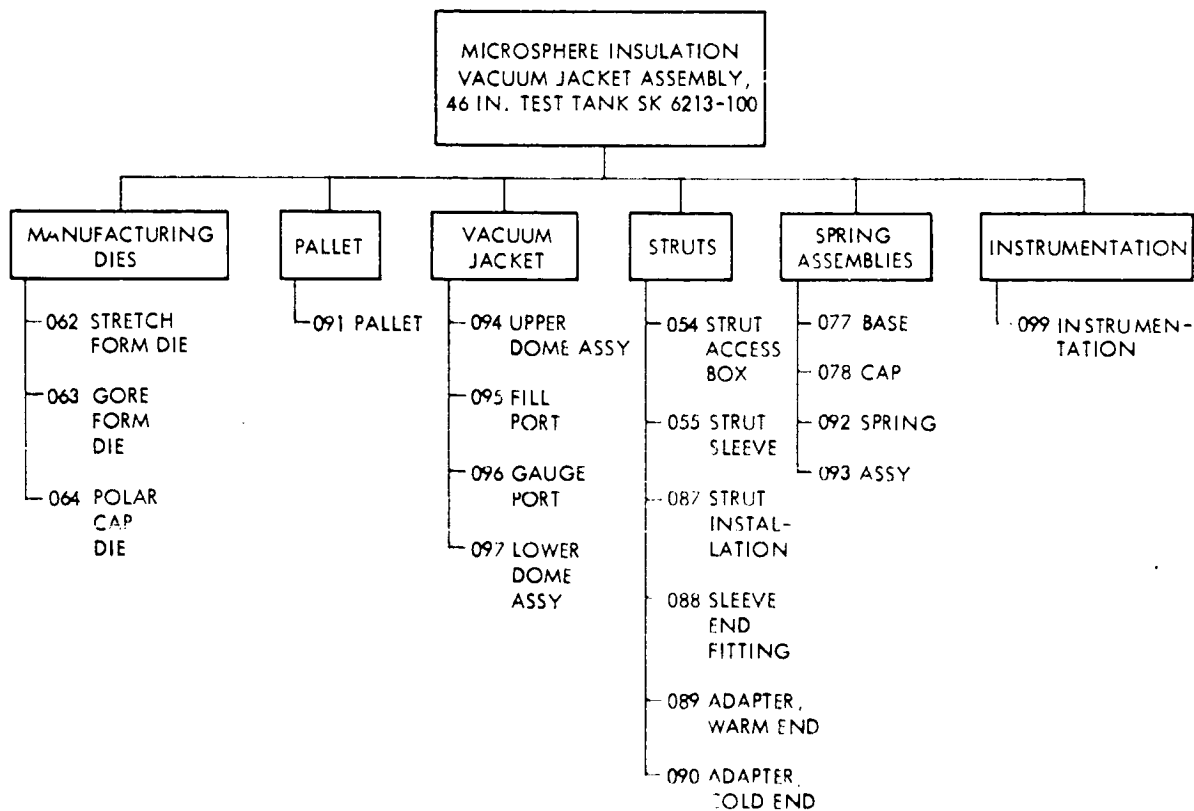


Fig. 3-1 Test Article Drawing Tree

The flight-weight spherical 2219 aluminum test tank, 117.1 cm (46.12 in.) in diameter, is supported by three pairs (six struts total) of filament-wound glass fiber/epoxy struts. The struts are attached to an aluminum pallet; the pallet simulates the hard attach points of the Space Tug outer load carrying shell and also provides a convenient interface for mounting or transport of the test article.

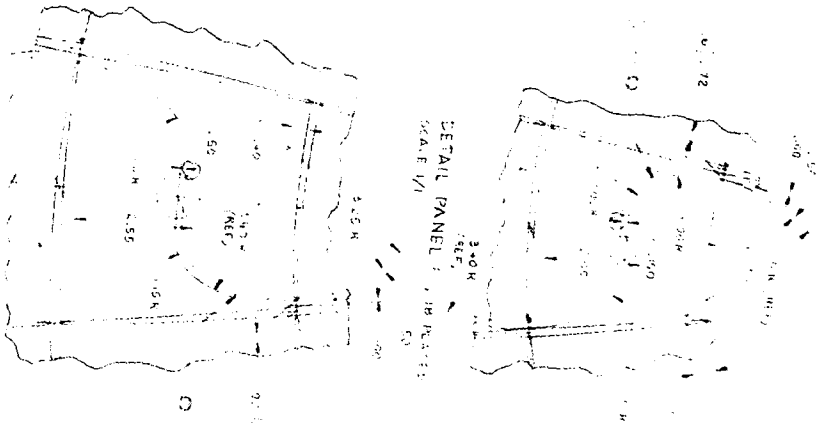
The tank is enclosed within a 0.08 mm (0.003 in.) thick, formed 321 stainless steel jacket. Staggered vertical and horizontal expansion wedges allow the jacket to stretch or compress elastically when the aluminum tank dimensions change (due to cryogen fill, warmup, or pressurization). Diagonal polar cap wedges provide the necessary transition between the biaxially flexing jacket and the rigid polar cap regions. In between the wedges, the jacket is stiffened with formed "X" or "Y" shaped stiffeners. The jacket is made in two halves, each hemisphere consisting of nine gore panels and one polar cap panel welded together as shown in Fig. 3-2. The final soldered closure joint is a combination flange and overlap design. The jacket is installed in a stretched condition and supported off the tank by 165 low-heat-leak spring/Kevlar assemblies shown in Fig. 3-3. The assemblies are epoxy bonded to the tank and soldered to the jacket.

The six fiberglass support struts are enclosed in stainless-steel vacuum jacket sleeves (Fig. 3-4) that can sustain a 1-atmosphere compressive load unsupported. A 0.13-mm (0.005-in.) thick stainless steel diaphragm seals off the warm end of the strut, permitting differential movement between the strut and the strut jacket sleeve during cryogen cooldown. A low-heat-leak "bicycle-wheel"-type spacer near the cold end of the strut (Fig. 3-4) keeps the strut centered in the strut cover. The "spokes" are Kevlar filaments.

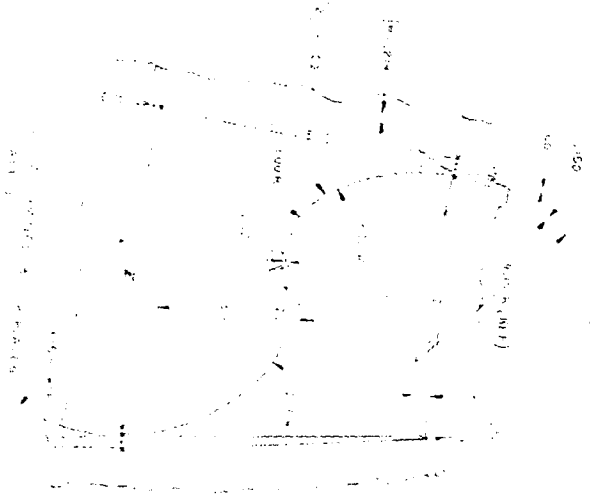
The outer surface of the tank and the inner surface of the vacuum jacket are coated with a 0.015-mm (0.0006-in.) epoxy coat followed by a 1000-Å low-emittance gold coating to reduce radiation heat transfer. The annulus between the tank and the vacuum jacket is filled with uncoated, hollow-glass processed microsphere insulation.

FOLIOUT FRAME

REPRODUCIBILITY OF THE ORIGINAL PAGE IS POOR



DETAIL PANEL 1 - 3 PLACES
SCALE 1/4\"



DETAIL PANEL 2 - 4 PLACES
SCALE 1/4\"



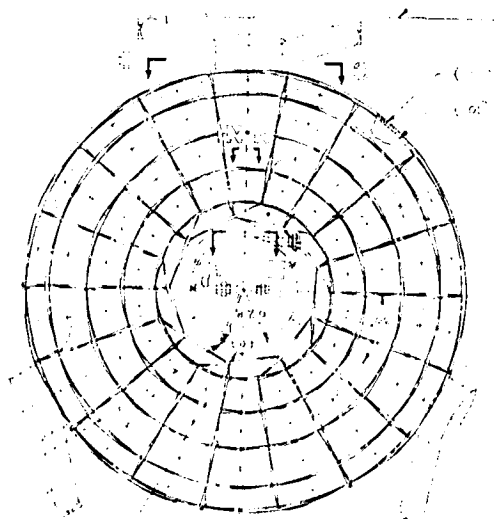
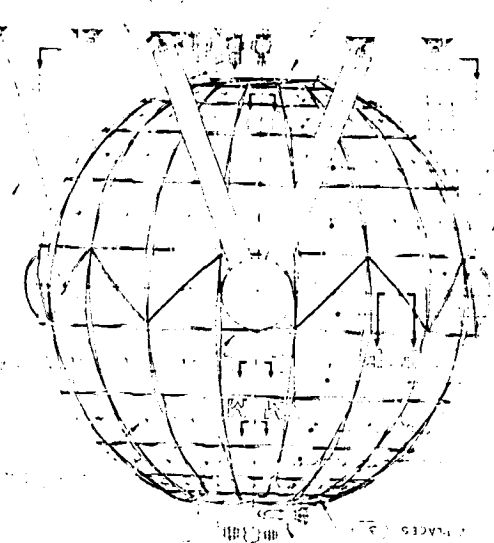
DETAIL PANEL 3 - 3 PLACES
SCALE 1/4\"

Fig. 3-2 Vacuum Jacket Assembly

QTY	ITEM NO.	PART OR IDENTIFYING NO.	DESCRIPTION OF MATERIAL SPECIFICATION	UNIT OF MEASURE	REMARKS
1	1
1	2
1	3
1	4
1	5
1	6
1	7
1	8
1	9
1	10
1	11
1	12
1	13
1	14
1	15
1	16
1	17
1	18
1	19
1	20
1	21
1	22



1. ...
 2. ...
 3. ...
 4. ...
 5. ...
 6. ...
 7. ...
 8. ...
 9. ...
 10. ...
 11. ...
 12. ...
 13. ...
 14. ...
 15. ...
 16. ...
 17. ...
 18. ...
 19. ...
 20. ...
 21. ...
 22. ...

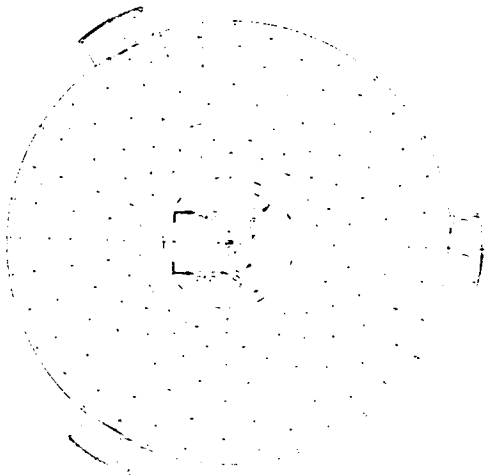


REPRODUCIBILITY OF THE ORIGINAL PART IS POOR

2

PRECEDING PAGE BLANK NOT FILMED

FOLDDOUT FRAME

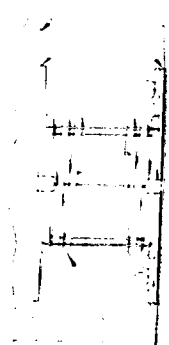


REF 1 (E)

[Handwritten scribbles]

REF 1 (E)

REF 1 (E)



SECTION 1
SECTION 2
SECTION 3
SECTION 4
SECTION 5
SECTION 6
SECTION 7
SECTION 8
SECTION 9
SECTION 10
SECTION 11
SECTION 12
SECTION 13
SECTION 14
SECTION 15
SECTION 16
SECTION 17
SECTION 18
SECTION 19
SECTION 20
SECTION 21
SECTION 22
SECTION 23
SECTION 24
SECTION 25
SECTION 26
SECTION 27
SECTION 28
SECTION 29
SECTION 30
SECTION 31
SECTION 32
SECTION 33
SECTION 34
SECTION 35
SECTION 36
SECTION 37
SECTION 38
SECTION 39
SECTION 40
SECTION 41
SECTION 42
SECTION 43
SECTION 44
SECTION 45
SECTION 46
SECTION 47
SECTION 48
SECTION 49
SECTION 50

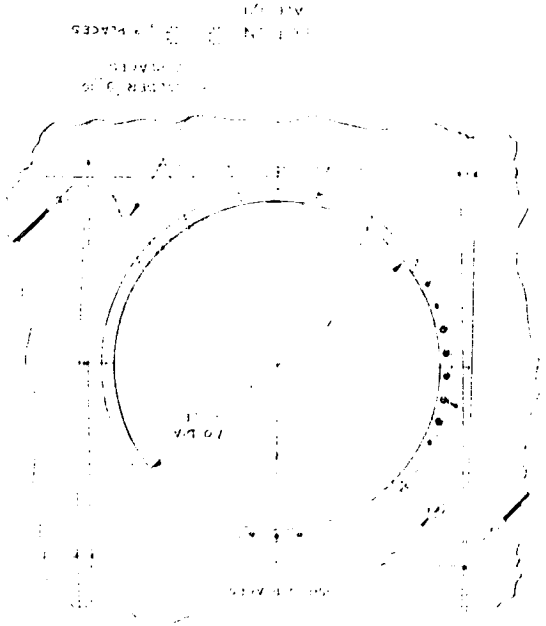
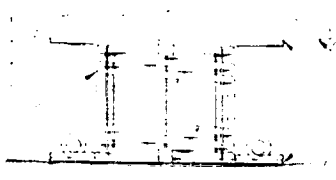
Fig. 3-2 (Cont.)

- 1. COORDINATE WITH SECTION 3-1
- 2. START WITH CENTER LINE AND FINISH WITH CENTER LINE
- 3. BOND PER SPECIFICATION WITH 1/2" MIN. THICK
- 4. REINFORCEMENT TO BE PER SPECIFICATION
- 5. GIVE RADIUS PER SPECIFICATION
- 6. CONTACT SURFACES WITH POWER RIGID CONNECTION
- 7. REINFORCEMENT TO BE PER SPECIFICATION
- 8. FOR MAINTENANCE OF CLEARANCE
- 9. FOR MAINTENANCE OF CLEARANCE
- 10. FOR MAINTENANCE OF CLEARANCE
- 11. FOR MAINTENANCE OF CLEARANCE
- 12. FOR MAINTENANCE OF CLEARANCE
- 13. FOR MAINTENANCE OF CLEARANCE
- 14. FOR MAINTENANCE OF CLEARANCE
- 15. FOR MAINTENANCE OF CLEARANCE
- 16. FOR MAINTENANCE OF CLEARANCE
- 17. FOR MAINTENANCE OF CLEARANCE
- 18. FOR MAINTENANCE OF CLEARANCE
- 19. FOR MAINTENANCE OF CLEARANCE
- 20. FOR MAINTENANCE OF CLEARANCE

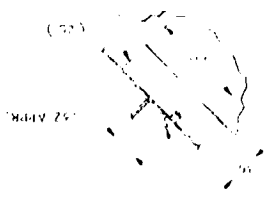
SECTION 1-1
SECTION 2-2
SECTION 3-3
SECTION 4-4
SECTION 5-5
SECTION 6-6
SECTION 7-7
SECTION 8-8
SECTION 9-9
SECTION 10-10
SECTION 11-11
SECTION 12-12
SECTION 13-13
SECTION 14-14
SECTION 15-15
SECTION 16-16
SECTION 17-17
SECTION 18-18
SECTION 19-19
SECTION 20-20



SECTION 1-1
SECTION 2-2
SECTION 3-3
SECTION 4-4
SECTION 5-5
SECTION 6-6
SECTION 7-7
SECTION 8-8
SECTION 9-9
SECTION 10-10
SECTION 11-11
SECTION 12-12
SECTION 13-13
SECTION 14-14
SECTION 15-15
SECTION 16-16
SECTION 17-17
SECTION 18-18
SECTION 19-19
SECTION 20-20



SECTION 1-1
SECTION 2-2
SECTION 3-3
SECTION 4-4
SECTION 5-5
SECTION 6-6
SECTION 7-7
SECTION 8-8
SECTION 9-9
SECTION 10-10
SECTION 11-11
SECTION 12-12
SECTION 13-13
SECTION 14-14
SECTION 15-15
SECTION 16-16
SECTION 17-17
SECTION 18-18
SECTION 19-19
SECTION 20-20



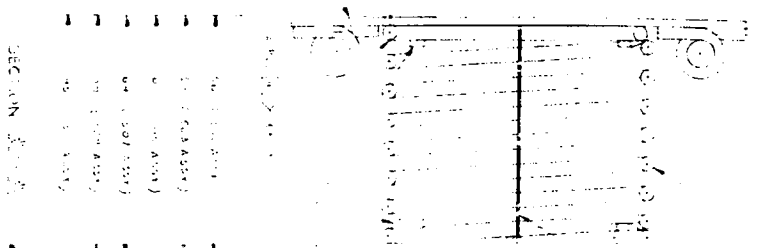
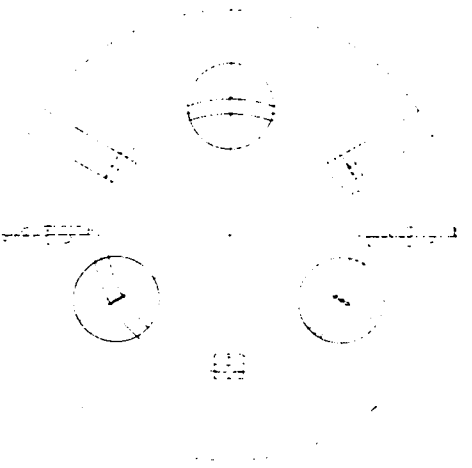
SECTION 1-1
SECTION 2-2
SECTION 3-3
SECTION 4-4
SECTION 5-5
SECTION 6-6
SECTION 7-7
SECTION 8-8
SECTION 9-9
SECTION 10-10
SECTION 11-11
SECTION 12-12
SECTION 13-13
SECTION 14-14
SECTION 15-15
SECTION 16-16
SECTION 17-17
SECTION 18-18
SECTION 19-19
SECTION 20-20

SECTION 1-1
SECTION 2-2
SECTION 3-3
SECTION 4-4
SECTION 5-5
SECTION 6-6
SECTION 7-7
SECTION 8-8
SECTION 9-9
SECTION 10-10
SECTION 11-11
SECTION 12-12
SECTION 13-13
SECTION 14-14
SECTION 15-15
SECTION 16-16
SECTION 17-17
SECTION 18-18
SECTION 19-19
SECTION 20-20

2 FOLDOUT FRAME

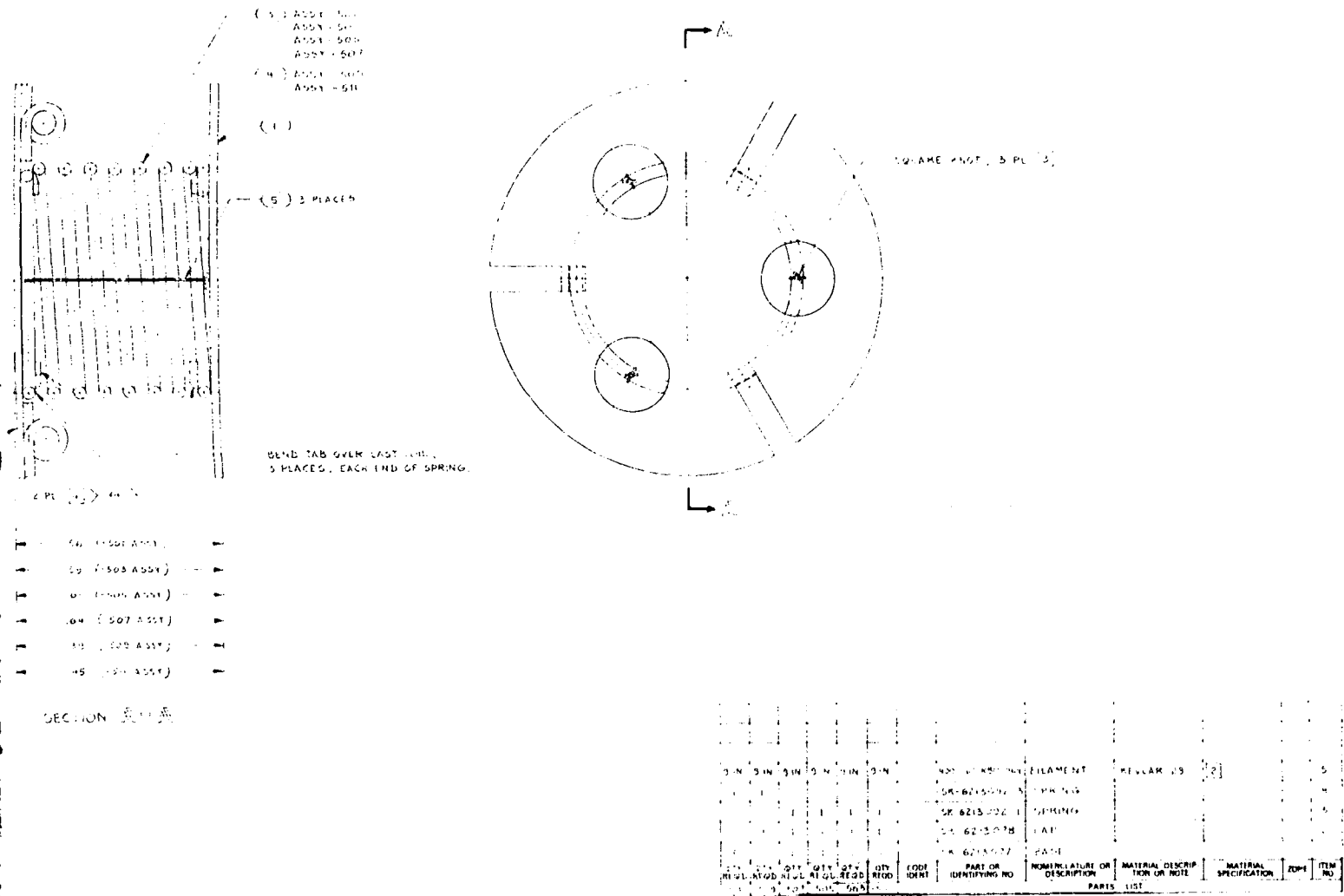
PRECEDING PAGE BLANK NOT FILLED

FOLIOUT FRAME



REPRODUCIBILITY OF THE ORIGINAL PAGE IS POOR

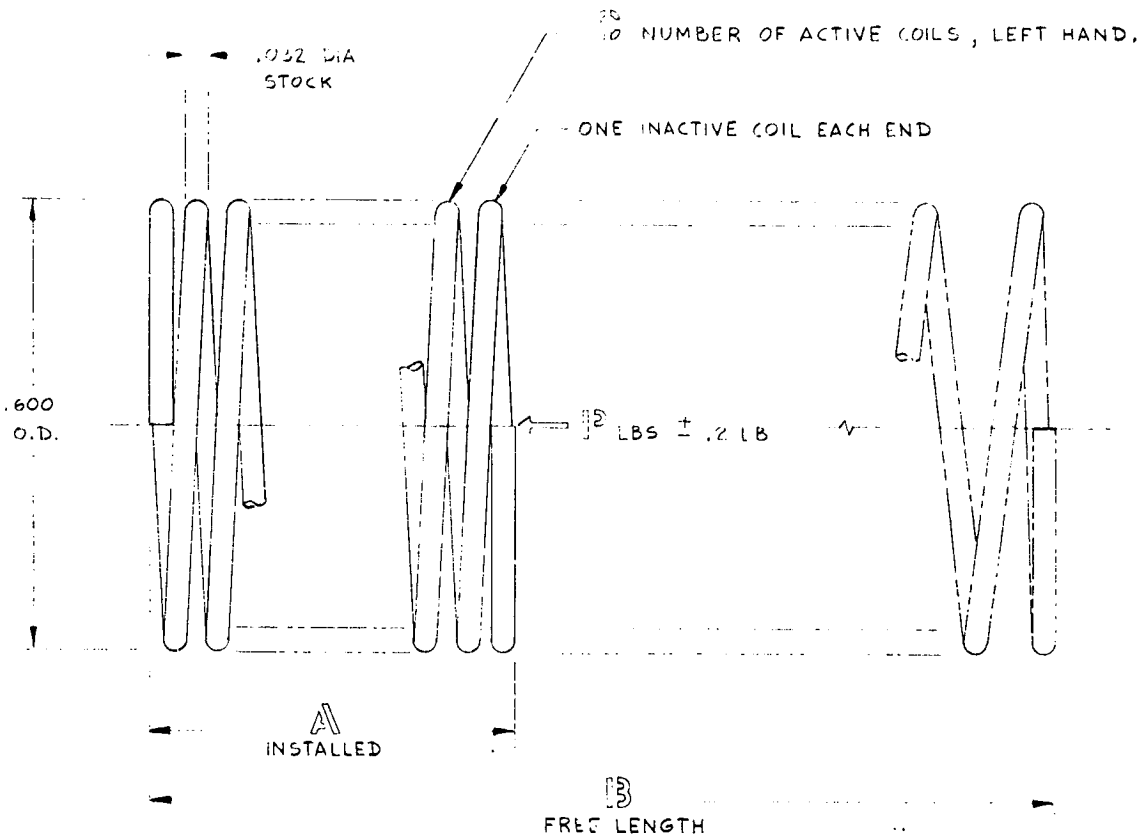
FOLLOUT FRAME 2



1. DRAWING ITEM 3 & 4 TO ITEM 2 PER SPEC. LAL 3500
 2. FABRICATE PER SPEC. LAL 3500
 3. PRODUCT OF DOMESTIC MANUFACTURE
 4. FABRICATE PER SPEC. LAL 3500
 NOTES

Fig. 3-3 Spring/Kevlar Attachment Assembly

PRECEDING PAGE BLANK NOT FILMED



DASH NO.	A	B	C	D
-1	.48	2.04	7	1.75
-3	.22	.89	3	1.75

SPRING RATE: 226 N/M (1.29 LB/IN.)

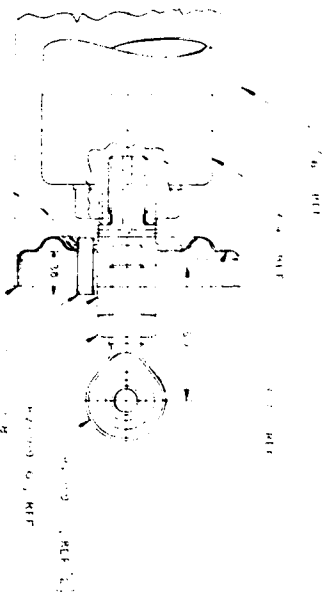
WIRE DIAM.: 0.081 CM (0.032 IN.), 17-7 PH STAINLESS STEEL
AMS 5677, COND. C

Fig. 3-3 (Cont.)

PRECEDING PAGE BLANK NOT FILMED

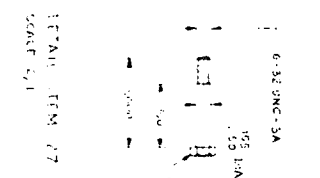
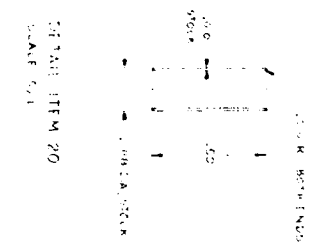
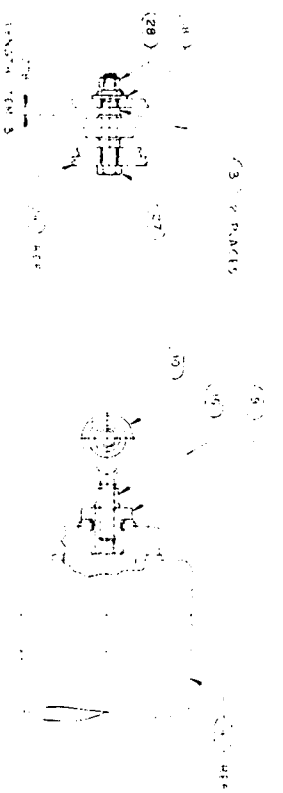
FOLDDOUT FRAME

REPL
ORIG



SECTION 28
SCALE 2/1 3 VIEWS AS SHOWN
SCALE 2/1 3 VIEWS WITHOUT ITEM 201

SECTION 27
SCALE 2/1

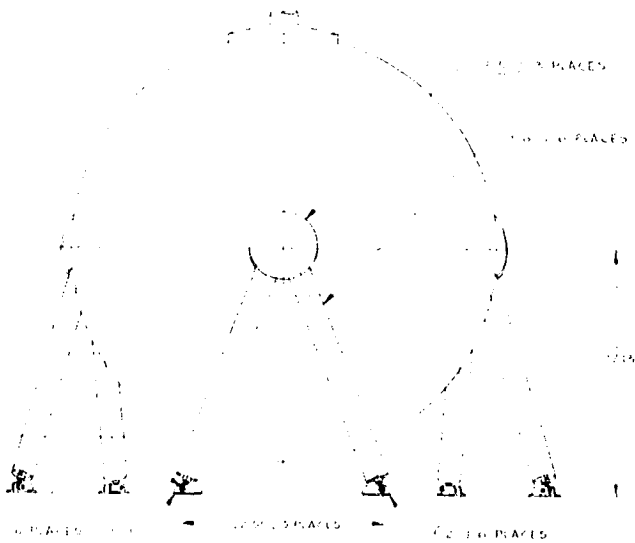
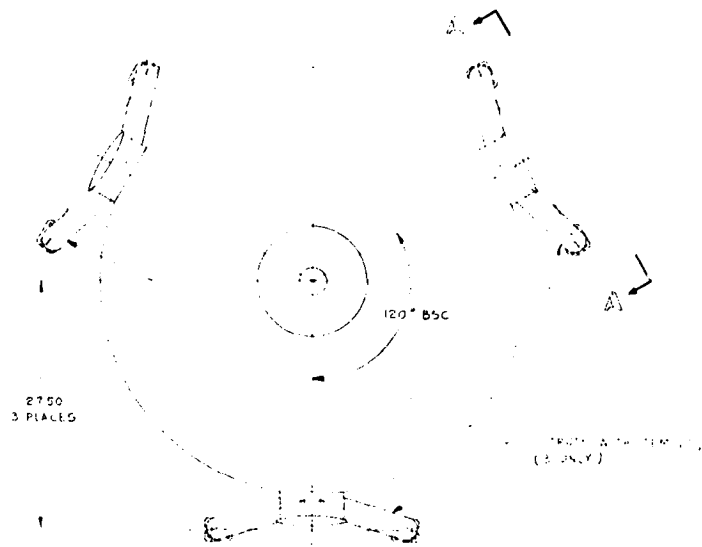


SECTION 27
SCALE 2/1

SECTION 27
SCALE 2/1

SECTION 27
SCALE 2/1

REPRODUCIBILITY OF THE ORIGINAL PAGE IS POOR



1. 27.50 DIA. HOLE - 3 PLATED
2. 27.50 DIA. HOLE - 3 PLATED
3. 27.50 DIA. HOLE - 3 PLATED
4. 27.50 DIA. HOLE - 3 PLATED
5. 27.50 DIA. HOLE - 3 PLATED
6. 27.50 DIA. HOLE - 3 PLATED
7. 27.50 DIA. HOLE - 3 PLATED
8. 27.50 DIA. HOLE - 3 PLATED
9. 27.50 DIA. HOLE - 3 PLATED
10. 27.50 DIA. HOLE - 3 PLATED
11. 27.50 DIA. HOLE - 3 PLATED
12. 27.50 DIA. HOLE - 3 PLATED
13. 27.50 DIA. HOLE - 3 PLATED
14. 27.50 DIA. HOLE - 3 PLATED
15. 27.50 DIA. HOLE - 3 PLATED
16. 27.50 DIA. HOLE - 3 PLATED
17. 27.50 DIA. HOLE - 3 PLATED
18. 27.50 DIA. HOLE - 3 PLATED
19. 27.50 DIA. HOLE - 3 PLATED
20. 27.50 DIA. HOLE - 3 PLATED
21. 27.50 DIA. HOLE - 3 PLATED
22. 27.50 DIA. HOLE - 3 PLATED
23. 27.50 DIA. HOLE - 3 PLATED
24. 27.50 DIA. HOLE - 3 PLATED
25. 27.50 DIA. HOLE - 3 PLATED
26. 27.50 DIA. HOLE - 3 PLATED
27. 27.50 DIA. HOLE - 3 PLATED
28. 27.50 DIA. HOLE - 3 PLATED

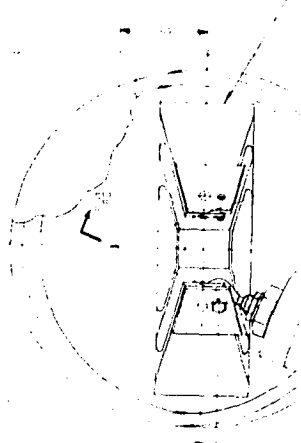
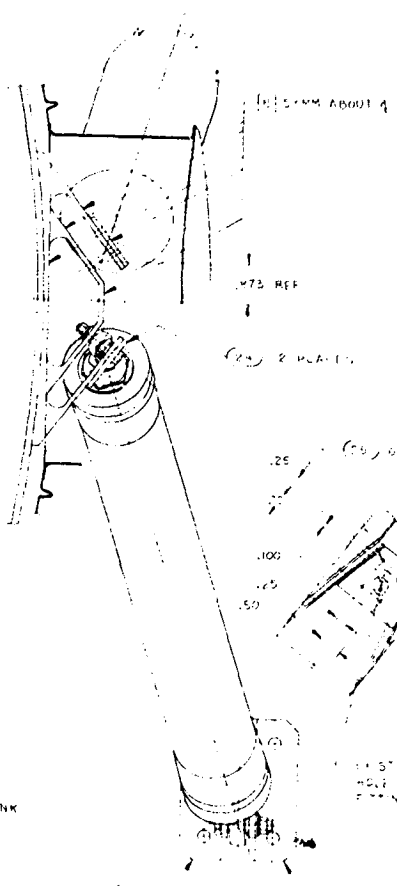
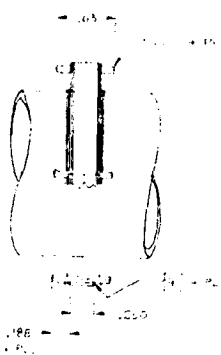
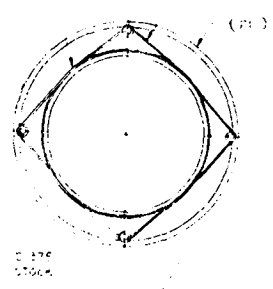
QTY	CODE	PART OR IDENTIFYING NO.	NOMENCLATURE OR DESCRIPTION OF PARTS LIST	MATERIAL DESCRIPTION OR NOTE	MATERIAL SPECIFICATION	UNIT	ITEM NO.
1		2542637	NUT				28
6			BOLT	WANT FROM			27
6		54265508-19	BOLT				26
6		54265508-19	BOLT				25
6		54265508-19	BOLT				24
6		54265508-19	BOLT				23
6		54265508-19	BOLT				22
6		54265508-19	BOLT				21
6		54265508-19	BOLT				20
6		54265508-19	BOLT				19
6		54265508-19	BOLT				18
6		54265508-19	BOLT				17
6		54265508-19	BOLT				16
6		54265508-19	BOLT				15
6		54265508-19	BOLT				14
6		54265508-19	BOLT				13
6		54265508-19	BOLT				12
6		54265508-19	BOLT				11
6		54265508-19	BOLT				10
6		54265508-19	BOLT				9
6		54265508-19	BOLT				8
6		54265508-19	BOLT				7
6		54265508-19	BOLT				6
6		54265508-19	BOLT				5
6		54265508-19	BOLT				4
6		54265508-19	BOLT				3
6		54265508-19	BOLT				2
6		54265508-19	BOLT				1

Fig. 3-4 Strut Installation

PRECEDING PAGE BLANK NOT FILMED

FOLDOUT FRAME

ENLARGEMENT ITEM 23 BONDED TO STRUT ITEM 4 WITH EPOXY. SCALE 2/1



DETAIL 20 SCALE 2/1



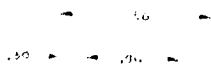
WINDING PATTERN ITEM 23. ALL METAL FORMING AND ITEM 4 ON EACH SIDE OF ITEM 21.

4 OF TANK

REF (2)

EXISTING HOLES HOLD IN SUPPORT PLATING.

2750 REF

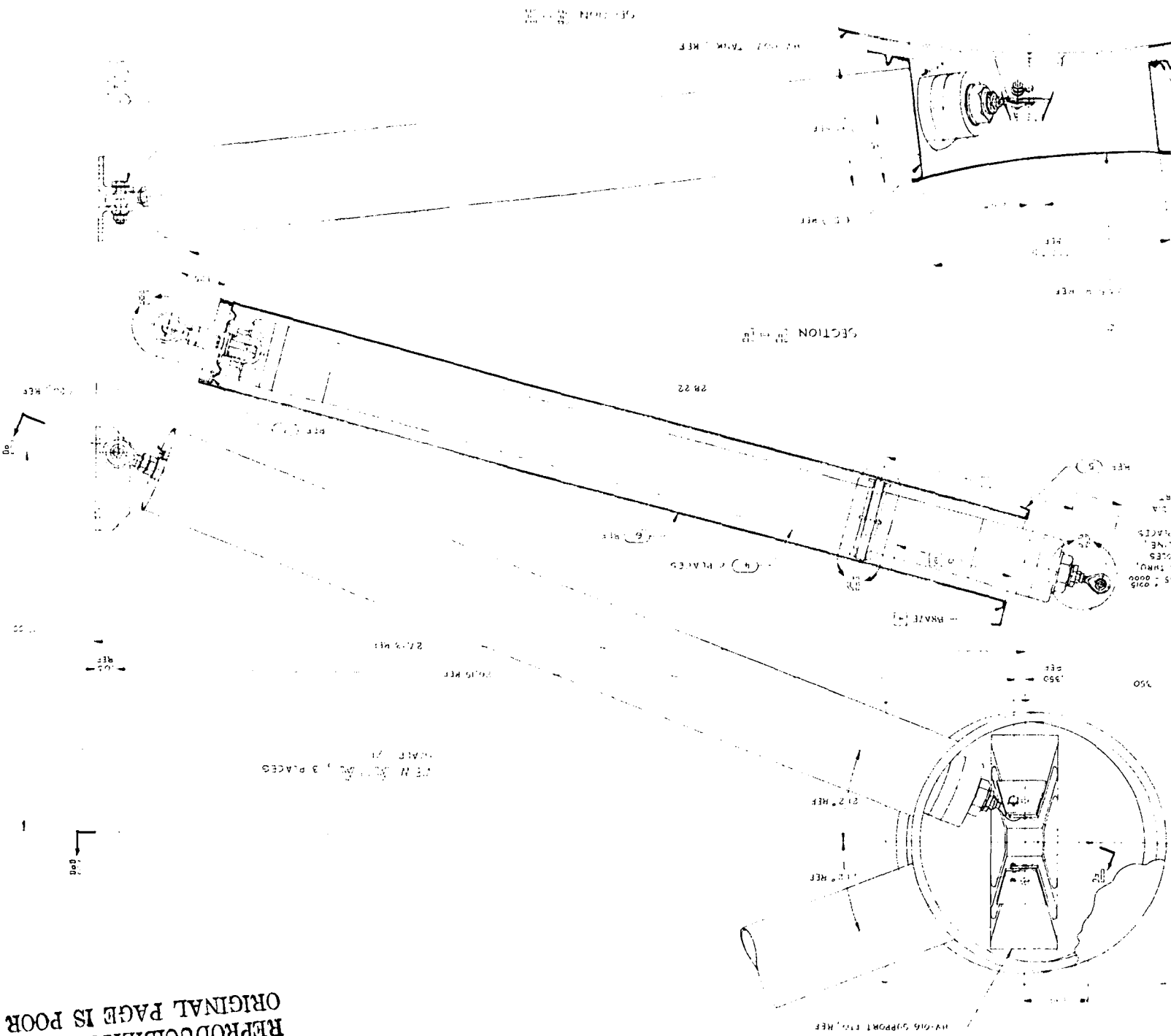


0.0625 STOCK

DETAIL ITEM 24 SCALE 2/1

REPRODUCIBILITY OF THE ORIGINAL PAGE

FIG. 3-4 (Cont.)



REPRODUCIBILITY OF THE ORIGINAL PAGE IS POOR

FOLDOUT FRAME 2

Concentric fill and vent lines (items 9 and 5), thermally guarded with a wrap around LN₂ heat-exchanger tube (item 8), enter the tank through a top-mounted access cover as shown in Fig. 3-5 (using an aluminum to stainless steel transition joint, item 27). A line for monitoring/controlling tank pressure (item 46) exits through the side of the vent line. The tank cover, with a 20.3-cm (8-in.) diameter opening into the tank, is sealed with a metal gasketed Conoseal flange joint. The inner fill line extends to near the tank bottom, and is protected by a perforated tube. The tank is filled with 41-kg (90-lb) of coarse aluminum wool to achieve isothermal conditions during heat-transfer tests. A vacuum pumping and sealoff port (item 11) and a microsphere fill port (item 18) are also mounted near the plumbing penetrations on the vacuum jacket.

The vacuum pumping port allows the insulation to be either evacuated or back-filled with a dry gas and then sealed, depending on the desired test sequence. Note the 5- μ m, 16.8-cm (6.6-in.) diameter screen that permits evacuation yet contains the microspheres.

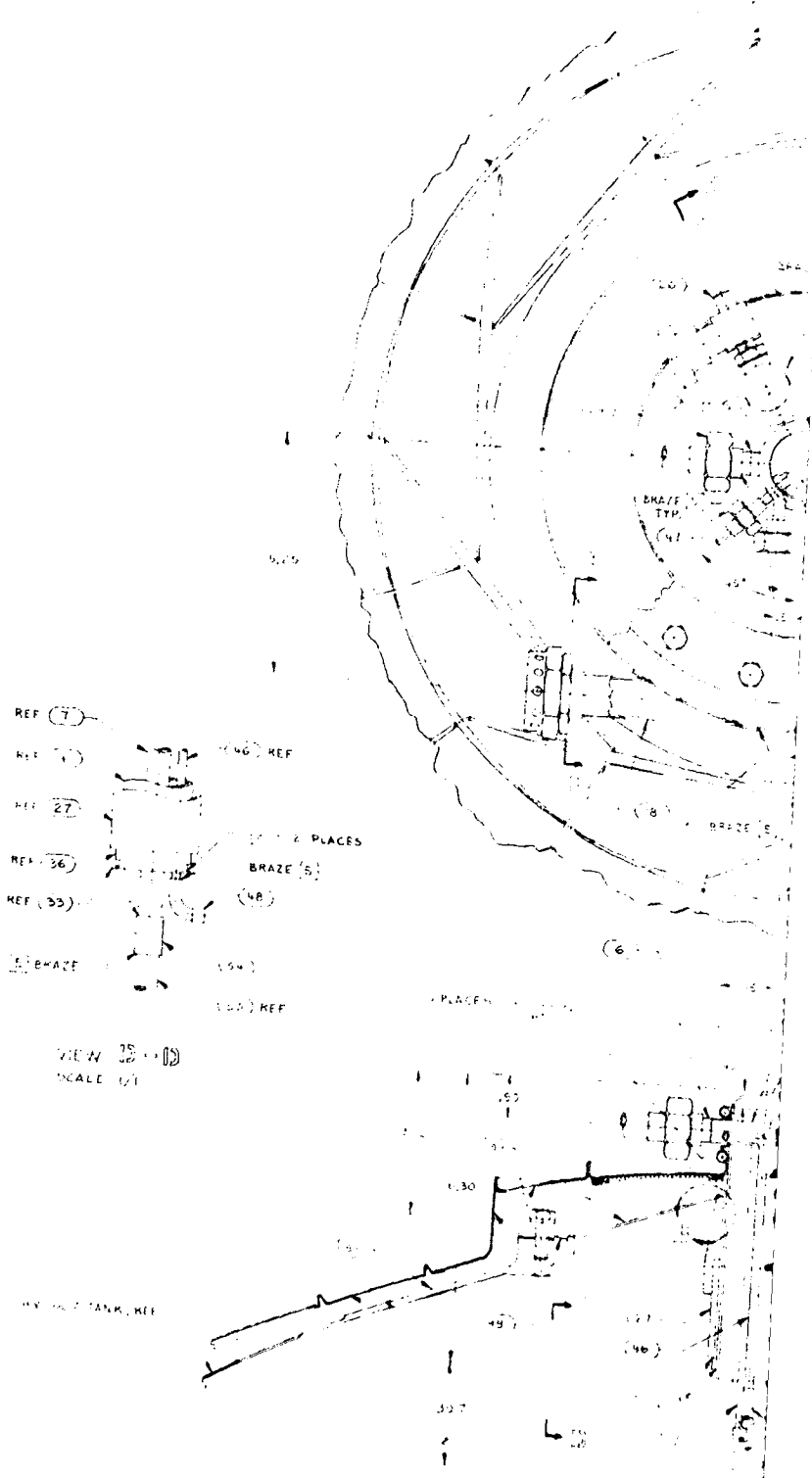
The microsphere fill port allows the insulation annulus to be filled initially with microspheres. Transfer is accomplished through a transparent plastic line from the vacuum bakeout and transfer apparatus by a gas fluidizing technique. Gas is vented out the bottom of the vacuum jacket.

Ports for measuring insulation pressure both at the top and the bottom of the jacket are available as shown in Figs. 3-5 and 3-6. The temperature and liquid level sensor leads, internal to the aluminum tank (platinum resistance thermometers, thermocouples, and carbon resistors), are brought out through an epoxy-potted connection through the side of the vent tube.

PRECEDING PAGE BLANK NOT FILMED

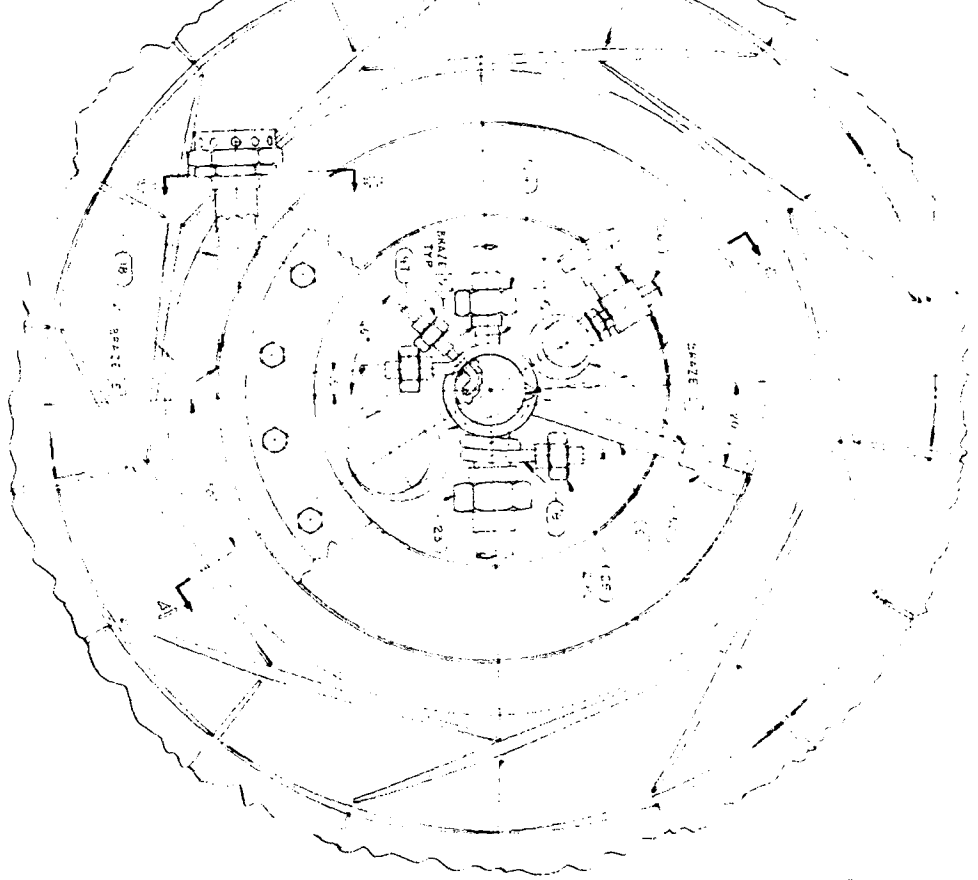
PRECEDING PAGE BLANK NOT FILMED

FOLDOUT FRAME |

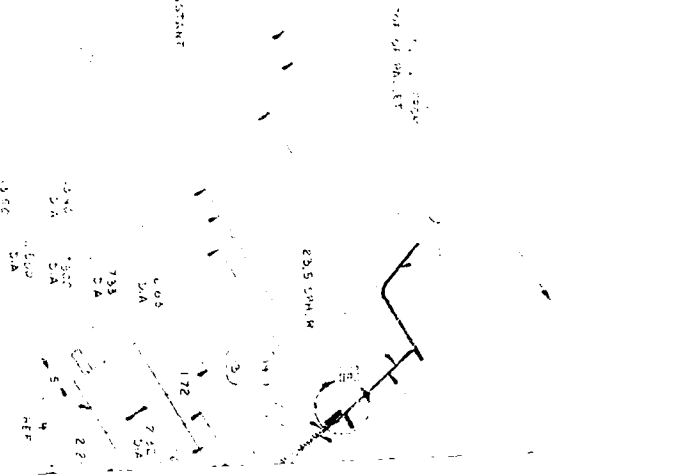
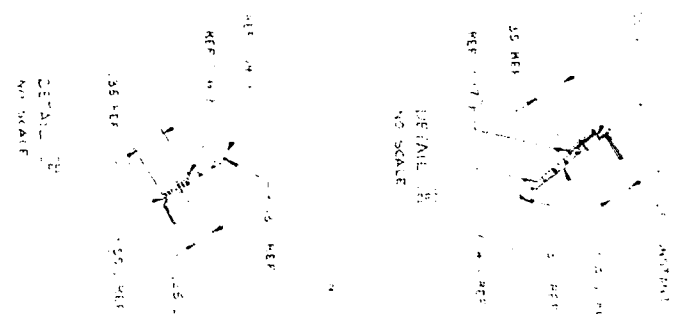
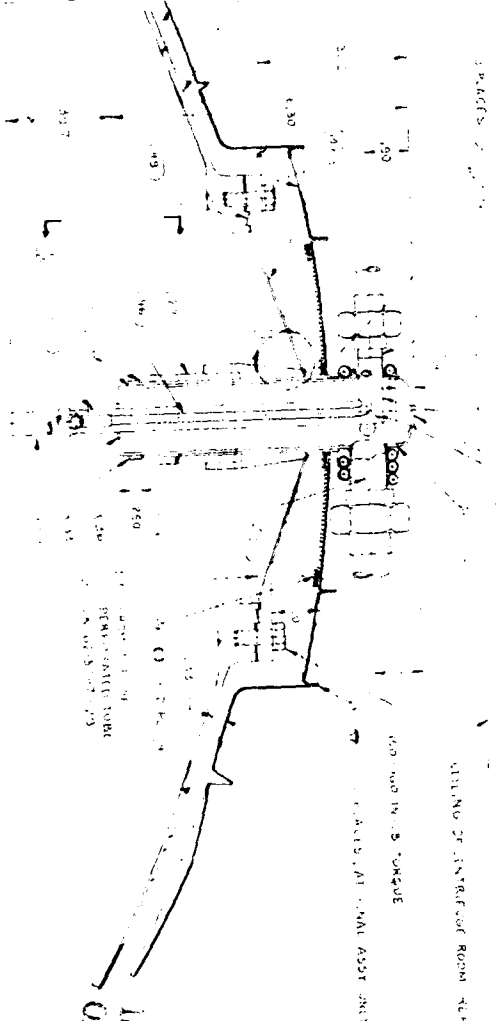


REPRODUCIBILITY OF THE ORIGINAL PAGE IS 100%

COLLUMPT FRAME 2



(6)



SECTION 1-1

REPROD.
ORIGINAL

1. PRODUCT OF VARIOUS...
2. PRODUCT OF VARIOUS...
3. PRODUCT OF VARIOUS...
4. PRODUCT OF VARIOUS...
5. PRODUCT OF VARIOUS...
6. CLEAN PER SPEC...
7. SHAZE PER SPEC...
8. SHAZE PER SPEC...
9. SHAZE PER SPEC...
10. SHAZE PER SPEC...

DETAIL OF INTERIOR ROOM

DETAIL OF INTERIOR ROOM

DETAIL OF INTERIOR ROOM

DETAIL OF INTERIOR ROOM

DETAIL OF INTERIOR ROOM

DETAIL OF INTERIOR ROOM

DETAIL OF INTERIOR ROOM

DETAIL OF INTERIOR ROOM

DETAIL OF INTERIOR ROOM

DETAIL OF INTERIOR ROOM

DETAIL OF INTERIOR ROOM

DETAIL OF INTERIOR ROOM

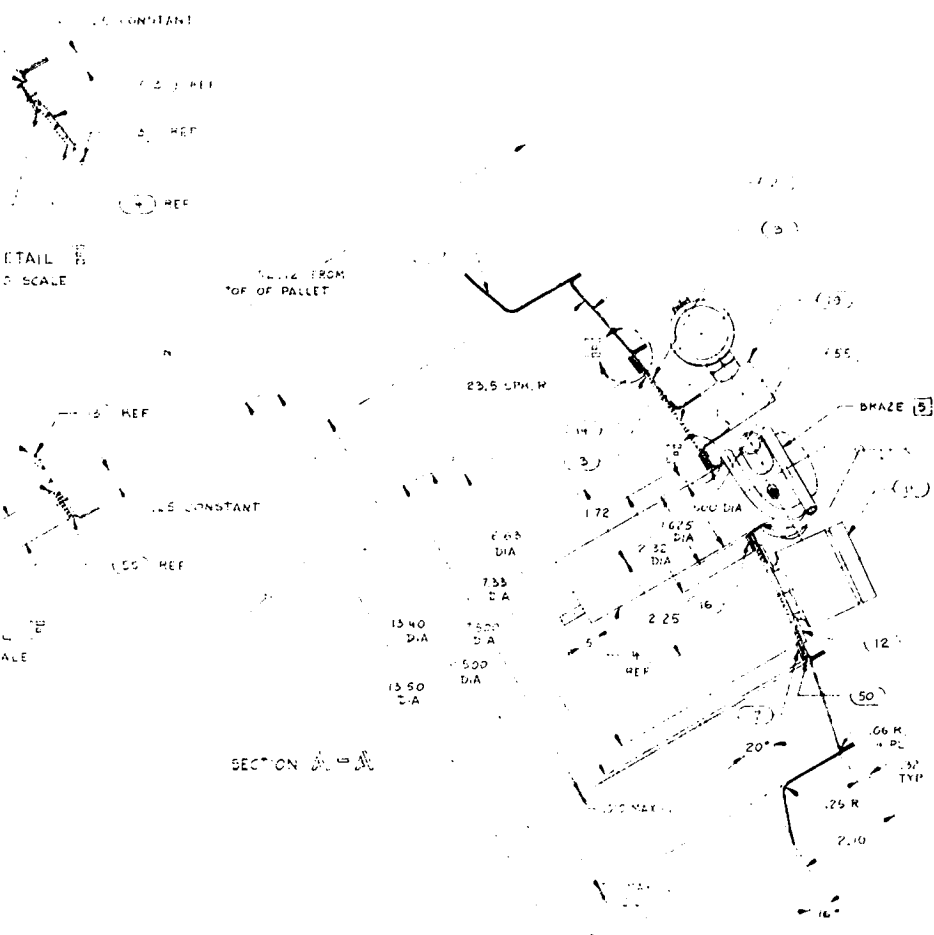
DETAIL OF INTERIOR ROOM

DETAIL OF INTERIOR ROOM

FOLDOUT FRAME 3

FOLDOUT FRAME 2

REPRODUCIBILITY OF THE ORIGINAL PAGE IS POOR



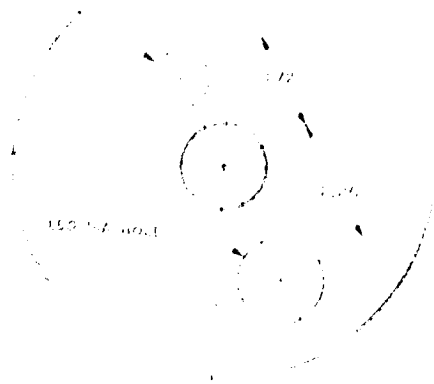
QTY	CODE	PART OR IDENTIFYING NO	NOMENCLATURE OR DESCRIPTION	MATERIAL DESCRIPTION OR NOTE	MATERIAL SPECIFICATION	ZONE	ITEM NO
		5K 4213096	GAUGE PORT				19
		5K 6213095	FLANGE PORT				8
		-33	FLANGE	304 SS	QQ-5-766		7
		-31	FLANGE	304 SS	QQ-5-766		18
		-27	SCREEN	304 SS	QQ-5-766		14
		-25	SCREEN	304 SS	MR-W-260		13
		-23	RING	304 SS	QQ-5-766		12
		2	VACUUM PORT	MARK FROM			10
		19	FLANGE	304 SS			9
		7	TUBE	304 SS	MIL-T-8845		5
		5	COIL	304 SS	WH-T-709		8
		15	TUBE	304 SS	MIL-T-8845		7
		11	TUBE	304 SS	MIL-T-8845		6
		9	TUBE	304 SS	MIL-T-8845		11
		2	TUBE	304 SS	MIL-T-8845		4
		6	FLANGE	304 SS	QQ-5-766		15
		4	FLANGE	304 SS	QQ-5-766		16
		1	FLANGE	304 SS	QQ-5-766		17

- 1. PRODUCT OF B. CHAZE CORP. WENDELL, N.Y.
- 2. PRODUCT OF NUPRO CO. CLEVELAND, OHIO.
- 3. PRODUCT OF AERQUIP CORP. LOS ANGELES, CALIF.
- 4. PRODUCT OF CRYOLAB. LOS ANGELES, CALIF.
- 5. PRODUCT OF O & H PRODUCTS CORP. KENOSHA, WIS.
- 6. CLEAN PER SPEC. LAG 3605.
- 7. BRAZE PER SPEC. LAG 3650.
- 8. FLAMEWELD PER SPEC. LAG 3650.
- 9. WELD PER SPEC. LAG 3655.
- 10. MACHINE PER SPEC. LAG 3661.
- 11. FABRICATE PER SPEC. LAG 3605.
- 12. FINISH

Fig. 3-5 Upper Dome Assembly

PRECEDING PAGE BLANK NOT FILMED

FOLDOUT FRAME |



DATA ITEM 3
SCALE 1/1

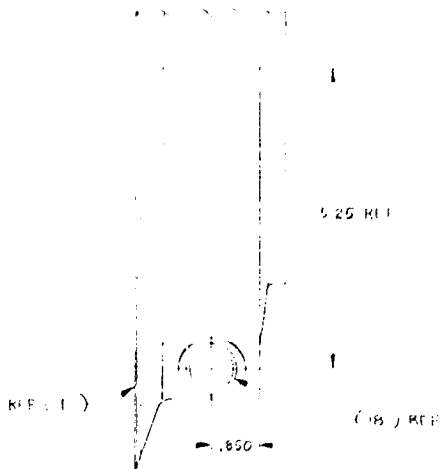
1000
0.001

23

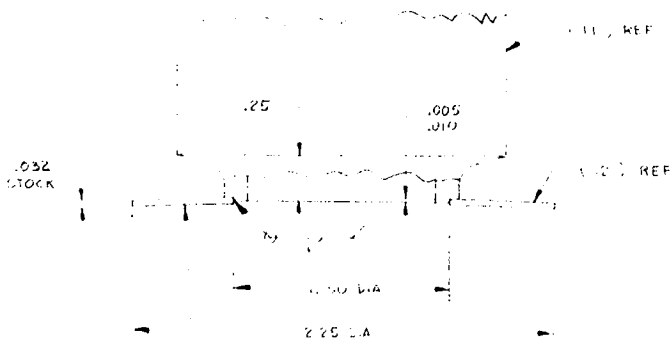
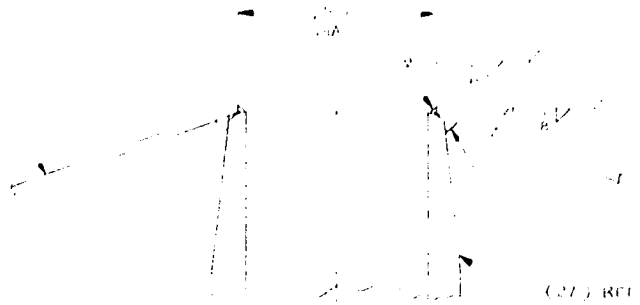
08

10

FOLDOUT FRAME 2

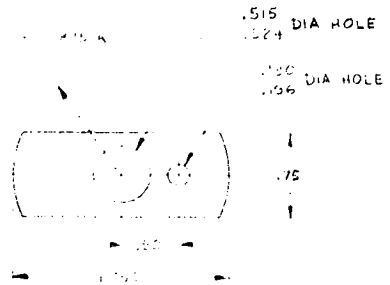
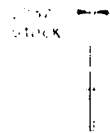


TANK ACCESS
2.187 REF



23.5 SPH R

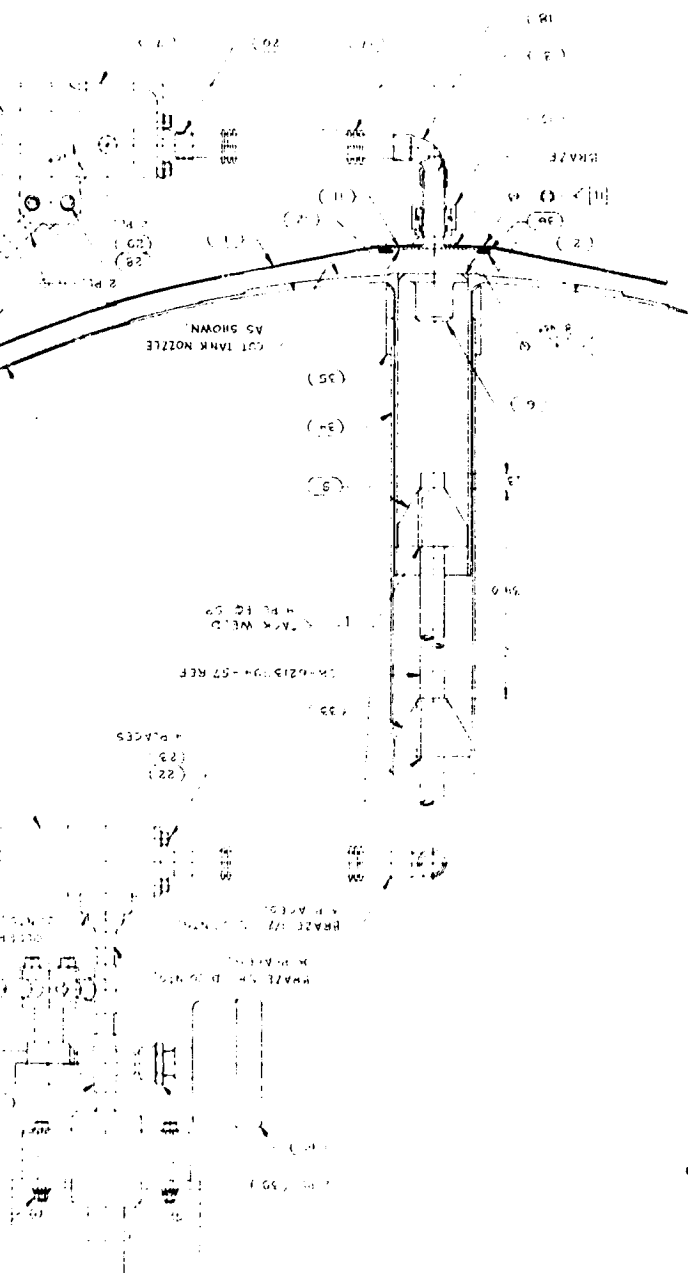
DETAIL (3) ITEM 11 & 12
NO SCALE



REPRODUCIBILITY OF THE
ORIGINAL PAGE IS POOR

Fig. 3-5 (Cont.)

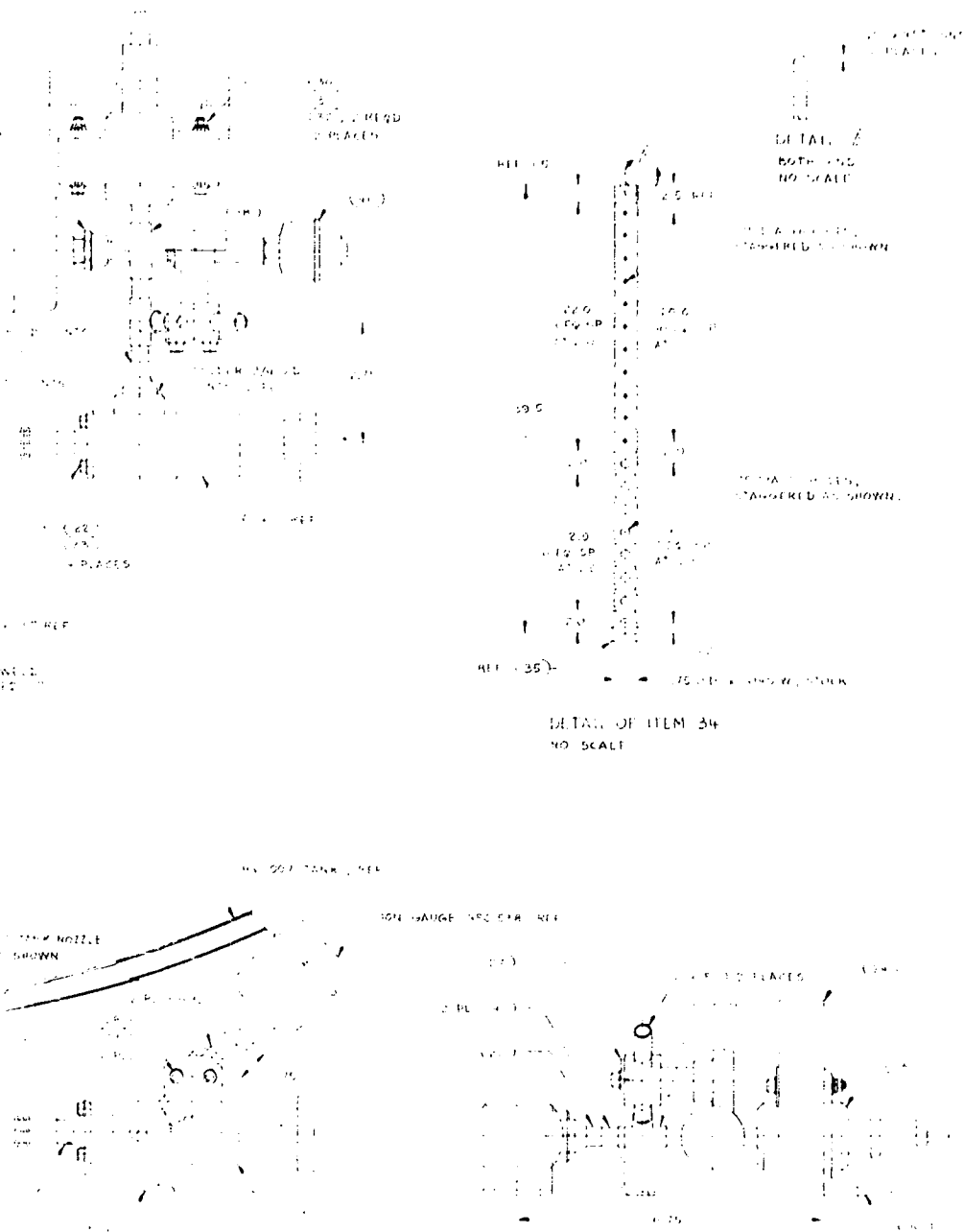
1. INSTALL PER DRAWING
 2. PRODUCT OF WELD MANUFACTURE
 3. PRODUCT OF WELD MANUFACTURE
 4. ORDER FOR SPECIAL TREATMENT



FOLDOUT FRAME

PRECEDING PAGE BLANK NOT FILMED

REPRODUCIBILITY OF THE ORIGINAL PAGE IS POOR



QTY	LIST IDENT	PART OR IDENTIFYING NO	DESCRIPTION	MATERIAL SPEC	CRIP	MATERIAL SPECIFICATION	ZON	ITEM NO
1	17	17	IM					17
1	18	18	VALVE					18
1	19	19	GAUGE					19
1	20	20	DIAPHRAGM					20
1	21	21	ADAPTER					21
1	22	22	ROD					22
1	23	23	ROD					23
1	24	24	INSERT					24
1	25	25	FLANGE					25
1	26	26	TUBE					26
1	27	27	FLANGE					27
1	28	28	FLANGE					28
1	29	29	WASHER					29
1	30	30	BOLT					30
1	31	31	WASHER					31
1	32	32	WASHER					32
1	33	33	WASHER					33
1	34	34	BRACKET					34
1	35	35	WASHER					35
1	36	36	WASHER					36
1	37	37	WASHER					37
1	38	38	WASHER					38
1	39	39	WASHER					39
1	40	40	WASHER					40
1	41	41	WASHER					41
1	42	42	WASHER					42
1	43	43	WASHER					43
1	44	44	WASHER					44
1	45	45	WASHER					45
1	46	46	WASHER					46
1	47	47	WASHER					47
1	48	48	WASHER					48
1	49	49	WASHER					49
1	50	50	WASHER					50
1	51	51	WASHER					51
1	52	52	WASHER					52
1	53	53	WASHER					53
1	54	54	WASHER					54
1	55	55	WASHER					55
1	56	56	WASHER					56
1	57	57	WASHER					57
1	58	58	WASHER					58
1	59	59	WASHER					59
1	60	60	WASHER					60
1	61	61	WASHER					61
1	62	62	WASHER					62
1	63	63	WASHER					63
1	64	64	WASHER					64
1	65	65	WASHER					65
1	66	66	WASHER					66
1	67	67	WASHER					67
1	68	68	WASHER					68
1	69	69	WASHER					69
1	70	70	WASHER					70
1	71	71	WASHER					71
1	72	72	WASHER					72
1	73	73	WASHER					73
1	74	74	WASHER					74
1	75	75	WASHER					75
1	76	76	WASHER					76
1	77	77	WASHER					77
1	78	78	WASHER					78
1	79	79	WASHER					79
1	80	80	WASHER					80
1	81	81	WASHER					81
1	82	82	WASHER					82
1	83	83	WASHER					83
1	84	84	WASHER					84
1	85	85	WASHER					85
1	86	86	WASHER					86
1	87	87	WASHER					87
1	88	88	WASHER					88
1	89	89	WASHER					89
1	90	90	WASHER					90
1	91	91	WASHER					91
1	92	92	WASHER					92
1	93	93	WASHER					93
1	94	94	WASHER					94
1	95	95	WASHER					95
1	96	96	WASHER					96
1	97	97	WASHER					97
1	98	98	WASHER					98
1	99	99	WASHER					99
1	100	100	WASHER					100

Fig. 3-6 Lower Dome Assembly

PRECEDING PAGE BLANK NOT FILMED

ROLLOUT FRAME

FOLDOUT FRAME 2

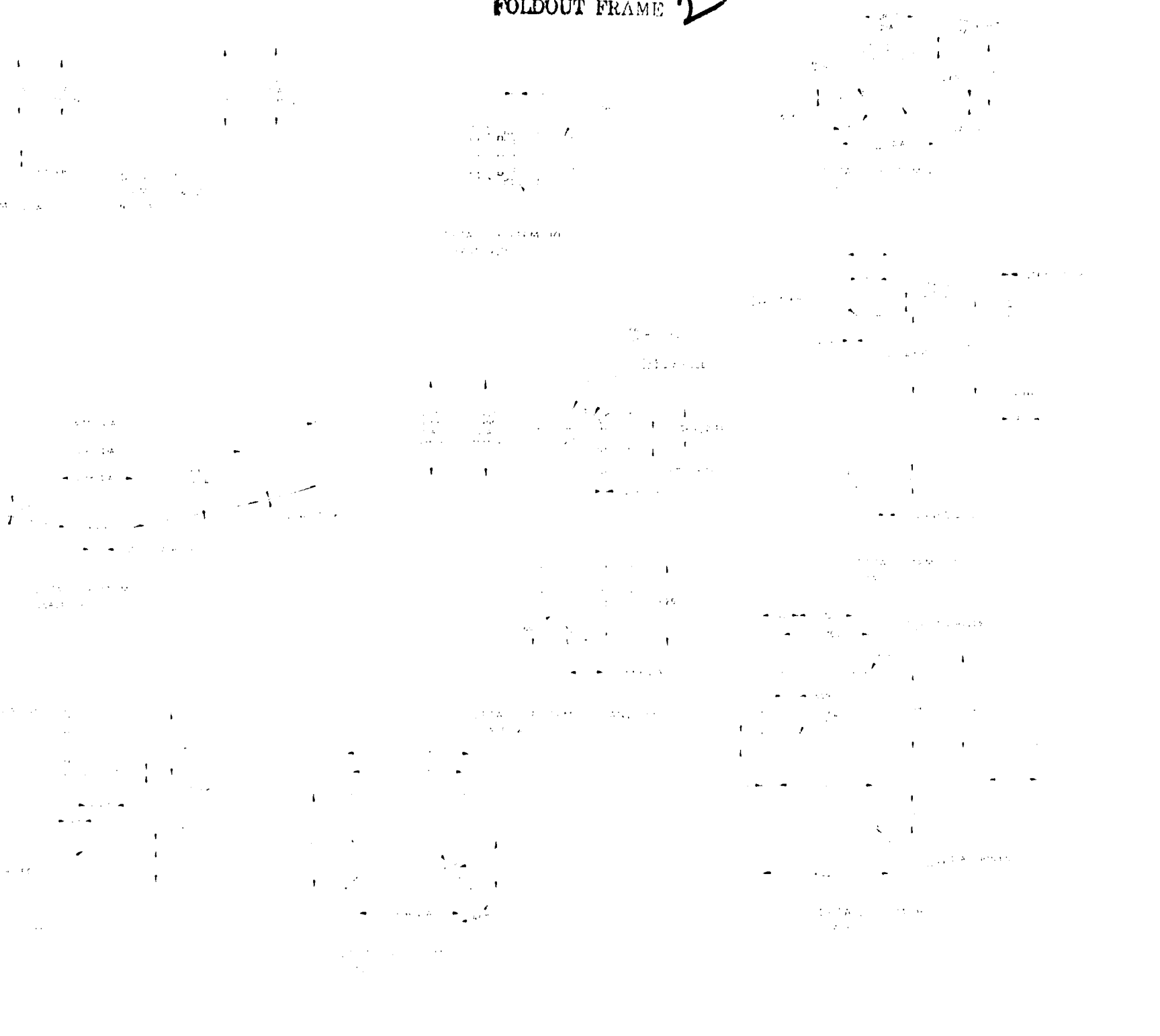


Fig. 3-6 (Cont.)

Section 4
SYSTEM CONCEPT DEVELOPMENT

The test article described in Section 3 resulted from development work performed both on the stainless-steel vacuum jacket and the load-bearing microsphere insulation.

This Section describes the work performed to develop the vacuum jacket and process the microsphere insulation. A summary of microsphere insulation physical and thermal properties concludes this Section.

4.1 VACUUM-JACKET DEVELOPMENT

To provide a sound engineering basis for designing, fabricating, and assembling the vacuum jacket on the test tank, development work was undertaken in the following areas:

- Flexure characteristics of flat jacket panels
- Effect of wedge angle on jacket flexure
- Jacket joining
- Jacket repair
- Prototype jacket hemisphere forming, joining, and leak checking
- Flexure characteristics of the jacket hemisphere (as opposed to flat panels)
- Development of jacket/tank standoffs
- Properties of gold coatings on the tank and jacket

This section provides the details and recommended approaches derived from the work performed.

4.1.1 Flat Panel Vacuum Jacket Flexure Tests

Using an existing flat metal die with expansion wedges from a previous in-house program (Fig. 4-1), three plaster casts were made from the die. These casts were joined

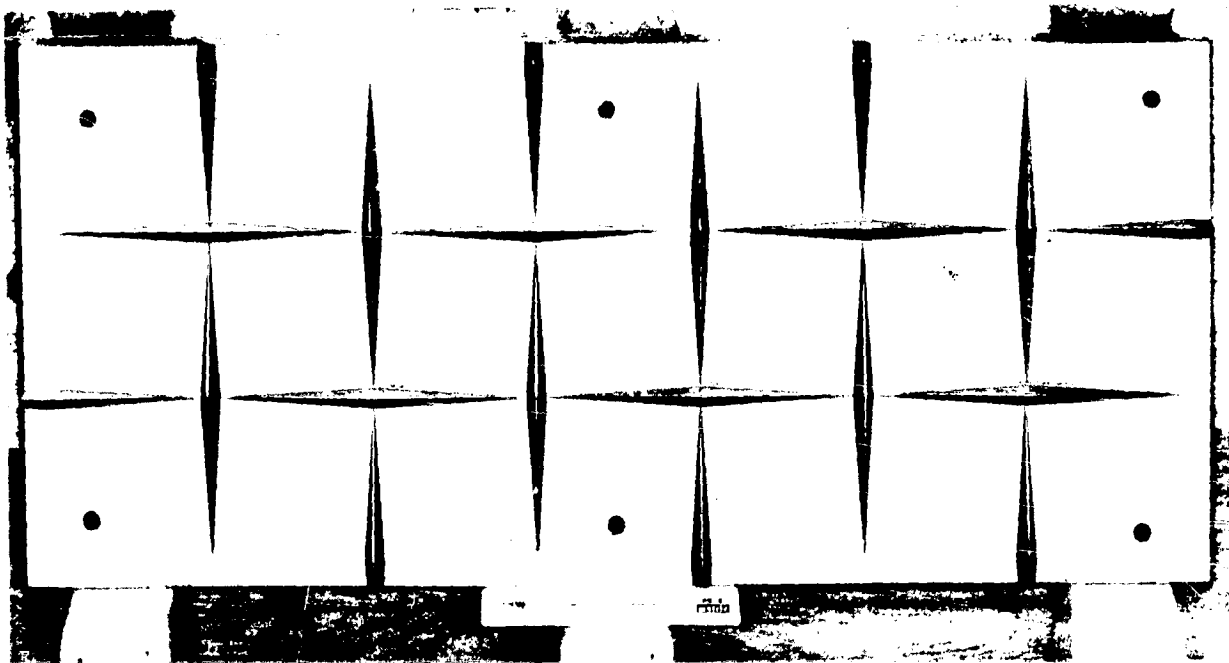


Fig. 4-1 Flat Male Metal Die for Vacuum Jacket Forming

together to form a square mold 0.61 m (24 in.) on a side. A polyurethane/fiberglass male die was cast from the plaster mold.

The 0.008-cm (.003-in.) thick 321 annealed stainless-steel sheet was precision sheared into a square and placed over the forming die. The sheet was approximately 2.5 cm (1 in.) smaller than the die to prevent trapping the sheet around the edges during forming. An oiled adiprene sheet was placed over the top of the stainless steel sheet on the Verson-Wheelon hydropress. The part formed to the full design depth at 2.06×10^7 N/m² (3000 psi) with excellent bead definition around the wedge/flat area intersection and over the wedge ridge. The sheet was stiffened greatly in the plane of the sheet after forming, and no splitting of the metal occurred. (Initial samples that had been hand sheared did split in a couple of places near the edge; apparently the sheared edge rolled over slightly and was trapped during the forming process, preventing drawing in of the sheet during forming.)

The die collapsed inward slightly during forming about 0.04 cm (0.02 in.) over an area of 10 by 15 cm (4 by 6 in.), apparently where there was a void in the die. Also,

the surface finish of the die was rough, imparting surface imperfections in the formed parts. Because of these imperfections in the panel, the tip of each wedge did not always touch the adjacent wedge 90 deg to it. This flat area was measured at 32 locations on the panel in the area where expansion measurements were being made: the average flat area length was 0.18 cm (0.07 in.).

The test setup shown in Fig. 4-2 was assembled to biaxially stretch two vacuum-jacket test panels of the type shown in Fig. 4-3. The biaxial loads were applied at seven reinforced points along each of the four sides using a whiffle tree arrangement as shown in Fig. 4-3. Load cells in both the horizontal and vertical axes were connected to the whiffle tree attach points and the loads were recorded on an X-Y plotter accurate to $\pm 2\%$. Equal expansion loads were applied separately to each axis using two hand-actuated hydraulic rams. The measured load was expressed as a load/unit width applied in each axis (the loads were equal in all cases). The unit width of 50.8 cm (20 in.) is five "squares" on each edge as shown in Fig. 4-3. This conservative approach is used since the effect of the half "squares" around the edges was not known at that time; consequently, the reported force/unit width values are slightly higher than if the full panel width value was used in the calculations.

The expansion of the panel was measured in three directions vertically and three horizontally. A center hole micrometer, accurate to 0.005 cm (0.002 in.) was fitted with special needle tips 0.033 cm (0.013 in.) in diameter. Holes of the same diameter were drilled in the nine center squares to act as reference points for expansion measurements.

Earlier tests recorded the panel expansion by painting the panel black and bonding white dots in the nine center squares. The expansion was recorded photographically and the distance between the dots measured on the negatives using a shadowgraph viewer. When it was found that the panel tended to bow toward the camera during expansion changing the "scale" on the negatives in the test series, this method of measurement was discontinued and the direct measurement method described above was substituted. All data that were taken by the photographic technique and are reported here have a correction factor was derived from reference points of known spacing on the panel that did not change dimensions during the expansion tests.



Fig. 4-2 Biaxial Stretch Test Apparatus

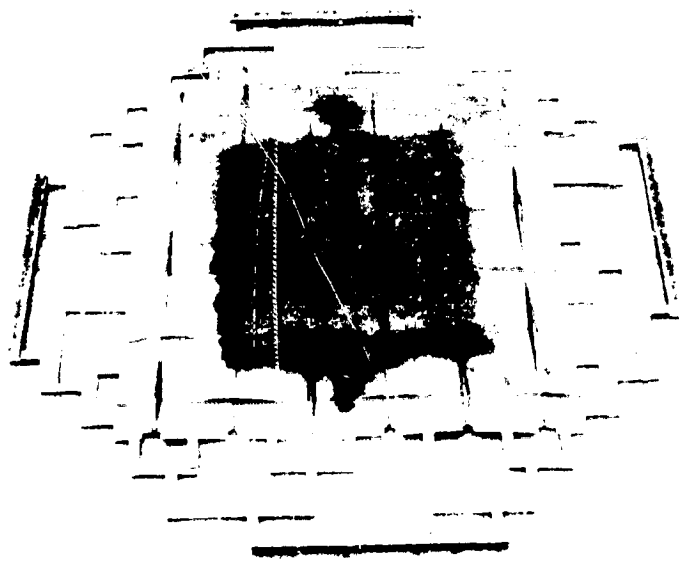


Fig. 4-3 Biaxial Expansion Test Panel

The results of the elastic limit tests are shown in Fig. 4-4. The load was applied, and released, and then a higher load applied. Each point shown is an average of six data points, three horizontal and three vertical, using the direct measurement technique. (These measurements were initially taken photographically and the test repeated using direct measurements.) Note that at > 0.56 percent expansion, the panel did not return to its original dimensions under a no-load condition. However, at even the highest loads applied, there was no visible evidence of panel deformation. Also note the good agreement between the data from two separate test panels.

Since the panels expanded well even with the flat areas at the wedge tips, the effective width of this flat area was increased by bonding 0.48 cm (0.19 in.) strips of 0.008 cm (.003 in.) stainless steel across the tips of all wedges on the flat side of one panel. The test results show that the panels expand along the same stress-strain slope as previously, but the elastic/plastic transition point is lowered to 0.4 percent as shown in Fig. 4-5. These expansion data were recorded photographically and corrected to account for the panel bulging.

The results of these tests led to three very significant conclusions. First, a small flat area at the tip of a wedge can be used for joining gore panels together in a zig-zag overlap pattern and a combination flange/overlap flange joint can be used for the final closure as shown in Fig 4-6.

No joining up over wedges is required and no further expansion panel tests with sample joints are needed since the slope of the stress-strain curve is independent of the length of the flat area at the wedge tip (over the range tested). These designs simplify jacket joining procedures.

Second, it is no longer required to match expansion wedges very accurately at gore joints. Consequently, the very tight dimensional tolerances thought to be required for the contoured forming dies can be relaxed.

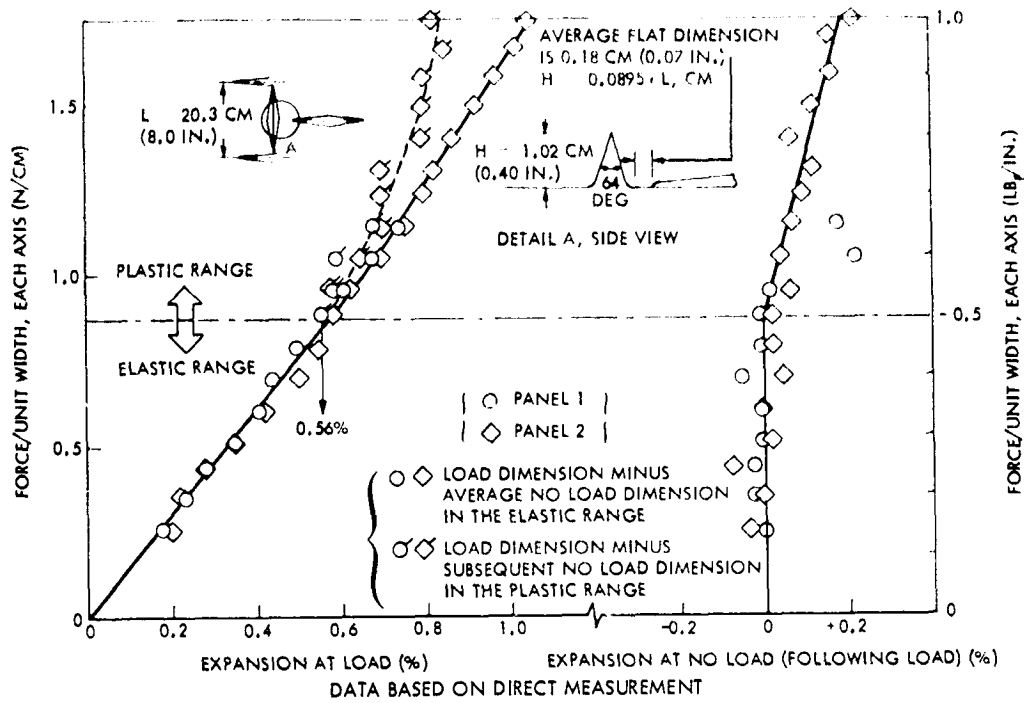


Fig. 4-4 Elastic-Plastic Range Definition of Flat Test Panels

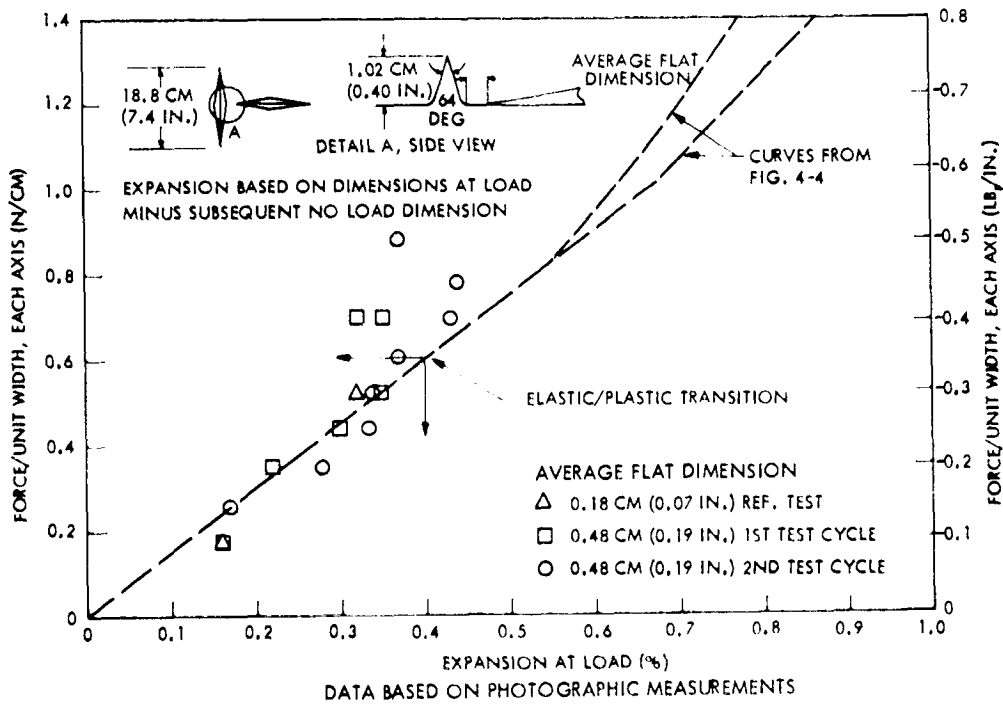
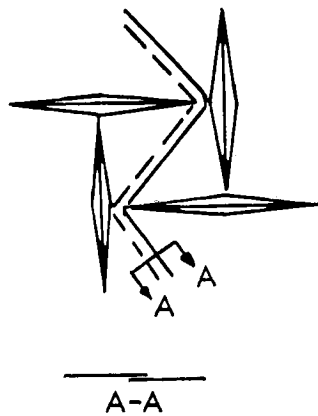


Fig. 4-5 Elastic-Plastic Range Definition for Larger Joint Flat Areas in the Flat Test Panels

OVERLAP GORE JOINT



FLANGE FINAL CLOSURE JOINT

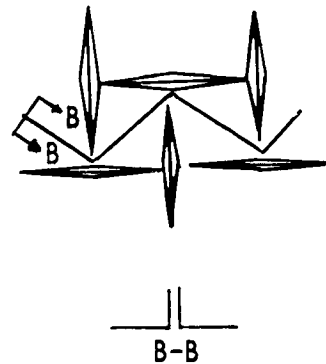


Fig 4-6 Joint Designs

Third, the imperfections present in the test panels due to imperfections in the forming die have no discernible effect on the panel's expansion capability. This conclusion was reached by comparing the six individual measurements at each load. All six measurements followed the same trend and no connection between a local imperfection and panel expansion could be found. Therefore, a jacket that is dented accidentally (to a level consistent with the tested panels) will require no repair in future large-scale systems as long as the jacket does not leak.

4.1.2 Minimum Wedge Angle Tests

During a normal Space Tug flight cycle for this insulation system, the tank contracts as it cools to cryogen temperature, and the evacuated jacket moves inward because of the 1-atmosphere compressive load. Microspheres partially flow out of the wedges at this time (since the wedges close slightly) and into the insulation bulk. Once in space, the atmospheric load is removed and the microspheres can redistribute themselves back into the unstressed, expanded wedges prior to reentry and reapplication of the 1-atmosphere load. However, if the evacuated insulation system is cycled thermally on

the ground, the migration of a portion of the microspheres back into the wedges is opposed by the 1-atmosphere load. This situation represents a series of ground tests where the tank is cycled between ambient and cryogenic temperature.

A special test apparatus shown in Fig. 4-7 was fabricated to determine the effect the wedge angle has on the ability of microspheres to redistribute themselves during this thermal cycling under a 1-atmosphere load. The microspheres are evacuated and the dimension across each of the three triangular expansion sections (with initial angles of 58, 42, and 28 deg) is measured at three reference points to within 0.003 cm (0.001 in.). A formed 64-deg wedge is also attached to the jacket using a silicone rubber sheet intermediary strip. The measurements are repeated when the aluminum can is cooled to LN₂ temperature and then warmed to ambient temperature. This thermal cycle is performed four times.

The delta change in the gradual closing of the triangular sections (due to redistribution of microspheres) both at ambient temperature and at LN₂ temperature was measured. When these data are plotted on a net change basis, the results show there is not a significant difference between the three angles tested as shown in Fig. 4-8. Also, no permanent deformation was noted visually on the wedge or on the three triangular test angles. Consequently, a narrower wedge angle was chosen for the contoured forming dies to extend the elastic range of the jacket (as discussed later in this Section). Other considerations on wedge angle choice include forming limitations and draft angle effect on removing the formed part from the die. Based on these considerations, a wedge angle of 30 deg was selected for the contoured forming dies for the test article.

4.1.3 Resistance Seam Weld Development

The selection of the overlap, zig-zag joint for gore panels and the polar cap which bypasses the expansion wedges simplifies the joining requirements and allows the use of a resistance seam weld technique. The resistance weld process is highly controllable and requires no flux, and a specified narrow weld width can be maintained accurately.

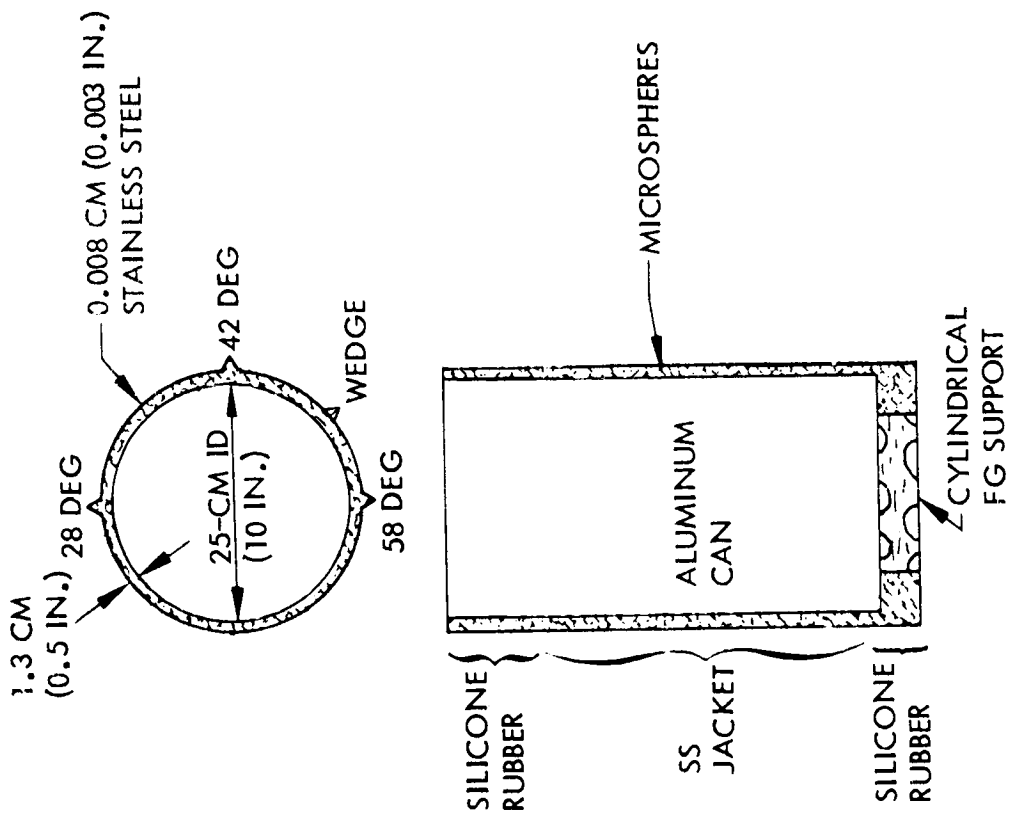
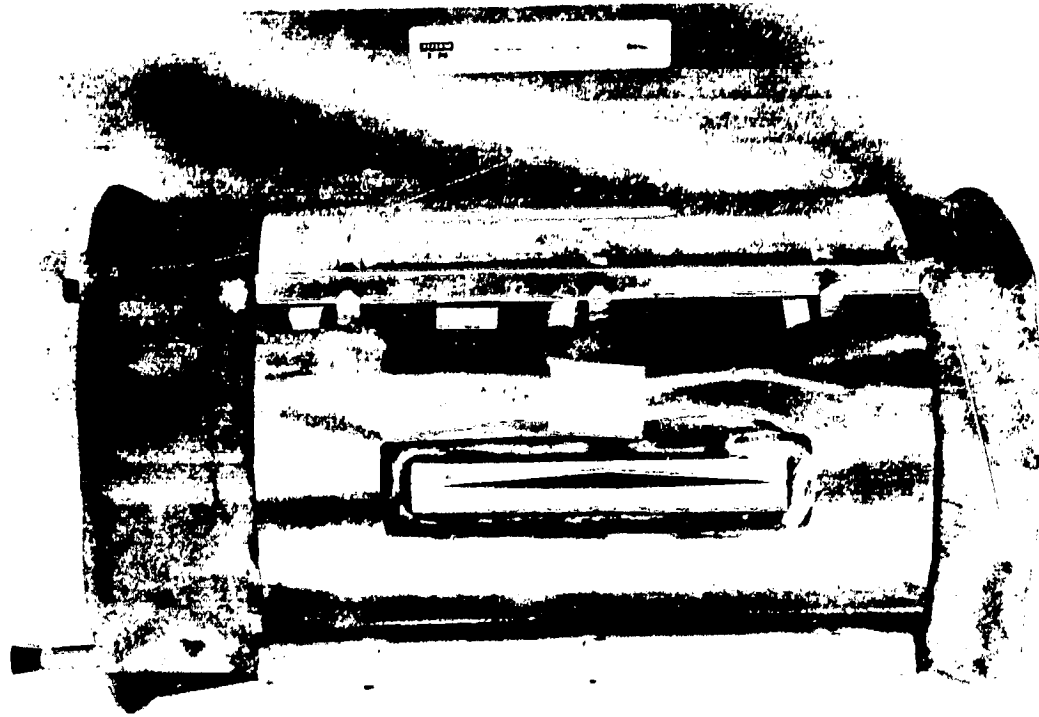


Fig. 4-7 Wedge Angle Test Apparatus

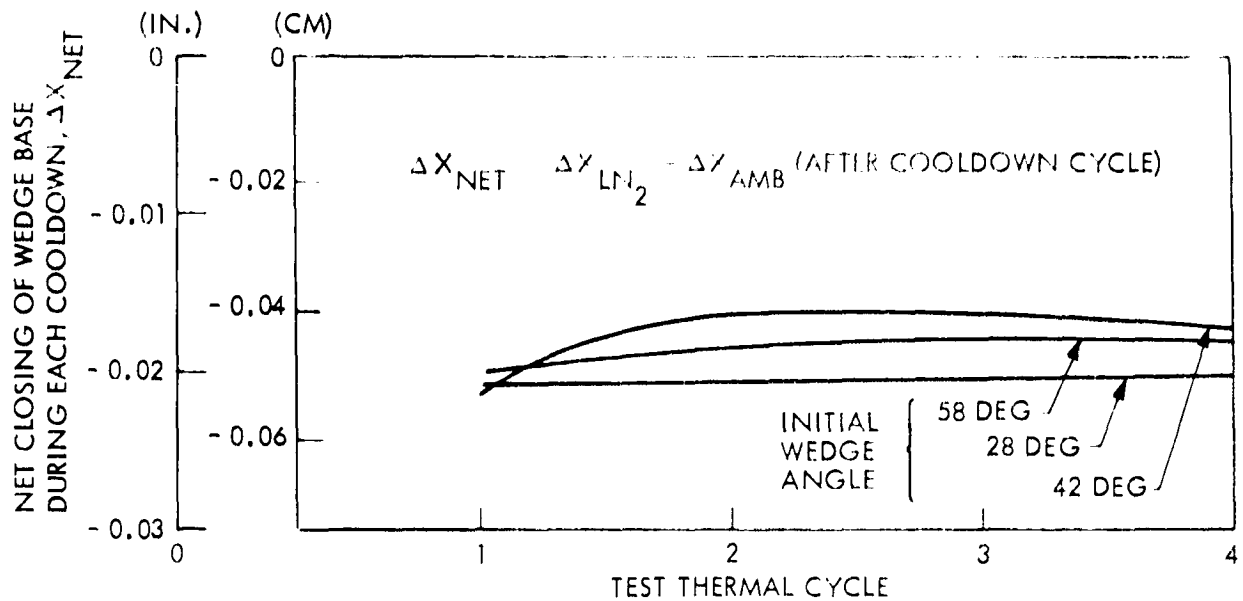


Fig. 4-8 Net Change in Wedge Base Dimension as a Function of Thermal Cycles

The resistance-weld process is particularly suitable for the joining of gore sections and the polar cap because the necessary access to both surfaces is available, and the 0.38 cm (0.15 in.) overlap of the panels in flat areas can be controlled by pre-trimming the parts to a standard template. The overlap in the flat area around the wedge tips is reduced to 0.25 cm (0.10 in.) for greater flexure capability of the jacket.

The welding is accomplished on a 50 kVA Sciaky seam welder (Fig. 4-9) using 7.6 cm (3 in.) diameter copper wheels on both sides with approximately a 0.25 cm (0.1 in.) face width. The seam weld is approximately 0.2 cm (0.08 in.) wide. The fusion zone is continuous and uniform, and the 24 pitch (24 individual overlapping welds per inch) produces a solid weld nugget that ensures vacuum integrity. The panels are vapor degreased prior to the welding.

To determine the vacuum integrity of the selected overlap resistance-seam-weld technique, two square pieces of 321 stainless steel 35 cm (14 in.) on a side and 0.005 cm (0.003 in.) thick were spot welded together at approximately 1.3 cm (0.5 in.) intervals around the edge. A continuous seam weld 1.5 m (5.0 ft) long was then made as shown in Fig. 4-10. The sheets are separated by a coarse screen to provide an evacuation path to the centrally located tube.

LOCKHEED
LOCKHEED
A SUBSIDIARY
OF THE LOCKHEED CORPORATION
MEMPHIS, TENNESSEE



Fig. 4-9 50-kVA Sciaky Seam Welder

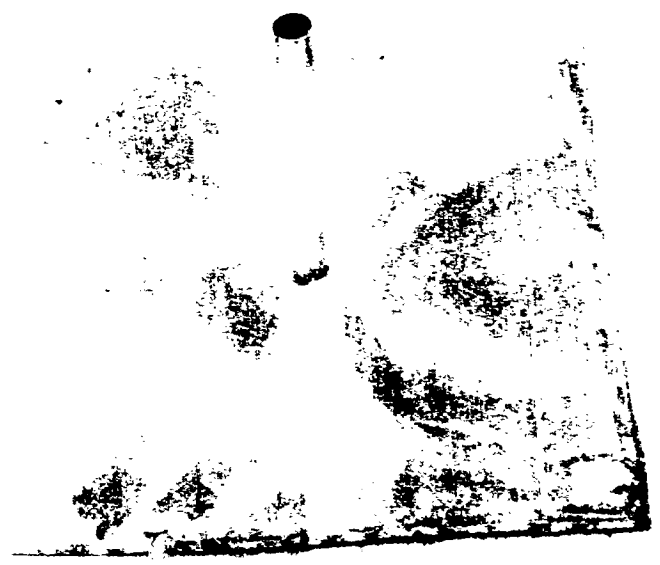


Fig. 4-10 Leak Check Test Panel

The interior of the panel was evacuated and the joints helium leak-checked with a Model 925 Helium Mass Spectrometer sensitive to 2×10^{-8} cc/s. No leaks were detected when the joints were flooded with helium. The results of these tests show both the joining technique and the basic 0.008 cm (0.003 in.) stainless-steel panel provides a vacuum-tight system. The length of the joint tested is 7 percent of the total length of the joints in the 1.19 m (47 in.) diameter test-tank jacket.

4.1.4 Jacket Final Closure Development

The jacket final closure occurs after the two individual jacket hemispheres have been leak-checked and coated on the inside surface with a 0.01 mm (0.0006 in.) coat of epoxy and 1000 Å of gold. (Joints and solder coated surfaces are masked prior to this coating.) The limitations on the joining methods that can be used on this combination flange and overlap closure are as follows:

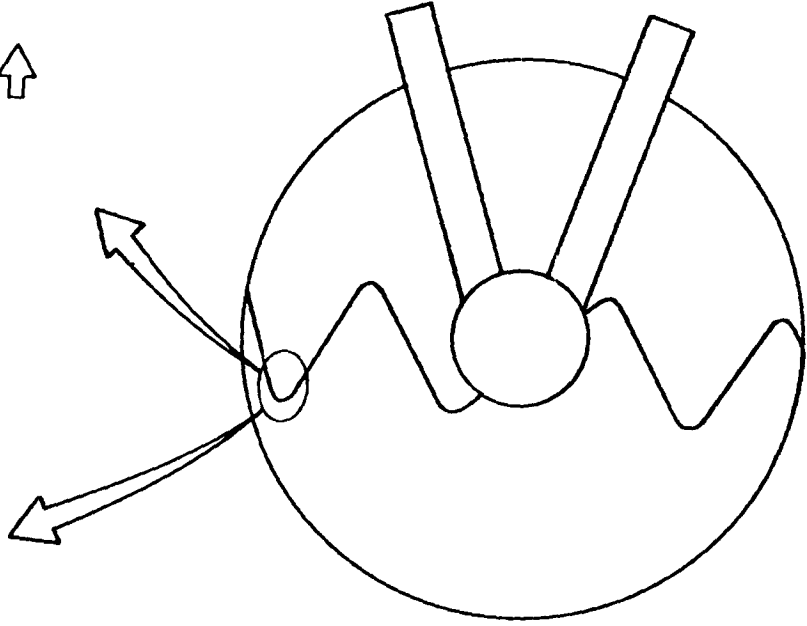
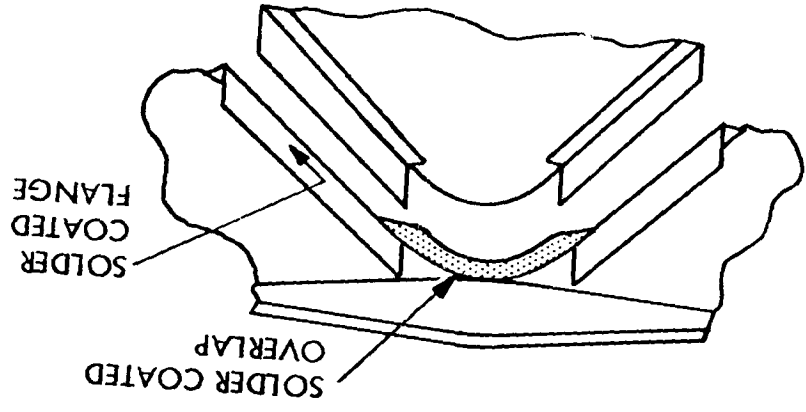
- The epoxy coating can withstand up to $\sim 205^{\circ}\text{C}$ (400°F) for a short period of time in an inert atmosphere.
- No corrosive fumes can be allowed to enter the vacuum jacket interior.

The final closure design selected for the test article consists of a combination of soldered flanges and overlaps as shown in Fig. 4-11.

To obtain better wetting of the solder on the stainless steel at the final closure overlap joint and around the strut assemblies, the area is brush plated with a nickel strike followed by successive coats of copper 0.004 mm (0.00015 in.) and tin 0.003 mm (0.0001 in.) per Mil A 865. The joints are then coated with solder. The flanges were solder coated using 157 flux (before the pretinning technique was tried). Later work shows the pretinning method provides better wetting action and eliminates the use of corrosive 157 flux, which can cause corrosion pits to form in the jacket.

To assemble the two vacuum jacket hemispheres, the flanges are held together with spring clamps and spot welded every 0.6 cm (0.25 in.) at the base of the flange and

Fig. 4-11 Soldered Final Closure Design



4-18

LOCKHEED PALO ALTO RESEARCH LABORATORY
LOCKHEED MISSILES & SPACE COMPANY, INC.
A SUBSIDIARY OF LOCKHEED AIRCRAFT CORPORATION

every 1.3 cm (0.5 in.) at the top of the flange. The overlap joints are then soldered by preheating the specially designed soldering tool shown in Fig. 4-12 to approximately 250°C (482°F). The individual beryllium-copper "foot-prints" adjust to the spherical overlap jacket surface because of the "U" shaped spring design. The soldering tool is mounted off the wooden ring shown in Fig. 4-13 and pressed securely against the surface by adjusting the screw shown. (The jacket is supported by a Teflon disk placed between the tank and the jacket.) The thermostatically controlled heater is left on for 15 to 20 s and then turned off. The tool is cooled with an air blower until the temperature reaches approximately 60°C (140°F), at which time (~30 s) it is removed.

The second special copper soldering tool (shown in Fig. 4-14) is preheated to 290°C (554°F), using a thermostatically controlled heater, then clamped over the flanges as shown in Fig. 4-15. After 5 to 10 s when the solder flows out of the joint, the heater is turned off and the tool cooled with an air blower to 60°C (140°F) in about 45 s.

Random leaks developed in the flanges, at the flange/overlap intersection, and in the overlaps. Repairs in the overlap were made using a lower melting (~204°C or 400°F) 50-50 Pb-Sn solder and soldering iron with a rosin flux to form a solder fillet over the joint. (The lower melting solder prevents the joint from opening.) The flange overlap intersection leaks were sealed by placing a small 0.05 mm (0.002 in.) thick copper strip around the end of the flange and soldering it manually using the 50-50 solder and rosin flux. The flange leaks were repaired by forming a "U" shaped cap of solder coated copper foil 0.05 mm (0.002 in.) thick and placing it over the top of the pretinned flange using rosin flux. The copper is then soldered to the flange using the pre-heated clamping tool described above. Some pinhole leaks were also found where the flanges were spot welded together. These leaks can be closed by pretinning the area and soldering with 50-50 solder and rosin flux or cleaning the area to the bare metal and covering the pinholes with Epibond 123/9615-10 epoxy adhesive.

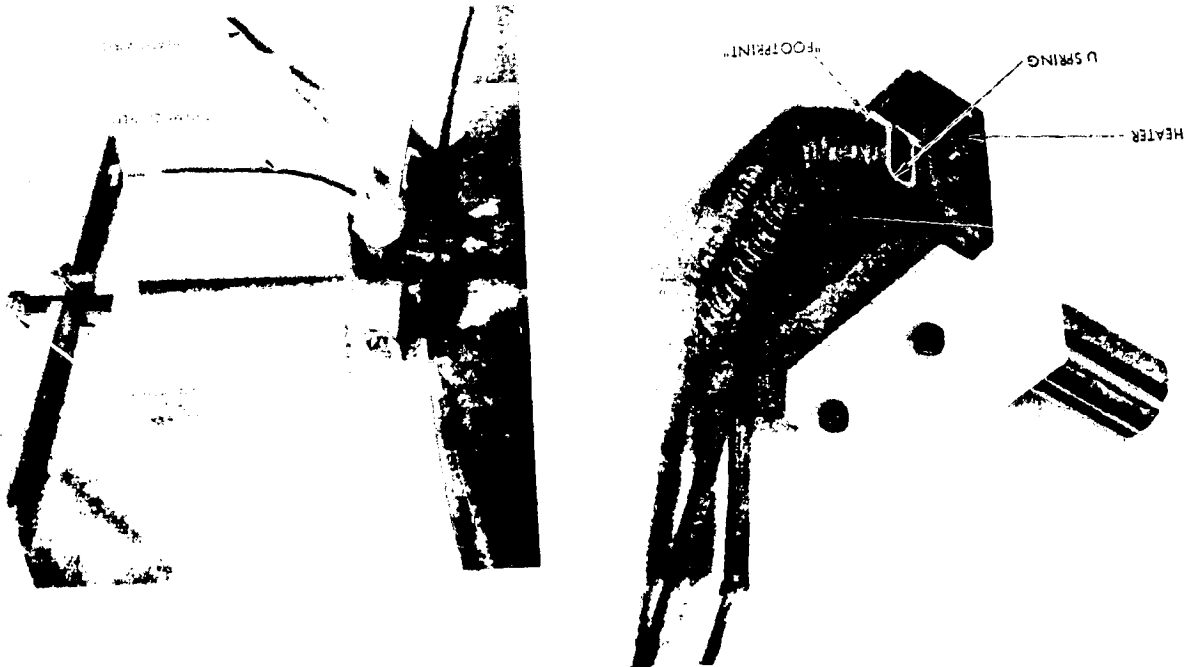
4-13

Fig. 4-13 Wooden Support Ring



PHOTOGRAPHED BY
ORIGINATOR'S NAME

Fig. 4-12 Overlap Joint Soldering Tool



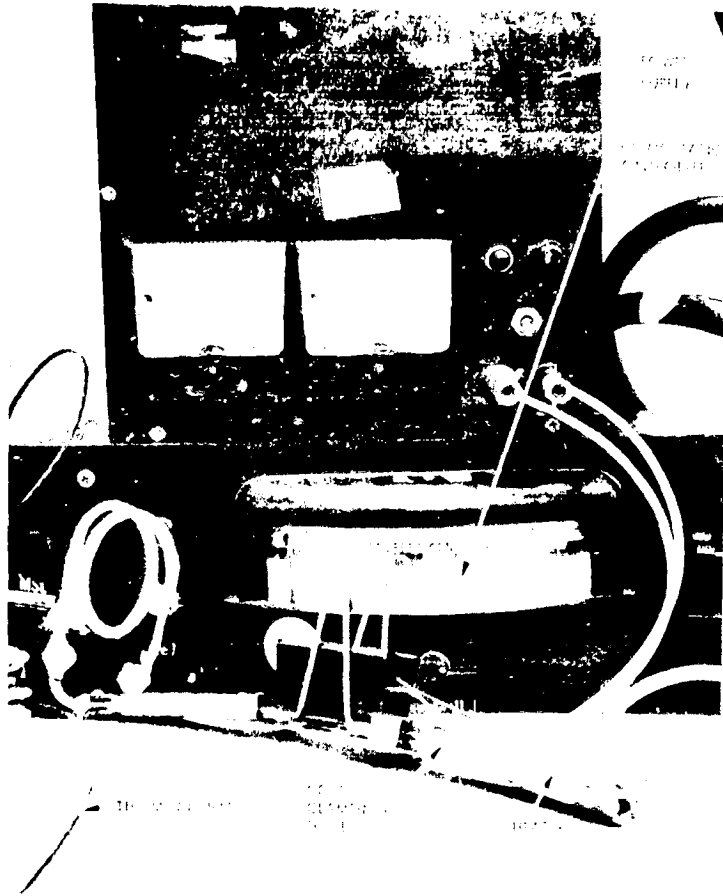


Fig. 4-14 Flange Joint Soldering Tool

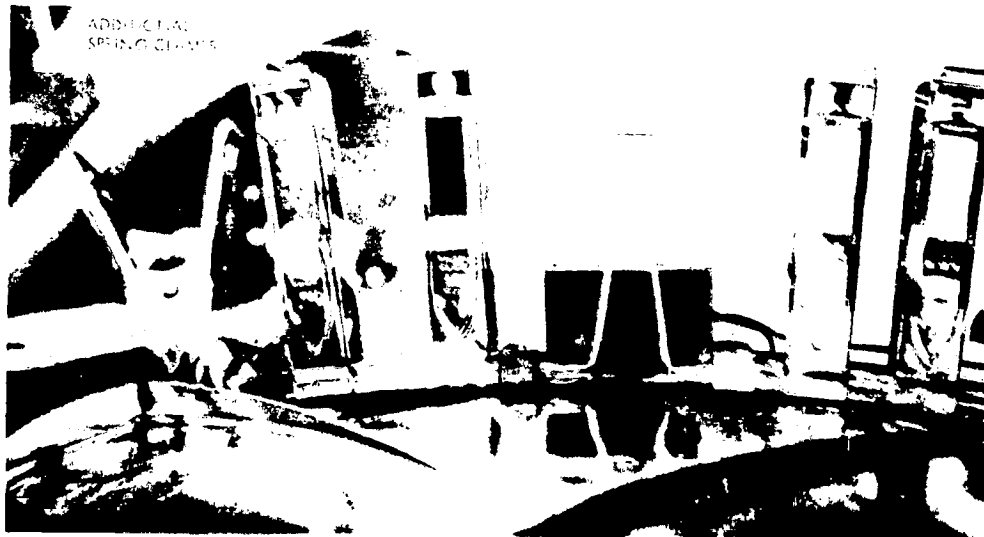


Fig. 4-15 Flange Tool Installed

4-16

LOCKHEED PALO ALTO RESEARCH LABORATORY
 LOCKHEED MISSILES & SPACE COMPANY, INC.
 A SUBSIDIARY OF LOCKHEED AIRCRAFT CORPORATION

Experience with the test jacket final closure joint assembly shows soldering is a difficult process to control and repair when an active (corrosive) flux cannot be used. Even when using a noncorrosive rosin flux, the tank and jacket has to be vacuum baked prior to filling with microspheres (because of residual rosin inside the jacket) to reduce the outgassing load to an acceptable level.

Consequently, it is recommended in any future work that the final closure joint be resistance seam welded using the design shown in Fig. 4-16.

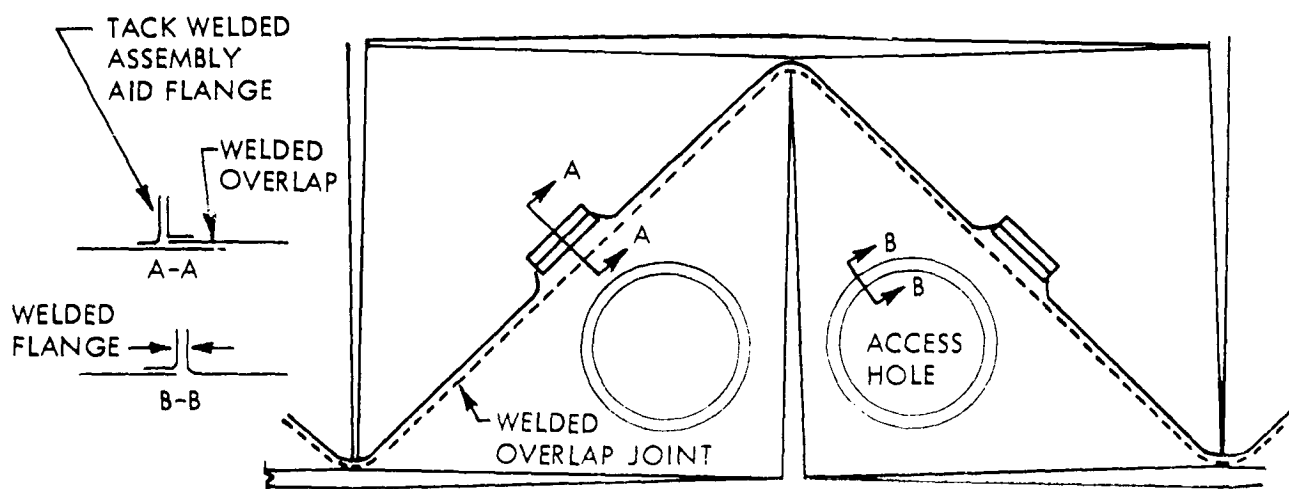


Fig. 4-16 Welded Final Closure Joint Design




The joint is a continuous overlap seam. The two jacket halves are held in place during the welding by clamping the assembly flanges together and tack welding them. (These flanges are not the seal.)

A specially designed air-cooled welder head with copper wheels on the ends of a scissors-type clamp is inserted through the access holes and the overlap weld is made in the same manner as gore joints - i.e., tack weld then seam weld. Suitable

clamping pressure is accomplished pneumatically. The weld is leak checked by pressuring with helium and sniffing with a mass spectrometer. (The access holes are plugged with rubber stoppers.) When the joint is leak tight, the access hole covers are resistance welded into place and leak checked. The access hole welds increase the total length of welded joints on the test article jacket by 15%.

4.1.5 Jacket Repair Methods

The following recommended jacket repair methods have been demonstrated to be vacuum leak tight following 30 thermal shock cycles (direct liquid nitrogen immersion followed by rapid warming to ambient temperature using a hot air gun).

<u>Type of Repair</u>	<u>Recommended Method</u>
In-Process Overlap Joint Leak	Reweld with 50 kVA Sciaky resistance seam welder
	
In-Process Puncture	Reweld lenticular patch of 0.08 mm (0.003 in.) 321 stainless steel over hole.
	
In-service overlap joint leak, or puncture in flat or flex areas.	Apply CREST 7450A and B polyurethane adhesive to cleaned area. Allow to cure for 24 hours at ambient temperature. Bond 0.005 cm (0.002 in.) stainless steel patch if hole is large.
	

4.1.6 Preliminary Insulation Thickness Optimization

To obtain the same magnitude of heat flux for the test tank as for the full-scale LH₂ tank on the Space Tug, an insulation thickness optimization was performed on the Tug hydrogen tank. The optimum thickness occurs when the insulation weight equals the prorated boiloff weight $[(\partial W_I / \partial W_{BO}) = 0.39]$ for a 163-hour mission. Using the thermal conductivity model from section 4.3 for uncoated microspheres with gold boundaries at $T_H = 222^\circ\text{K}$ (400°R) and $T_C = 21^\circ\text{K}$ (37°R), the $\delta_{opt} = 1.32$ cm (0.52 in.).

4.1.7 Deflection Requirements of the Test Tank Vacuum Jacket

Thermal analyses show the average temperature of a Space Tug LH₂ tank vacuum jacket during ground hold will be on the order of 280°K (504°R) while the space operating and initial reentry temperature extremes are 261 to 167°K (470 to 300°R). Consequently, if the vacuum jacket is designed and installed so its unstressed condition is at a temperature higher than any listed above, the jacket will always apply a slight compressive load on the microspheres at any lower temperature from ground hold through orbit flight and reentry into the atmosphere. This compressive load will eliminate any voids in the insulation minimizing migration of microspheres under flight loads when the Tug is outside the atmosphere.

Since the spring/Kevlar attachments hold the jacket standoff distance nearly constant at the attach points, independent of vacuum jacket temperature changes, the compressive load applied on the microspheres between the attachments depends on how much the jacket "bows" inward between the spring/Kevlar attachments as the jacket temperature drops. Results from later hemisphere expansion tests show that the "bowing" inward and resultant compressive load on the microspheres is minimal and has only a small effect on insulation heat transfer over the orbit temperature range of the jacket.

Using this design concept for the test tank, the expansion requirements for the vacuum jacket are calculated as follows. The average membrane outer radius of the test tank is:

Ambient temperature radius:	58.57 cm (23.06 in.)
LN ₂ temperature radius:	<u>58.36 cm (22.98 in.)</u>
	Δ0.21 cm (0.08 in.)

(LN₂ temperature was selected for these calculations since all thermal performance tests will be conducted at this temperature; however, the jacket is also designed to flex further if the tank is cooled to LH₂ temperature.)

Selecting a nonstressed jacket temperature of 294°K (530°R), a ΔT of 14°K (25°R) above the highest operating jacket temperature on the ground, in orbit, or during initial reentry, the ambient temperature jacket dimension is:

Tank radius at LN ₂ temperature:	58.36 cm (22.98 in.)
Optimized insulation thickness:	<u>1.33 cm (0.52 in.)</u>
Jacket radius at ambient temperature:	59.69 cm (23.50 in.)

By holding this thickness constant with the spring/Kevlar attachments, the jacket radius is increased to the following value when the entire assembly warms up to ambient temperature.

Tank radius at ambient temperature:	58.57 cm (23.06 in.)
Insulation thickness:	<u>1.33 cm (0.52 in.)</u>
Expanded jacket radius, ambient temperature:	59.90 cm (23.58 in.)

Therefore, the jacket must expand

$$100 \left(\frac{59.90 - 59.69}{59.69} \right) = 0.35\%$$

Since the maximum jacket radius movement due to the aluminum tank cooling from ambient to cryogenic temperature is

0.39% (tank at LN ₂ temperature)
0.42% (tank at LH ₂ temperature)

The jacket must also contract

$$0.39 - 0.35 = 0.04\% \text{ (tank at LN}_2 \text{ temperature)}$$

$$0.42 - 0.35 = 0.07\% \text{ (tank at LH}_2 \text{ temperature)}$$

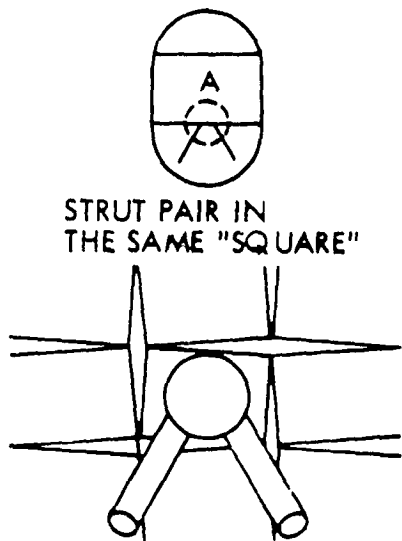
4.1.8 Contoured Forming Dies

Design Procedure. The prior analyses and development work established the following requirements for designing the vacuum jacket expansion wedges:

Wedge angle:	30 deg
Max. elastic expansion requirement:	0.35%
Max. elastic contraction requirement:	-0.07%
Unstressed jacket radius at ambient temperature:	0.597 m (23.500 in.)
Flat area at wedge tips for overlap joints:	0.18 cm (0.07 in.)
Flat area to wedge tip final closure joint:	0.43 cm (0.17 in.)

The flat panel expansion tests also established the elastic limits for the design.

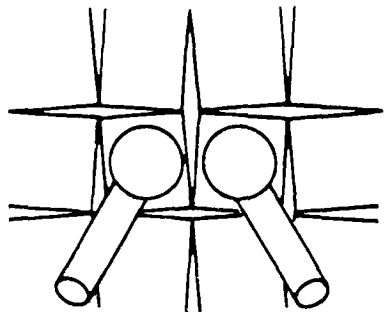
The spacing of the wedges is constrained by the number and location of the tank support struts as shown.



Detail A

Tank Support Struts		Minimum No. of Squares Allowed at the Circumference	Total No. of Squares. N. Must be a Multiple of
Pairs	Total		
3	6	6	6
4	8	4	4
5	10	10	10
6	12	6	6
7	14	14	14
8	16	8	8
⋮	⋮	⋮	⋮

STRUT PAIR IN
ADJACENT
"SQUARES"
DETAIL A

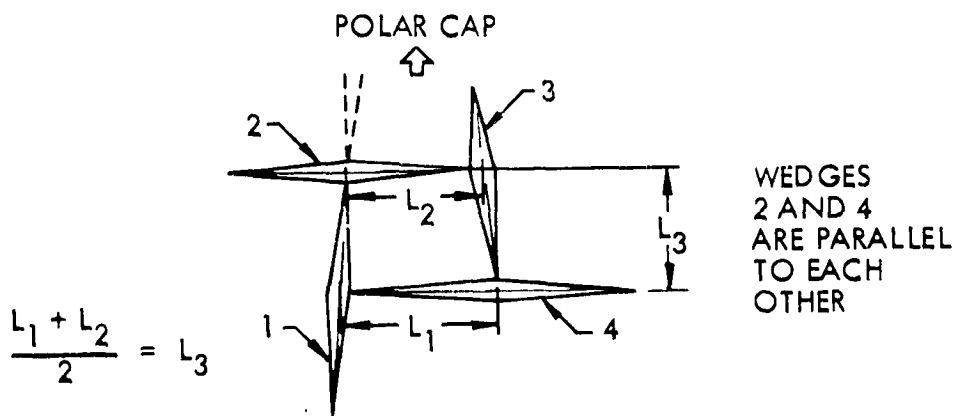


Tank Support Struts		Minimum No. of Squares Allowed at the Circumference	Total No. of Squares. N, Must be a Multiple of
Pairs	Total		
3	6	6	6
4	8	8	4
5	10	10	10
6	12	12	6
7	14	14	14
8	16	16	8
⋮	⋮	⋮	⋮

The squares must be an even number for the pattern to "close" on itself.

The size of the largest square is determined by the clearances required around the support/tank attachment area. The jacket circumference is then divided by the appropriate multiples from the above tabular listing, and a square size is selected that is equal to or slightly greater than the square size set by support clearance requirements.

The wedge patterns become progressively smaller going from the equator up to the polar cap. The size of the wedge pattern is set so the following relationship holds.

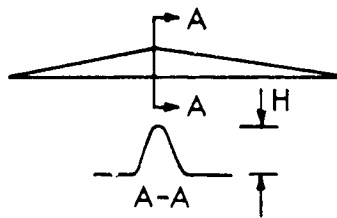


The L dimension to use in the following equations are shown below:

<u>Wedge No.</u>	<u>Square Dimension</u>
1	L_1
2	L_1
3	L_2
4	L_2

Based on the flat panel test results, the height of the wedges at their apex was set for the contoured forming dies by the following relationship:

$$H = 0.179 \epsilon L (SF)$$



where

- H = maximum wedge height, cm
- ϵ = required jacket expansion, %
- L = "square" length, cm
- SF = safety factor (1.25)

This relationship used test data from a flat panel with a single wedge height, H, of 1.02 cm (0.40 in.). The expansion capability was assumed to vary linearly with H for different size wedges. However, the hemisphere tests with wedges of different heights showed the expansion capability of the wedges in the elastic range varied as

$$a + bH + cH^2 \propto \epsilon L$$

From the hemisphere test data, the empirical constants a, b, and c were obtained solving simultaneous equations. The relationships which should be used in any future designs for forming dies are shown below. (Note: The current forming die designs meet the design goal of 0.35 percent elastic expansion for the different size wedges.)

For vertical, single curvature wedges, i.e., 1, 3

$$H = \frac{19.1 + \sqrt{80.6 \epsilon L - 276}}{40.3}$$

For the horizontal, double curvature wedges, i.e., 2, 4

$$H = \frac{10.05 + \sqrt{55.8 \epsilon L - 150.1}}{27.9}$$

where

H = maximum wedge height, cm ($0.5 < H < 1.25$)

ϵ = desired expansion, % (use a safety factor of 1.25)

L = wedge spacing, cm

For the spherical test tank a design procedure has been developed to calculate the wedge pattern dimensions L as they progress up the dome. (A similar procedure can be worked out for ellipsoidal tank shapes.) The procedure is as follows, using Fig. 4-17 as a reference:

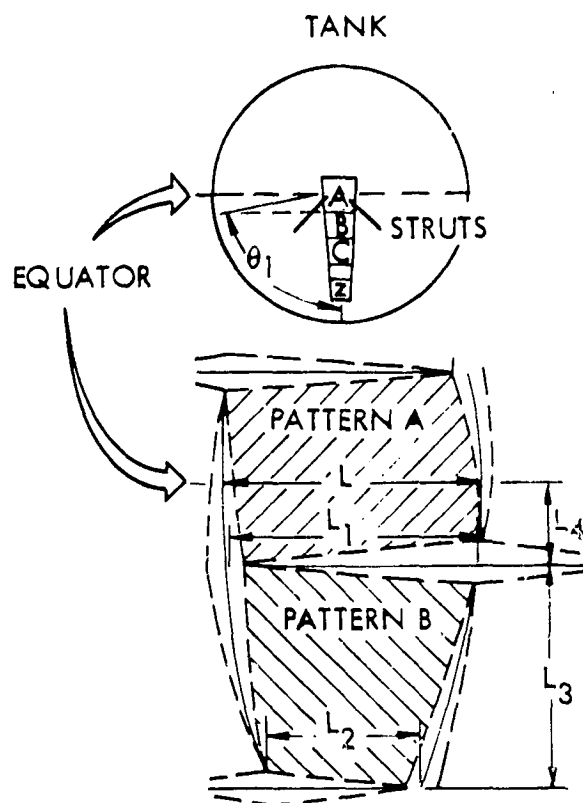


Fig. 4-17 Wedge Design Procedure

1. Calculate L at the equator. $L = 2\pi R/N$ where R is the ambient temperature radius of the jacket and N is the total number of squares around the equator.
2. Calculate the dimensions of the patterns A through Z. First calculate values of L_1 and L_4 . $L_1 = L \sin \theta_1$.

where

$$\theta_1 = 90 - 180/N \text{ in degrees}$$

$$L_4 = L/2$$

Then solve the right-hand side of the following equation knowing θ_1 .

$$\sin \theta_2 + \frac{N\theta_2}{180} = \frac{N}{180} \theta_1 - \sin \theta_1$$

From Fig. 4-18, θ_2 can be determined. Then $L_2 = L \sin \theta_2$

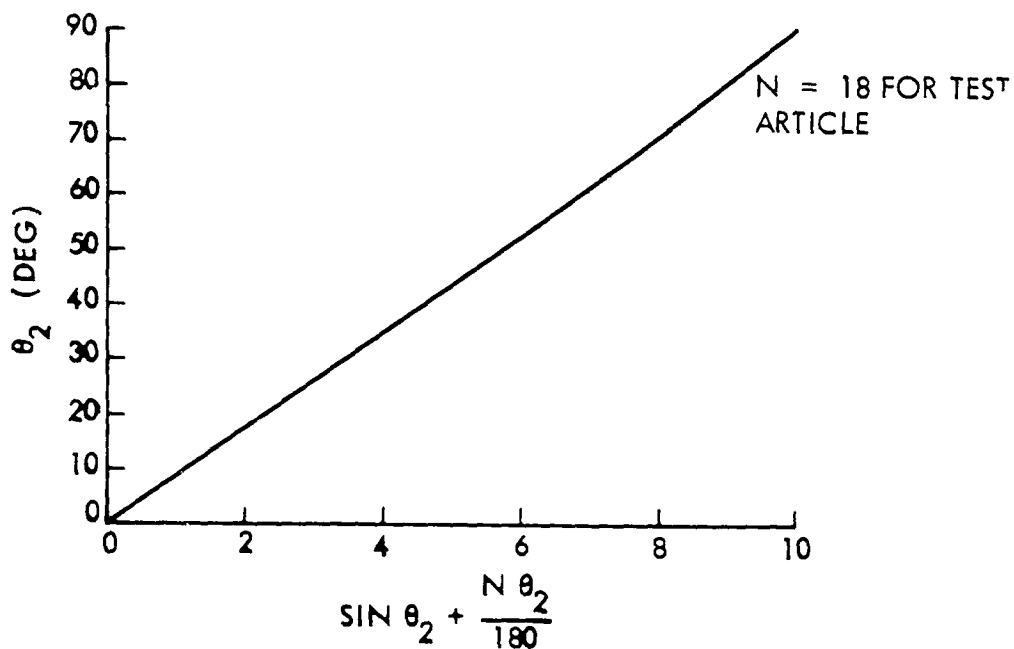


Fig. 4-18 Expansion Pattern Relationship

and

$$L_3 = \frac{L_1 + L_2}{2}$$

This procedure is repeated as many times as required up to the polar cap transition area.

Die Design. Based on the previously described design procedure, designs were prepared for:

- A stretch form block to contour flat sheets to a 0.597 m (23.5 in.) radius (Fig. 4-19)

REPRODUCIBILITY OF THE ORIGINAL PAGE IS POOR



Fig. 4-19 Stretch Form Block

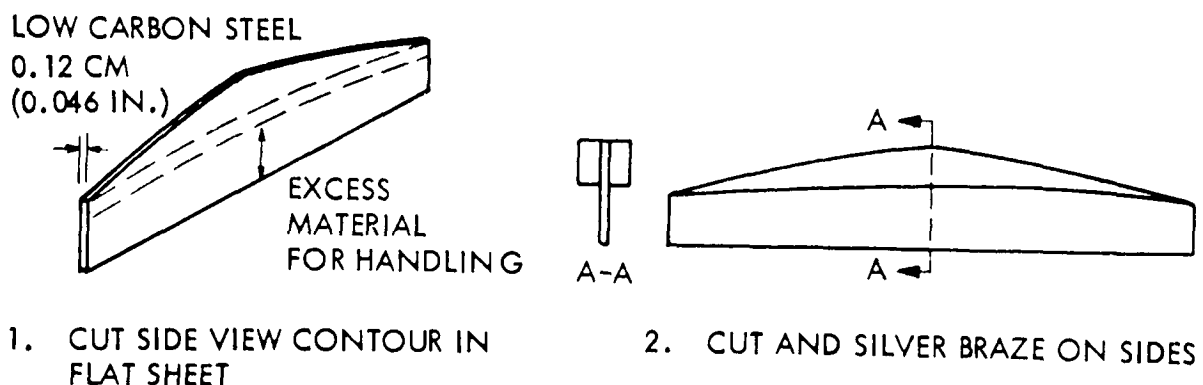
- A forming die for the jacket gore panels (Fig. 4-20)
- A polar cap die for terminating the gore panels at the poles of the tank (Fig. 4-21)

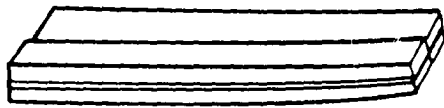
The Teflon coating on the stretch form block reduces the coefficient of friction for the stretch-form operation.

Die Fabrication. All three dies were cast from 356-T6 aluminum. The spherical surface was machined to a $\sqrt[32]{\text{---}}$ finish using a tracer lathe. Porosity holes in the machined surface were filled with Devcon F (an aluminum powder/epoxy mix) and the surfaces highly polished.

The spherical surface of the stretch form die was coated at a vendor with 0.013 mm (0.0005 in.) thickness of TFE Teflon. The coating was fused on at 399°C (750°F). The low coefficient of friction of Teflon allows the stretch forming of stainless steel parts to proceed without the use of an oil lubricant, eliminating the intermediate vapor degreasing step required previously. Slots for installing the wedges on the polar cap die were cut with a slitting saw; an end mill was used on the gore forming die as shown in Figs. 4-22 and 4-23.

The wedges for the polar cap and gore forming die were fabricated as follows:





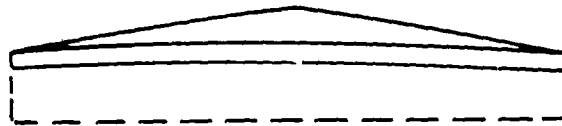
2a. ROLL CONICAL CONTOUR
(HORIZONTAL WEDGES ONLY)



3. MACHINE TOP VIEW CONTOUR



4. MACHINE AND HAND FINISH
FINAL CONTOUR



5. CUT OFF EXCESS MATERIAL

The partial wedges on the gore forming die were cast from the full-size wedges using a silicone rubber mold and a zinc-base casting alloy (Cast-a-loy 1). These partial wedges are required to prevent wrinkling of the stainless steel sheets during forming yet are trimmed off before joining the gores. Consequently, these partial wedges do not have to be as dimensionally accurate as the full wedges and castings will suffice.

All wedges are bonded into the machined slots using epoxy adhesive. The stiffening bead attachment to the gore die used a metal locating pin at the center plus epoxy adhesive. The tips of the stiffening beads are contoured with Devcon F.

The finished dies are shown in Figs. 4-24, 4-25, and 4-26.

4.1.9 Vacuum-Jacket Fabrication

The following steps are required to fabricate and assemble a vacuum-jacket hemisphere:

REPRODUCIBILITY OF THE ORIGINAL PAGE IS POOR

FOLDOUT FRAME

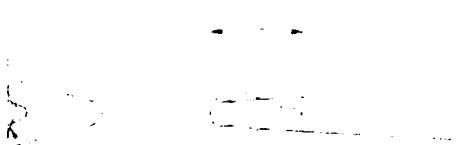


FIG. 1. FOLDOUT FRAME ASSEMBLY
DRAWING BY T. H. BRYAN



FIG. 2. DETAIL OF FOLDOUT FRAME
NO SCALE

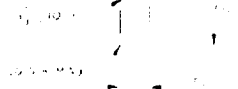
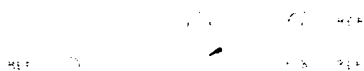


FIG. 3. DETAIL OF FOLDOUT FRAME
NO SCALE

1. THIS DRAWING IS A TECHNICAL DRAWING OF A FOLDOUT FRAME ASSEMBLY.
2. THE DRAWING IS A TECHNICAL DRAWING OF A FOLDOUT FRAME ASSEMBLY.
3. THE DRAWING IS A TECHNICAL DRAWING OF A FOLDOUT FRAME ASSEMBLY.
4. THE DRAWING IS A TECHNICAL DRAWING OF A FOLDOUT FRAME ASSEMBLY.
5. THE DRAWING IS A TECHNICAL DRAWING OF A FOLDOUT FRAME ASSEMBLY.
6. THE DRAWING IS A TECHNICAL DRAWING OF A FOLDOUT FRAME ASSEMBLY.
7. THE DRAWING IS A TECHNICAL DRAWING OF A FOLDOUT FRAME ASSEMBLY.
8. THE DRAWING IS A TECHNICAL DRAWING OF A FOLDOUT FRAME ASSEMBLY.
9. THE DRAWING IS A TECHNICAL DRAWING OF A FOLDOUT FRAME ASSEMBLY.
10. THE DRAWING IS A TECHNICAL DRAWING OF A FOLDOUT FRAME ASSEMBLY.



PRECEDING PAGE BLANK NOT FILMED

REPRODUCIBILITY OF THE ORIGINAL PAGE IS POOR

FOLDOUT FRAME

MOUTH ... HARD
... EDGED ... BURNERS
WITH EPOXY

.005
.000

DETAIL ... 3 PLACES
SCALE NONE

27.510
10V.R

1.8
2 PL.

1500-3 UN.
100 MM. FU.
2 PLACES

4 TO
REF

015

25.5 K 2 PL.

5.574
2

25.5 K

25.5 R

5.330
2

25.5 K

... ...
... ...
... ...

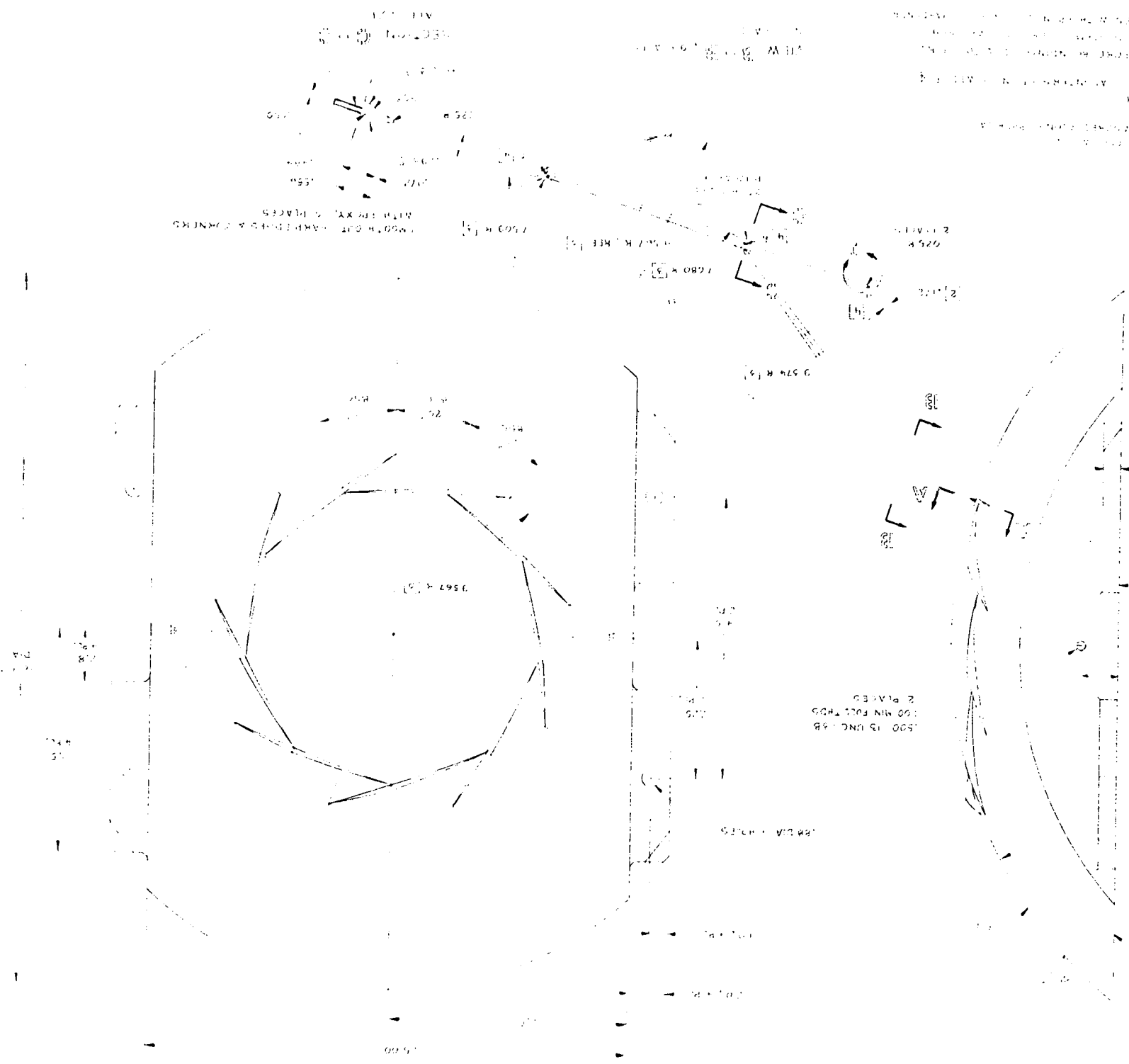
1.8
4 PL.

075 R
2 PL.

- NOTES
1. THE ...
 2. ...
 3. ...
 4. ...
 5. ...
 6. ...
 7. ...
 8. ...
 9. ...
 10. ...

... ...

Fig. 4-21 Polar Cap Die



POLOUT FRAME 2

TY OF THE GE IS POOR

FIG. 4-23. Closing of Mill Operation



FIG. 4-22. Setup for Milling Wedge Slots

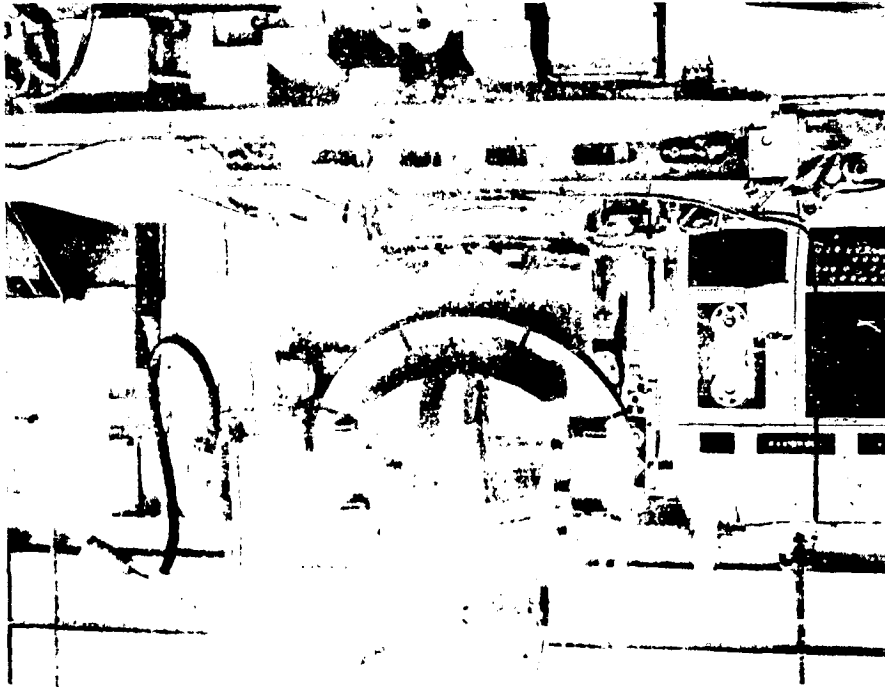




Fig. 4-24 Stretch Form Block

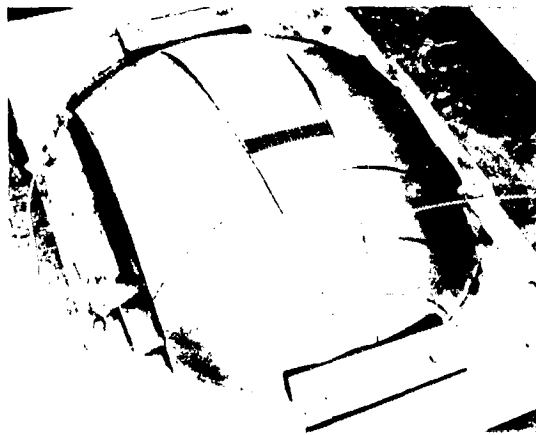


Fig. 4-25 Gore Forming Die
(Minus Stiffening
Beads)

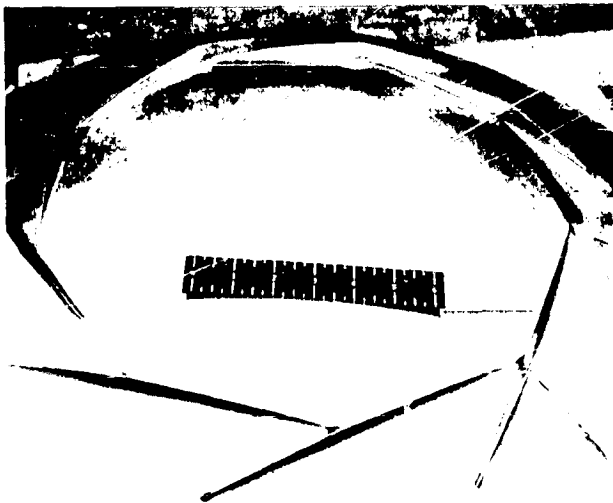


Fig. 4-26 Polar Cap Die

- Stretch-form a spherical contour into the 321 stainless steel sheets.
- Using the stretch-formed sheets, hydropress-form the wedge patterns into gore and polar cap panels.
- Trim, clean, and resistance-seam-weld the panels together; form, solder, coat, and resistance-seam-weld the final closure flange to the hemisphere.
- Leak-check the dome and repair leaks, if any, using the resistance seam welder.
- Solder-coat the spring/wire attach points and final closure joint overlap areas.
- Epoxy- and gold-coat the hemisphere interior.

The work required to develop these processes is given here.

4.1.9.1 Stretch-Forming Stainless Steel Sheets. 304 stainless steel sheets 0.41 mm (0.016-in.) thick were stretch-formed on the stretch form block using a Huffer Stretch Press. The 59.7 cm (23.5-in.) spherical radius panels are suitable for use as holding and shipping fixtures for the thin stainless steel vacuum-jacket sheets. Enough sheets of 0.08 mm (0.003-in.) 321 annealed stainless steel sheets were then stretch-formed to fabricate a test-jacket hemisphere as shown by the sequence of photos in Fig. 4-27. The formed parts are stored on and taped to the thicker sheets. Sheets of 0.05 mm (0.002 in.) and 0.03 mm (0.001 in.) were also stretch-formed successfully to demonstrate thinner sheets can be formed.

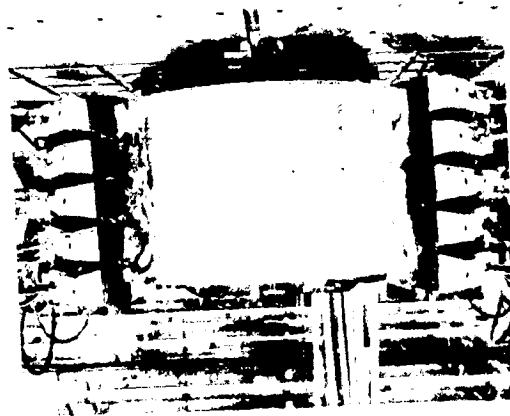
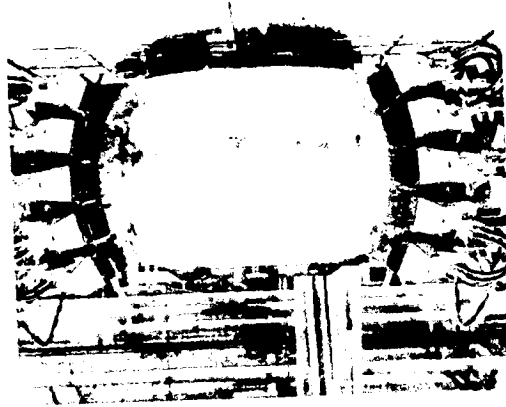
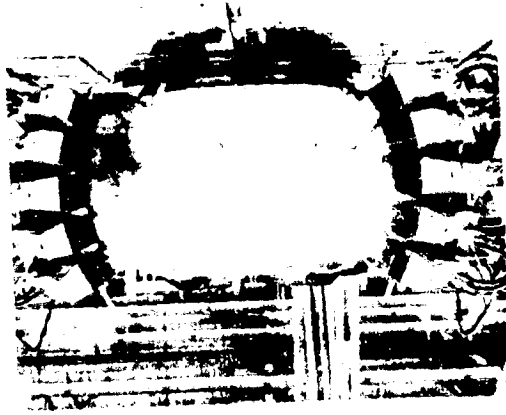
The initial stretch-form operation required oiling the forming die and vapor-degreasing the parts afterward. After Teflon-coating the die, the oiling and vapor-degreasing steps were no longer required.

4.1.9.2 Hydropress-Forming the Wedge Shapes. During the hydropress-forming development, three areas were identified that required special attention. They are:

- Shipping formed parts without damaging them
- Forming parts without tearing the stainless steel material
- Eliminating wrinkling in formed parts

4-88

Fig. 4-27. Stencil Forming Sequence of Stainless Steel Panels



Shipping Containers. In order to ship the spherically stretch-formed stainless steel sheets to Burbank, California, for hydropress-forming the wedges, special shipping containers were fabricated. A hole was punched in each of the four corners of the 0.41 mm (0.016-in.) stainless steel stretch-formed sheets. The sheet was installed over four vertical rods inside a wooden box. Three 0.08 mm (0.003-in.) stainless steel sheets are taped to the thicker sheet. Additional sheets are slipped over the rods in the same manner, using rubber grommet spacers between sheets. The tops of the threaded rods are secured with wooden blocks. The parts were then shipped by truck to the Lockheed-California Company in Burbank, California, for forming. The formed parts were shipped back to Palo Alto, California, in a similar manner. This packaging design proved successful as no parts were damaged during any of the shipments.

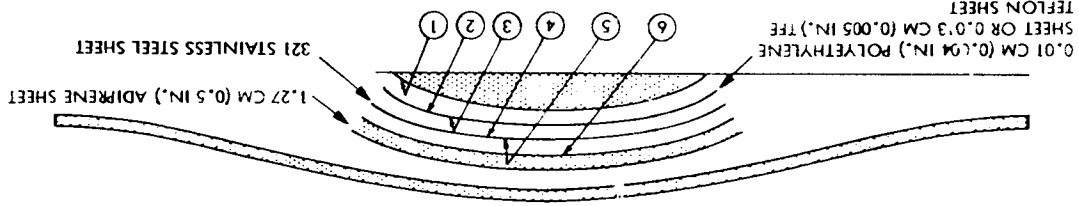
Gore Panel-Forming. During forming development of the gore panels, two basic problems were encountered. These were: (1) tearing of the panels at the base of wedges or at the stiffening beads and (2) wrinkling of the panels at various points on the gore die.

The various parameters that were varied to eliminate tearing are shown sequentially in Table 4-1. The key to successful forming without tearing was found to be use of a contoured polyethylene slipper sheet and an oil lubricant, and forming in two steps. This method allowed the material to move inward (when trapped between the bag and the die) to prevent exceeding the material's elongation at any point on the die. Earlier in the forming development before the polyethylene sheet method was tried, the stretch-form sheets were vacuum-annealed to see if this treatment would increase the stainless steel sheets' elongation and stop the tearing. As can be seen from Table 4-2, the vacuum-annealing decreased rather than increased the material's elongation, apparently because of choice of too high an annealing temperature. Subsequent forming development showed acceptable parts could be formed with or without a vacuum-anneal using the polyethylene sheet, so the vacuum-anneal cycle was not used on the test-article vacuum-jacket.

Methods used to eliminate the wrinkling varied with the location; the solution to each wrinkling problem is summarized in Table 4-3. Since wrinkling is caused by excess material in a specific location, various shaped trap beads were used to pull out this excess material.

REPRODUCIBILITY OF THE ORIGINAL PAGE IS POOR

Table 4-1
SUMMARY OF GORE-FORMING DEVELOPMENT TO ELIMINATE TEARING



Results	Surface Lubrication (See Drawing Above)						Use Polyethylene or Teflon Sheet?	Forming Pressure (psi)	Forming Temperature (°F)	Remarks
	1	2	3	4	5	6				
Tears at base of wedges	-	-	-	-	-	-	No	1.5 x 10 ⁴ (1500)	500	No
Tears at base of wedges; excessive wrinkles	-	-	-	-	-	-	Follow	4.5 x 10 ⁴ (4500)	500	No
Tears at base of wedges; parts on about one-half of	Oil (a)	Oil (a)	Oil (b)	Oil (a)	Oil (a)	Oil (a)	Polyethylene moved for second hit	7.5 x 10 ⁴ (7500)	1000	Yes
No tears; Tears at base of wedges	Oil (a)	Oil (a)	Oil (a)	Oil (a)	Oil (a)	Oil (a)	Polyethylene moved for second hit	9.0 x 10 ⁴ (9000)	1000	Yes
No tears; Tears at base of wedges	Oil (a)	Oil (a)	Oil (a)	Oil (a)	Oil (a)	Oil (a)	Polyethylene moved for second hit	1.3 x 10 ⁵ (13000)	1000	Yes
No tears;	Oil (a)	Oil (a)	Oil (a)	Oil (a)	Oil (a)	Oil (a)	Polyethylene moved for second hit	2.0 x 10 ⁵ (20000)	1000	Yes
No tears; No tears;	Oil (a)	Oil (a)	Oil (a)	Oil (a)	Oil (a)	Oil (a)	Polyethylene moved for second hit	6.0 x 10 ⁵ (60000)	1000	Yes
No tears; No tears;	Oil (b)	Oil (b)	Oil (b)	Oil (b)	Oil (b)	Oil (b)	Polyethylene moved for second hit	1.7 x 10 ⁶ (170000)	1000	No
No tears; New pattern used for Task IV changed to eliminate this wrinkling; from end of cross-stiffeners over wedge; stiffening pattern	Oil (b)	Oil (b)	Oil (b)	Oil (b)	Oil (b)	Oil (b)	Polyethylene moved for second hit	6.0 x 10 ⁶ (600000)	1000	No
No tears; New pattern used for Task IV changed to eliminate this wrinkling; from end of cross-stiffeners over wedge; stiffening pattern	Oil (b)	Oil (b)	Oil (b)	Oil (b)	Oil (b)	Oil (b)	Polyethylene moved for second hit	1.7 x 10 ⁷ (1700000)	1000	No

(a) Light vegetable oil; (b) Light vegetable oil, 10% (LHV).
 (c) Polyethylene sheet was wiped free of oil on both sides between hits. Each sheet was used approximately four to five times.



2.8

2.5

3.2

2.2



4.0

2.0



1.8



1.6

2-N

Table 4-2
EFFECT OF VACUUM-ANNEAL ON JACKET PROPERTIES

		Ultimate Tensile Strength 10^6 N/m^2 (ksi)	Yield Strength 10^6 N/m^2 (ksi)	Elongation (%)
Nonvacuum-Annealed ^(a)	Parallel ^(b)	672 ± 10 (97.5 ± 1.4)	520 ± 51 (75.4 ± 7.4)	27.7 ± 3.8
	Transverse ^(b)	620 ± 2 (89.9 ± 0.3)	450 ± 28 (65.4 ± 4)	39.7 ± 6.0
Vacuum-Annealed ^(a)	Parallel ^(b)	594 ± 69 (86.2 ± 10)	296 ± 40 (43.0 ± 6)	26.9 ± 5.3
	Transverse ^(b)	496 ± 13 (72 ± 1.9)	221 ± 13 (32.1 ± 1.9)	26 ± 1.6

(a) The 0.008 cm (.003 in.) 321 stainless steel was in the annealed condition as received prior to any forming. The vacuum-anneal cycle used was heat-in-vacuum (.01 Pa) at 444°C/hr (800°F/hr) to 982 ± 14°C (1800 ± 25°F) and hold for 15 ± 5 min. Rapidly cool to 93°C (200°F) with an Argon backfill.

(b) With respect to stretch-form direction.

Table 4-3

SUMMARY OF GORE-FORMING DEVELOPMENT TO ELIMINATE WRINKLING

Problem Area	Solution
1. Wrinkles Extending Off the Half-Wedge Tips Into the Trim Area (Wedges 2a, 4a, 6a, 8a, 10a, and 11)	1. Contour the tip into a flat bulbous shape.
2. Wrinkles Extending Off of Wedge Tips (Wedges 2, 4, 6, and 8)	2. Use curved 0.64 cm (0.25 in.) diameter wire trap beads with feathered ends outside the tips to pull out excess material; hand-planish if required.
3. Wrinkle Extending Off Wedge Tip 1	3. Use 0.64 cm (0.25 in.) diameter beads outside trim line at a 45-deg angle to the tip; feather ends of trap beads.
4. Wrinkle Extending Off Wedge Tip 9	4. Use a combination of trap beads to pull out excess material; hand-planish if required.
5. Surface Ripples in Equator Flat Area Near Wedge 2	5. Continue the wedge pattern past the trim area to pull out excess material. (The gore die was too small to incorporate this modification.)
6. Minor Wrinkles at Wedge Tip/Wedge Apex Junction (Wedge Intersections 2/1, 4/1, 6/3, 8/5, and 10/7)	6. This wrinkling did not occur during Task II forming but only during Task IV forming. The wrinkling was minimized by cutting down on the oil lubricant film in these areas and hand-planishing.
7. Wrinkle From End of Cross Stiffener Over the Intervening Wedge to the Next Cross Stiffener	7. This wrinkling did not occur during Task II forming, but only during Task IV forming. The reason for the different behavior is not known. The wrinkling was eliminated by changing the stiffening pattern so the ends of the stiffeners are no longer in line.

The forming sequence that was selected for the test article gore panels is illustrated in Fig. 4-28. Approximately five panels were formed per hour using this sequence. The wedge-forming essentially removed any slight wrinkles or "half-moons" that were present in the stretch-formed part (from prior handling).

Three 0.05 mm (0.002 in.) gore panels were formed to see if thinner sheets were practical. Once the panels were formed, they were handled nearly as easily as the 0.08 mm (0.003 in.) panels; the wedges rigidized the gores out of the plane of the skins as desired. The stiffening beads increased this stiffening effect in the areas between the wedges. However, the 0.08 mm (0.003 in.) gore panels appear to be the better choice when larger tank sizes are considered. Skins 0.03 mm (0.001 in.) in thickness were also formed on the gore die to determine the feasibility of using them as repair patches. The skins formed without tearing but did not form to as tight a radius of curvature as the thicker skins. For wedge replacement patches, skins of 0.05 mm (0.002 in.) or greater in thickness should be used. For localized repair over a wedge or in areas between wedges and along joints, material down to 0.03 mm (0.001 in.) is satisfactory for use.

Polar Cap Forming. The same forming sequence shown previously in Fig. 4-28 for the gore panels was used for the polar cap, with one exception. On the second hit, the pressure was increased to $2.1 \times 10^7 \text{ N/m}^2$ (3000 psi) to provide better definition around the wedges. Wrinkling off the wedge tips and near the wedge apex was minimized using trap beads. Any residual wrinkles were hand-planished.

4.1.9.3 Assembly Sequence for a Vacuum-Jacket Hemisphere. An assembly sequence was developed for trimming, cleaning, and welding the 9 gore panels, the polar cap, plus the 15 final closure flanges into a leak-tight hemisphere as illustrated in Fig. 4-29. First, a trim template is made from a formed gore panel. The right edge and top of the template is trimmed net while the left edge is left oversize. This template is placed over untrimmed gore panels (Fig. 4-29, Step 1) and the edges are marked by spraying with an MEK-soluble black paint. The gore is then trimmed

with scissors and the cut edges planished with a Teflon block (Fig. 4-29, Step 2). The polar cap is trimmed oversize and placed on the fiberglass hemisphere fitup and welding fixture tool. The nine gore panels are fitted to the polar cap using masking tape to hold them in place. The joint overlaps are sprayed with black paint, and the panels are removed. The left edge of the gore panels plus the polar cap are final-trimmed to allow for a 0.38 cm (0.15 in.) overlap in the joints and a 0.25 cm (0.1 in.) overlap at wedge tips.

The trimmed panels are vapor-degreased and placed back on the fiberglass hemisphere tool (Fig. 4-29, Step 3). The 1.19 m- (47 in.) diameter fiberglass hemisphere tool is mounted over the top of the lower copper welding wheel. A slot is cut at the pole of the fiberglass dome so the top of the wheel protrudes through and is tangent to the outside of the fiberglass surface.

With the gores aligned and taped together, tack welds are made on the overlap region in between the pieces of tape by manually guiding the hemisphere under the opposing wheels. The tape is removed and additional tack welds are made until the tack welds are approximately 1.3 cm (0.5 in.) apart. Continuous seam welds on the nine gores are made by sliding the gores around the hemisphere and guiding the joint under the welding wheels.

The polar cap is then taped to and aligned with the joined hemisphere. Tack welds and an overlap seam weld are made on the polar cap joint. The 15 flanges are taped in place, tack-welded, and welded at the final closure joint edge. To ensure a good fitup between flanges on opposing jacket hemispheres, the second hemisphere is mounted on a fiberglass sphere and aligned with the first hemisphere. The flanges are taped in place so they exactly mate with the opposing flange. The jacket hemisphere is removed from the sphere and placed on the hemisphere tool. The flanges are tack welded and then resistance seam welded.

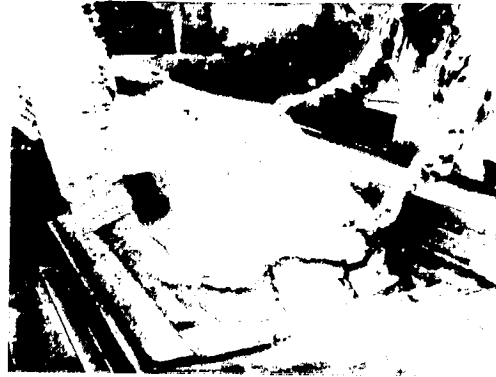
4.1.9.4 Leak-Checking the Jacket Hemispheres. The welded hemispheres are attached to a hemispherical tubular frame with tape. All jacket openings are closed off

FOLDOUT FRAME

REPRODUCIBILITY OF THE ORIGINAL PAGE IS POOR



a. Oil the die.



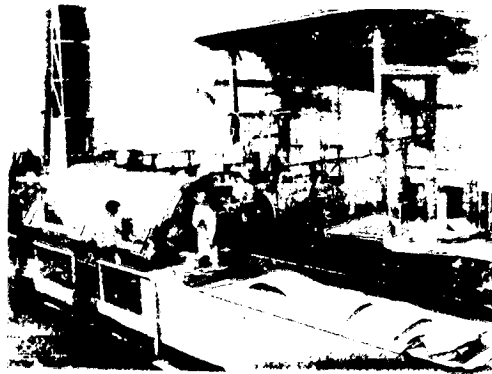
b. Place polyethylene sheet over the die.



c. Oil the die.
steel
steel
sheet



e. Roll rubber sheet over Adiprene sheet.



f. Form part at $6.9 \times 10^6 \text{ N/m}^2$ (1000 psi); remove blank and polyethylene sheet; replace blank and form at $1.7 \times 10^7 \text{ N/m}^2$ (2500 psi).



g. Hold part
re
an

FOLDCUT FRAME

2



sheet over



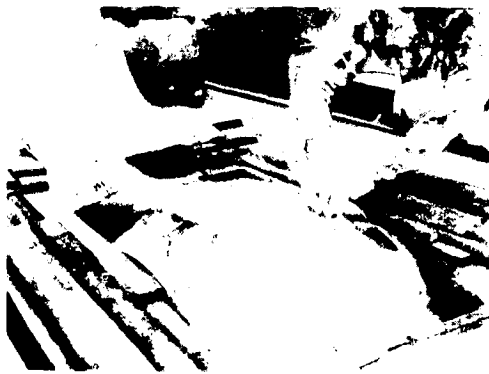
c. Oil inside of trimmed stainless steel blank. Place stainless steel blank over polyethylene sheet.



d. Oil bottom surface of Adiprene sheet; place sheet over stainless steel blank.



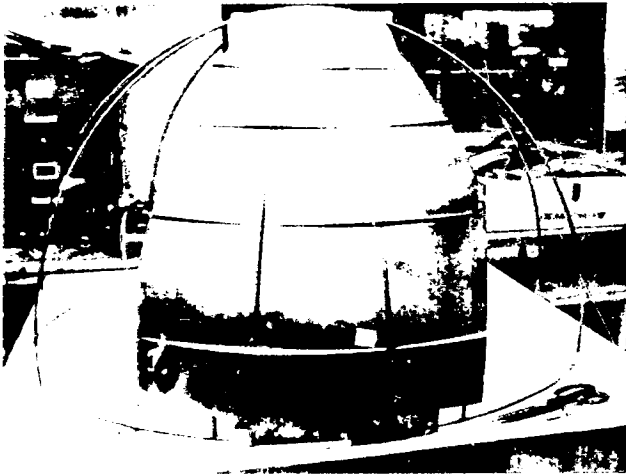
6 N/m^2 (1000
and polyethy-
blank and form
2500 psi).



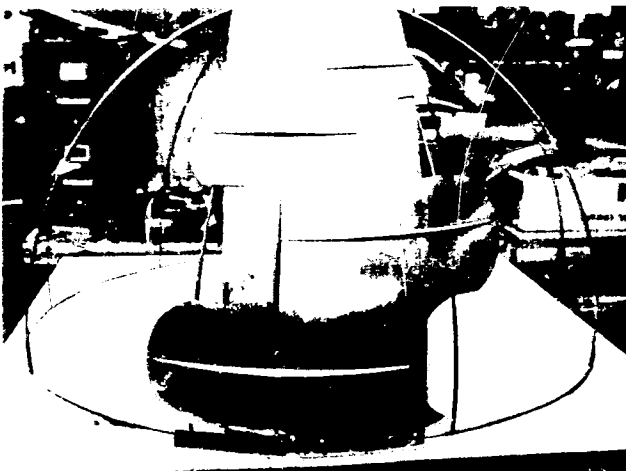
g. Hand-planish wrinkles where required; remove part using an air hose.

Fig. 4-28 Gore Panel-Forming Sequence for the Test Article

4-17



1. Untrimmed Gore Panel



2. Trimmed Gore Panel



3. Final Fitup

Fig. 4-29 Jacket-Hemisphere Assembly Sequence (Does not Include Final Closure Joint)

REPRODUCTION OF THIS
ORIGINAL PAGE IS
PROHIBITED

PERFORMING PAGE BLANK NOT FILMED

and the frame is placed in a pool of water so the equatorial final closure joint is under water. The frame is held down with 45 kg (100 lb) of lead bricks. The jacket is purged of air with helium and pressurized to 2.5 cm (1.9 in.) of water. The joints are then sniffed with a helium mass spectrometer leak detector. Leaks at four places along the joints were repaired by rewelding the leaking area. No leaks were found in any of the formed areas away from the joints.

4.1.10 Test of the Hemispherical Vacuum Jacket

A series of tests were performed on a prototype hemisphere of the vacuum jacket to obtain the following design information:

- The pressure versus deflection curve of the jacket as a function of wedge width
- The elastic to plastic transition point of an expanding wedge as a function of wedge geometry
- A check between prior flat-panel and hemispherical curved-panel expansion data
- The uniformity of radial expansion of the jacket under point loads (simulating spring/Kevlar attachments) for different stiffening patterns

From these data, the following information can be derived:

- Data necessary to design the vacuum-jacket expansion wedges for other tank shapes and sizes
- The compressive load a stretched jacket exerts on the tank and the insulation
- The spring force required to expand the jacket
- The necessity for stiffening patterns in the flat areas

Hemisphere Pressure Expansion Tests. The vacuum-jacket hemisphere is mounted over the top of a plexiglas hemisphere (that simulates the tank surface) as shown in Fig. 4-30. The jacket was initially sealed off at the equator using a bonded rubber membrane. In addition, the jacket is tied down to the flange at each of the 18 panels with stainless-steel wires. The wires are brazed to a horizontal strip which in turn

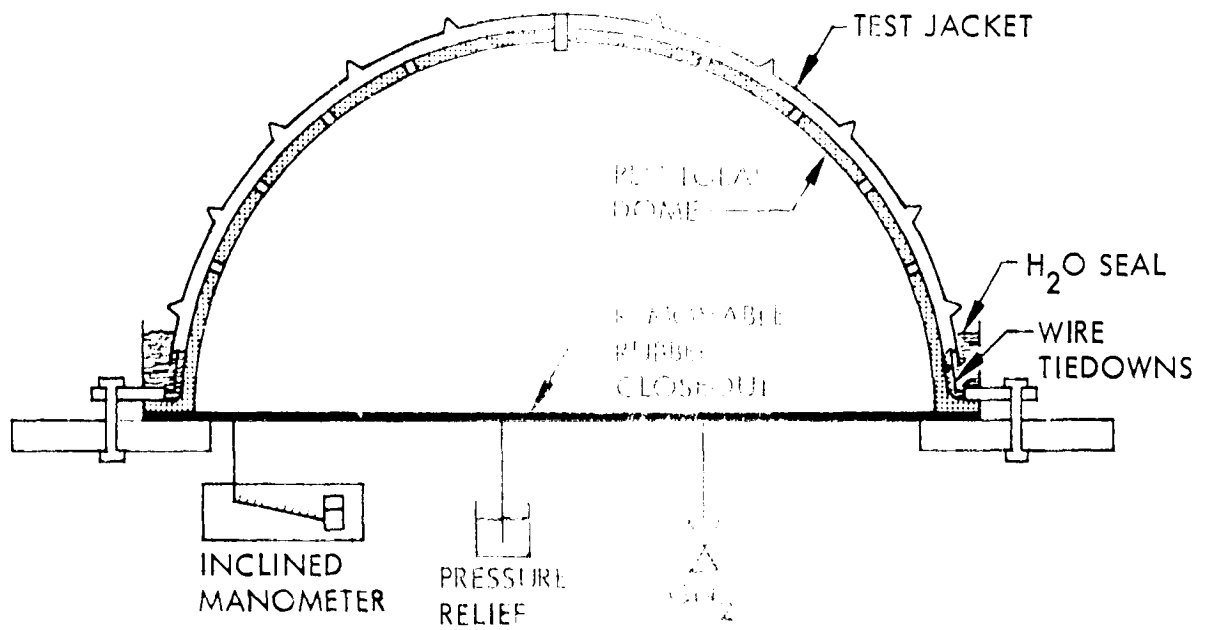
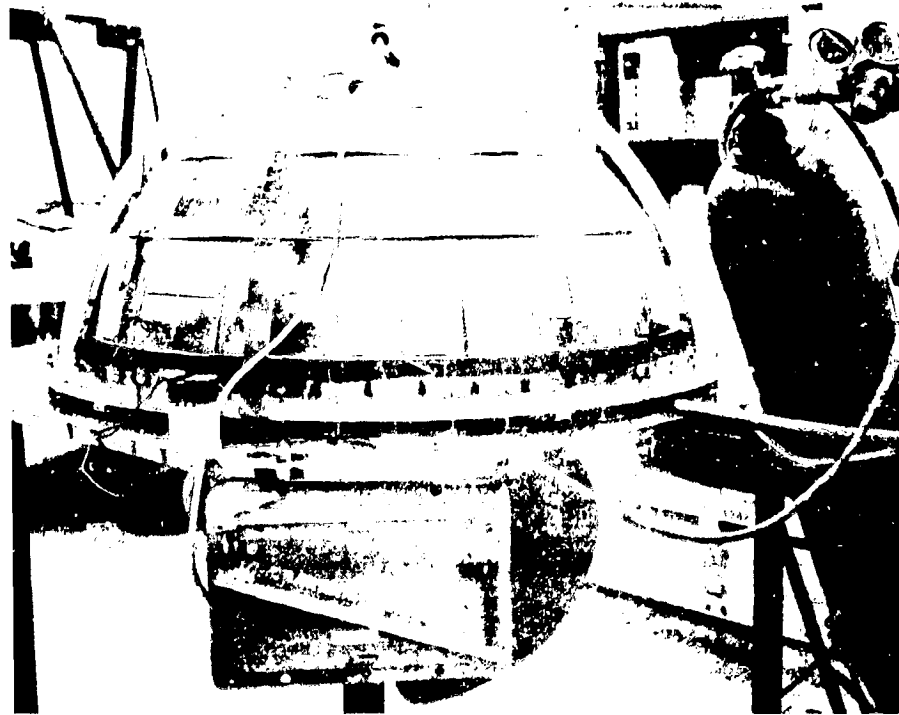


Fig. 4-30 Jacketed Pressure Vessel Test Setup

is bonded to the inside of the jacket just above horizontal wedge 2. These wire supports hold the jacket as it is pressurized, yet allow the jacket to grow radially at the equator. This support method, however, prevents horizontal wedge 2 from expanding in the vertical direction.

Initial pressure tests showed that the rubber membrane inhibited radial growth at the equator to too great a degree. Therefore, the rubber membrane was cut and a 10 cm (4 in.) aluminum dike was bonded around the jacket equator. The space between the dike and the plexiglas dome was partially filled with water, immersing the jacket edge on both sides and providing a gas-tight liquid seal. The jacket expands at the equator radially within the constraints of the wire supports.

Opening of the wedges under pressure is measured by bonding small screws on each side of the wedge apex for 11 wedges and repeating this at approximate 90-deg intervals around the dome. Using a micrometer accurate to 0.025 mm (0.001 in.), the distance between the screws is measured before, during, and after pressure application as shown in Fig. 4-31, and the delta wedge opening is calculated. For each type of wedge, four measurements are taken and averaged as shown in Table 4-4. The pressure is measured with an inclined manometer accurate to 0.03 cm (0.01 in.) of water as shown previously in Fig. 4-30.

Using these test data and the wedge characteristics shown in Table 4-5, the expansion characteristics of the vertical wedges (Fig. 4-32) and horizontal wedges (Fig. 4-33) are plotted. Analysis of this family of straight lines showed they could be characterized by the equations given on the respective figures to within a precision of several percent. The vertical and horizontal wedges were analyzed separately because the vertical wedges have a single curvature while the horizontal wedges use a double curvature.

The elastic to plastic transition region for each wedge was determined by the point at which the wedge no longer returned to its original dimension following the pressure

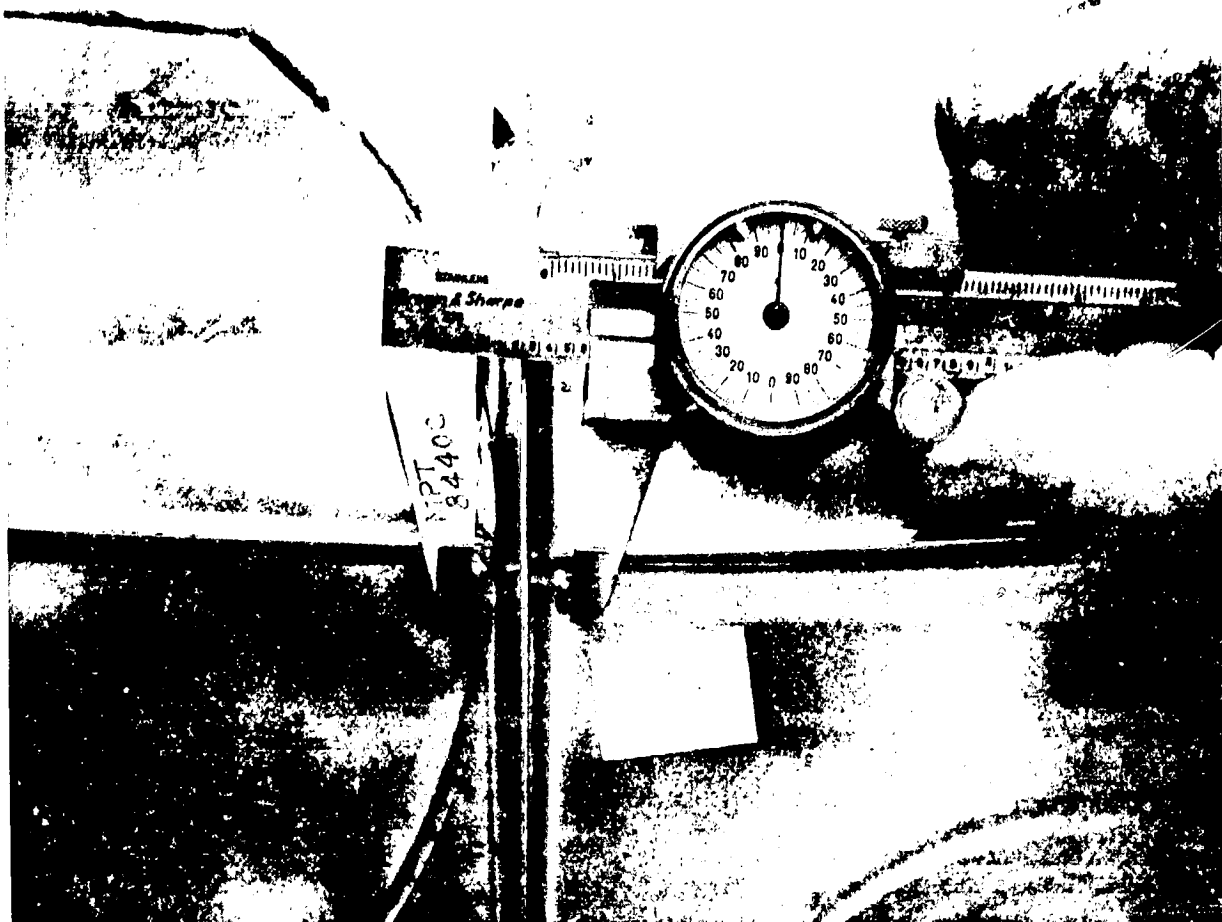


Fig. 4-31 Measuring Wedge Expansion

test as shown in Fig. 4-34. As can be seen from this figure, wedges 3 through 6 have yielded at various expansion values while wedges 7 and 8 have not. Wedges 9, 10, and the polar cap wedge were analyzed separately since they provide the transition region into the rigid polar cap. Note in Fig. 4-35 all these wedges are still in the elastic range at the highest pressure tested. When the amount each of these wedges in Figs. 4-34 and 4-35 have opened (at yield or at the highest pressure tested while still in the elastic range) is plotted against wedge height, the curve in Fig. 4-36 results. Empirically fitted equations for these curves are also shown.

Table 4-4
WEDGE EXPANSION TEST DATA
(PRESSURE TEST)

Wedge No.	Internal Pressure N/m ² (psi)						
	148 (0.022)	187 (0.027)	209 (0.030)	247 (0.036)	278 (0.040)	321 (0.047)	350 (0.051)
	$\Delta W^{(a)}$ mm (in.)						
3	1.35 ± 0.15 (0.053 ± 0.006)	1.68 ± 0.08 (0.066 ± 0.003)	1.98 ± 0.23 (0.078 ± 0.009)	2.13 ± 0.15 (0.084 ± 0.006)	2.36 ± 0.08 (0.093 ± 0.003)	2.77 ± 0.15 (0.109 ± 0.006)	2.90 ± 0.18 (0.114 ± 0.007)
4	1.19 ± 0.1 (0.047 ± 0.004)	1.52 ± 0.05 (0.060 ± 0.002)	1.75 ± 0.23 (0.069 ± 0.009)	2.01 ± 0.05 (0.079 ± 0.002)	2.18 ± 0.13 (0.086 ± 0.005)	2.49 ± 0.18 (0.098 ± 0.007)	2.77 ± 0.30 (0.109 ± 0.012)
5	0.76 ± 0.1 (0.030 ± 0.004)	0.99 ± 0.03 (0.039 ± 0.001)	1.17 ± 0.03 (0.046 ± 0.001)	1.27 ± 0.08 (0.050 ± 0.003)	1.52 ± 0.08 (0.060 ± 0.003)	1.68 ± 0.1 (0.066 ± 0.004)	1.80 ± 0.08 (0.071 ± 0.003)
6	0.58 ± 0.13 (0.023 ± 0.005)	0.89 ± 0.05 (0.035 ± 0.002)	1.12 ± 0.18 (0.044 ± 0.007)	1.22 ± 0.1 (0.48 ± 0.004)	1.30 ± 0.05 (0.051 ± 0.002)	1.63 ± 0.1 (0.64 ± 0.004)	1.68 ± 0.13 (0.066 ± 0.005)
7	0.36 ± 0.05 (0.014 ± 0.002)	0.51 ± 0.03 (0.020 ± 0.001)	0.56 ± 0.18 (0.022 ± 0.007)	0.64 ± 0.05 (0.25 ± 0.002)	0.76 ± 0.08 (0.030 ± 0.003)	0.89 ± 0.05 (0.035 ± 0.002)	0.89 ± 0.1 (0.035 ± 0.004)
8	0.30 ± 0.25 (0.012 ± 0.010)	0.43 ± 0.03 (0.017 ± 0.001)	0.53 ± 0.08 (0.021 ± 0.003)	0.48 ± 0.1 (0.019 ± 0.004)	0.58 ± 0.03 (0.023 ± 0.001)	0.69 ± 0.03 (0.027 ± 0.001)	0.79 ± 0.08 (0.031 ± 0.003)
9	0.28 ± 0.2 (0.011 ± 0.008)	0.28 ± 0.03 (0.011 ± 0.001)	0.28 ± 0.03 (0.011 ± 0.001)	0.28 ± 0.08 (0.011 ± 0.003)	0.33 ± 0.03 (0.013 ± 0.001)	0.41 ± 0.05 (0.016 ± 0.002)	0.41 ± 0.03 (0.016 ± 0.001)
10	0.18 ± 0.1 (0.007 ± 0.004)	0.30 ± 0.05 (0.012 ± 0.002)	0.41 ± 0.15 (0.016 ± 0.006)	0.36 ± 0.15 (0.014 ± 0.006)	0.51 ± 0.15 (0.020 ± 0.006)	0.51 ± 0.08 (0.020 ± 0.003)	0.56 ± 0.1 (0.022 ± 0.004)
Polar Cap	0.43 ± 0.1 (0.017 ± 0.004)	0.51 ± 0.05 (0.020 ± 0.002)	0.69 ± 0.05 (0.027 ± 0.002)	0.74 ± 0.05 (0.029 ± 0.002)	0.86 ± 0.08 (0.034 ± 0.003)	1.04 ± 0.05 (0.041 ± 0.002)	1.12 ± 0.08 (0.044 ± 0.003)

(a) $\Delta W = W_{\text{pressure}} - W_{\text{prior to pressure application}}$ average of 4 measurements around sphere ~ 90° apart.

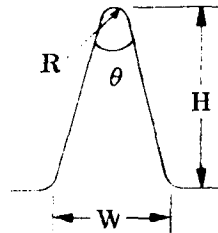
Table 4-5
WEDGE DIMENSIONS

Wedge	Maximum				Characteristic Length, L		
	Wedge Width, W		Wedge Height, H		cm	in	
	cm	in	cm	in			
1	0.762	0.300	1.240	0.488	41.04	16.16	
2	0.762	0.300	1.240	0.488	40.24	15.84	
3	0.691	0.272	1.105	0.435	36.58	14.40	
4	0.691	0.272	1.105	0.435	35.98	14.16	
5	0.579	0.228	0.897	0.353	29.71	11.70	
6	0.579	0.228	0.897	0.353	29.66	11.68	
7	0.465	0.183	0.683	0.269	22.64	8.91	
8	0.465	0.183	0.683	0.269	22.90	9.01	
9	0.366	0.144	0.503	0.198	16.61	6.54	
10	0.366	0.144	0.503	0.198	12.24	4.82	
Polar Cap	0.757	0.298	1.229	0.484	(Ver)	22.22	8.67
					(Hor)	13.44	5.29

$$H = \frac{0.5W}{\tan \theta/2} - R \left(\frac{1}{\sin \theta/2} - 1 \right)$$

$$\theta = 30^\circ$$

$$R = .064 \text{ cm } (.025 \text{ in})$$



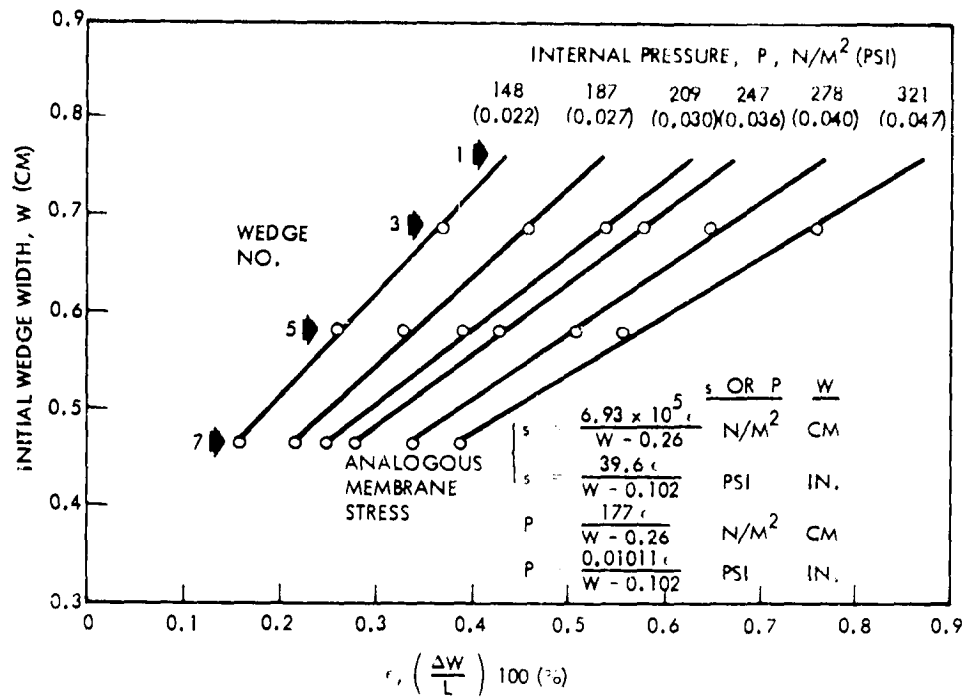


Fig. 4-32 Vertical Wedge Expansion in the Elastic Range

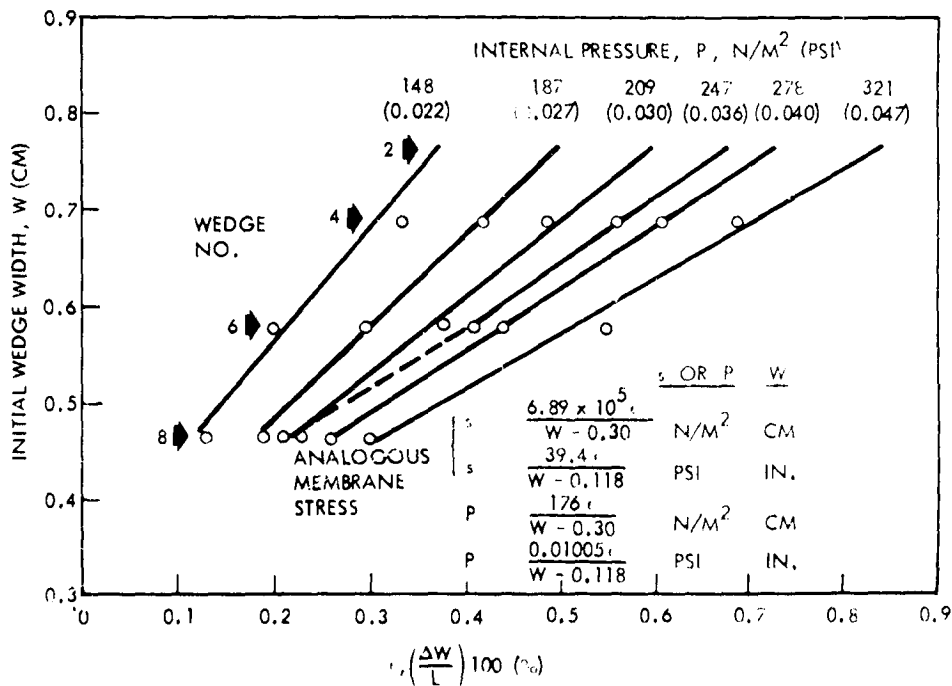


Fig. 4-33 Horizontal Wedge Expansion in the Elastic Range

4-55

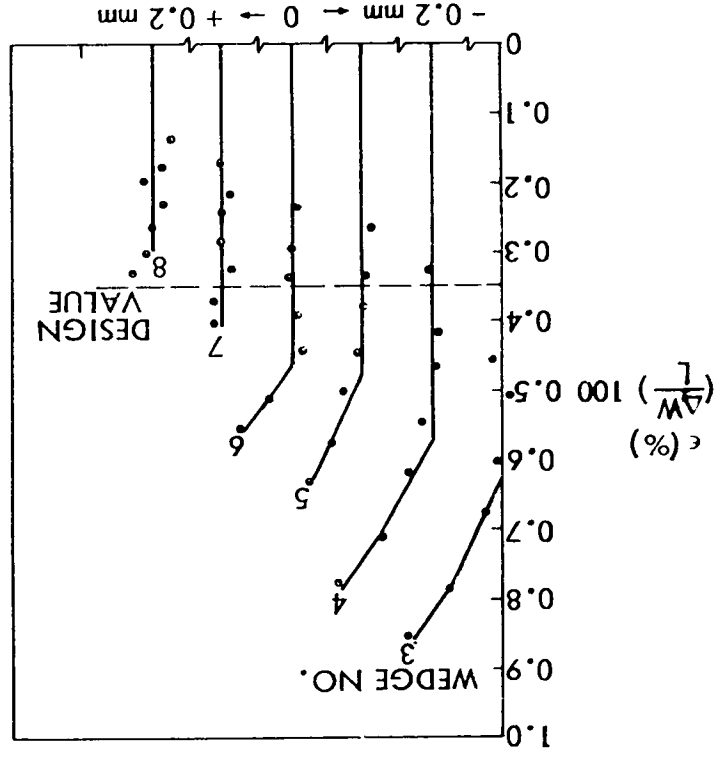


Fig. 4-34 Elastic to Plastic Transition
 Point of Wedges

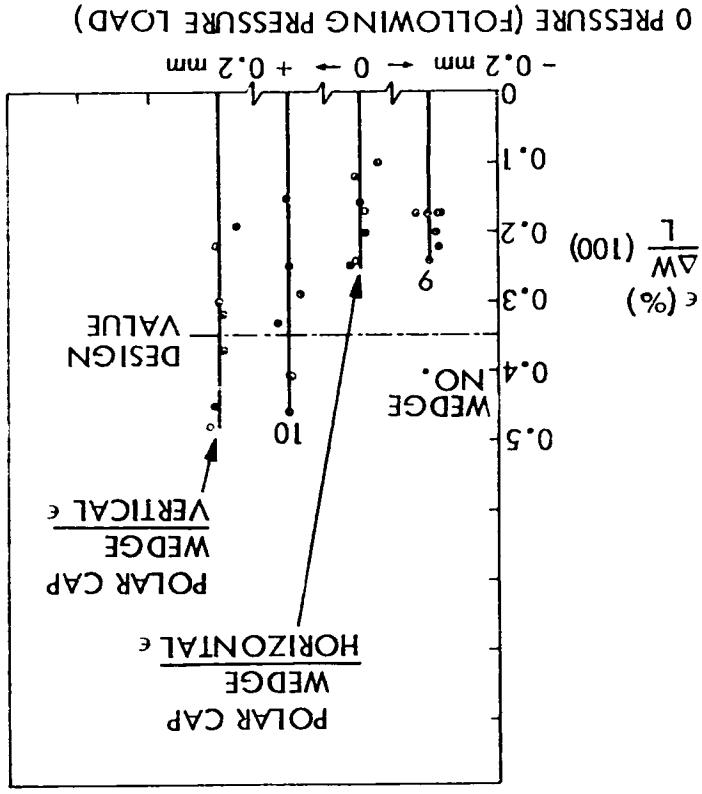


Fig. 4-35 Elastic Range Tested for Polar Cap
 Transition Wedges

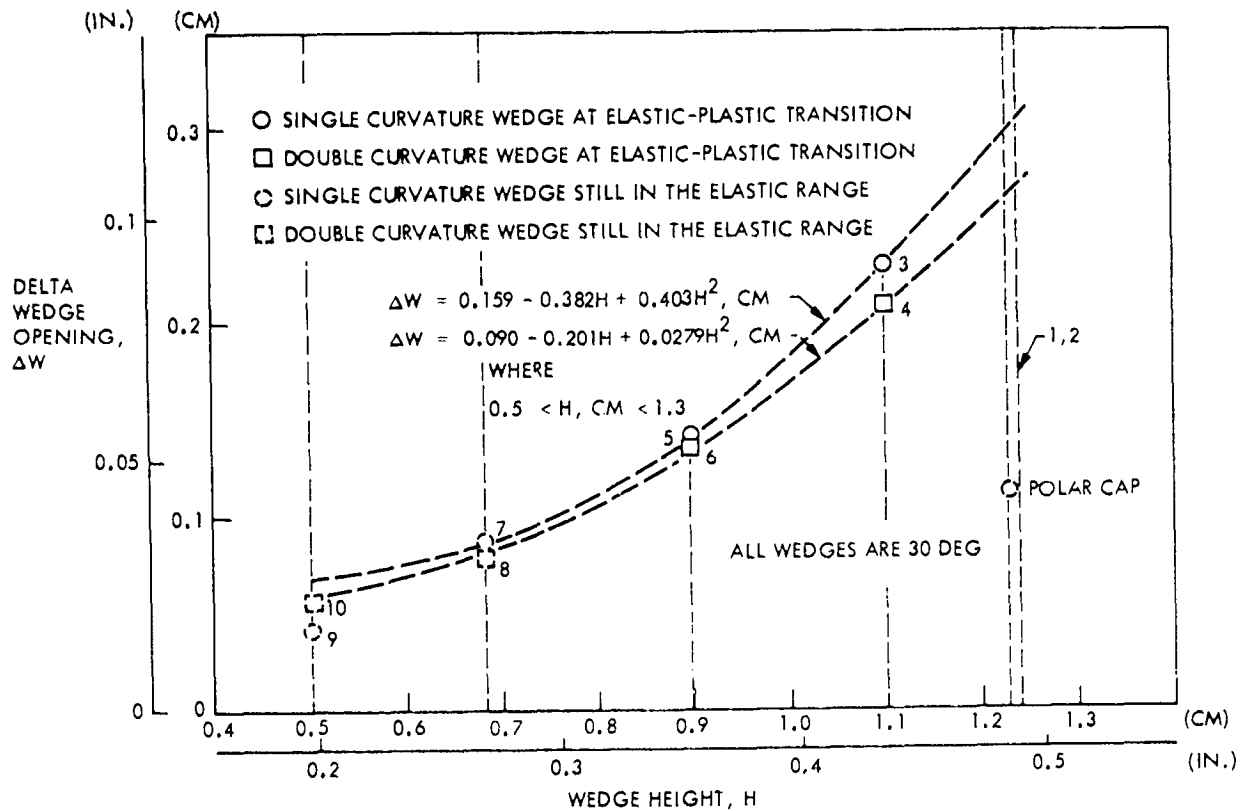


Fig. 4-36 Elastic-Plastic Transition Points Versus Wedge Height

The following conclusions can be reached from Figs. 4-34 through 4-36. Wedges 3 to 8, 10, and the polar cap wedge remain in the desired elastic range for the design value of 0.35 percent. Because of the higher yield point as the wedge size increases, wedges 1 and 2 can be assumed to be in the elastic range by extrapolation. Wedge 9 is still in the elastic range at 0.25-percent expansion (the highest pressure tested) and probably does not have to go any higher than this value to function properly. The reason for this statement is the jacket is going from 0 expansion at the solid polar

cap out to the full 0.35 percent expansion in a horizontal direction just below wedge 9. Therefore, it is logical to assume wedge 9's expansion will be somewhere between these values in this transition zone, as indeed it is. Additional tests have shown changing the rigid polar cap from 0.08 mm (0.003 in.) in thickness to 0.041 mm (0.016 in.) has no effect on the jacket expansion characteristics.

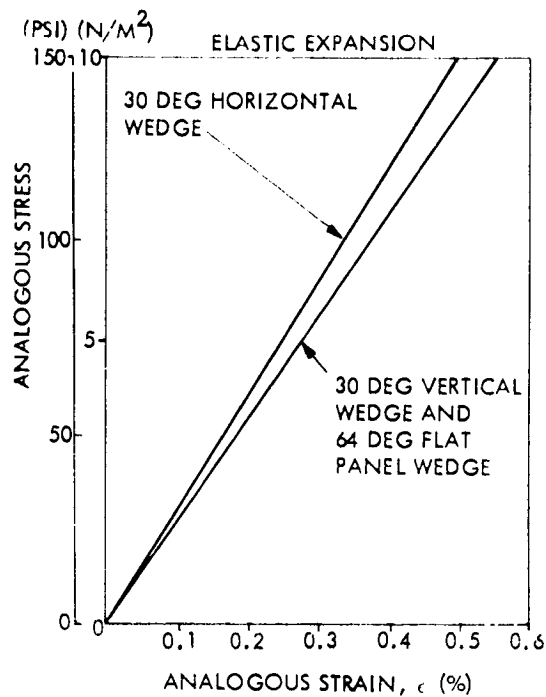
The elastic stress-strain curve and yield point for the flat panel and hemisphere are compared in Fig. 4-37 for wedges of identical height. Note the flat panel and the hemisphere stress-strain slopes are identical for a single curvature vertical wedge. The hemisphere double curvature horizontal wedge is about 10 percent lower than the other two wedges. The significance of this agreement is as follows. For any future design improvements, test results from lower cost flat panel tests can be extrapolated with confidence to curved panel designs. Also, these data are applicable to other jacket shapes such as ellipsoids or cones as long as the radius of curvature at any point is equal to or greater than that tested, 0.60 m (23.5 in.)

Also note in Fig. 4-37 that decreasing the wedge angle from 64 to 30 deg increased the wedge opening ΔW before yielding occurred. To see if the yield point as a function of wedge angle could be predicted, a mechanism was postulated that contributes to this plastic deformation. As a wedge opens up during expansion, the wedge tips move down as shown.



However, the movement normal to the plane of the panel is resisted by the adjacent wedge located 90 deg to the tip.





ELASTIC LIMIT
(VERSUS WEDGE ANGLE)

WEDGE ANGLE (DEG)	MEASURED Δw , CM (IN.)	PREDICTED Δw , CM (IN.) $\propto (\Delta Y / \Delta w)^{-1/2}$
FLAT PANEL 64	0.11 (0.045)	REF.
HEMISPHERE 30 (V)	0.19 (0.074)	0.17 (0.067)
30 (H)	0.18 (0.069)	0.17 (0.067)

Fig. 4-37 Comparison of Flat Panel and Hemisphere Expansion Data

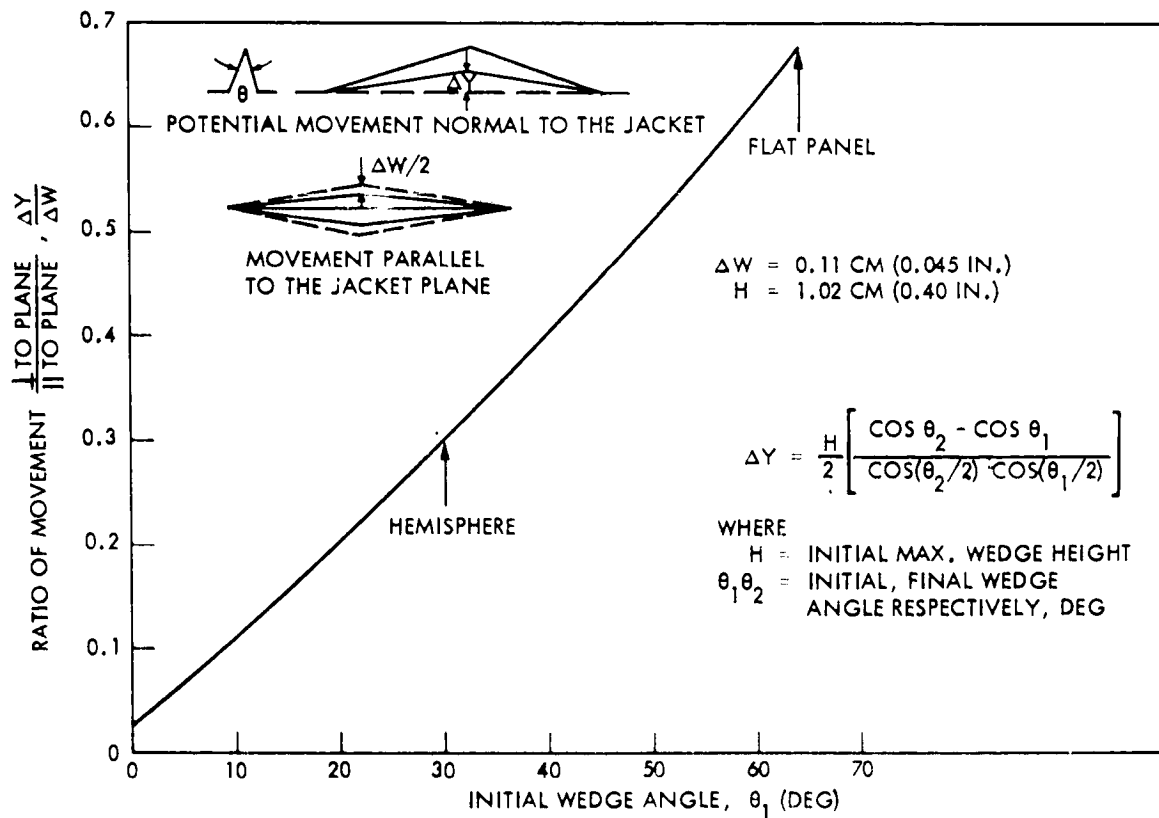


Fig. 4-38 Potential Out-of-Plane Movement of the Vacuum Jacket

As the wedge angle θ decreases, the ratio of potential movement of the jacket normal to the panel ΔY to expansion in the plane of the panel ΔW decreases as shown in Fig. 4-38. Consequently, the narrower wedge can open further before the same potential movement out of the plane of the panel occurs. (Note that the movement is independent of the length of the wedges.) It is believed that the magnitude of this potential out of plane movement, being resisted by the opposing wedges at 90 deg, contributes to the elastic-to-plastic transition region measured.

If it is assumed that the yield point is inversely proportional to $\sqrt{\Delta Y/\Delta W}$, then the predicted values shown in Fig. 4-37 agree relatively well with the measured values, although no attempt was made to account for the differences between the single curvature (vertical) and double curvature (horizontal) wedges.

Hemisphere Point Load Expansion Tests. To simulate the spring/Kevlar attachment design, the jacket is expanded by pushing outward in the center of designated panels. Bolts (mounted in the plexiglas dome) with swivel pads 1.3 cm (0.5 in.) in diameter attached to the ends of the bolts are bonded to the inside of the vacuum jacket as shown in Fig. 4-39.

The relative radial expansion over the surface of the jacket is measured from the outside of the jacket using a curved swing arm as the reference surface with the pivot point located over the pole. The other end of the swing arm is located accurately at the equator using pointed screws and matching center punch marks on the equator flange. Radial holes drilled in the swing arm allow a depth gage to be inserted at 16 points going from the equator to the pole. The depth gage, accurate to 0.025 mm (0.001 in.), is connected to a battery operated electric buzzer as shown in Fig. 4-40. When the gage just touches the jacket, the buzzer sounds, allowing very accurate, repeatable measurements to be made. At three of the locations, a calibrated compression spring device mounted in the plexiglas dome is used to measure the force required to expand the jacket at that point over a given distance.

4-60



Fig. 4-39 Point Load Expansion Test (as Viewed From Inside the Plexiglas Hemisphere)



Fig. 4-40 Radial Expansion Measurements

The following panels are supported for these tests:

Between Wedges

2 - 4	all 18
4 - 6	all 18
6 - 8	none
8 - 10	9 (every other one)

For the initial test, the jacket is expanded radially 0.21 percent at the point supports. This value simulates the maximum dimensional change the stainless-steel vacuum jacket can experience going from below its minimum orbit temperature of 167°K (300°R) to ambient temperature. Radial deflection measurements are taken in the following panels:

- Nonstiffened panel
- Adjacent panel with joint

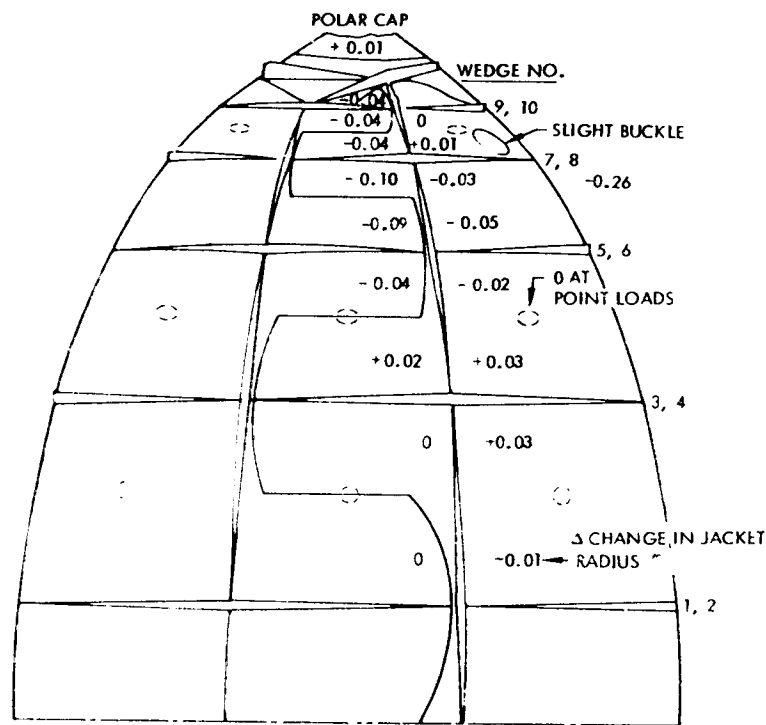
} Fig. 4-41

- Vertical stiffener panel
- "Cross" stiffener panel
- Panel with joint located between the two stiffened panels

} Fig. 4-42

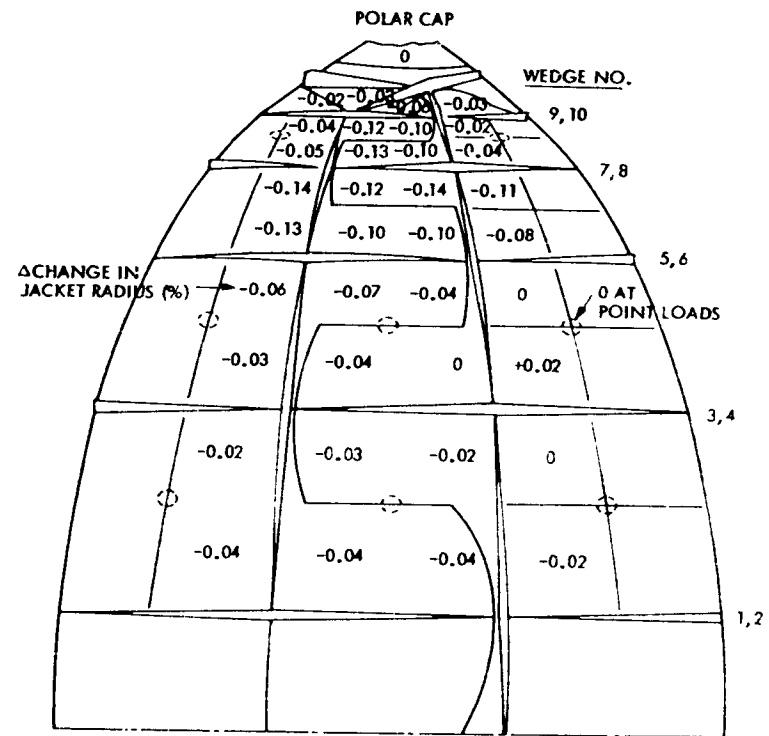
The results are presented as the percent change in radius of the jacket in between the point load supports; at the point load supports, the percent change is by definition zero. A negative change indicates a decrease in thickness of the vacuum space. Each value shown is an average of four to five measurements. Comparing Fig. 4-41 with Fig. 4-42 shows that the unstiffened panel is best at keeping the vacuum space uniform, followed closely by the cross stiffener panel. The vertical stiffener is the least efficient of the three designs at keeping the vacuum space uniform. However, on the unstiffened panel, a small buckle formed in the panel between wedges 8 and 10. Note the larger movement inward for the unsupported panels as compared to the supported panels.

4-62



THE 0.21% EXPANSION IS EQUIVALENT TO A CHANGE IN THE VACUUM JACKET TEMPERATURE FROM 158°K (285°R) TO 299°K (538°R). MINIMUM JACKET ORBIT TEMPERATURE IS 167°K (300°R)

Fig. 4-41 Point Load Expansion Increase in Jacket Radius for Unstiffened Panels (0.21%)



THE 0.21% EXPANSION IS EQUIVALENT TO A CHANGE IN THE VACUUM JACKET TEMPERATURE FROM 158°K (285°R) TO 299°K (538°R). MINIMUM JACKET ORBIT TEMPERATURE IS 167°K (300°R).

Fig. 4-42 Point Load Expansion Increase in Jacket Radius for Stiffened Panels (0.21%)

The bolts were screwed out further until the point load radial expansion equaled 0.43 percent, a value slightly higher than the 0.35 percent required during installation of the jacket. As can be seen from Figs. 4-43 and 4-44, the cross stiffener is slightly superior in maintaining a uniform vacuum space as compared to the unstiffened panel between wedges 2 and 4 and 4 and 6 while the reverse is true between wedges 8 and 10. For the unstiffened panel, slight buckles formed in all the supported panels radiating out from the support point toward a corner as shown. The vertically stiffened panel allowed greater inward movement than the others. Unsupported panels moved inward the greatest amount. Some buckles are also noted in several of the joint supported panels.

Based on these test results, the following design choices were made. The support point area at the spring/Kevlar attachments was increased by a factor of four, with a selected diameter of 2.5 cm (1 in.). The cross-stiffening pattern was selected for the panels. All panels are supported by the spring/Kevlar attachments.

Force measurements at three panel locations plus the pressure expansion data described previously provided the data for calculating the spring force required to expand the jacket 0.35 percent during installation as shown in Table 4-6.

4.1.11 Spring Assembly Development

To support the vacuum jacket under acceleration loads outside the atmosphere (when the compressive load on the jacket is removed) and maintain a relatively constant jacket spacing off the tank wall independent of tank or external temperature changes, spring assemblies are used.

These assemblies, held in compression by three Kevlar strands, are designed to minimize the heat leak to the tank yet provide the required structural support. Tests described in section 4.1.10, plus analyses of the acceleration loads in section 2.2, established the following requirements:

- Spring force in the compressed condition: $\geq 5.5\text{N}$ ($> 1.24\text{ lb}$)
- Tensile strength of the assembly: 22 N (5 lb)

Fig. 4-43 Point Load Expansion Increase in Jacket Radius for Unstiffened Panels (0.43%)

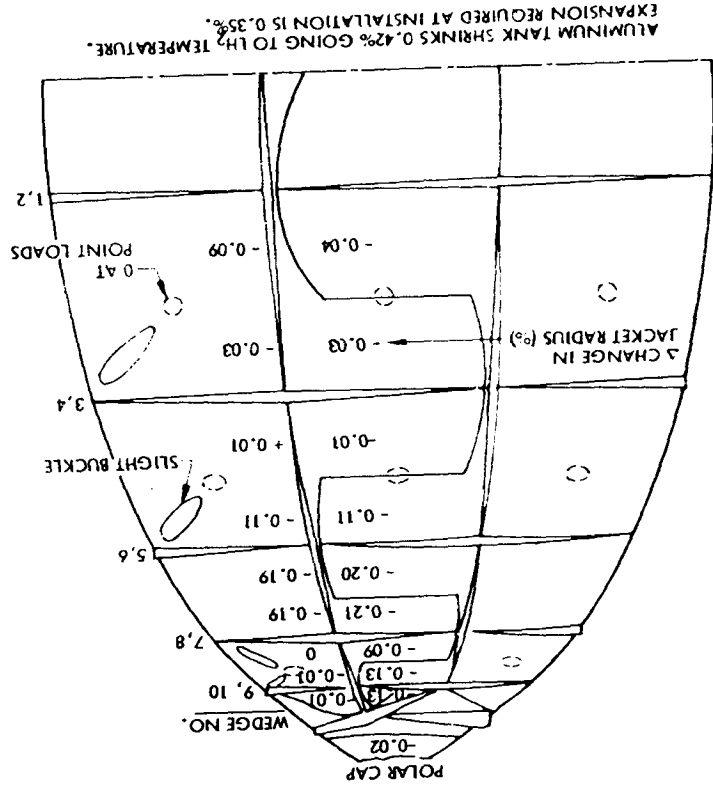


Fig. 4-44 Point Load Expansion Increase in Jacket Radius for Stiffened Panels (0.43%)

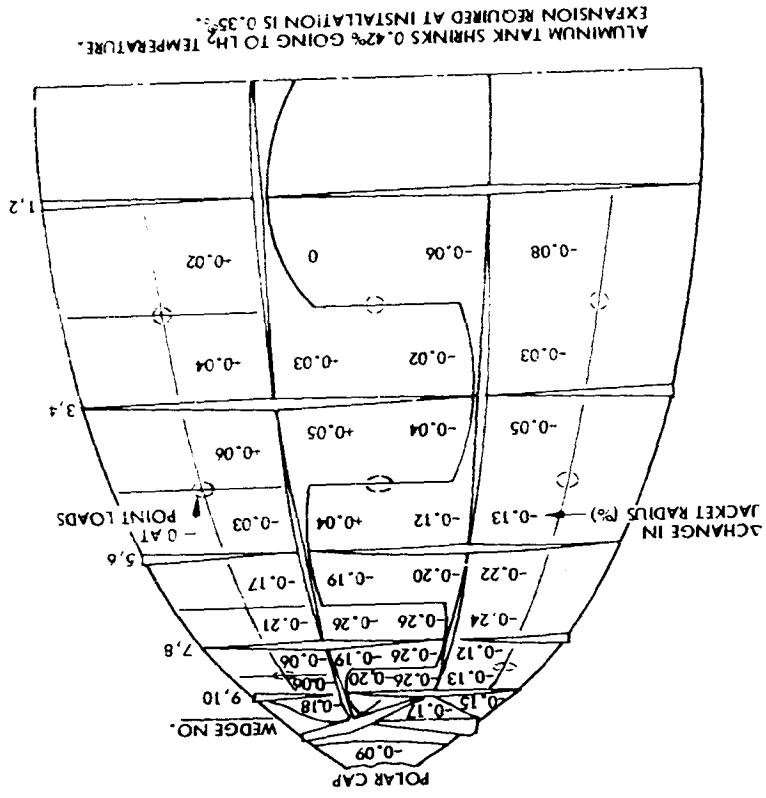


Table 4-6

SPRING FORCE REQUIRED FOR VACUUM JACKET EXPANSION

Jacket Panel Between Wedges	Area m^2 (in^2)	Pressure Required for Expansion of 0.35% N/m^2 (psi)	Spring Force Required $N(lb_f)$
2-2 (Equator)	0.0432 (66.95)	128 (0.0186)	5.52 (1.24)
2-4	0.0380 (58.88)	139 (0.0202)	5.29 (1.19)
4-6	0.0276 (42.84)	179 (0.0260)	4.94 (1.11)
6-8	0.0172 (26.64)	272 (0.0395)	4.67 (1.05)
8-10	0.0096 (14.95)	548 (0.0795)	5.29 (1.19)

	Calculated from Pressure Expansion Test Data (Each of 162 panels is supported)	Direct Point Load Measurements (a) (106 out of the 162 panels are supported)
Total Force Required for 0.35% Expansion of Jacket Sphere $N(lb_f)$	827 (186)	667 (150)
Avg. Force/Unit Area N/m^2 (psi)	186 (0.027)	152 (0.022)

(a) The unsupported panels don't move out the full 0.35%; therefore, the total force required is less than when all panels are supported.

- Rotational capability of 0.5 deg during jacket movements
- Capability to move inward 0.25 cm (0.1 in.) under a 1-atmosphere compressive load (to prevent jacket damage in case of microsphere voids)

To meet these requirements, the design shown in Fig. 4-45 was developed.

Properties of the Kevlar strands that make it attractive for holding the spring compressed are as follows:

- Filament diameter 0.001 cm (0.0004 in.)
- Number of filaments in a strand ~400
- Ultimate tensile strength: 2.8×10^9 N/m² (400,000 psi)
- Knot strength: 0.35 of ultimate tensile strength
- Thermal expansion coefficient -2×10^{-6} cm/cm°C (-1×10^{-6} in./in.°F)
- Maximum use temperature: 238°C (460°F)
(higher for short periods of time)
- Thermal conductivity (see Fig. 4-46)
- Remains flexible at cryogenic temperatures

The key features of the design that required testing are

- Structural integrity of the epoxy bond to the tank under repeated thermal cycles
- Tensile strength of the assembly

To thermally cycle the epoxy bond, the following test is performed.

Two hexagonal sheets of 2219-T37 aluminum were bonded to a 2219 T-37 Al plate simulating the test tank. (The shape was later changed to circular.)

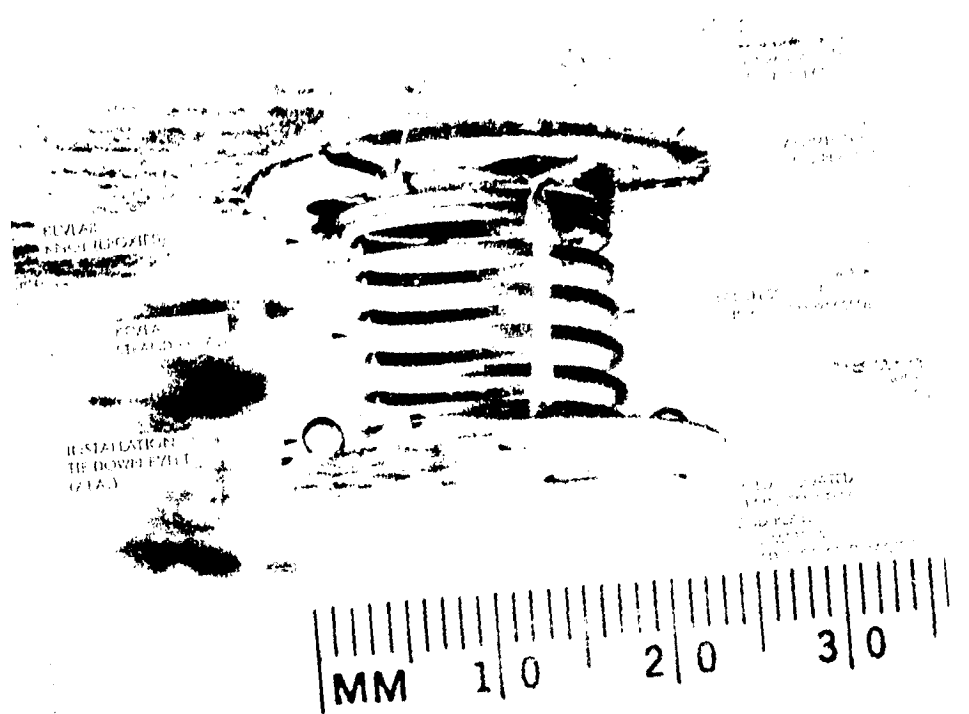
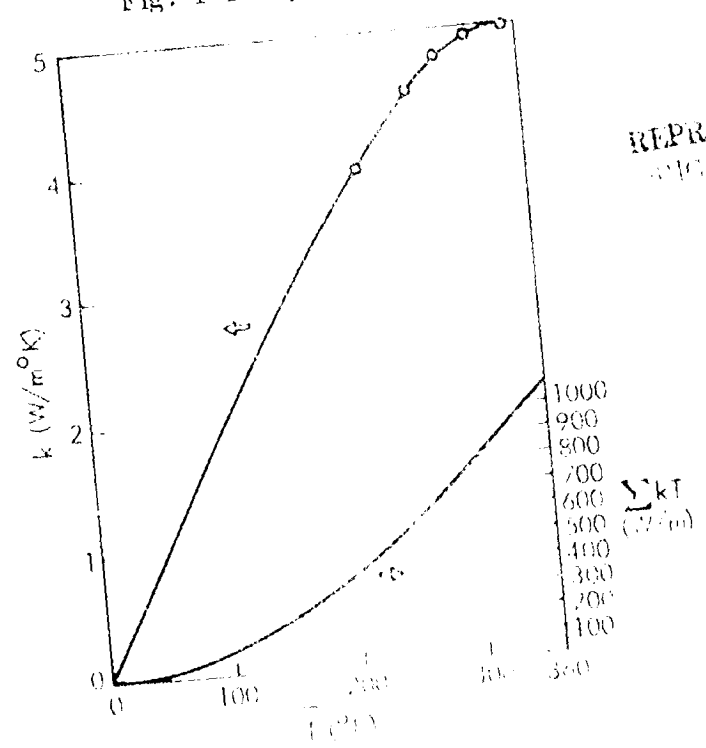


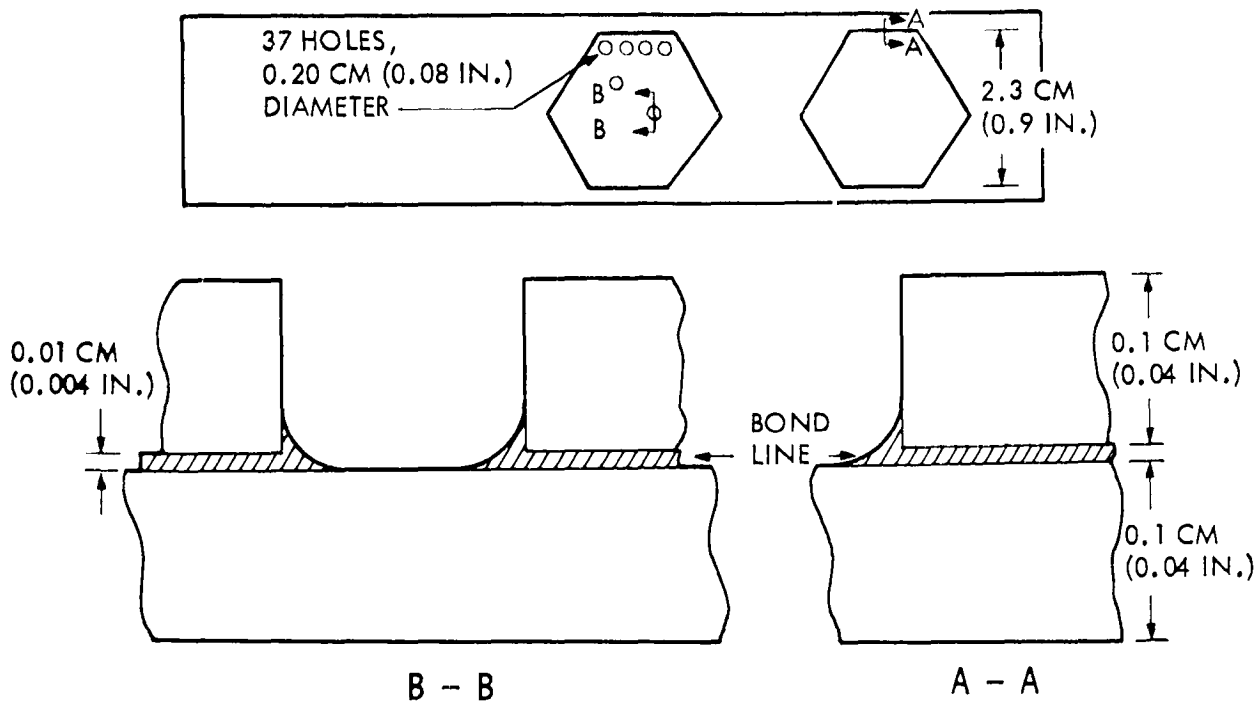
Fig. 4-45 Spring Assembly



REPRODUCTION OF THE ORIGINAL PAGE IS POOR

Fig. 4-46 Kevlar 49 Thermal Conductivity

167

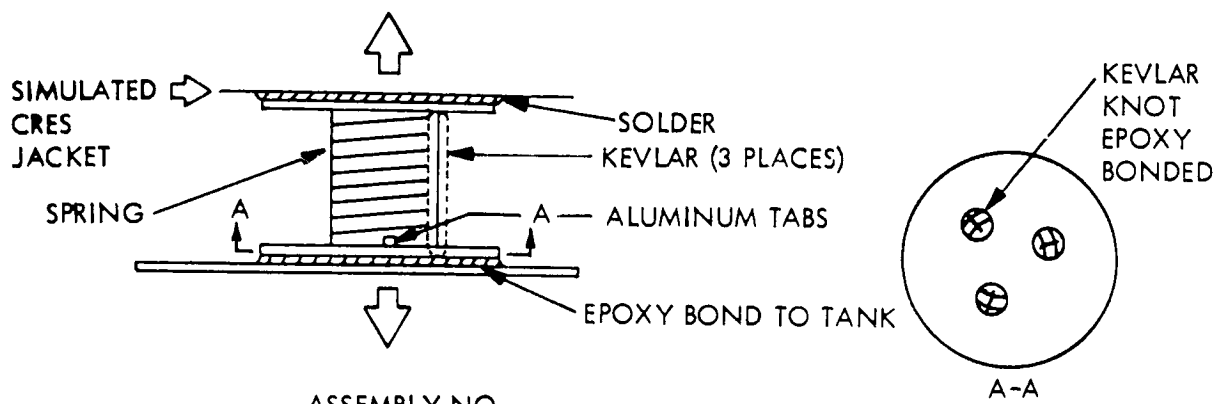


The surfaces were cleaned with MEK prior to bonding with Epibond 123/9615-10 epoxy adhesive. The two-part adhesive formed fillets around the edges and into the holes of the perforated plate. These fillets are placed in shear during thermal cycling and act as "peel stoppers" in the bond line.

The adhesive is allowed to cure 24 hr at room temperature and then taken to $\sim 113^{\circ}\text{C}$ (235°F) for 1 hr to simulate the hot-gas purge that was originally planned for use prior to filling the jacket with microspheres. The test specimens are immersed in LN_2 ; after 15 s the rapid boiling subsided; the specimen is held in the LN_2 for an additional 15 s and then removed. The test specimen is brought back to ambient temperature within 60 s using a hot air gun. This thermal shock cycle was repeated 100 times with no evidence of bond-line crazing or delamination on either specimen. Since 100 cycles exceeds the design requirement by a factor of 5 and going to LN_2 temperature simulates 94 percent of the contraction the aluminum will experience going to LiH_2 temperature,

this bonding method has been selected for attaching the spring wire attachments to the tank surface. Prior tests (Ref. 4-1) have also shown there is no outgassing of this type of adhesive at LO_2 or LH_2 temperature.

Structural integrity of the assembly was demonstrated by the following tests. The Kevlar strands were flexed in LN_2 with no signs of brittleness. The spring/Kevlar attachment was assembled, including a simulated bonding to the aluminum tank and a simulated soldering to the vacuum jacket. The assemblies were pulled in tension to see if the soldering temperature affected the Kevlar strength and where the weak link in the assembly is located. The results are shown in Fig. 4-47.



ASSEMBLY NO.

- 1 ALUMINUM TABS, EPOXY BOND TO SPRING LET GO AT 236 N (53 LB_f). THE KEVLAR STRANDS WERE UNBROKEN.
- 2 THE TOP COATED CRES PLATE WAS SOLDERED OVER ONLY ONE-HALF THE SURFACE TO SIMULATE THE WORST MISMATCH POSSIBLE DURING INSTALLATION. THE SOLDER JOINT PEELLED AT 53 N (12 LB_f); THE KEVLAR STRANDS WERE INTACT.

Fig. 4-47 Tensile Tests of the Spring Assembly

Two out of the three Kevlar strands were cut. With the end plates attached to the simulated tank and jacket, the assembly remained stable and did not buckle. Since the design tensile requirement for the assembly is 22 N (5 lb_f), the assembly is more than adequate for (1) a mismatched solder joint and (2) up to two strands of the Kevlar breaking.

In fact, on future programs, smaller Kevlar strands can be used to reduce the heat leak as the current size Kevlar strands can theoretically sustain a 512 N (115 lb_f) load and are over-designed from a strength requirement standpoint. The elongation for the assemblies tested varied between 1.4×10^{-4} to 3.6×10^{-4} mm/N (6×10^{-4} to 16×10^{-4} in./lb_f). Consequently, the change in assembly length at design loads is very small as desired.

An assembly sequence was developed for the spring assembly as follows:

- Attach the aluminum end plate to the spring by bending the three tabs over the spring wire.
- Spot weld the two eyelets to the stainless-steel end plate in a jig fixture.
- Attach the stainless-steel end plate to the spring by spot welding.
- Coat the outer surface of the stainless-steel end plate with 95%Sn-5%Ag solder. Rinse off the residual flux in hot water.
- Compress the spring assembly to the design height between special jaw attachments in a vise that allows access to the three holes in the end plates.
- Run the Kevlar strand through the end plate holes and around the spring at three locations. Tie a knot at the aluminum end plate. Place a drop of epoxy adhesive on the Kevlar knot. Cut off the excess Kevlar strands after the epoxy cures. [The design height was held to ± 0.03 cm (± 0.01 in.) using this assembly method.]

The spring assemblies are installed on the tank in the following manner. The aluminum end plate is bonded to the aluminum tank with Epibond 123/9615-10 epoxy adhesive. The adhesive is allowed to cure overnight at ambient temperature with the assembly

held in place with rubber strips. Following installation of the jacket, the stainless-steel end plate is soldered to the inside of the jacket by heating from the outside with a circular shaped copper soldering iron 0.38 cm (0.15 in.) larger in diameter than the end plate. The temperature of the iron is controlled by a voltage regulator. Although the temperature was not measured, it was hot enough to ensure uniform solder flow within 5 s. The iron was removed after 15 s, and the joint area cooled with an air gun for 45 s. To inspect this blind joint, tape is attached to the outside surface of the jacket and the tape is pulled with the device shown in Fig. 4-48.

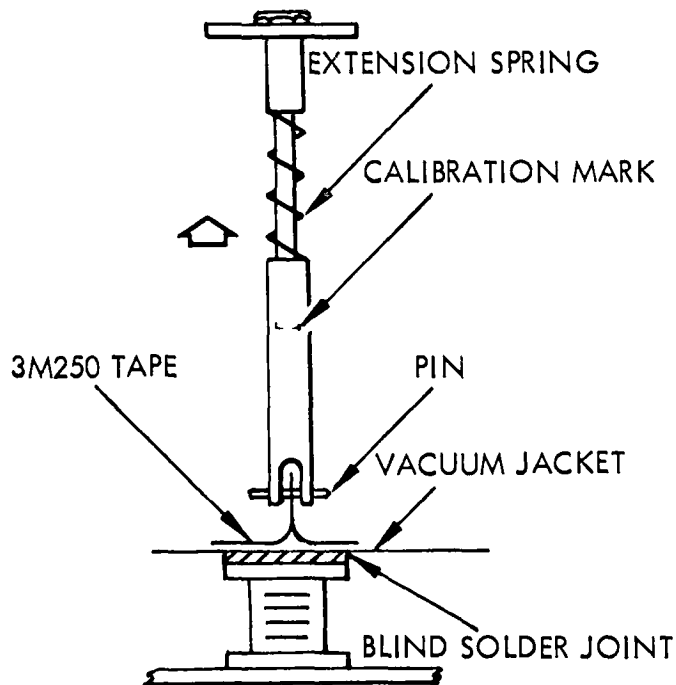


Fig. 4-48 Inspection Method for Spring/Jacket Solder Joint

The calibration mark on the device is set at 4.4 N (1 lb_f). To avoid potential damage to the jacket in case the joint fails, one hand rests against the jacket in the joint area as the spring is extended with the other hand. If the joint fails, the area is reheated

to obtain a better solder joint and then reinspected. Installation of the tape, performing the pull test, and removal of the tape takes slightly under 1 min for each joint that is inspected.

4.1.12 Tests of Gold Coatings

Gold coatings with an epoxy substrate are deposited on both the inside of the vacuum jacket and the outside of the tank surface to reduce radiation heat transfer through the uncoated microspheres. A series of thermal shock tests were conducted to determine if large temperature changes would cause the gold coating to peel or to increase its emittance value.

Earlier in the program, a 400-Å gold coating was selected when metallic coated microspheres were being considered. When uncoated microspheres were selected, the gold coating thickness was increased to 1000 Å to reduce emittance values to a minimum and reduce the radiation component of heat transfer. Consequently, test data are reported for both 400 Å and the selected 1000-Å gold coatings.

Samples of the formed stainless-steel vacuum jacket 13 cm (5 in.) by 18 cm (7 in.) by 0.08 mm (0.003 in.) are coated with a 0.01 mm (0.0005 in.) thickness of epoxy followed by 400 or 1000 Å of gold. The epoxy is required to provide good adhesion of the gold. The samples were immersed in LN₂; boiling stopped in 5 s; the samples were held in the LN₂ for an additional 10 s. Following removal from the LN₂, the samples were brought back to ambient temperature within 20 s using a hot air gun. The test results are shown in Fig. 4-49.

Samples of alodined 2219 aluminum 17.8 cm (7 in.) by 8.9 cm (3.5 in.) by 0.81 mm (0.032 in.) were coated with a 0.01 mm (0.0005 in.) thickness of epoxy followed by 400 or 1000 Å of gold. The epoxy is required to provide good adhesion of the gold. The 400-Å samples were immersed in LHe and then brought back to ambient temperature with a hot air gun. The 1000-Å samples were immersed in LN₂. Because of the rapid helium boiloff and the difficulty in ascertaining whether the sample reached LHe

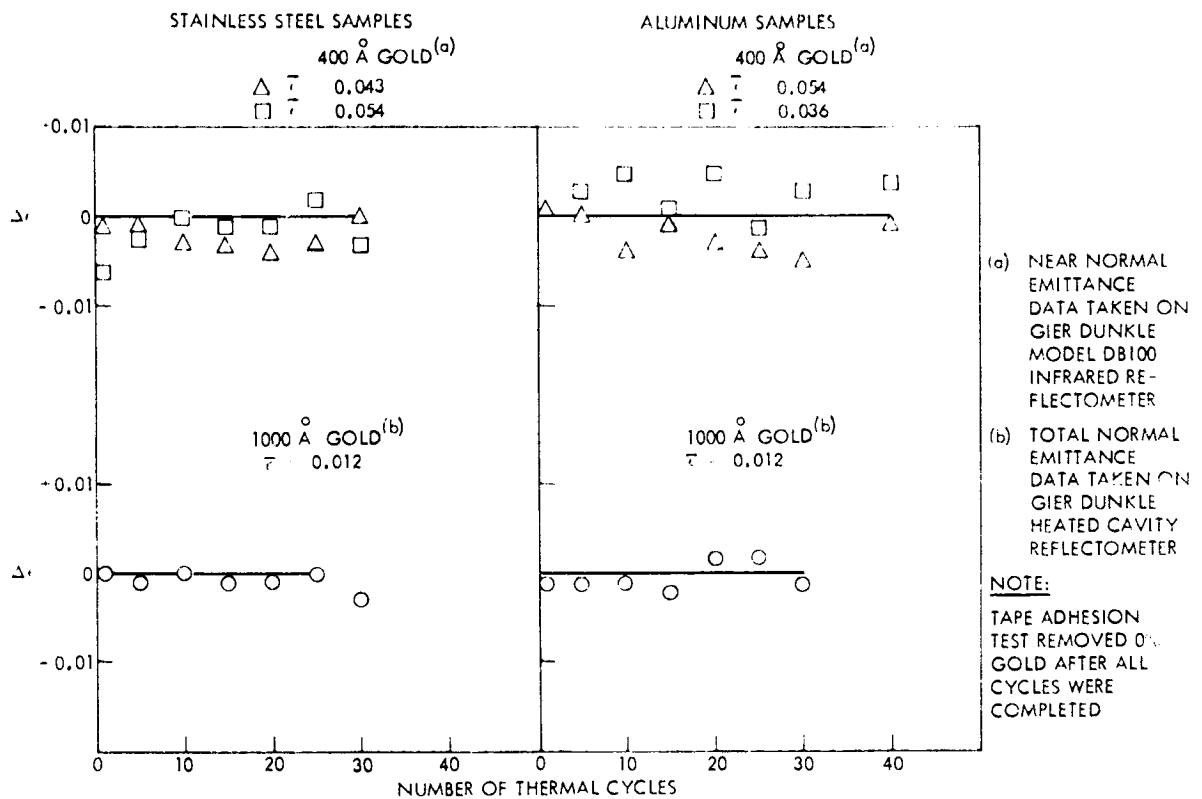


Fig. 4-49 Effect of Thermal Cycling on Gold Coated Samples

temperature, an additional 20 cycles were performed between LN_2 and ambient temperature for the 400-Å gold coatings. The test results are shown in Fig. 4-49.

No significant change in emittance was noted in any of the tests. A tape test also showed good gold adhesion; 0 percent gold removal was noted before and following any of the thermal shock cycles.

4.2 MICROSPHERE INSULATION PROCESSING DEVELOPMENT

Thirty-two kg (71 lb) of glass microspheres were fabricated at the 3M Company, New Business Development Department in Minneapolis, Minnesota. The resulting borosilicate glass spheres are designated B12AX. Processing steps were developed to

obtain the desired physical characteristics of lower density, removal of weak spheres and broken particles, and evacuation of the microsphere's interior. Details of each of these steps follow.

4.2.1 Sizing

The desired microsphere size range was obtained by processing the microspheres in an air classifier at the Donaldson Co. in Tulsa, Oklahoma. The desired larger diameter spheres were separated from the smaller spheres in a size 1 Majac Air Classifier at feed rates ranging from 3.6 to 7 kg/h (7.9 to 15.4 lb/h) using an injector operating on 0.6 standard m³/min (21 ft³/min) of air at 3.4×10^5 N/m² (49 psi) gage pressure and 300 to 306°K (540 to 551°R) temperature. The classifier settings were 3000 rpm and 9.5 m³/min (335 ft³/min) of fan air at 314 to 322°K (565 to 580°R) temperature and up to 0.25 m (0.8 ft) of water pressure drop.

The microspheres were processed in eight batches and the yield of the desired larger diameter spheres ranged from 39 to 47 percent. The measured size ranges for the larger diameter particle fraction and smaller diameter particle fraction are shown in Fig. 4-50. The random close-packed bulk densities of the two fractions were measured

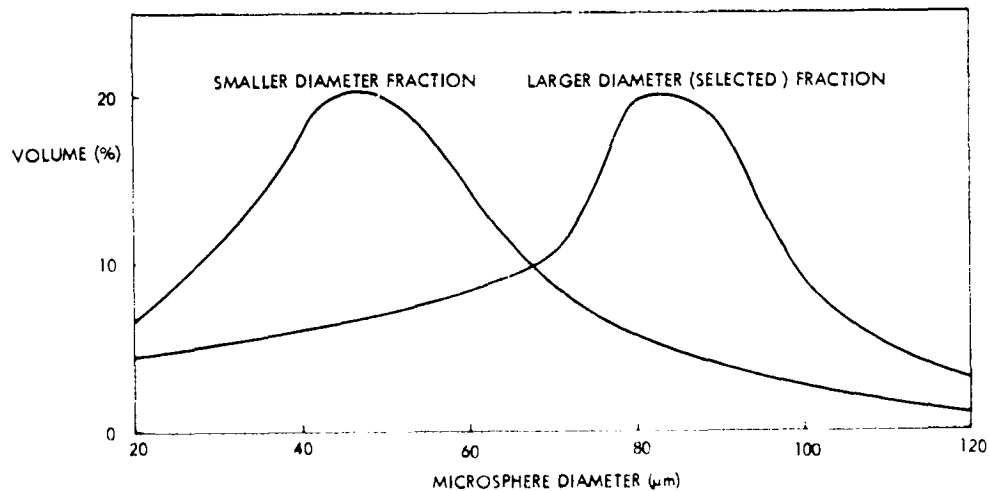


Fig. 4-50 Microsphere Size Distribution

and found to be

- Larger diameter spheres: 0.0718 g/cc (4.48 lb/ft³)
(selected for use)
- Smaller diameter spheres: 0.0856 g/cc (5.34 lb/ft³)
(contained large fraction of broken spheres)

The densities include any broken or solid spheres.

4.2.2 Compression

To eliminate those microspheres incapable of withstanding a 1-atm compressive stress, a metal cylinder, with a 0.24 m (9.45 in.) ID, was constructed as shown in Fig. 4-51. The outer cylindrical shell rests on eight springs placed over eight guide rods. The center piston is fixed, and a split nylon O-ring seals between the cylinder and the piston. The piston volume is nearly filled with microspheres and the metal disk (with an O-ring seal) is placed on top of the cylinder. The apparatus is compressed to 1.33 atm and held for several seconds. The load is released and the microspheres removed with a metal scoop. Initially, a new, clean commercial vacuum cleaner (lined with a polyethylene bag) was used to remove the microspheres from the compression test apparatus. This method was discontinued when microspheres escaped into the air through the vacuum filter attach area. It is felt the vacuum cleaner removal method will work if the filter is attached more securely and the polyethylene bag liner is contained in a framework to prevent it from being sucked in covering the central filter area.

4.2.3 Separation of Unbroken Spheres

The broken and solid spheres are removed in the flotation apparatus shown in Fig. 4-52. The sized microspheres are poured into the upper rotating can and mixed with water. The rotating elbow discharges the slurry beneath the water surface into a 0.21 m³ (55 gal) drum where most of the broken and solid particles sink to the bottom and the unbroken spheres rise to the top. The unbroken spheres flow over the spillway onto a fabric filter. The water is pumped back into the rotating upper drum and the processed spheres are scooped off the filter with a stainless steel spatula and then dried in an oven.

LOCKHEED PALO ALTO RESEARCH LABORATORY
A SUBSIDIARY OF LOCKHEED AIRCRAFT CORPORATION
LOCKHEED MISSILES & SPACE COMPANY INC

4-76

Fig. 4-52 Microsphere Plotation Apparatus

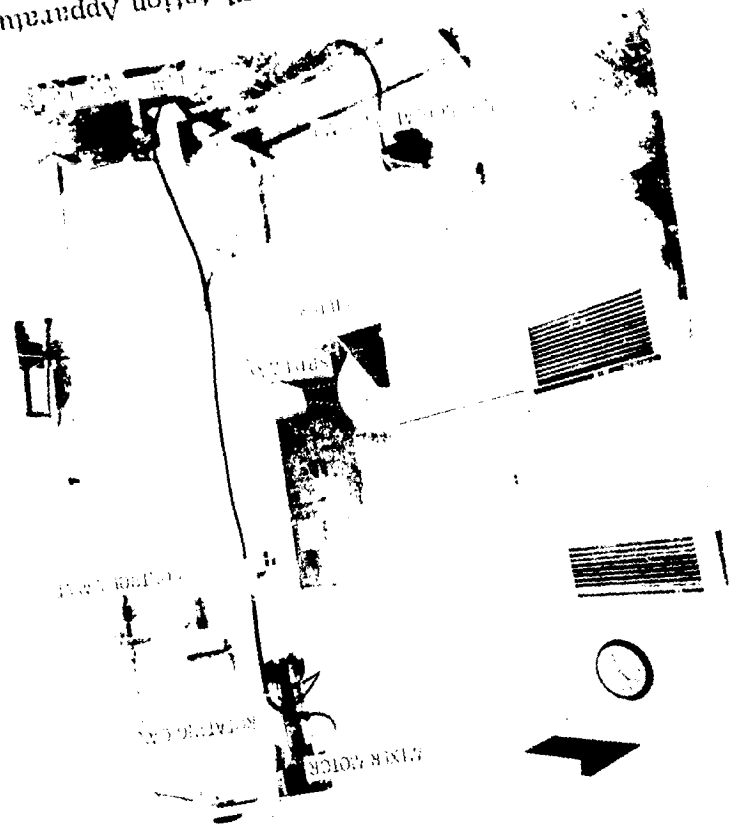
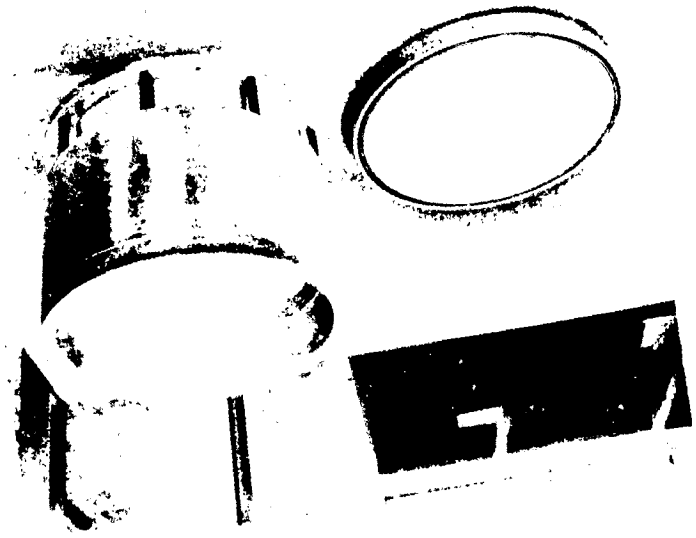


Fig. 4-51 Microsphere Compression Apparatus



The flotation apparatus works well. The microspheres eject beneath the water's surface in an expanding plume, and the unbroken spheres spiral to the top as the expulsion orifice rotates. The processed microspheres are easily removed from the filter with the spatula and the fabric filters work well in separating the microspheres from the water.

The average count of cracked spheres left after three flotations is approximately 7 percent. The measured bulk density of the processed spheres is 0.069 g/cc (4.3 lb/ft³).

To determine whether the spheres' compressive strength is reduced by the water immersion process used to separate broken particles, a load vs. sphere breakage curve was performed and compared to a previous curve (where the microspheres were not processed through the flotation bath). No significant difference was noted between the two samples as shown in Fig. 4-53.

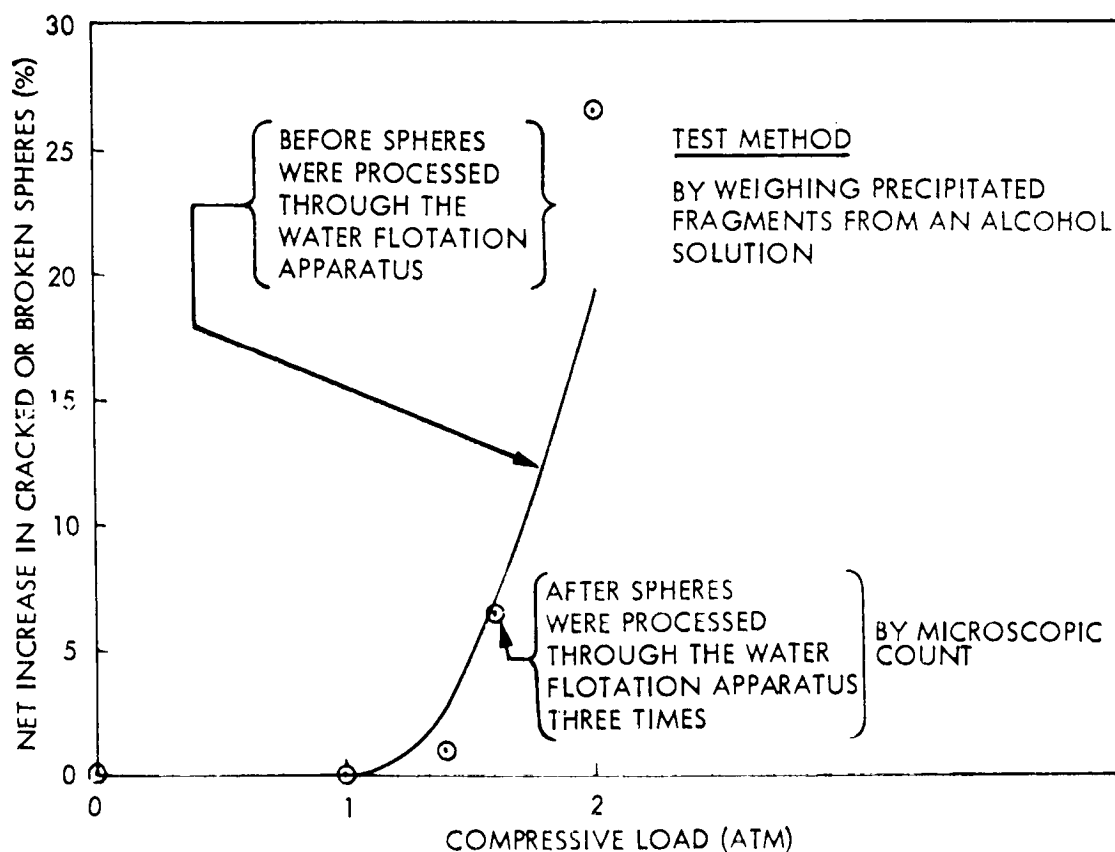


Fig. 4-53 The Effect of Water Immersion on the Microspheres Compressive Strength Capability

4-77

4.2.4 Microsphere Vacuum Bakeout and Transfer

A microsphere vacuum bakeout and transfer container was fabricated as shown in Fig. 4-54. The apparatus allows vacuum bakeout of the microspheres while in the horizontal position, and microsphere transfer to the vacuum jacket by gas fluidization in the vertical position.

The system can be operated at temperatures as high as 427°C (800°F) and pressures down to .0013 Pa. The bakeout function of the apparatus was checked out by the following tests.

Microsphere Vacuum Bakeout. Microspheres were placed in three 1-liter stainless-steel cans. The cans were lowered into the bakeout apparatus and the pressure was lowered to .0027 Pa. The heaters were turned on and the microspheres were vacuum baked out for slightly over 18 days at 421°C (790°F), as shown in Fig. 4-55. The heaters were turned off and the microspheres were kept in vacuum for a total of 35 days until compression tests on the microspheres were ready to be performed. The apparatus was then back-filled with GN₂ to 1 atmosphere.

Note the pressure spike that occurred the first day due to the heating; after approximately 5 days the pressure was back to the preheating pressure value. The pressure continued to decline slowly during the heating cycle and dropped to .0013 Pa for a short time when the heating was discontinued.

The vacuum-baked microspheres were placed in a compression apparatus within hours after they had been removed from the bakeout apparatus. The microspheres were compressed over the range of 1 to 2 atmospheres. Five samples of the microspheres were taken after each load application; the broken particles were counted under a microscope. Figure 4-56 shows there apparently was a slight increase in the percentage of broken particles at 1-atmosphere load, with no significant changes at the three higher loads (as compared to microspheres that had not been vacuum-baked). These variations could be due to the sampling technique and/or the normal statistical fluctuations in the counting. In any event, the increased magnitude of breakage does not appear to be large enough to be of concern in the Tug insulation application.

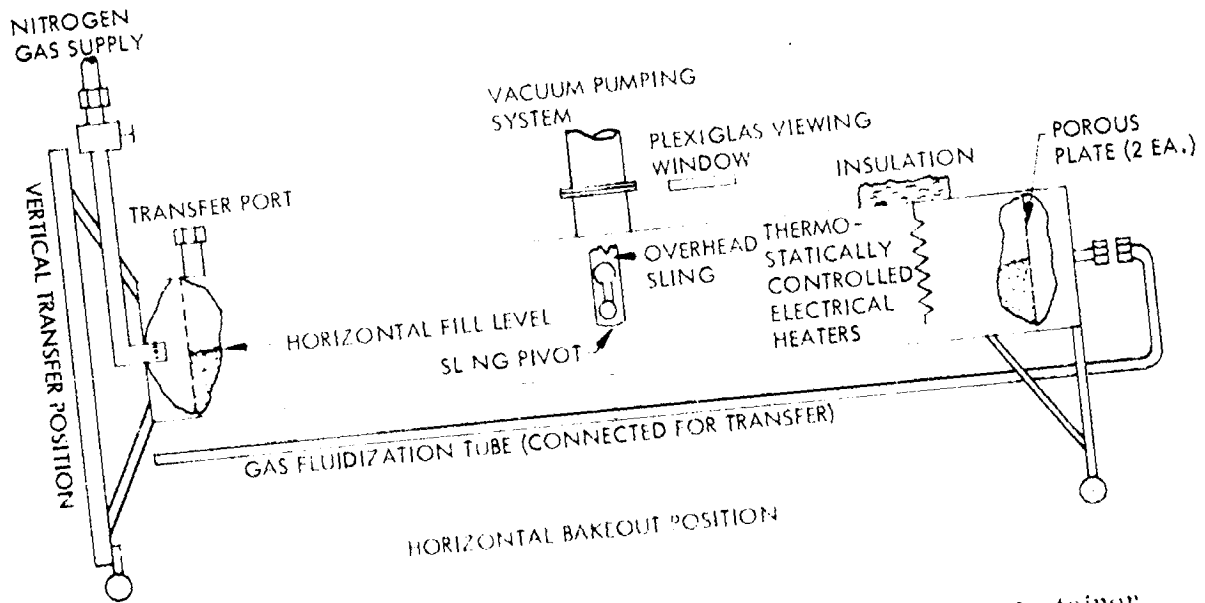
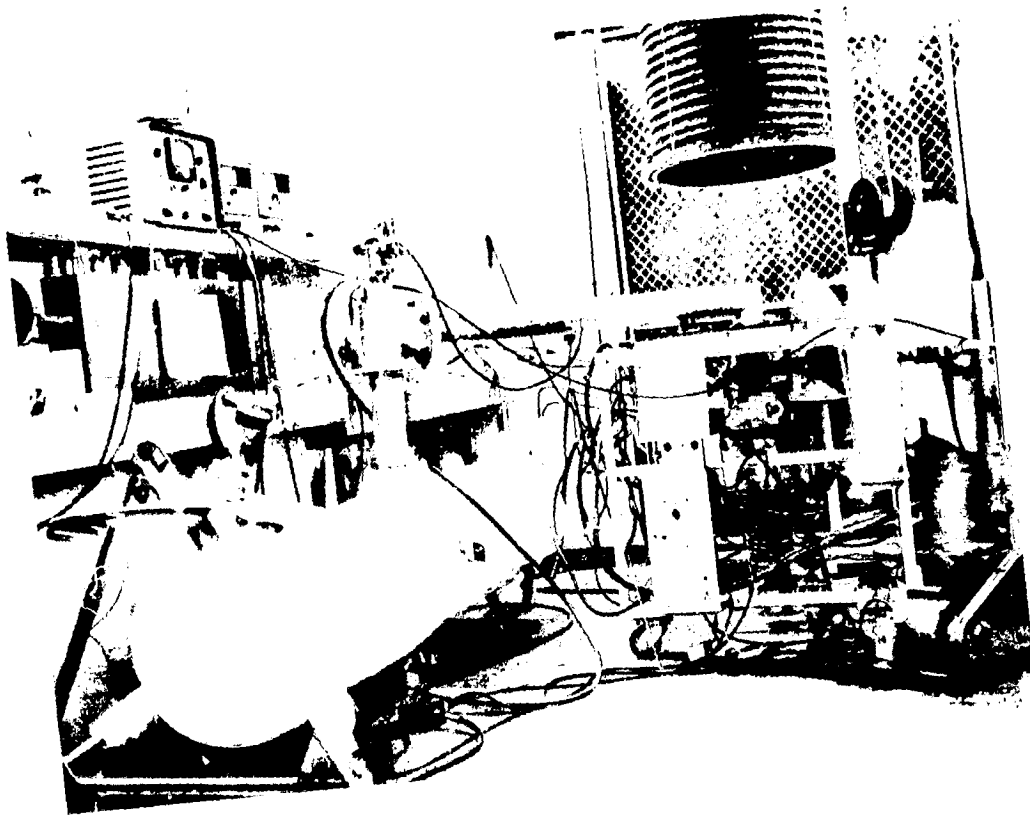


Fig. 4-54 Microsphere Vacuum Bakeout and Transfer Container

4-79

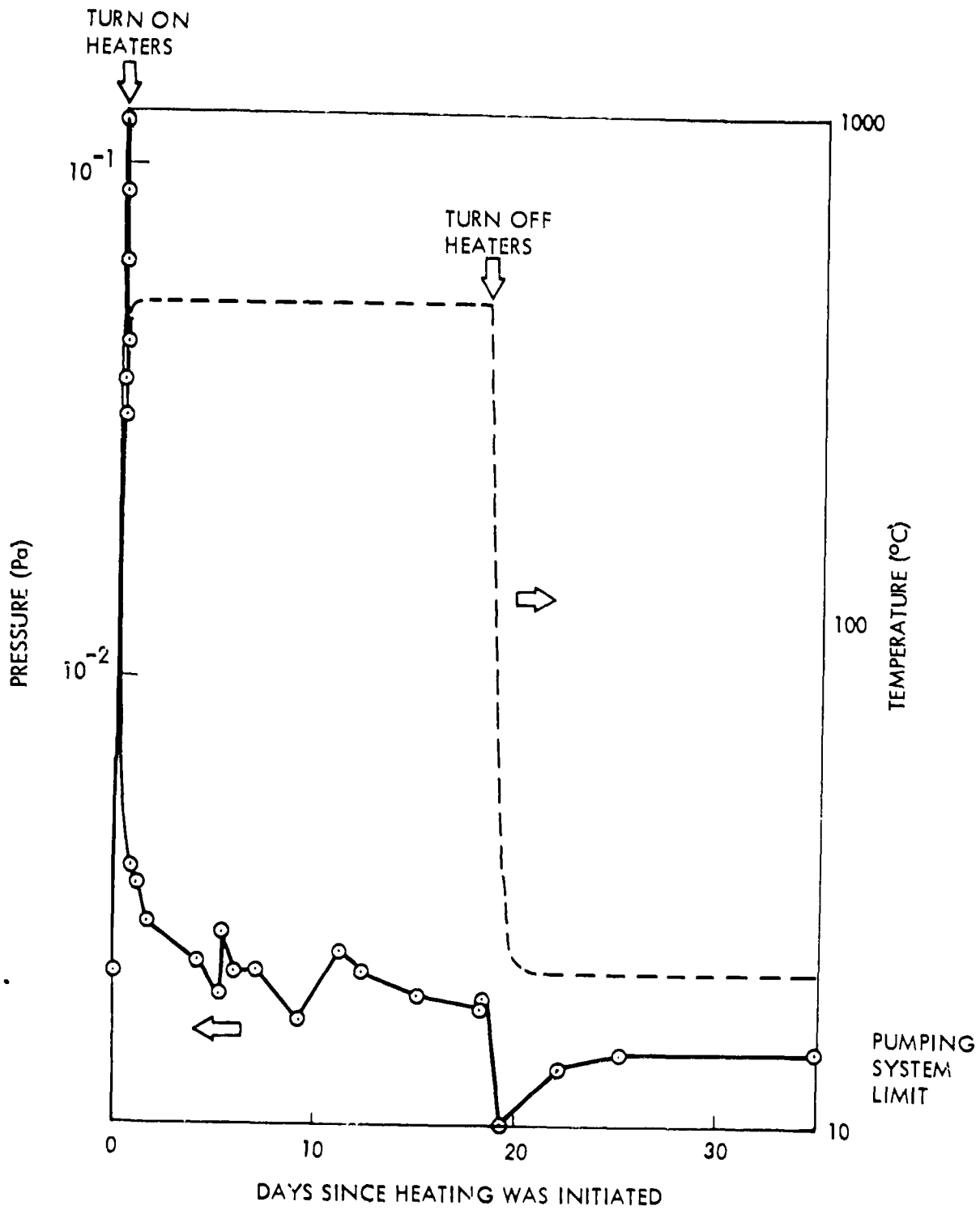


Fig. 4-55 Temperature-Pressure History of the Vacuum Bakeout Apparatus

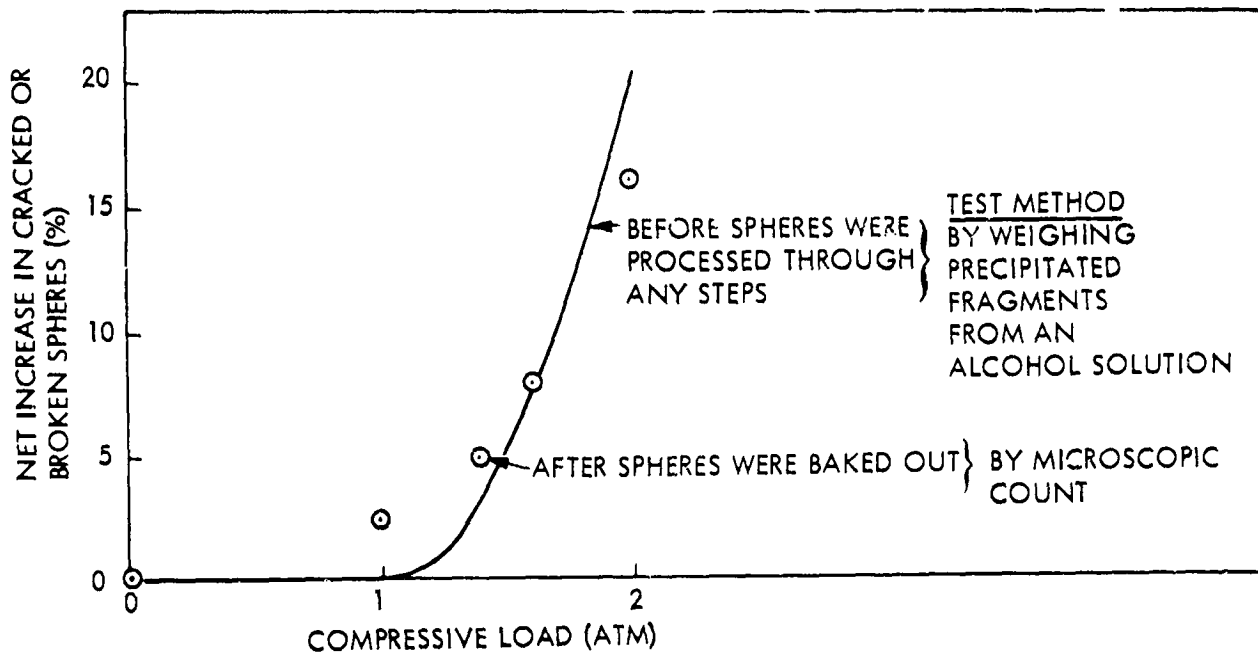


Fig. 4-56 Effect of Vacuum Bakeout on Microsphered Compressive Strength

To determine if the vacuum bakeout reduced the internal gas pressure in the microspheres, the following tests were conducted. A known quantity of unbaked microspheres was placed in a stainless-steel container along with stainless-steel balls and connected to a vacuum pumping system. The container volume was calibrated, pumped down to .013 Pa and shut off from the vacuum system. The container was shaken while mounted on an ultrasonic vibrator causing the steel balls to vibrate rapidly and break the microspheres. The new pressure was measured. The container was then taken to LN₂ temperature and the pressure measurement was again taken. The percent of spheres broken was measured by an alcohol flotation technique. This whole procedure was repeated using microspheres that had been vacuum baked-out. The results of these tests are as follows:

Internal Microsphere Pressure (Pa)

	Internal Microsphere Pressure (Pa)	
	At LN ₂ Temperature	At Ambient Temperature
Unbaked Microspheres	933 ± 666	28,200 ± 2,400
Vacuum Baked Microspheres for 18 days	Data not available	320 ± 177

The gas composition of the unbaked microspheres was determined by use of a mass spectrometer using the gas sampling method described previously. The gas was determined to be 99.97% SO₂ with 0.03% air and no water vapor. Consequently, the partial pressure of air is 8 Pa. If some of the microspheres are broken during flight, the pressure in the jacket can rise, increasing heat-transfer rates. However, if the tank is at LH₂ temperature, the gases will cryopump and no pressure rise will be noted.

Gas	Vapor-Pressure (Pa)		
	LO ₂ 90°K (162°F)	LN ₂ 77°K (139°R)	LH ₂ 21°K (37°R)
SO ₂ (a)	< .013	< .013	<< .013
O ₂	1 × 10 ⁵	1.9 × 10 ⁴	1.3 × 10 ⁻¹³
N ₂		1 × 10 ⁵	1.3 × 10 ⁻⁹

(a) Melting Point = 198°K (356°R)

At LO₂ or LN₂ temperature, the SO₂ will cryopump, but the vapor pressure of the O₂ and N₂ trace gases will be high.

A substantial pressure drop can be effected in the microspheres by a vacuum bakeout as shown in Fig. 4-57. Gas permeation rates through glass are an exponential function for a constant temperature so a plot of pressure versus time is a straight line on a

semilog plot as shown. This relationship is only strictly true for a single gas but applies in this case because of the preponderance of SO₂ present.

The air partial pressure versus time is also plotted in Fig. 4-57, assuming O₂ and N₂ permeation rates are equal to SO₂. Since gas permeation rates through glass generally go up as the molecular weight decreases, the slope of the O₂ (M W = 32) and N₂ (M W = 28) curve should, if anything, be steeper than SO₂ (M W = 64), and the curve shown should be conservative.

A pressure of < .013 Pa is required to obtain optimum thermal performance; therefore, a 60-day bakeout is required as shown in Fig. 4-57 to prevent pressure rise above .013 Pa.

Microsphere Transfer. The microsphere vacuum bakeout and transfer apparatus was partially filled with microspheres and then raised to a vertical position using a sling and overhead crane. A nitrogen gas supply is attached to the bottom port and clear plastic tube to the transfer port as shown in Fig. 4-58.

Gas flow was increased through the bottom port until the microspheres started to flow through the tube. A gas pressure of 1030 N/m² (0.15 psi) and a gas flow rate of 8×10^{-4} m³/min (0.03 cfm) initiated flow of the microspheres through the transfer tube. The flow was very smooth and nonturbulent, similar in appearance to pouring milk from a tube. A microscope count of the microsphere breakage before and after transfer showed no measurable breakage occurred during transfer.

A separate test was performed to determine if high-frequency vibrations would also start microsphere flow through the transfer line. An ultrasonic vibrating table was attached to the base of the transfer apparatus and turned on. The vibration caused the microspheres to settle slightly but did not start the microspheres flowing through the downward slanted transfer tube.

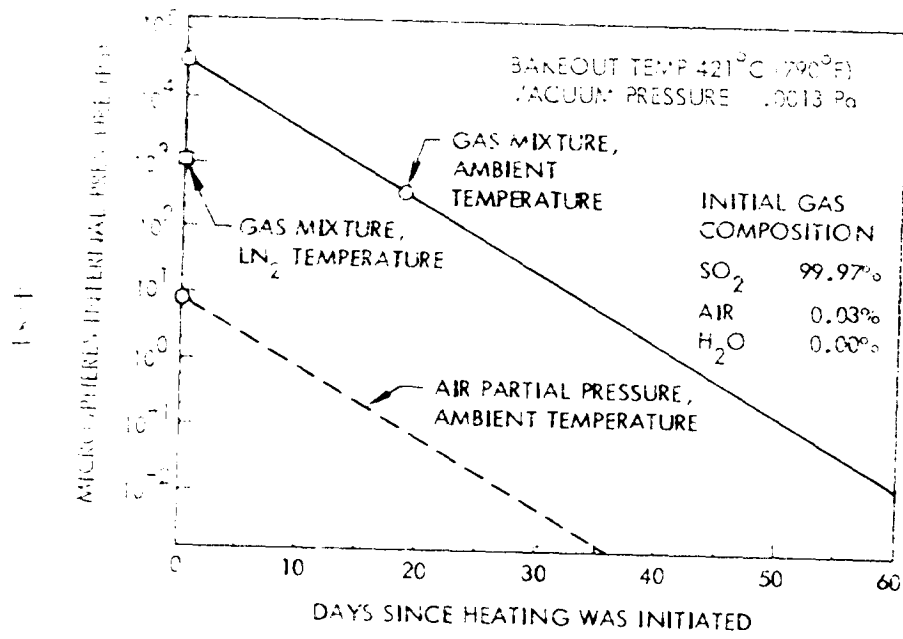


Fig. 4-57 Pressure Decay of Microspheres as a Function of Bakeout Time

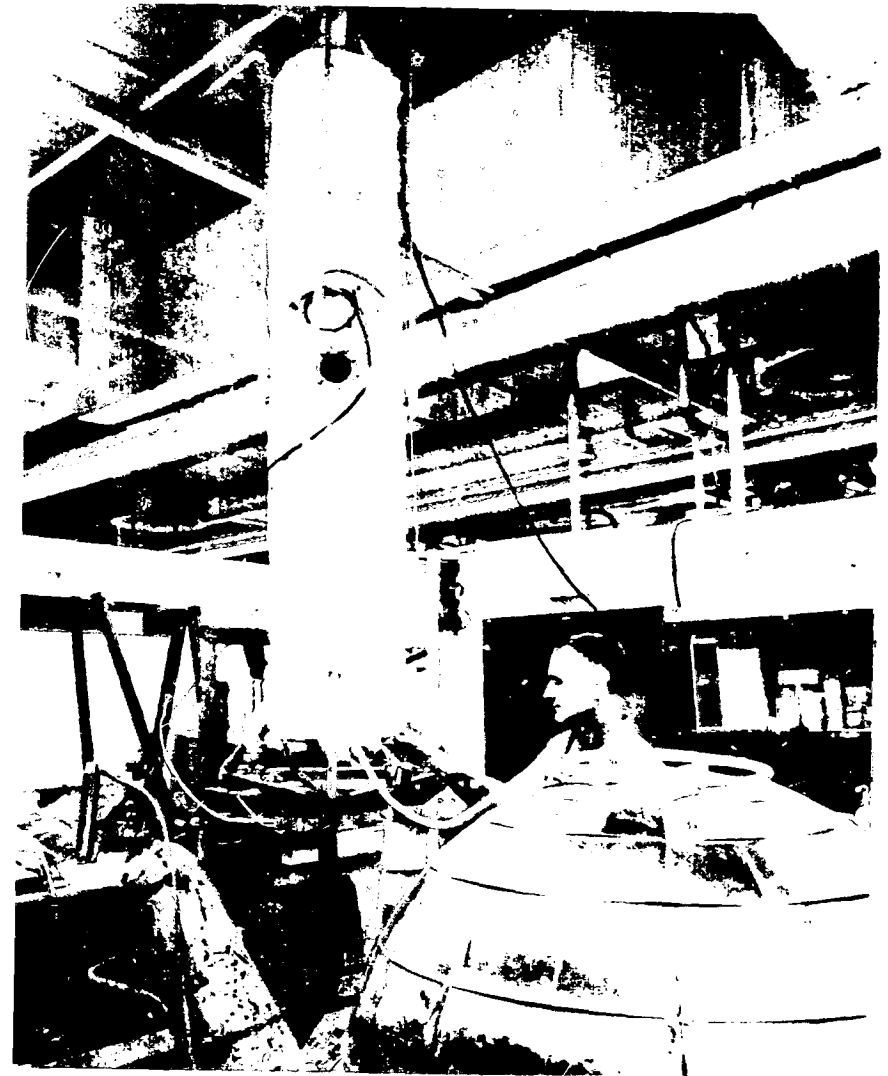


Fig. 4-58 Microsphere Transfer Apparatus

4.3 MICROSPHERE INSULATION PROPERTIES

Microsphere insulation properties which have been obtained on Lockheed technology programs as well as on this contract are summarized here as a convenience for use in engineering performance calculations.

Physical properties are shown in Fig. 4-59; evacuation characteristics are given in Fig. 4-60.

Thermal performance of microspheres as a function of compressive load, gas pressure and boundary temperature and emittance is characterized by the following model. This model is developed in Section 6.6.1.

SPHERES (812 AX, 3M CO.)	BEFORE PROCESSING	AFTER PROCESSING
● SPHERE MATERIAL:	BOROSILICATE GLASS	SAME
● INTERNAL PRESSURE:	2.8×10^4 Pa	.013 Pa
● INTERNAL GASES:	SO ₂ 99.97% AIR 0.03 %	-
● BULK DENSITY:	0.072 g/CC (4.5 PCF)	0.069 g/CC (4.3 PCF)
● MAXIMUM TEMPERATURE:	482°C (900°F)	SAME

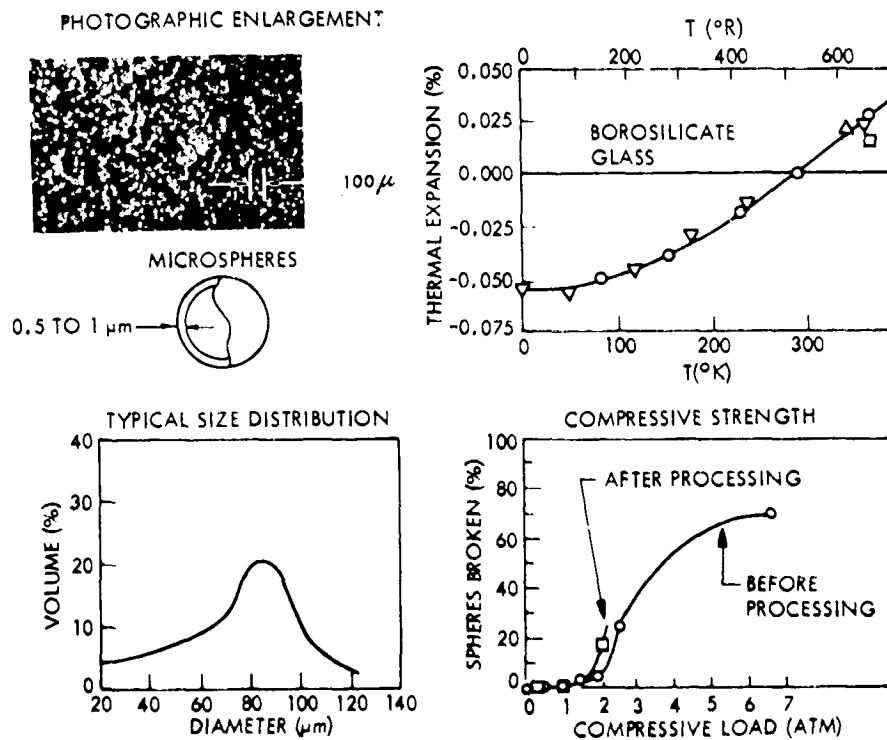


Fig. 4-59 Microsphere Insulation Physical Properties

98-4

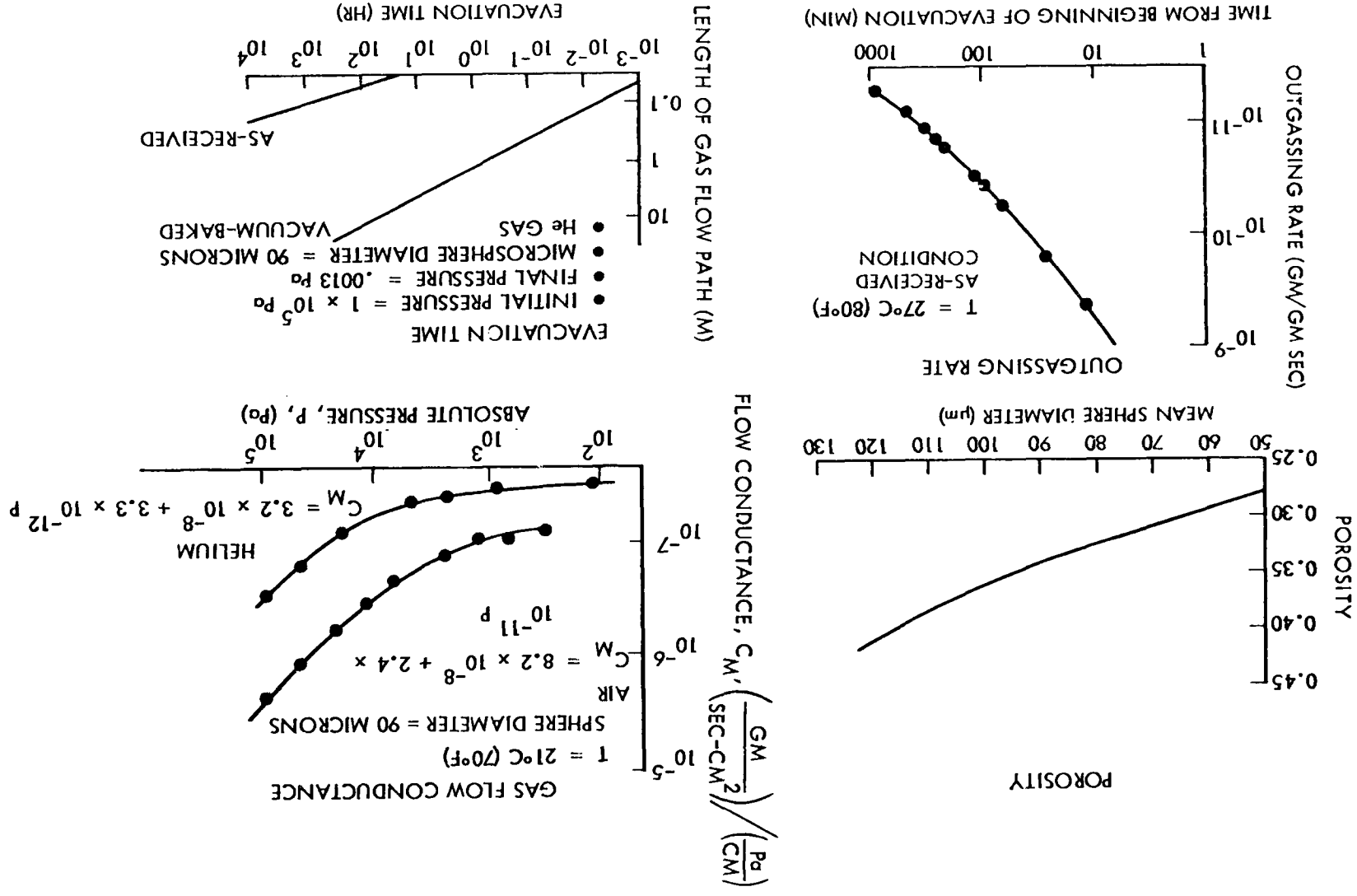


Fig. 4-60 Microsphere Evacuation Characteristics

$$k = k_{sc} + k_{gc} + k_r$$

$$\text{SOLID CONDUCTION } k_{sc} = (1.07 \times 10^{-5}) (P+H)^{.535} \left[3.13 \times 10^{-3} T_H (1+\theta) - 2.61 \times 10^{-6} T_H^2 (1-\theta^3/1-\theta) \right]$$

$$\text{GAS CONDUCTION } k_{gc} = k_g \left[\frac{5.8 (1-m)^2}{1 - \frac{k_g}{k_{gr}}} \left(\frac{1}{1 - \frac{k_g}{k_{gr}}} \ln \frac{k_{gr}}{k_g} - 1 - \frac{K}{2} \right) + 1 \right]$$

$$\text{RADIATION } k_r = \left[\frac{n^2}{0.75 \beta l + \frac{1}{n \epsilon_H} + \frac{1}{n \epsilon_C} - 1} \right] \sigma l T_H^3 (1+\theta) (1+\theta^2)$$

where

A = area of jacket (m²)

d_{gr} = microsphere diameter (m)

F = deflection force/spring assembly (N)

H = integrated microsphere self-weight, $1.87h - .00525 h^2 + 6.37 \times 10^{-6} h^3$, Pa (h < 120 cm)

h = maximum vertical height of jacket (cm)

k = thermal conductivity (W/m^oK)

k_g = $\frac{k_{go}}{1 + \frac{2\lambda L}{\delta_a}}$ (W/m^oK)

k_{go} = gas thermal conductivity at standard conditions (W/m^oK)

k_{gr} = $k_s \left[\frac{1 + \frac{2m(1-\nu)}{(2\nu+1)}}{1 - \frac{m(1-\nu)}{(2\nu+1)}} \right]$ (W/m^oK)

k_{gs} = gas thermal conductivity inside the sphere (W/m^oK)

k_s = thermal conductivity of glass (W/m^oK)

K = $1 - k_{gs}/k_s$

l = insulation thickness (m)

L = mean free path (m)

m = void fraction

REPRODUCIBILITY OF THE
ORIGINAL PAGE IS POOR

- n = refractive index of microspheres, 1.56
- N = number of spring assemblies
- P = external compressive load, Pa for $1.3 > P > 2 \frac{NF}{A}$
- Pr = Prandtl No.
- T_H, T_C = absolute hot and cold boundary temperatures, respectively (°K)
- a = accommodation coefficient
- β = extinction coefficient of microspheres, $9450 \text{ (m}^{-1}\text{)}$
- γ = specific heat of gas (Cal/g°K)
- δ = $\frac{2md}{gT}$ (m)
- H, C = gold coating boundary temperature total hemispherical emittance, metal to vacuum
- $\epsilon(T) = \sigma T^{0.67}$ for thicknesses $> 1000 \text{ \AA}$
- T_H = T_C
- k/k_g = Stefan Boltzmann constant, $5.6 \times 10^{-8} \text{ (W/m}^2\text{°K}^4\text{)}$
- σ = $\frac{\gamma+1}{2\gamma} \frac{Pr}{1-\frac{\sigma}{2\gamma}}$
- x =

Section 5
SUBSCALE TEST ARTICLE FABRICATION

Procedures were developed for forming, joining, leak checking, and repairing the vacuum jacket as described in Section 4. In addition, methods for fabricating and installing the spring/Kevlar assemblies and processing the microspheres are also described in Section 4. Consequently, details of these procedures will not be repeated here. This section provides the assembly sequence of the total test article plus any significant details on fabrication and assembly that were not covered in Section 4.

The overall assembly sequence of the test article is shown in Fig. 5-1. The following steps refer back to this figure.

Stretch forming of the 0.08 mm (0.003 in.) 321 stainless steel jacket (Step J1) is followed by hydropress forming of 18 gore panels and 2 polar cap panels (Step J2) plus spares. The panels are trimmed and welded together including spun-form polar cap closeouts and the final closure flanges (Step J3).

Leak check of the jacket consists of helium pressurization to 249 N/m^2 (0.036 psi) and sniffing with a mass spectrometer leak detector. A water seal is used at the jacket equator.

Solder coats are applied to the jacket using Kapton tape masks and Eutector 157 flux and solder to both the spring assembly areas and final closure joint flanges. Overlap areas of the final closure joint are pretinned prior to the solder coat. A doubler for strut access box attachment is held on the inside of the jacket with brass screws and Teflon nuts. The doubler and screws are soldered to the jacket after which the Teflon nuts are removed. Use of the 157 flux caused microscopic corrosion pits to form in the jacket, even after thorough rinsing with bicarbonate

of soda solution and water. Upon discovering these pits, use of the flux was discontinued and pretinning plus use of a neutral rosin flux was substituted for any solder repairs required.

Joint areas are masked off prior to epoxy and gold coating on the inside surface to prevent entrapment of air; solder coats and screens are also masked off. An area of 0.32 m^2 (3.4 ft^2) is masked (approximately 7 percent of the jacket surface area is not gold coated).

Concurrently with jacket fabrication, work proceeded on the tank. The tank support tangs are reinforced, the plumbing penetration at the tank bottom is welded shut, and platinum resistance thermometers are epoxy bonded to the inside of the tank wall.

The tank-exterior is epoxy coated followed by a gold coating (Step A) in a fixture that allows 360 deg rotation. Approximately 0.12 m (1.29 ft^2) of the tank is masked for the spring assemblies and access cover bolts. The area not gold coated amounts to 2.8 percent of the tank surface.

The spring/Kevlar assemblies are fabricated and epoxy bonded to the tank (Step B). Rubber strips hold the assemblies on the tank while the epoxy cures overnight.

Kevlar strands are inserted through eyelets in the lower surface of the upper end plate of each spring assembly (as shown in P2). The Kevlar strand starts at the top polar cap (bonded to a screw in a special circular installation fixture), runs down the tank through eyelets on one side of a row of spring assemblies, reverses direction 180 deg at a special installation eyelet fixture at the lower pole, and is threaded through the eyelets on the other side of the same spring assemblies going back up the same side of the tank. The other end of the Kevlar strand is also bonded to a separate screw in the top installation fixture, next to the first screw. This procedure is repeated for each row of spring assemblies. To compress the spring assemblies, the two adjacent screws are rotated, shortening the length of the Kevlar strands. This process is continued until the spring bottoms out, providing a stable configuration that allows the spring assemblies to be straightened by hand.

FOLDBOUT FRAME

(J1) STRETCH FORM PANELS; ROUGH TRIM.



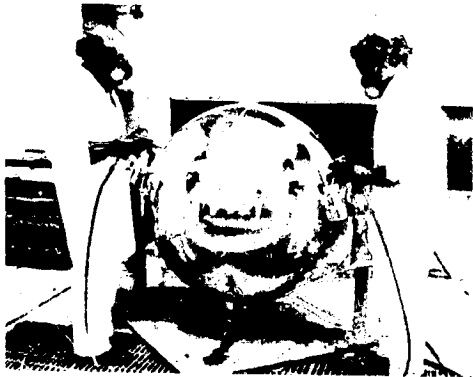
(J2) FORM GORE AND POLAR CAP PANELS, FLANGES, POLAR CAP CLOSEOUTS.



(J3) TRIM, WELD PANELS, POLAR CAP CLOSEOUTS, FLANGES TOGETHER (2 HEMISPHERES). LEAK CHECK; SOLDER COAT; GOLD COAT.



(A) MODIFY TANK; LEAK CHECK; INSTRUMENT; GOLD COAT.



(B) FAB SPRING ASSEMBLIES, BOND TO TANK. COMPRESS WITH KEVLAR STRANDS.

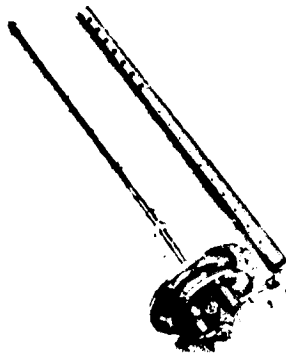


(C) INSTALL HEMISPHERES, SOLDER FINAL CLOSURE JOINT; LEAK CHECK. RELEASE SPRING ASSEMBLIES; SOLDER.



REPRODUCIBILITY OF THE ORIGINAL PAGE IS POOR

(P1) FAB UPPER PLUMBING ASSEMBLY; LEAK CHECK; INSTRUMENT.



(P2) INSTALL PERFORATED TUBE, ALUMINUM WOOL, PLUMBING ASSEMBLY IN TANK. COLD LEAK CHECK.

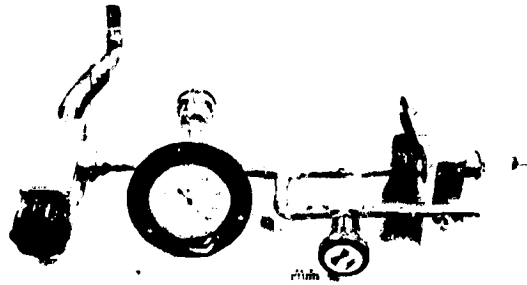


FOLDOUT FRAME 2 REPRODUCIBILITY OF THE ORIGINAL DESIGN AS BUILT

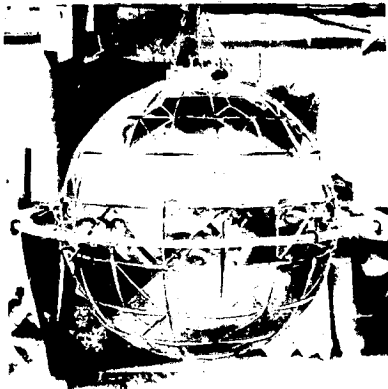
(J3) TRIM, WELD PANELS, POLAR CAP CLOSEOUTS, FLANGES TOGETHER (2 HEMISPHERES). LEAK CHECK; SOLDER COAT; GOLD COAT.



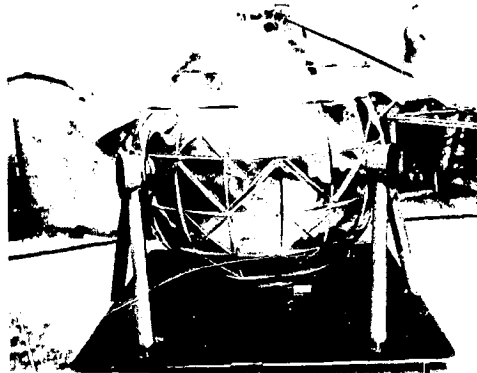
(P3) FAB LOWER PLUMBING ASSEMBLY; LEAK CHECK.



(C) INSTALL HEMISPHERES, SOLDER FINAL CLOSURE JOINT; LEAK CHECK. RELEASE SPRING ASSEMBLIES; SOLDER.



(D) BOLT STRUT BOX; SOLDER; LEAK CHECK; INSTALL STRUTS, WELD CLOSEOUT; LEAK CHECK. INSTALL PALLET WITH LOWER PLUMBING; VACUUM BAKEOUT.



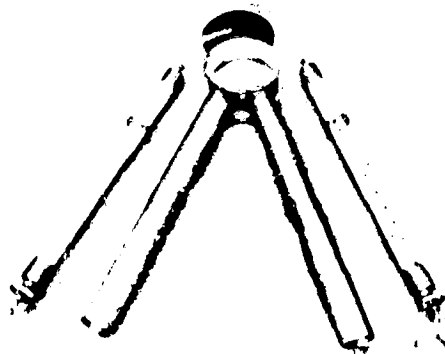
(E) WELD 3 STRUT COVERS, TOP; INSTALL MICROSPHERES, EV; LEAK CHECK.



(P2) INSTALL PERFORATED TUBE, ALUMINUM WOOL, PLUMBING ASSEMBLY IN TANK. COLD LEAK CHECK.



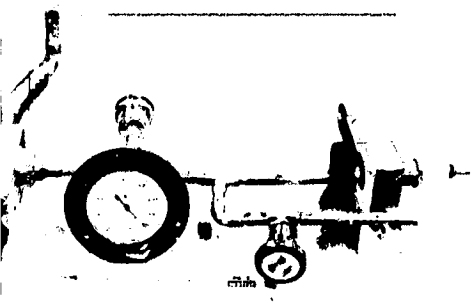
(S) FAB STRUT CLOSEOUTS, FITTINGS, "SPOKE" SPACER. INSTALL ON STRUT, INSTRUMENT. FAB STRUT JACKET COVERS, LEAK CHECK, GOLD COAT, SOLDER COAT FLANGE.



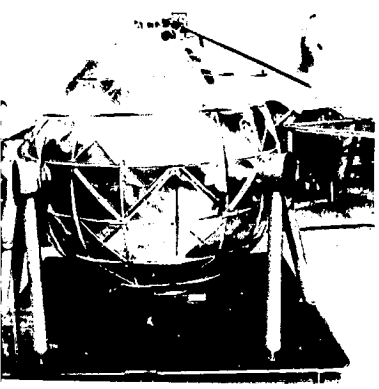
REPRODUCIBILITY OF THE
ORIGINAL PAGE IS POOR

FOLDOUT FRAME 3

LOWER PLUMBING ASSEMBLY;
LEAK CHECK.



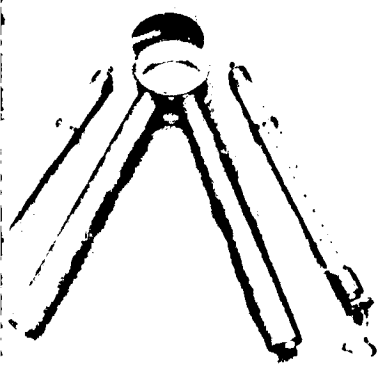
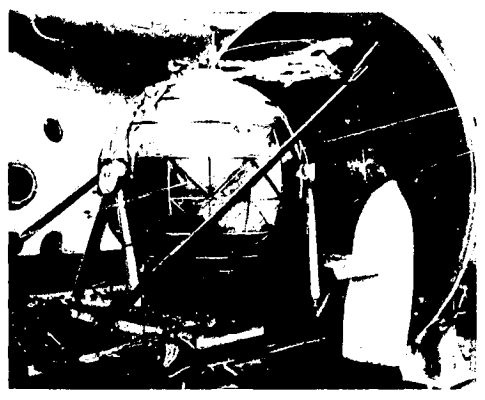
STRUT BOX; SOLDER; LEAK CHECK;
INSTALL STRUTS; WELD CLOSEOUT; LEAK
CHECK. INSTALL PALLET WITH LOWER
PLUMBING; VACUUM BAKEOUT.



(E) WELD 3 STRUT COVERS, TOP DOUGHNUT,
INSTALL MICROSPHERES, EVACUATE;
LEAK CHECK.



(F) COMPLETE JACKET INSTRUMENTATION.



STRUT CLOSEOUTS, FITTINGS,
1/2" SPACER. INSTALL ON STRUT,
INSTRUMENT. FAB STRUT JACKET
COVERS, LEAK CHECK, GOLD COAT,
GOLD COAT FLANGE.

REPRODUCIBILITY OF THIS
ORIGINAL PAGE IS POOR

Fig. 5-1 Test Article Assembly Sequence

The upper plumbing assembly is fabricated, welded and brazed together, leak checked at appropriate times in the fabrication procedure, and instrumented with carbon resistor liquid-level sensors, chromel constantan thermocouples, and platinum resistance thermometers (Step P1).

A perforated tube is installed inside the tank and the tank is filled with approximately 41 kg (90 lb) of coarse aluminum wool. The upper plumbing assembly fill tube is slipped inside the perforated tube and the Conoseal access cover is bolted onto the tank with a torque of 17 m-N (150 in.-lb_f). The tank is moved to the vacuum chamber for a cold leak check, the chamber pressure is lowered to 2.3×10^{-5} torr, and the tank is partially filled with LN₂ until the tank assembly is essentially at LN₂ temperature. The tank is then pressure drained with helium and the pumping port on the vacuum chamber is monitored for helium with a helium mass spectrometer leak detector.

No leaks were detected over an hour's time so the test was terminated. The tank is allowed to warm up to ambient temperature, at which time the chamber is back-filled with air.

The tank is removed from the pallet, the struts are removed, and the tank is rested on a foam pad; the upper vacuum jacket is installed. The tank is picked up with an overhead crane and a chain is attached to four clips bolted to the access cover. The lower vacuum jacket is installed and the final closure flanges are held together by spring clamps (Step C). The overlap joints are soldered followed by tack-welding and soldering of the flanges per the methods described in Section 4. The jacket is pressurized to 149 N/m² (0.022 psi) with helium and then leak checked. Leaks in the flanges are repaired using copper strips soldered with 50/50 Pb/Sn solder over the top of the flanges. Leaks at the flange/overlap interface are soldered using copper foil repair patches and 50/50 Pb/Sn solder. Leaks at the overlap joints are repaired using 50/50 Pb/Sn solder fillets and, in one case, a copper foil soldered patch. The lower melting 50/50 Pb/Sn solder is used to prevent breaking the 95/5 Sn/Ag solder joint already made.

The alignment of the jacket on the tank is checked before the compressed spring assemblies are released in incremental steps. Wedges 1 and 2 appeared to be overexpanded following the spring release. The jacket is locally pulled out at each spring location with tape to allow the spring to seat properly. A preheated soldering tool is then pressed against the jacket for approximately 15 s at each spring location to flow the solder on the pre-coated surfaces. The tool is removed and the jacket surface is cooled for approximately 30 s with an air gun. The attachment of the jacket to the spring assembly is checked by pulling on the jacket surface using a calibrated extension spring scale attached to the jacket with tape. All of the springs attached properly at the panels with stiffeners. However, 22 of the panels did not attach at the panels with the welded joints. Waviness of the jacket at the joint prevented good mating of the soldered surfaces. Overall, 86 percent of the spring assemblies attached properly, ensuring good structural support of the jacket. The Kevlar strands that previously held the springs compressed are then pulled out through the top of the jacket and the Teflon spacing blocks removed.

Measurements of the jacket diameter were made at different spring assembly locations to allow calculation of the standoff distance from the tank. At the equator, measurements showed the spring assemblies "bottomed out." This compression will cause the equator springs to thermally short out.

Therefore, rectangular pieces of load bearing rigidized silica fiber (LI 900) were inserted between the jacket and the tank next to the equator spring assemblies to provide the proper spacing and allow the equator springs to expand.

The blocks are held in place by a brass screw inserted through the jacket and piercing the insulation block. The screw is soldered to the jacket.

In future designs, setting wedge dimensions so the jacket expands uniformly with pressure would solve this problem at the equator.

Sleeve end fittings are spun form for the six available fiberglass struts and welded to machined rod end adaptors (Step S). On three of the struts, a thermocouple

feedthrough tube is welded in the adapter flange area. A "bicycle spoke" type spacer is fabricated and assembled to the strut with Kevlar filaments as the "spokes." This low heat leak spacer keeps the strut centered in the jacket sleeve at the cold end. Rod-end adapters are also machined for the cold end of the struts. The adapters and rod ends are screwed into the struts; chromel constantan thermocouples are bonded along the length of three of the struts. The wires are stripped of their insulation and covered with epoxy where they pass into the feedthrough tube. After the epoxy cures, the leads are epoxy potted into the feedthrough tube.

The vacuum jacket strut access cylinder flanges are spun form, the two sleeves brazed to the box, and the joints leak-checked. Holes for the brass screws are drilled in the flange-to-jacket joint using a master template. The inside of the cylinder, the jacket flange and 10 cm (4 in.) inside the sleeves are electrolytically gold coated. The jacket flange on the strut cylinder is then solder coated.

In Step D, the strut access assemblies are bolted to the jacket using brass screws (already soldered to the jacket) plus brass nuts. The flange plus screws and nuts are soldered using rosin flux and the joint leak checked by pressurizing the jacket. The struts are then installed in the sleeves and the rod ends bolted to the tank. A doubler is installed inside the warm sleeve end fitting of the strut and the fitting is welded shut. The joints are leak checked by bagging the end of the sleeve with helium and pulling a partial vacuum inside the sleeve connected to a sniffer on the leak detector.

The lower plumbing assembly (Step P3), which has been brazed together and leak checked, is bolted to the pallet along with the six struts. The overhead crane is disconnected from the access cover. Access cylinder number one was touching the tank along the left edge of the box. This condition is caused by an improper angle on the box flange which forced the jacket into the tank. The condition was corrected by bonding a Kevlar strand to the box and tying the strand to the fiberglass leg, pulling the box flange away from the tank.

The test article is vacuum-baked out prior to filling the vacuum annulus with microspheres to remove the rosin flux used in jacket repairs. The test tank with the installed vacuum jacket (mounted to a pallet with six fiberglass struts) is installed in a vacuum chamber. An aluminum box enclosure with black interior surfaces is installed around the test article. Electrical heaters, mounted to the outside of the five walls plus the pallet, are connected to Variac voltage controllers. The pallet is insulated from the supporting chamber I-beams using four nylong pads. The chamber is pumped down to .013 Pa pressure and the heaters turned on. Hot nitrogen gas is also passed through the tank interior to bring the tank up to temperature. The chamber pressure rose to a maximum of .12 Pa while the test article was brought up to 77°C (170°F) over a period of a day. The test article was held at this temperature for 3 days, at which time the chamber pressure had nearly leveled out at .007 Pa. The heaters were turned off and after one day the chamber was back-filled with dry nitrogen. The chamber pressure had dropped to .002 Pa prior to the gas back fill.

The jacket openings plus the plumbing connections are closed off after the test article is removed from the chamber. The microsphere transfer container is raised to a vertical position and the microspheres fluidized using dry nitrogen gas. The six strut sleeves and lower third of the vacuum jacket are filled with microspheres through the strut cover openings using the fluidizing transfer technique described in section 4.2.4. The three strut covers are welded in place. The remainder of the vacuum jacket is then nearly filled with microspheres through the doughnut opening in the top of the jacket. The tank is tipped to different angles and the pallet is vibrated at low frequencies to aid in settling the microspheres. The doughnut shaped enclosure is welded into the top of the vacuum jacket and the insulation is topped off with microspheres through the fill port with the tank at different angles. The microspheres are hand poured and tamped with a rod the size of the fill tube to complete the fill.

A fabric covered screen is installed using a snap ring followed by an O-ring sealed cap. The microsphere fill went smoothly; the fluidizing technique worked well in transferring the microspheres.

It was noted after the fill that the jacket bent inward around one of the strut covers and one wedge was damaged, apparently due to a clamping procedure used during the welding of the strut cover. X-rays showed the jacket does not thermally short out against the tank. The damaged wedge still flexes sufficiently to allow for adequate jacket movement. It is of interest to note x rays are not sensitive enough to detect the position of the microsphere insulation in the jacket.

The jacket was evacuated slowly over a period of about 0.5 hr, and the wedges were examined for damage. No wedge damage was noted.

Leak-checking of the jacket uncovered one leak at a brazed plumbing fitting and multiple pin hole leaks on the solder final closure joint flanges where they had been tack-welded together. One leak was found in a jacket weld repair area and at a welded closeout at the warm end of one strut. The solder and braze joint leaks were repaired by applying Epibond 123/96510 epoxy adhesive over the pinholes with a 1-atmosphere pressure differential across the jacket (to push the adhesive into the hole). The weld leaks were repaired with Crest 7450, A and B, polyurethane adhesive. Following the fourth pumpdown of the jacket while leak-checking was in progress, partial buckling of some of the wedges surrounding the strut cylinders was noted. This buckling apparently occurred due to the flow of microspheres from the jacket bulk (where the microspheres are loaded in compression) into the rigid strut covers (where the microspheres could still shift if a void is present). Consequently, the jacket was forced slightly inward around the struts. The bottom cone also buckled inward. The buckles were pulled out using tape. The leak checking was stopped and additional microspheres were added to these areas to prevent any further wedge damage. The damaged wedges do not leak and still expand properly.

The external surface of the vacuum jacket was instrumented with chromel-constantan thermocouples. The thermocouples are bonded to the jacket with a conducting epoxy adhesive (silver filled). Connectors (to mate with leads from the vacuum chamber feedthroughs) are attached to the thermocouple leads. Instrumentation leads from the inside of the tank were epoxy potted in an exit tube. A helium mass spectrometer

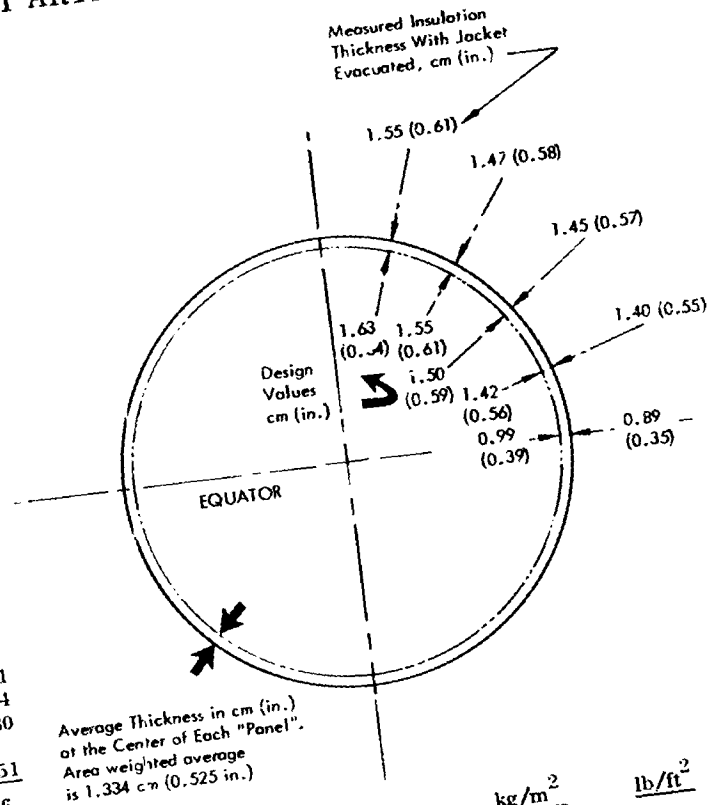
leak check found the jacket to be leak tight. Measurements were made on the width of all 165 wedges with the jacket evacuated. The weight and thickness of the installed insulation system is shown in Table 5-1.

The following conclusions and recommendations resulted from the work in this Task:

- The resistance seam-welding technique is a highly reliable and reproducible joining technique for obtaining vacuum tight joints as demonstrated by only one leak in 23.2 m (76 ft) of welds on the test article vacuum jacket.
- The 0.08 mm (0.003 in.) thick stainless-steel vacuum jacket has no pinhole leaks in the raw stock nor has developed any subsequent leaks due to the stretch and hydropress forming operations.
- The soldered final closure joint was difficult to join and repair. Leak tests at 149 Pa (0.6 in. of H₂O) pressure differential, which showed the jacket to be leak tight initially, were not sensitive enough. At 10⁵ Pa (1 atmosphere) pressure differential, numerous leaks were detected. The final closure joint design should be changed in future programs to an overlap welded joint of the same type used for joining the gore panels.
- The doubler at the warm strut end closeout should be resistance welded to the flange and the strut sleeve normal to the the material thickness. This procedure increases the weld width minimizing the chance of leakage.
- Pumpdown to 1.3 Pa took approximately 6 hr from 1-atmosphere pressure. Lower pressures were obtained in the test program by cryo-pumping action of the tank during LN₂ fill. To obtain more rapid pumpdown below 1.3 Pa, higher flow conductance filter screens and larger flow areas should be used.
- The wedges should be designed using the equations from section 4.1.8 so the hemisphere expands uniformly on the radius with increasing pressure. Overexpansion of the wedges at the equator would not occur during assembly (as occurred with the test article).
- The rigid cover welded on the strut cylinders plus the cone at the lower pole should be replaced in future designs with a thin convoluted metal diaphragm.

Table 5-1
WEIGHT AND THICKNESS OF TEST ARTICLE INSULATION SYSTEM

	kg	lb
Vacuum Jacket		
Top Hemisphere		
• Screen Filters	0.086	0.190
• Vacuum Port	0.293	0.646
• Pressure Port	0.031	0.068
• Fill Port	0.070	0.154
• Rigid Dome Area	0.477	1.052
• Jacket With All Joints	1.334	2.94
• Epoxy/Gold	0.045	0.10
Subtotal	2.34	5.15
Lower Hemisphere		
• Screen Filters	0.011	0.025
• Plumbing Connection	0.014	0.030
• Cone	0.327	0.720
• Jacket With All Joints	1.35	2.98
• Epoxy/Gold	0.045	0.10
Subtotal	1.75	3.86
Assemblies Enclosing Struts		
• Cylinder + 2 Sleeves (3 each)	3.88	8.55
• Cylinder Cover (3 each)	0.245	0.541
• Screws, Nuts, Solder	0.038	0.094
• "Bicycle Spokes" (6 each)	0.059	0.130
• Warm End Closeout (6 each)	0.068	0.151
Subtotal	4.29	9.46
Tank Related Parts		
• Epoxy/Gold	0.091	0.20
• Spring Assemblies + Epoxy (165 each)	0.643	1.418
Subtotal	0.73	1.62
Microspheres		
Total	5.53	12.19
	14.64	32.28



	kg/m ²	lb/ft ²
Weight/Area for Sealing		
Jacket With Wedges and Joints	0.620	0.127
Epoxy/Gold Coating	0.010	0.002
Coarse Filter Screen	1.95	0.40
Fine Filter Screen	0.44	0.09
Spring Assemblies With Epoxy, Long, Each	3.96 g (0.009 lb)	
Spring Assemblies With Epoxy, Short, Each	2.19 g (0.005 lb)	

When the insulation is evacuated, the diaphragm would move inward compressing the microspheres in the cylinder or cone, preventing the microsphere migration noted previously. Separate fill ports on each of the strut cylinders is also recommended to visually verify the microsphere fill level.

- Pretinning of the jacket is required for solder attachment of the spring assemblies.
- The fluidizing technique is a rapid, efficient method for filling the jacket with microspheres.

Section 6
ENVIRONMENTAL AND OPERATIONAL TESTS

A series of tests were performed on the insulated, vacuum-jacketed tank to characterize its thermal performance as a function of boundary temperatures, compressive load, insulation gas pressure, and simulated Space Tug flight cycles. From these data, predictions can be made on the system's thermal performance when used on a Space Tug during ground hold and ascent, and in space. The required vacuum level for optimum performance plus the effect of a gas leak were determined by varying the insulation gas pressure. Jacket vacuum levels, jacket vacuum integrity, plus microsphere packing and shifting, if any, of the microspheres were also determined during the tests. Nineteen simulated flight cycles were planned for the program, but the testing was stopped after 13 cycles because of jacket damage caused by operator error during a leak repair.

This section provides a description of the test article, instrumentation, and setup; the test procedures used; plus the test results and discussion of results.

6.1 TEST ARTICLE

The article tested is described in Section 5; Fig. 6-1 shows it mounted on the vacuum chamber door. Concentric fill and vent lines, thermally guarded with a wrap-around LN_2 heat-exchanger tube, enter the tank through a top-mounted access cover. The insulation pumpout port is routed through the chamber door and back into the chamber with appropriate valves so the insulation can be either evacuated by the chamber, evacuated with a separate pumping station, or back-filled with gas, depending on the test sequence.

The aluminum pallet is insulated thermally from the chamber I-beam supports on four nylon pads. The test article is enclosed within an aluminum box shown in Fig. 6-2.

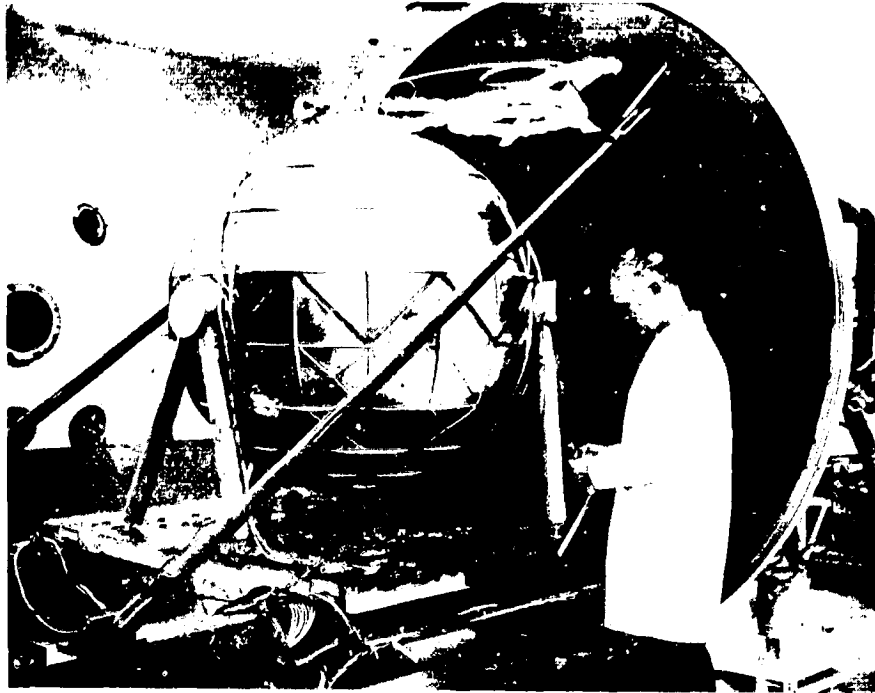


Fig. 6-1 Test Article Mounted on Vacuum Chamber Door

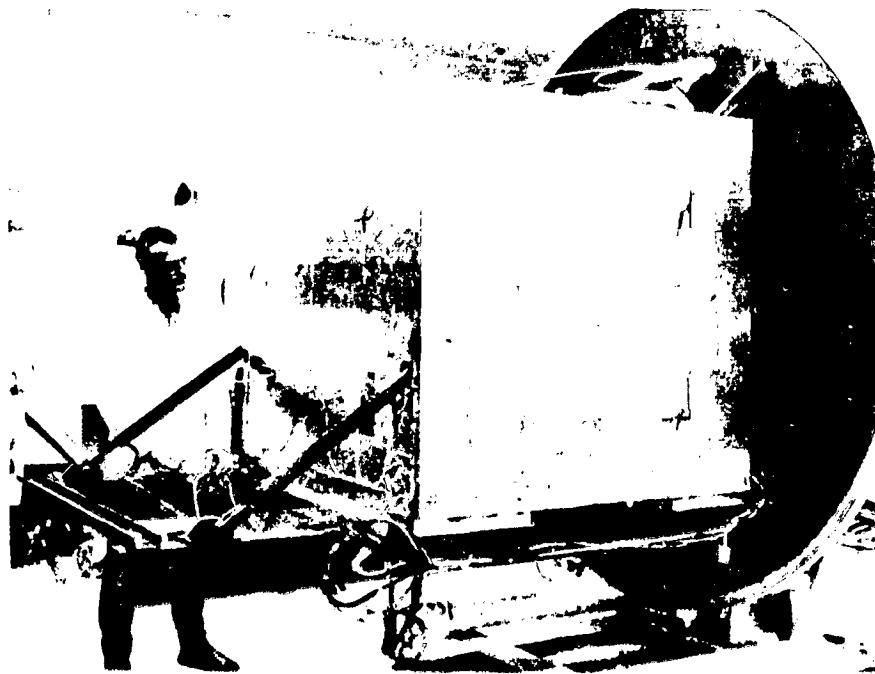


Fig. 6-2 Warm Boundary Temperature Control

6-2

REPRODUCIBILITY OF THE
OPERATIONAL PROCEDURE

LOCKHEED PALM DALTO RESEARCH LABORATORY
LOCKHEED, PALM DALTO, A LOCKHEED COMPANY, INC.
A SUBSIDIARY OF LOCKHEED AIRCRAFT CORPORATION

Four electrical heaters are located on each of the six sides. Warm boundary temperatures are controlled using these thermostatically controlled heaters; for the lower warm boundary temperature tests, the chamber LN₂ cold wall is used in conjunction with the heaters.

Thermostatically controlled heaters are also epoxy-bonded to the tank instrumentation feedthrough and the O-ring sealed insulation pumpout port. These heaters maintain these areas near ambient temperature, preventing thermal cycling and possible gas leakage.

6.2 INSTRUMENTATION

A summary of the instrumentation and data acquisition equipment used in the tests is presented in Table 6-1.

The primary instrumentation for the test tank is designed to measure temperature levels throughout the test article assembly, insulation pressure, and heat rate to the cryogen for accurate assessment of system thermal performance. Supporting instrumentation is also provided for measuring environmental simulation conditions and jacket mechanical motion.

6.2.1 Temperature

Test article thermometry is composed of platinum resistance thermometers (PRT) and thermocouples for absolute temperature measurements and differential thermocouples for gradient measurements. Carbon resistance thermometers are employed for cryogen level measurements. Locations of this instrumentation are shown in Fig. 6-3.

All thermocouples are 0.008 cm (0.003 in.) diameter chromel-constantan with Teflon insulation. This thermocouple was selected because of its high sensitivity and low thermal conductivity of both elements, this being of particular importance for thermal tempering of the junctions at the low temperatures. For differential thermocouples,

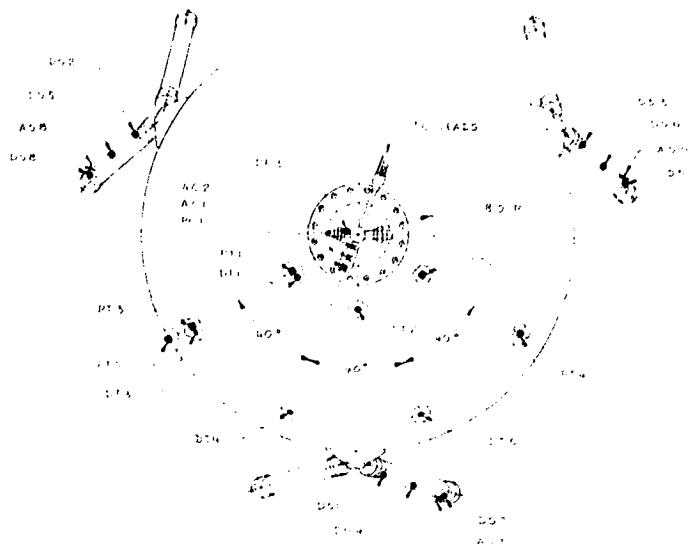
Table 6-1
INSTRUMENTATION AND DATA ACQUISITION EQUIPMENT

Function	Instrumentation	Measurement Range	Accuracy
Pressure, Tank Ullage and Barometric	Texas Instruments, Inc., Model 140 Fused Quartz Bourdon Tube Precision Pressure Gage	$0-1.8 \times 10^5$ Pa	3.5 Pa
Pressure, Vent Gas-Variable Area Meter	Wallace & Tiernan, Series 1500	$0-1.4 \times 10^5$ Pa	90 Pa
Pressure, Vacuum Chamber	Wallace & Tiernan, FA 145	$0-1.1 \times 10^5$ Pa	170 Pa
Pressure, Vacuum Chamber	NRC Series 810 Thermocouple Gage	0-133 Pa	-
Pressure, Vacuum Chamber	Varian Model 841 Autoranging Ionization Gage	5×10^{-8} to 13 Pa	1% + 1 digit
Pressure, Insulation Annulus	Varian Ionization Gage	1.3×10^{-5} to .6 Pa	-
Pressure, Insulation Annulus	Varian Model - Ion Pump	1×10^{-6} to 1×10^{-2} Pa	2 on Decade Range
Pressure, Insulation Annulus	Thermocouple Gage, Veeco DVIM	.7 to 133 Pa	-
Pressure, Insulation Annulus	Alphatron Model 520 Pressure Transducer	10^{-2} to 10^5 Pa	-
Space-Hold Boiloff	Precision Scientific - Wet Test Meter	$0-1.68 \text{ m}^3/\text{hr}$ ($59 \text{ ft}^3/\text{hr}$)	$\pm 1/2\%$
Ground-Hold Boiloff	Fisher & Porter No. 1017354 Variable Area Flow Meter	$0-25 \text{ m}^3/\text{hr}$ ($883 \text{ ft}^3/\text{hr}$)	$\pm 1\%$ Full-Scale
Tank Temperature	Rosemount Engineering 118G Platinum Resistance Thermometer, Calibrated	78-300°K (140-540°R)	0.1°K (0.2°R)
Temperature	Thermocouple of Chromel-Constantan, Calibrated	78-333°K (140-600°R)	0.5°K (0.9°R)
Vacuum Jacket Wedge Movement	Brown and Sharp Micrometer	0-2.5 cm (1 in.)	0.0025 cm (0.001 in.)
Data Acquisition	Honeywell Data Processor	0-0.01 V dc 0-750 V dc	0.05% Range or 5 μ V
Data Acquisition	Leeds Northrup Speedmax W, A2AR 10 - in strip chart recorders	0-100 MW dc, 5 ranges	0.3% Range

FOLDOUT FRAME

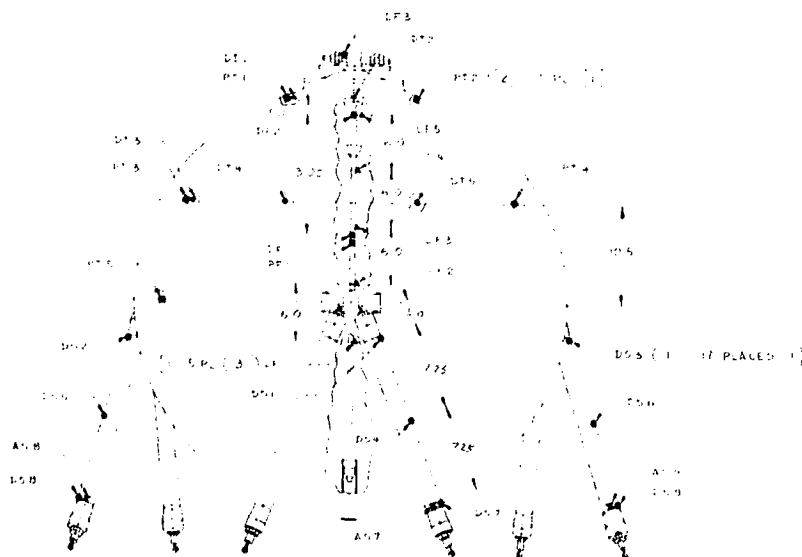
LEGEND

SYMB.	TR	DESCRIPTION
■	A	ABSOLUTE TEMPERATURE CHROMEL - CONSTANTAN T.C.
●	D	DIFFERENTIALLY CONNECTED CHROMEL - CONSTANTAN T.C.
■	P	PLATINUM RESISTANCE THERMOMETER.
▲	L	CARBON RESISTOR
□	B	ACCESS BOX
□	C	COVER, TANK
□	F	FILL TUBE
□	J	JACKET, VACUUM
□	S	STRUT
□	T	TANK
□	W	WEDGE
○	H	FEED THRU HEATER



TABLE

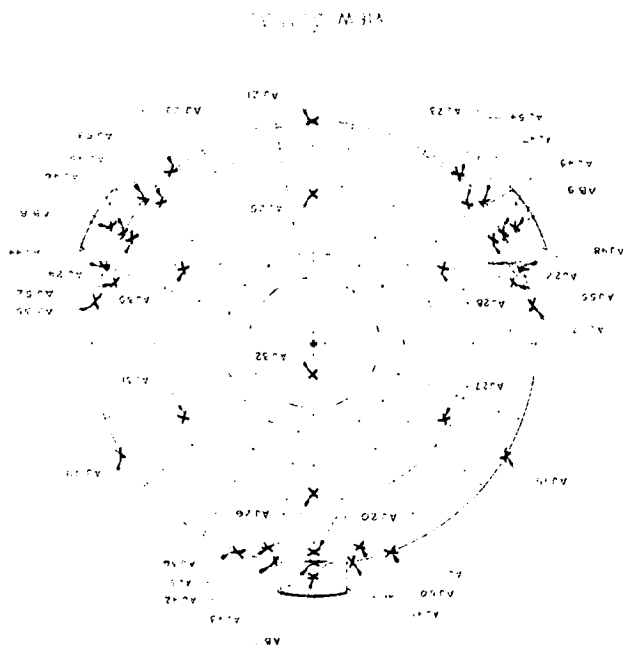
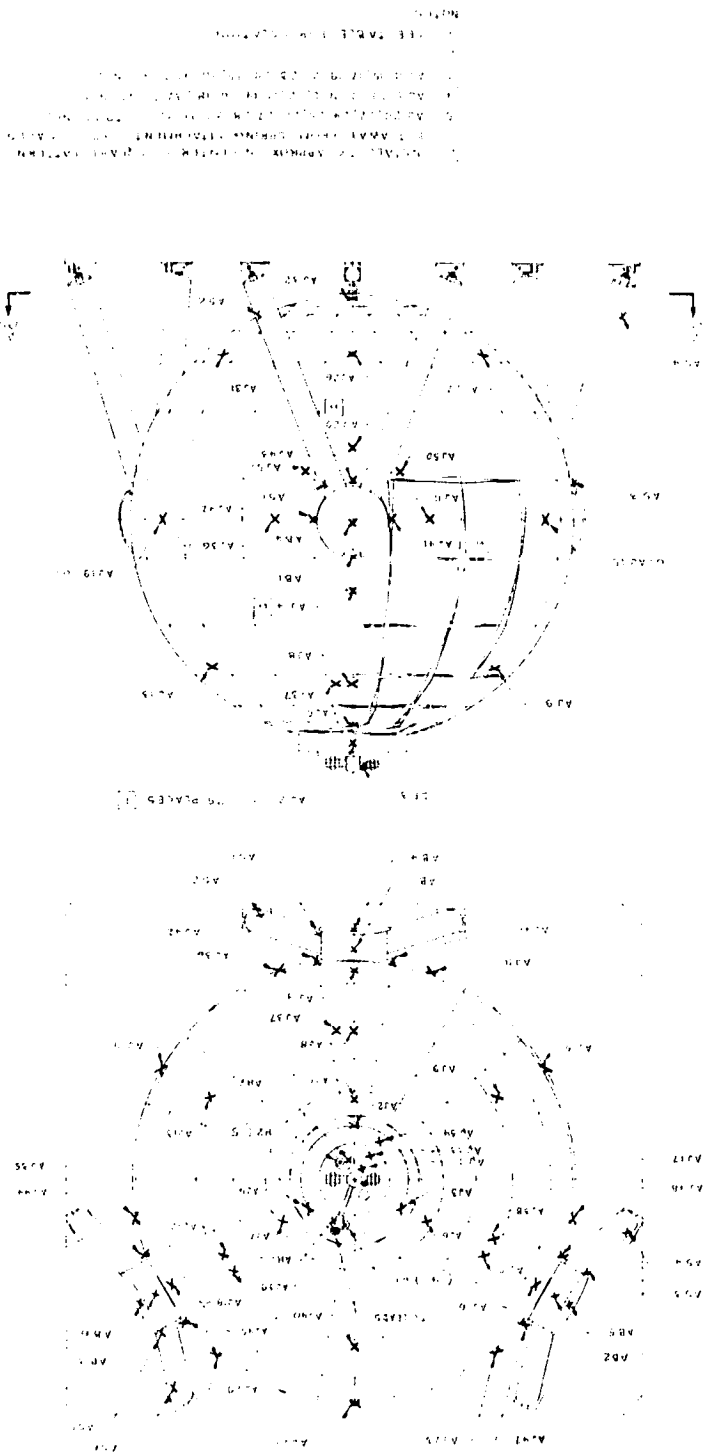
ID. NO.	LOCATION	QTY
A11, 33 & 34	VAC JACKET POLAR CAP	1
A22 TO A24	VAC JACKET NECK	3
SEE NOTE B	VAC JACKET ATOM	18
SEE NOTE A	VAC JACKET UPPER DOME	15
SEE NOTE B	VAC JACKET LOWER DOME	14
AB103, 103	ACCESS BOX CYLINDERS	6
AB4 TO AB6	ACCESS BOX COVERS	3
AS1 TO AS6	STRUT VAC JACKETS	6
AS7 TO AS9	STRUTS	3
AH1 & 2	FEED THRU HEATER	2
WI & 2	HEATER	1
DF1 TO DF2	FILL TUBE	2
DF3	FILL TUBE	1
DT1 TO DT4	TANK WALL	5
DT1 TO DT5	STRUTS	5
DT1 TO DT1	TANK WALL	5
DT1	TANK COVER	1
FF	FILL TUBE	1
LF TO LF5	FILL TUBE	5
	EXTERNAL VACUUM JACKET	17
	INSIDE TANK	19



REPRODUCIBILITY OF THE ORIGINAL PAGE IS POOR

TEST AND INSTRUMENTATION

Fig. 6-3 Test Article Instrumentation



2

INSTRUMENTATION

the chromel elements are brought to the reference junction to minimize errors at the juncture with the copper lead wires to the data acquisition system. Thermocouple junctions are attached to the surfaces with a silver-filled epoxy adhesive,* and the leads are taped parallel to the surface for 3 cm (1.2 in.) using Kapton tape. Differential thermocouple junctions are attached with an electrical insulating epoxy**, and the leads secured to the surface at 5-cm (2-in.) intervals with the same adhesive.

Seven Rosemount Engineering Company Model 118G 100-ohm platinum resistance thermometers are used for tank wall and plumbing-line temperature measurements. Each PRT is calibrated at fixed points to yield an accuracy of 0.1°K (0.2°R) in absolute temperature measurement between 78 and 300°K (140 to 540°R). These devices are used as four-wire thermometers at a constant current of 3-mA dc. Each thermometer is bonded to the surface with epoxy adhesive, and the 0.013-cm (0.005-in.) copper current and potential leads are attached to the surface for a distance of 4 cm (1.6 in.) from the thermometer. A precision current shunt is in series with each thermometer current leg for measurement of individual thermometer currents. Power dissipation in the seven thermometers was a maximum of 0.6 mW total.

Five carbon resistors are located along the fill tube [spaced approximately 1 cm (4 in.) from the tube] to serve as liquid level sensors. These resistors are connected in series, and potential leads across each resistor provide a voltage signal that is proportional to the resistor temperature. For the self-heating value of these resistors, the difference in heat transfer coefficient between a liquid and a gaseous cryogen environment results in a voltage change adequate for level sensing. The level sensor has a maximum heat input to the cryogen of 50 mW (0.17 Btu/hr) and, as this input is known to within 2 mW (0.007 Btu/hr), uncertainty in system performance introduced by this device is negligible.

All instrumentation leads within the cryogen volume exit the tank through an epoxied feedthrough with thermal grounding at the LN_2 guard coil on the vent-fill entrance

*No. 3021 E solder, Acme Chemicals and Insulation Co.

**Epibond 123, Furane Plastics, Inc.

fitting to the tank. The calculated maximum lead wire heat leak into the tank is 15 mW (0.05 Btu/hr) for continuous operation of the LN₂ guard. The strut sensor instrumentation leads are bonded around the circumference of the strut at each measuring location for thermal tempering.

6.2.2 Pressure

The pressure measurement instrumentation is for

- Tank ullage and barometric pressure monitoring
- Insulation pressure
- Environmental simulation chamber pressure

Initially, tank ullage pressure was to have been controlled to 3 Pa using a differential pressure transducer, set point pressure control unit, servo-valve, and an electronic/signal-conditioning unit together with a constant pressure reference. However, the system did not control pressure as designed. After repeated unsuccessful tries to correct the problem, tank pressure control was eliminated. Variations in tank pressure are calculated to affect the boiloff measurement accuracy less than 6.7 percent for the space-hold tests and progressively less for the other tests with higher heat rates (based on measured variations in tank pressure).

Measurement of tank ullage and barometric absolute pressure is made with a quartz bourdon tube gage (Texas Instruments 140A with No. 2 tube). This device has an accuracy of 3.5 Pa at tank operating pressure. In operation, the gage is manually nulled for reading of absolute value, and deviation from the prior reading is recorded by monitoring meter deflection.

Insulation pressure is measured by two thermocouple gages, two ion gages, one ion pump, and one alphasatron gage as shown in Fig. 6-4. These gages allow pressure measurements from 10^5 to 10^{-5} Pa at both the bottom and top of the vacuum jacket. A pump current versus pressure calibration curve is used to measure pressure with the ion pump.

6-9

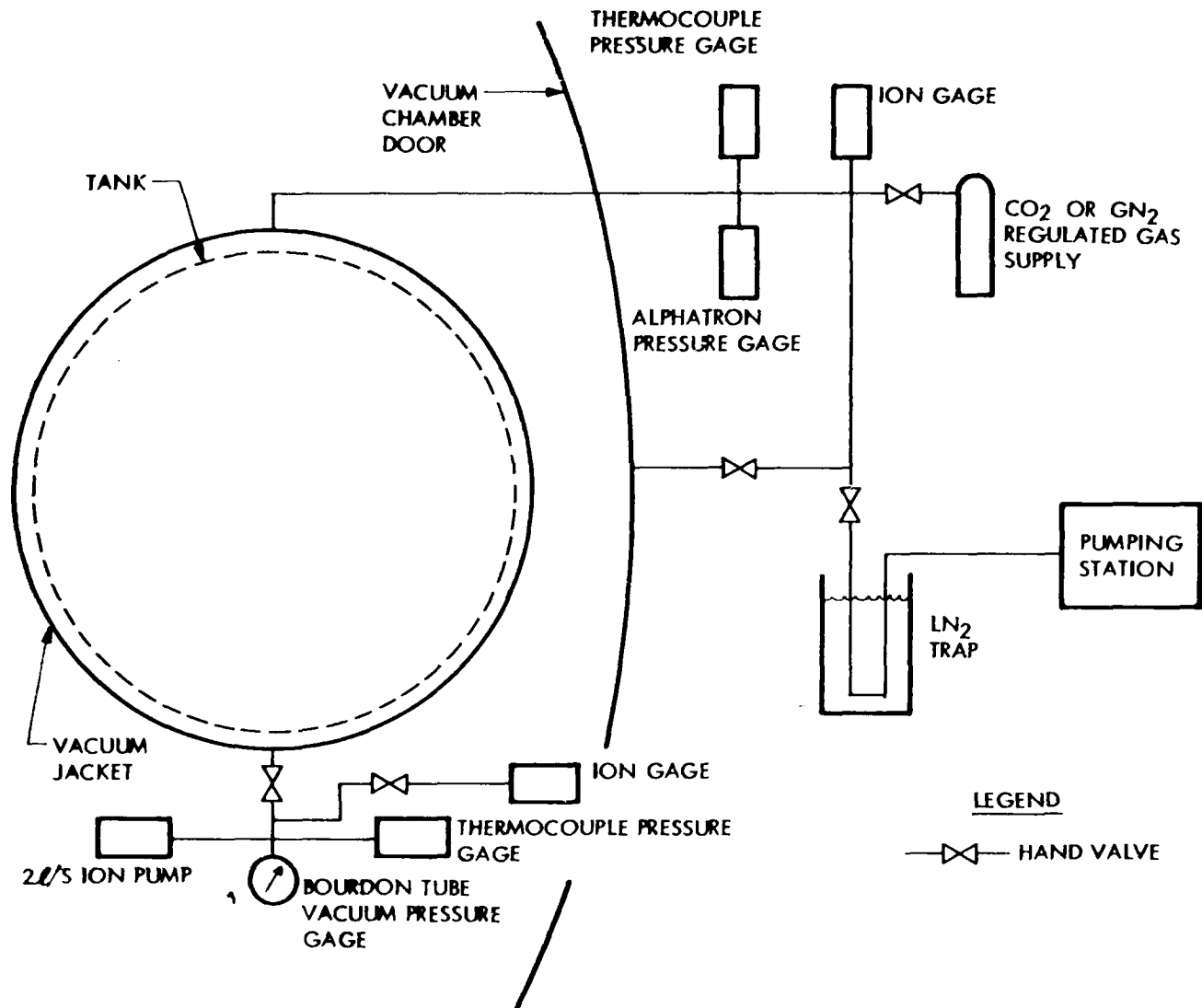


Fig. 6-4 Vacuum-Jacket Pressure Measurement and Control

Environmental chamber pressure is measured by bourdon tube, thermocouple, and ionization gages calibrated for the appropriate pressure ranges. Cryogen fill, vent line, and environmental shroud fluid pressures are measured using standard laboratory bourdon tube gages.

6.2.3 Tank Boiloff

The test-article cryogen boiloff instrumentation is shown in Fig. 6-5. During filling and ground-hold thermal performance evaluations, the cryogen volumetric boiloff is measured with a variable area flowmeter which accommodates the relatively high-volume flow rates associated with this operation. Visual recording of flow rate is carried out during these relatively short duration operations. Boiloff during space thermal performance testing is measured with a calibrated wet test meter. The wet test meter, with automatic recording of each full revolution, is used as the total boiloff measurement for heat-flux computations. Gas temperature and pressure upstream from each flow-measuring device is measured with thermocouples and bourdon tube pressure gages, respectively, after the gas has passed through a temperature-regulated water bath.

6.2.4 Jacket Deflections

Based on experience obtained with the vacuum-jacket expansion measurements made in Task II, relative vacuum-jacket movement is monitored by bonding small reference screws on each side of all wedges of the vacuum jacket. The amount the jacket moves locally is determined by the amount each wedge opens or closes as measured by a dial gage micrometer. The spring/Kevlar attachments keep the jacket spacing constant off the tank wall at the attach points so relative movement of the jacket with respect to the tank can only occur in the wedges.

All wedge dimensions are measured with the insulation evacuated prior to start of the tests. During the test series, selected wedges on opposite sides of the jacket are measured with the insulation evacuated.

6-11

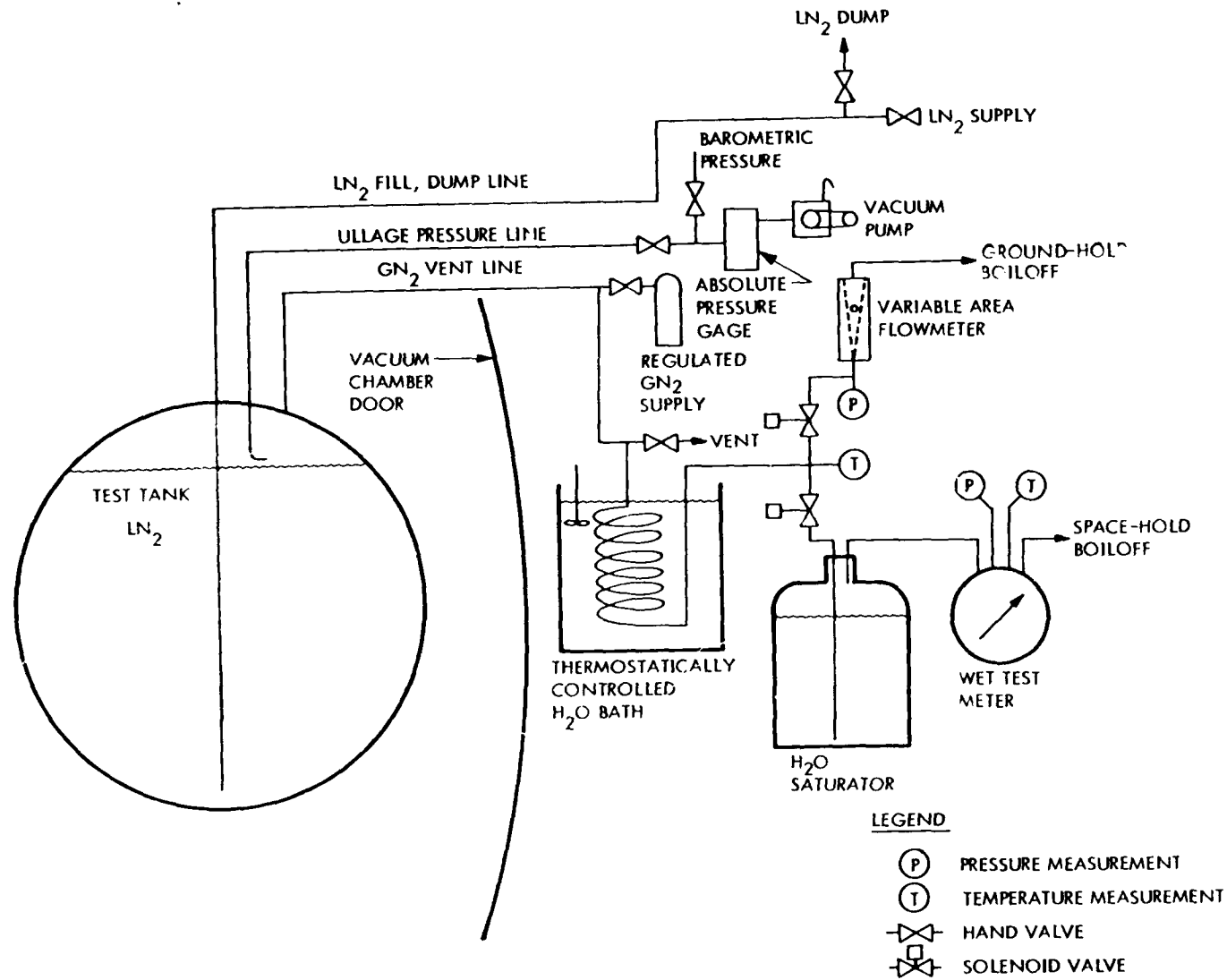


Fig. 6-5 Test Tank Fill, Dump, Vent, and Boiloff Instrumentation

6.3 TEST SETUP

The vacuum-jacketed microsphere insulated tank was tested in a space environmental simulation chamber. The chamber, 2.45 m (8.04 ft) diameter by 4.57 m (15 ft) long, is of the horizontal cylinder configuration having removable end domes from which experimental packages are mounted. This mounting arrangement provides for easy access and complete checkout of the test article and instrumentation prior to movement into the vacuum chamber.

The chamber is equipped with an LN₂ cold shroud. Chamber pumping is accomplished with roughing and turbine pumps. Ultimate chamber pressure with the test article installed is in the mid 10⁻⁴ Pa range. Chamber operation is through automatically controlled sequencing of functions, and the system is provided with safety controls in the event of pump or shroud failures.

Boiloff instrumentation and pressure readout equipment are shown in Fig. 6-6. Test article and chamber operation data are collected on strip-chart recorders and the Data Processor Terminal shown in Fig. 6-7. The Terminal inputs are scanned, measured by a digital voltmeter, and outputted as printed format and punched paper tape. The scanner is activated at preselected intervals by a crystal digital display clock. The system accuracy is 0.05 percent full scale, which corresponds to 5 μV for thermometry signals. Recorded data are computer-processed for temperature from thermocouple and resistance thermometer voltages.

6.4 TEST PROCEDURE

The test program was designed to investigate the effect of the following variables on insulation system thermal performance:

- Warm boundary temperature for both ground-hold and space-hold conditions
- The effect of compressive load on the jacket from 0 to 1 atm
- The effect of GN₂ pressure in the insulation from .013 to 4 Pa pressure

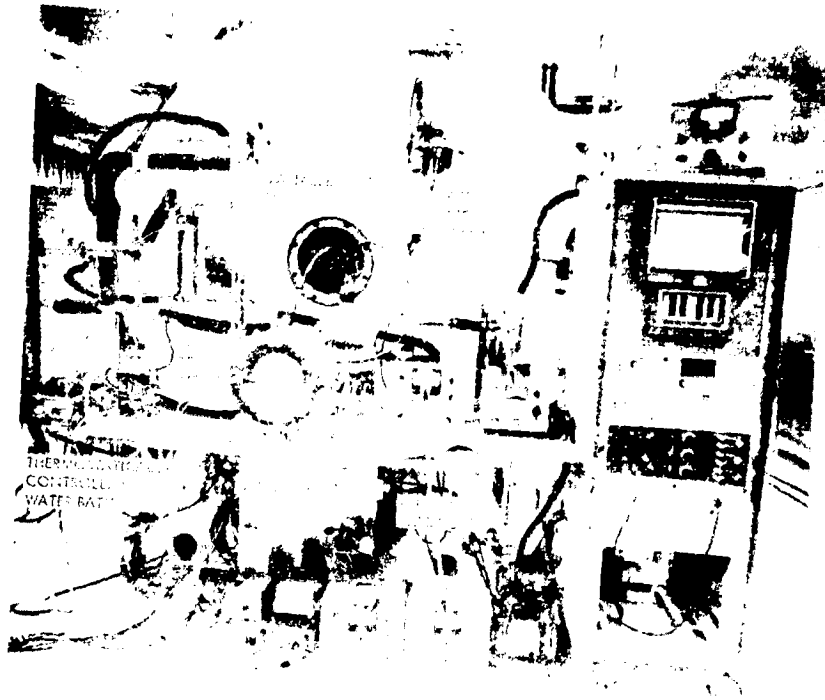


Fig. 6-6 Chamber Test Setup

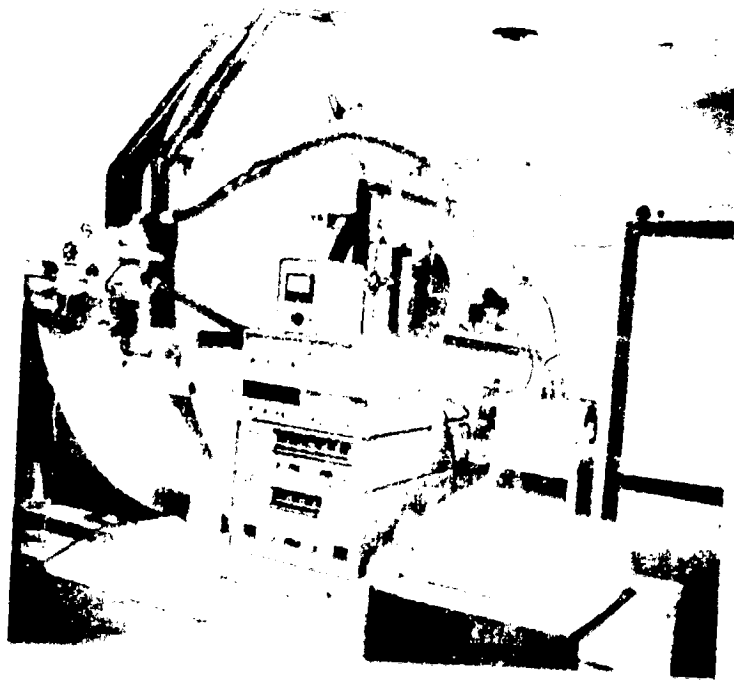


Fig. 6-7 Data Processor Terminal

- The effect of simulated flight cycles on thermal performance (Each cycle simulates a Space Tug flight of propellant loading on the ground, propellant drain in orbit, atmospheric reentry, and tank warmup to ambient conditions on the ground.)

The cold boundary for all tests is 78°K (140°R).

6.4.1 Ground-Hold Thermal Performance

This test sequence is started with the chamber at 9×10^4 Pa pressure of GN₂ and ambient temperature and the insulation pressure 1.3 Pa or lower of 99.99-percent CO₂. (For safety reasons, the chamber door cannot be bolted on; therefore, in order to maintain a good seal, less than 1-atm chamber pressure is required.) The tank is cooled down to LN₂ temperature with cold nitrogen gas. Liquid nitrogen fill is then started and maintained until a steady liquid level is achieved. Cryopumping reduces insulation pressure to < .013 Pa. The fill line is shut off, and cryogen boiloff recorded at 5-min intervals until equilibrium conditions have been achieved for 60 min, as indicated by boiloff constant within 1 percent, and jacket and tank temperatures constant to within 1°K (2°R). The jacket is maintained at $270 \pm 5^\circ\text{K}$ ($486 \pm 9^\circ\text{R}$) for the first test and $290 \pm 5^\circ\text{K}$ ($522 \pm 9^\circ\text{R}$) for the second test.

6.4.2 Space-Hold Thermal Performance

At the conclusion of ground-hold testing, the chamber pressure is reduced below .0013 Pa with the test tank still filled with LN₂. Boiloff, chamber, jacket, and tank pressures, and tank and jacket temperatures are monitored until equilibrium conditions are achieved for 8 hr [1-percent stability of boiloff and 1°K (2°R) of temperatures]. The initial test condition is for a jacket temperature of $310 \pm 5^\circ\text{K}$ ($558 \pm 9^\circ\text{R}$). After completion of this test phase, the liquid level is brought to the full condition, and testing is repeated at jacket temperatures of $280 \pm 5^\circ\text{K}$ ($504 \pm 9^\circ\text{R}$) and $250 \pm 5^\circ\text{K}$ ($450 \pm 9^\circ\text{R}$). At the conclusion of these tests, the LN₂ is emptied

from the tank, and the chamber is brought to 9×10^4 Pa GN_2 pressure and ambient temperature. The cryogen space is vented until the article is uniformly at ambient temperature.

6.4.3 Thermal Performance as a Function of Jacket Compressive Load

To date, the only compressive-load-effects data for uncoated microspheres have been derived from flat plate calorimeter tests using a flexible diaphragm-type of insulation container. At loads below 1000 Pa, accuracy has been compromised by uncertainties in the effective load area of the insulation containment device used for the flat-plate calorimeter. As the test article vacuum jacket is designed to exert pressures of less than 100 Pa, it is essential to further study these loading effects in the design operating region on the actual test article. These data also serve to verify the theoretical model in the region where self-load and externally applied compressive load effects are of comparable magnitude.

With the vacuum chamber at 9×10^4 Pa pressure and the insulation annulus at a pressure of 1.3 Pa of CO_2 or less, the tank is loaded with LN_2 . The chamber is pumped down to less than .0013 Pa pressure, and equilibrium boiloff rates are determined for a vacuum jacket temperature of $275 \pm 5^\circ\text{K}$ ($495 \pm 9^\circ\text{R}$).

These initial data provide a baseline value for evaluating changes in heat transfer with increasing compressive pressure. Vacuum chamber pressure is changed successively to 10, 100, 1000, 10,000, and 9×10^4 Pa using GN_2 , and equilibrium boiloff rates are measured for each chamber pressure with a jacket temperature of $275 \pm 5^\circ\text{K}$ ($495 \pm 9^\circ\text{R}$). The final test is with the vacuum chamber at .0013 Pa or less to evaluate recovery from loading.

6.4.4 Thermal Performance as a Function of Insulation Pressure

The objective of this test sequence is to determine the heat transfer by conduction through an insulation interstitial gas phase. These results will (1) verify the predicted

insulation annulus vacuum requirement (.013 Pa) for operational conditions and (2) demonstrate system thermal performance for conditions of atmospheric leakage into the insulation space. Gaseous N_2 is selected to be representative of the predominant species that would be present because of air leakage. The experimental results from this investigation are used to correlate the theoretical model for gas-phase conduction for system performance analysis over the total operational temperature range.

With the test article mounted in the vacuum chamber at 9×10^4 Pa pressure, and the insulation annulus at a pressure of 1.3 Pa of CO_2 or less, the tank is loaded with LN_2 . The chamber is pumped down to less than .0013 Pa, and equilibrium-boiloff rates are determined for a vacuum jacket temperature of $265 \pm 5^\circ K$ ($477 \pm 9^\circ R$). The insulation pressure is then increased to .13, .53, 1.07, 2.7, and 4 Pa with GN_2 . Equilibrium boiloff rates are obtained at each pressure level.

The pressures are chosen to define the onset of gaseous conduction and shape of the curve characteristic for a Knudsen number greater than 10 - i.e., free molecular regime. This pressure range defines the characteristic void dimension and effective accommodation coefficient necessary for correlation with the gas conduction model.

6.4.5 Thermal Performance Following Simulated Flight Cycles

To determine the effect of thermal/pressure flight cycles on system thermal performance, one ground-hold and one space-hold boiloff test are conducted after 3, 7, and 13 flight cycles. After 19 cycles, one ground-hold and two space-hold tests complete the sequence. Because of the jacket damage that occurred, tests were completed after 3 and 7 flight cycles only.

A flight cycle starts with a chamber pressure of 9×10^4 Pa, the insulation at 1.3 Pa or less of CO_2 , and the tank at ambient temperature. Following tank LN_2 fill, the

chamber is pumped down to less than .013 Pa, the LN_2 is dumped in 1 hr, and the chamber pressure is brought up to 9×10^4 Pa of GN_2 . The aluminum box shroud temperature is maintained at $300 \pm 5^\circ K$ ($540 \pm 9^\circ R$). After 48 hr, the tank is back to ambient temperature. This sequence completes one flight cycle. The ground-hold and space-hold tests are conducted as discussed previously with the shroud temperature held at $300 \pm 5^\circ K$ ($540 \pm 9^\circ R$). Before the initial flight cycle, jacket wedge dimensions are measured and recorded. At the completion of 3, 7, and 13 cycles, the dimension measurements were repeated before the jacket damage occurred.

6.5 TEST RESULTS

The results of the test article environmental and operational tests are discussed in five subsections covering the following:

- Test article thermal performance as a function of vacuum jacket temperature, external compressive loading of the vacuum jacket, insulation interstitial gas pressure, and resistance to thermal degradation by repeated simulated flight cycles
- Mechanical strength and packing of the microspheres as a function of the number of external compressive load cycles
- Post-test tank and jacket emittance measurements and tank/jacket spacing measurements around the strut attach points (for use in the thermal model)
- Separate test of the microsphere self-weight contact force (for use in the thermal model)
- Evacuation rate of the insulation and vacuum integrity of the jacket

6.5.1 Thermal Performance

A summary of the thermal test results is provided in Table 6-2. The heat rate values from the table are plotted as a function of the average jacket temperature for ground-hold and space-hold tests in Figs. 6-8 and 6-9. Also included on the figures are the

Table 6-2

SUMMARY OF TEST RESULTS

Test	Chamber Pressure Pa	Insulation Pressure Pa	Jacket Temperature ^(a)		Heat W	Rate (Btu/hr)
			°K	(°R)		
Ground Hold	9.13×10^4	< .013	290.6	(523.1)	342	(1167)
Ground Hold	9.13×10^4	1.07	268.2	(482.7)	269	(917)
(b)	9.13×10^4	< .013	268.2	(482.7)	260	(887)
Space	9×10^{-4}	< .013	306.5	(551.7)	59.6	(203.5)
Space	7×10^{-4}	< .013	279.6	(503.3)	44.2	(150.7)
Space	1×10^{-3}	< .013	244.0	(439.3)	29.8	(101.8)
Comp. Load ^(c)	< .0013	< .013	274.0	(493.2)	41.5	(141.5)
Comp. Load	12.8	< .013	278.9	(502.1)	42.6	(145.4)
Comp. Load	102	< .013	277.7	(499.9)	43.8	(149.6)
Comp. Load	986	< .013	272.9	(491.2)	61.4	(209.6)
Comp. Load	9.7×10^3	< .013	264.5	(476.1)	107	(365)
Comp. Load	9.13×10^4	< .013	277.0	(498.6)	290	(989)
Comp. Load	< .0013	< .013	274.0	(493.2)	41.7	(142.4)
Gas Pressure	< .0013	< .013	268.0	(482.4)	39.0	(133)
Gas Pressure	5×10^{-4}	.13	267.6	(481.7)	45.8	(156.2)
Gas Pressure	5×10^{-4}	.65	267.0	(480.6)	46.6	(159.1)
Gas Pressure	9×10^{-4}	1.0	268.2	(482.7)	48.1	(164.3)
Gas Pressure	8×10^{-4}	2.96	260.1	(468.2)	58.8	(200.5)
Gas Pressure	8×10^{-4}	4.05	258.4	(465.1)	63.8	(217.6)
Ground Hold, 3 cycles	9.12×10^4	< .013	278.3	(500.9)	295	(1006)
Ground Hold, 7 cycles	9.08×10^4	< .013	277.8	(500.1)	290	(990)
Space, 3 cycles	.027	< .013	288.8	(519.9)	49.3	(168.4)
Space, 7 cycles	.032	< .013	287.7	(517.9)	51.9	(177.2)

- (a) Average of 40 jacket temperatures. $T_c = 78^\circ\text{K}$ (140°R).
 (b) Gas conduction subtracted from above test results for comparison with insulation at pressure of less than .013 Pa.
 (c) Data interpolated from prior test results (Fig. 6-9) to obtain temperature identical with that for last data of test series.

△ FOLLOWING 3 THERMAL/PRESSURE CYCLES
 □ FOLLOWING 7 THERMAL/PRESSURE CYCLES

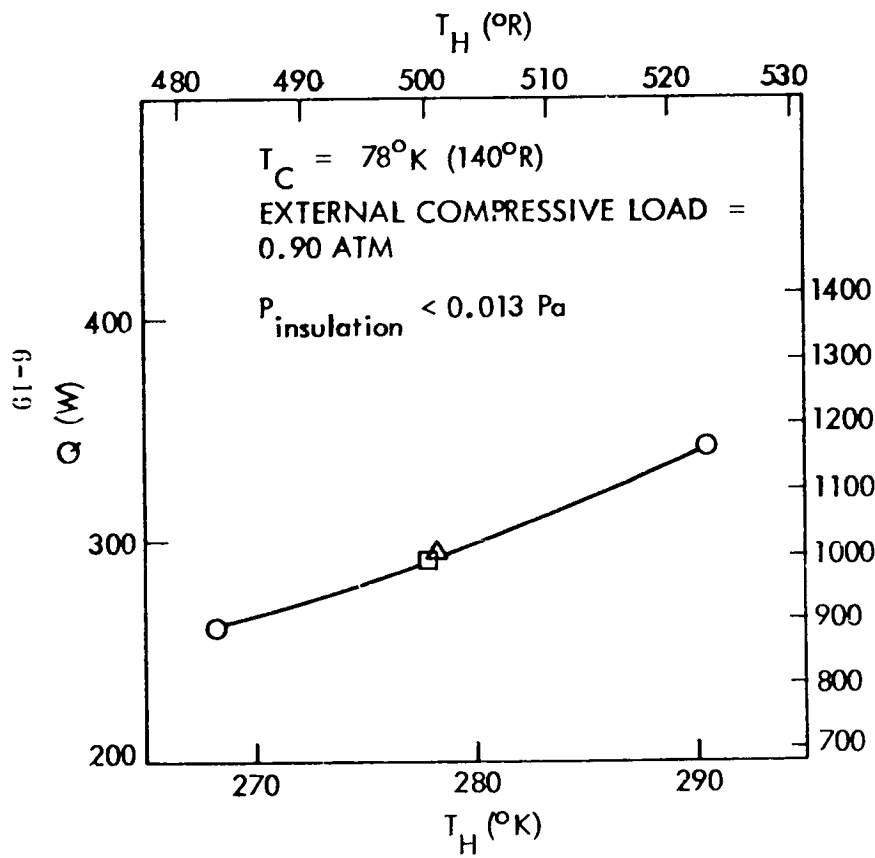


Fig. 6-8 Ground-Hold Heat Rates

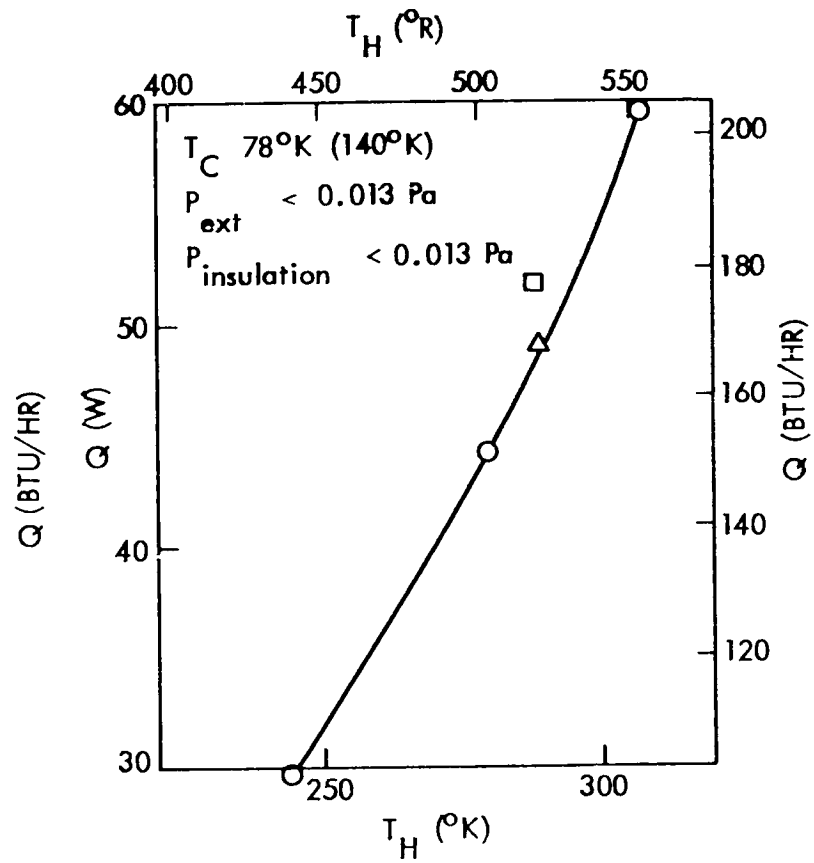


Fig. 6-9 Space-Hold Heat Rates

data points for repeat thermal tests following three and seven thermal/pressure cycles. No thermal performance degradation due to the cycling was observed from the ground-hold results. Space-hold performance was unaffected by three cycles. After seven cycles, however, an apparent heat rate increase of 7 percent was measured. As discussed in section 6.6.7, this higher rate is attributable to experimental uncertainty rather than an environmentally induced degradation of thermal performance.

Measured temperature distributions along the fiberglass tank struts for the space-hold tests are compared to calculated values in Fig. 6-10. The measured values are used to compute the heat leak to the tank through the tank supports. These data show much shorter struts can be used without materially affecting the already low strut-heat-leak rates.

The effect of insulation interstitial gas pressure on heat rate is plotted in Fig. 6-11. The deviation of the test point at .13 Pa from the smoothed curve is believed to be due to inaccuracy in the pressure measurement for this single case. The pressure was measured at the top of the insulation only for this test as the bottom jacket ion gage malfunctioned. Also, a very small leak developed in the tank access cover region allowing nitrogen gas into the insulation. This leak rate was sufficiently slow, so the insulation could be kept evacuated to less than .013 Pa by continuous pumping for the other test series, but, for the gas pressure tests, the insulation space was isolated from the pumping system. The average insulation pressure is also probably higher than the .13 Pa measured at the top of the jacket because a low flow conductance screen, for containment of the microspheres, is placed between the insulation space and the pressure gage.

For the tests at higher insulation pressures, the effects of the leak and the screen on the average insulation gas pressure measurement should be negligible. During the other gas-pressure tests, the measured insulation pressure at the top and bottom of the jacket stayed constant within a few percent.

The effect of compressive pressure on the insulation heat rate is plotted in Fig. 6-12. The no-load heat rate was subtracted from the total heat rate to determine the effect

6-21

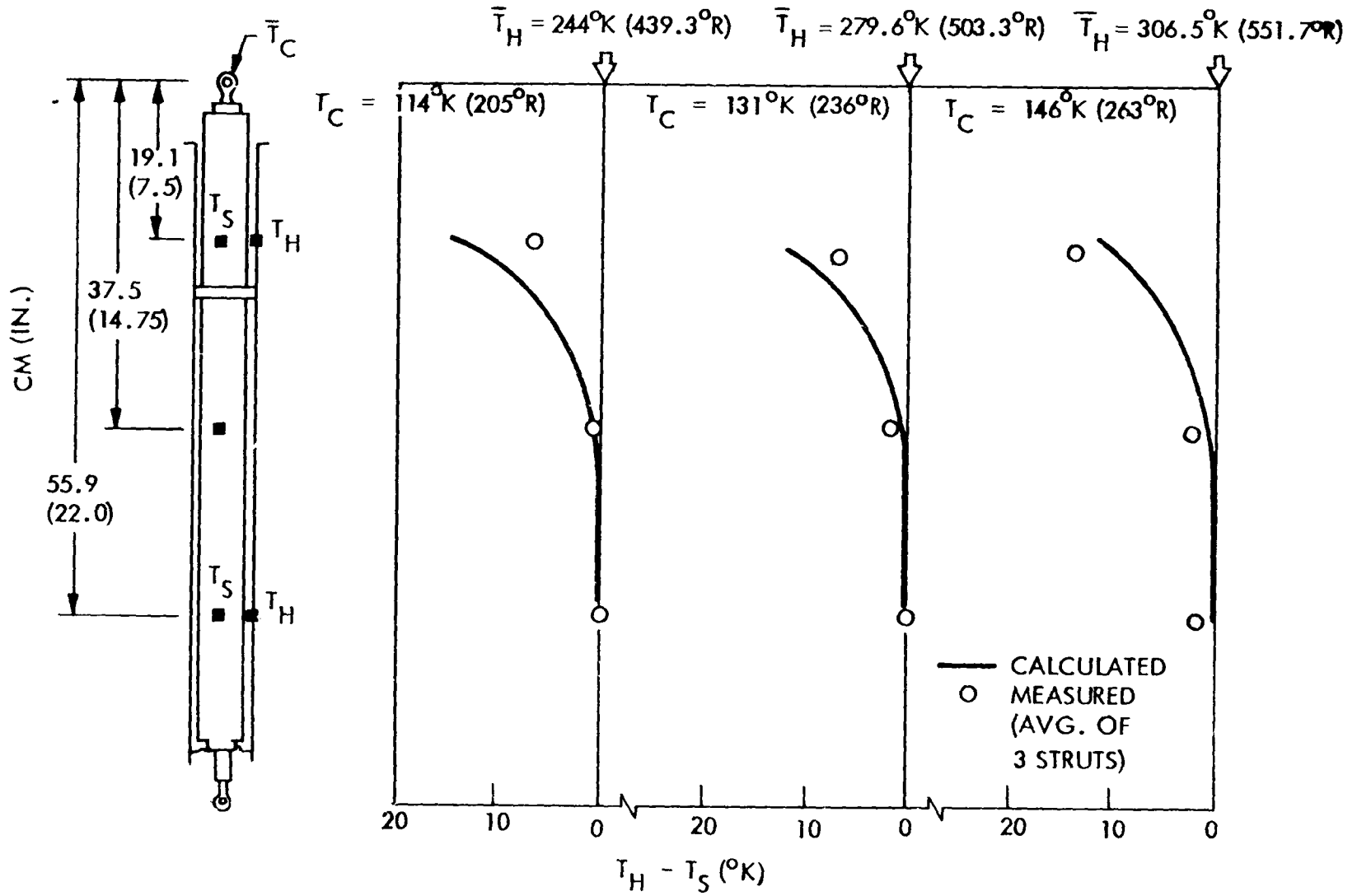


Fig. 6-10 Strut Temperature Profiles

6-22

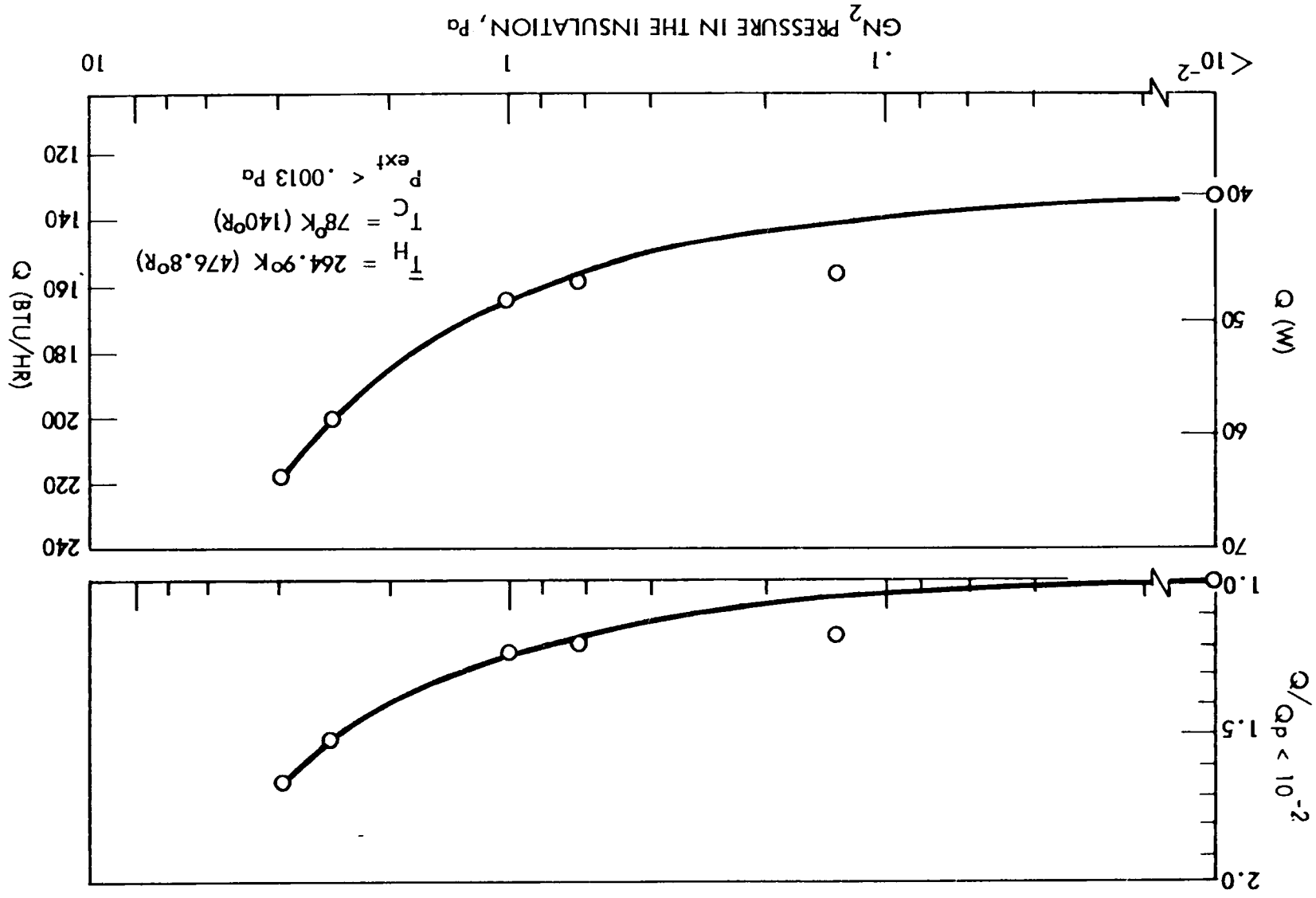


Fig. 6-11 Effect of Insulation Gas Pressure on Heat Rates

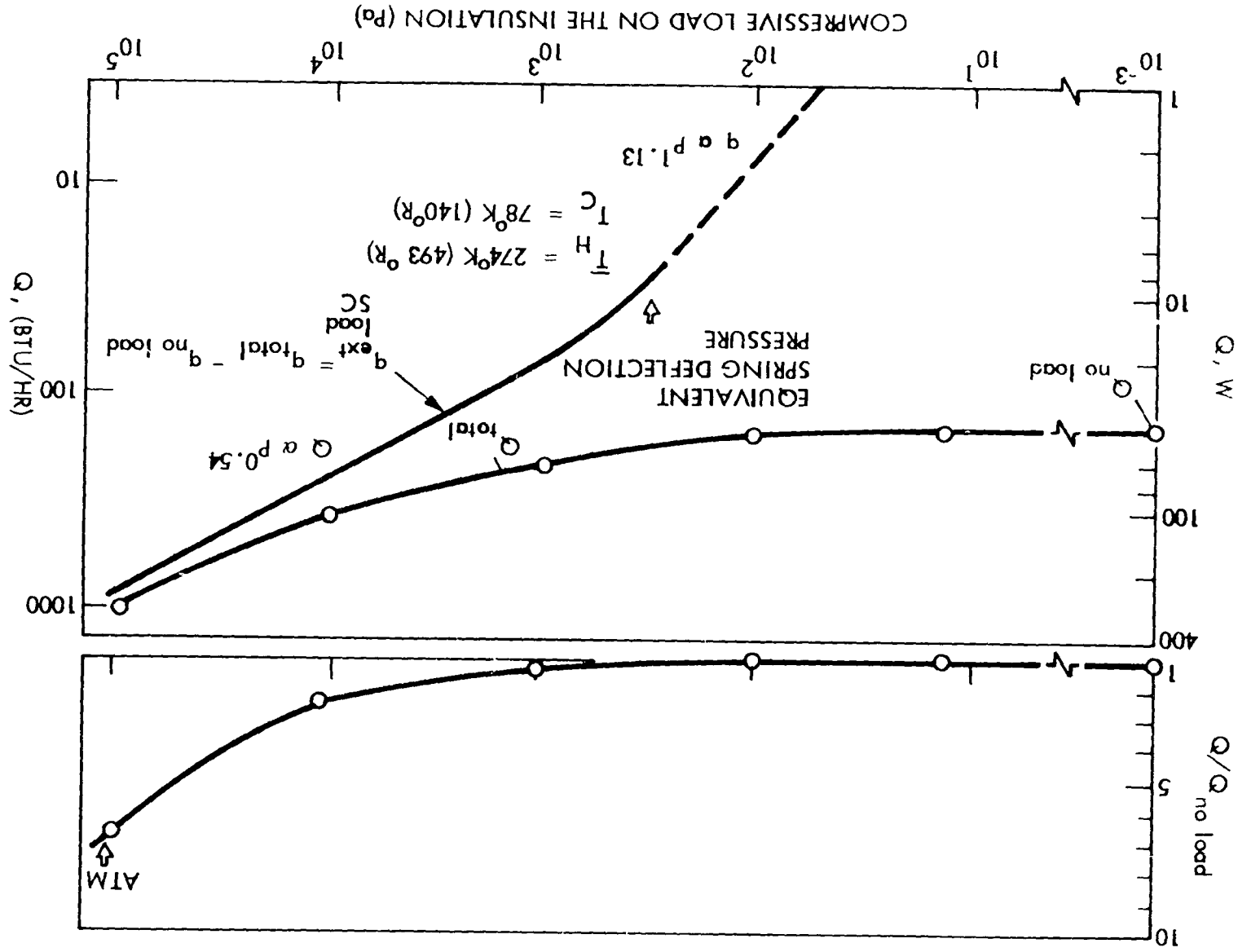


Fig. 6-12 Effect of Compressive Load on Heat Rates

6-23

of compressive load on thermal performance. Note the change in the slope of the curve in the region where the compressed spring assemblies start to deflect inward. (The equivalent spring deflection pressure is determined by dividing the load at which the springs start to deflect by the jacket area.) The $P^{0.54}$ relationship is a fundamental characteristic of the microsphere insulation, which describes the change in contact thermal resistance with increasing contact force. The region of the curve corresponding to a slope of 1.13 applies only to this particular jacket and spring geometry. The force, and subsequent contact resistance, is dependent not only upon the sphere packing geometry, but also upon the manner in which the load is transferred through the jacket to the insulation.

6.5.2 Mechanical Stability and Packing of Microsphere Insulation Under Load Cycling

The effect of repeated 1-atm load cycles on microsphere packing was determined by measuring the contraction of 55 wedges at different locations on the jacket. These results were then compared with previous test data taken in a flat-plate type of compression apparatus where the insulation thickness change was measured directly. Note in Fig. 6-13 the relatively good agreement between the two sets of data and the

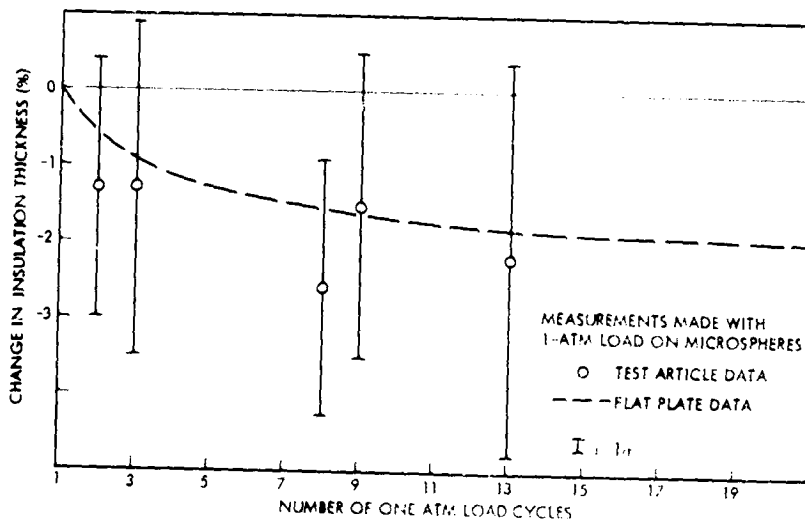


Fig. 6-13 Microsphere Packing as a Function of Load Cycles

fact that the packing had nearly reached its equilibrium value after 13 cycles. The change in packing occurs due to the particles rearranging themselves into a geometry having a higher solid fraction. The change in packing is not due to sphere breakage. Samples of microspheres were taken from 24 locations over the jacket and a broken particle count was performed. The results are compared with an equal number of counts from reference samples that were not subjected to repeated compressive loadings. The results below show no change in the percentage of unbroken spheres within the accuracy of the counting methods.

<u>% Broken Spheres</u>	
<u>Reference</u>	<u>Test Article</u>
9.5 ± 1.8	10.6 ± 2.4

No shifting of the microspheres occurred from one jacket area to another during the test program as determined by the wedge expansion/contraction measurements on different areas of the jacket.

6.5.3 Post-Test Emittance Measurements

Following 13 thermal/pressure cycles, the test article was removed from the chamber to measure jacket movement (wedge expansion/contraction) and to repair a jacket leak. A helium leak check of the jacket assembly isolated the leaks to the warm end of a strut and the soldered final closure joint. The strut leak was repaired but the final closure joint repair was attempted twice without success. Apparently the low viscosity Crest adhesive was pulled through the hole before it cured. To reduce the ΔP across the jacket, the insulation was to have been backfilled with CO_2 to a -10^4 Pa gage pressure. Inadvertently, however, the pressure was allowed to rise above atmospheric pressure, and the jacket overexpanded plastically. The damage was extensive enough to buckle the wedges as shown in Fig. 6-14 and prevent further testing of the jacket.

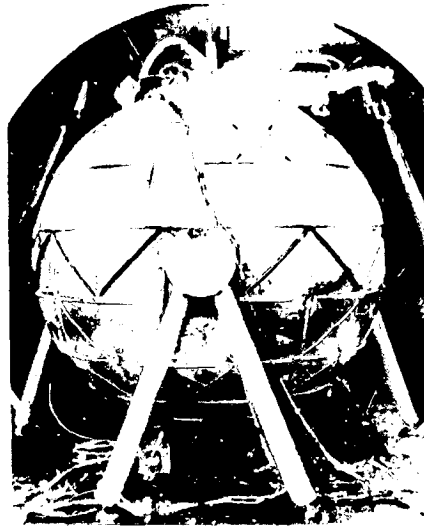


Fig. 6-14 Damaged Vacuum Jacket Caused by Accidental Overpressurization

Since the jacket was no longer usable, it was removed from the tank, and extensive emittance measurements were made on both the jacket and the tank (as shown in Table 6-3) to provide input data for the thermal model. No damage to the gold coating was observed on the jacket or tank (visually or under 40× magnification) except for some solder-flux-induced stains near the soldered final closure joint. However, the emittance values are higher than were measured on sample coupons made at the same time the gold coating was originally performed. None of the spring assemblies were damaged; all of them remained bonded to the tank and all Kevlar strands were intact. Measurements were made on the minimum clearance gap between the jacket strut cylinders and the tank surface to provide data for the thermal analysis. Table 6-4 shows the clearance was less than the minimum design value in a number of places. Whether the jacket overexpansion changed these clearances is not known.

6.5.4 Microsphere Self-Weight Contact Force

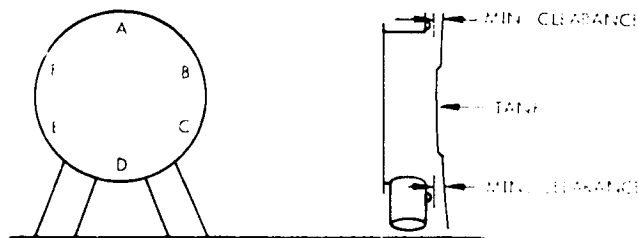
The "hydrostatic head" of a column of microspheres 0.30 m (12 in.) wide by 1.68 cm (0.66 in.) thick was measured as a function of height up to 1.17 m (46 in.) as shown in Fig. 6-15 to provide data in terms of the contact force due to self-weight for the solid conduction thermal analysis. The test was repeated using a thickness of 0.98 cm

Table 6-3
EMITTANCE MEASUREMENTS OF JACKET AND TANK AFTER 13 THERMAL/PRESSURE CYCLES

Item	Area m ² (ft ²)	No. of Measurements	ϵ_H ^(a)
JACKET			
Gold, Upper Hemisphere ^(b)	1.99 (21.38)	51	0.041 ± 0.017
Gold, Lower Hemisphere ^(b)	1.99 (21.38)	60	0.035 ± 0.004
Gold, Stain at Final Closure	0.006 (0.07)	3	0.203 ± 0.037 ^(c)
Gold, Inside Wedges at Stiffeners	0.22 (2.32)	9	0.393 ± 0.069 ^(c)
Weld Joints	0.12 (1.27)	30	0.110 ± 0.007 ^(c)
Solder Areas	0.11 (1.22)	30	0.149 ± 0.037 ^(c)
S.S. Spring Caps	0.07 (0.77)	30	0.146 ± 0.014 ^(c)
Filter Screens	0.03 (0.32)	3	0.360 ± 0 ^(c)
Area Averaged →			0.061
TANK			
Gold ^(c)	4.29 (45.19)	126	0.029 ± 0.003
Al Spring Caps	0.09 (0.99)	30	0.282 ± 0.036 ^(c)
Bolts, Bare Areas ^(d)	0.02 (0.20)	-	0.3 ^(c)
Area Averaged →			0.035

- (a) Measurements made with Gier Dunkle DR100 infrared reflectometer. Instrument calibrated so values approximate total hemispherical emittance.
 (b) $\epsilon_H = 0.028 \pm 0.003$ for coupons measured during gold coating procedure.
 (c) $\epsilon_H = 0.025 \pm 0.003$ for coupons measured during gold coating procedure.
 (d) Estimated. Inaccessible to measurement.
 (e) These values are relatively insensitive to temperature changes.

Table 6-4
CLEARANCE BETWEEN STRUT BOXES AND THE TANK



Strut Assembly	Minimum Clearance (mm)			
	A	B	C	D
1	1.02 (0.040)	0.80 (0.031)	0.80 (0.031)	0.80 (0.031)
2	1.27 (0.050)	0.80 (0.031)	0.80 (0.031)	0.80 (0.031)
3	1.27 (0.050)	0.80 (0.031)	0.80 (0.031)	0.80 (0.031)

(1) Not applicable to strut assembly 3.

(.039 in.) to cover the approximate range in thickness on the test tank. The force exerted by the microspheres on the bottom surface bar was measured using a transducer sensitive to 0.1 g. The apparatus was partially filled with microspheres, the pressure was measured, more microspheres were added, the pressure again was measured and so on until the apparatus was filled. The apparatus was emptied and the test was repeated several times. From Figs. 6-16 and 6-17, it can be seen that the measured pressure is less than that of an ideal liquid, with an equal density. Note that the pressure reaches a plateau, then rises abruptly to a higher plateau because of the bridging effect of the microspheres during each of the series of test measurements.



Fig. 6-15 Microsphere Self-Weight Test Apparatus

Also note the pressure rise is slightly less when the thickness is decreased. The upper limit of the pressure curves for the total number of test series was fitted empirically for use in the thermal model shown earlier in section 4.3. This equation was integrated with respect to height to provide the self-weight force exerted on the microsphere contacts going from the top (0 force) to the bottom (maximum force) of the jacket.

6.5.5 Vacuum Integrity and Evacuation Rate

The following general comments can be made regarding the performance of the system. Insulation pumpdown time to 1.3 Pa took approximately 6 hr as measured by the

6-29

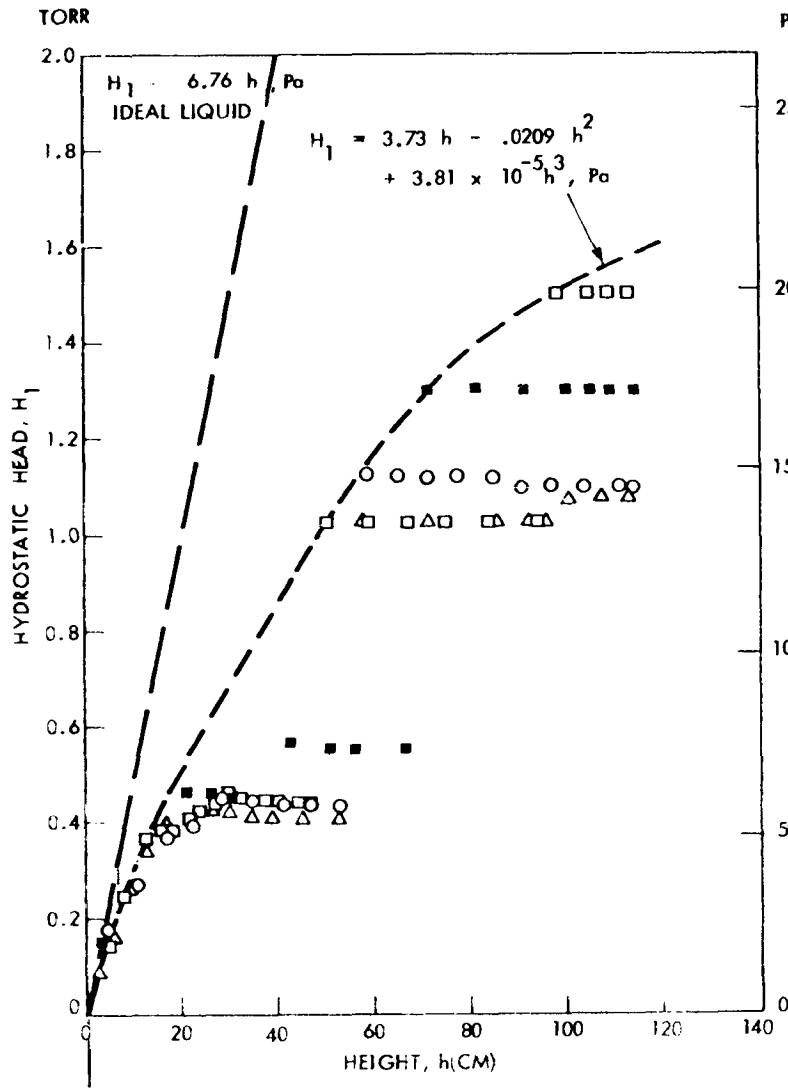


Fig. 6-16 Microsphere Self-Weight [$\delta = 1.69 \text{ cm}$ (0.66 in.)]

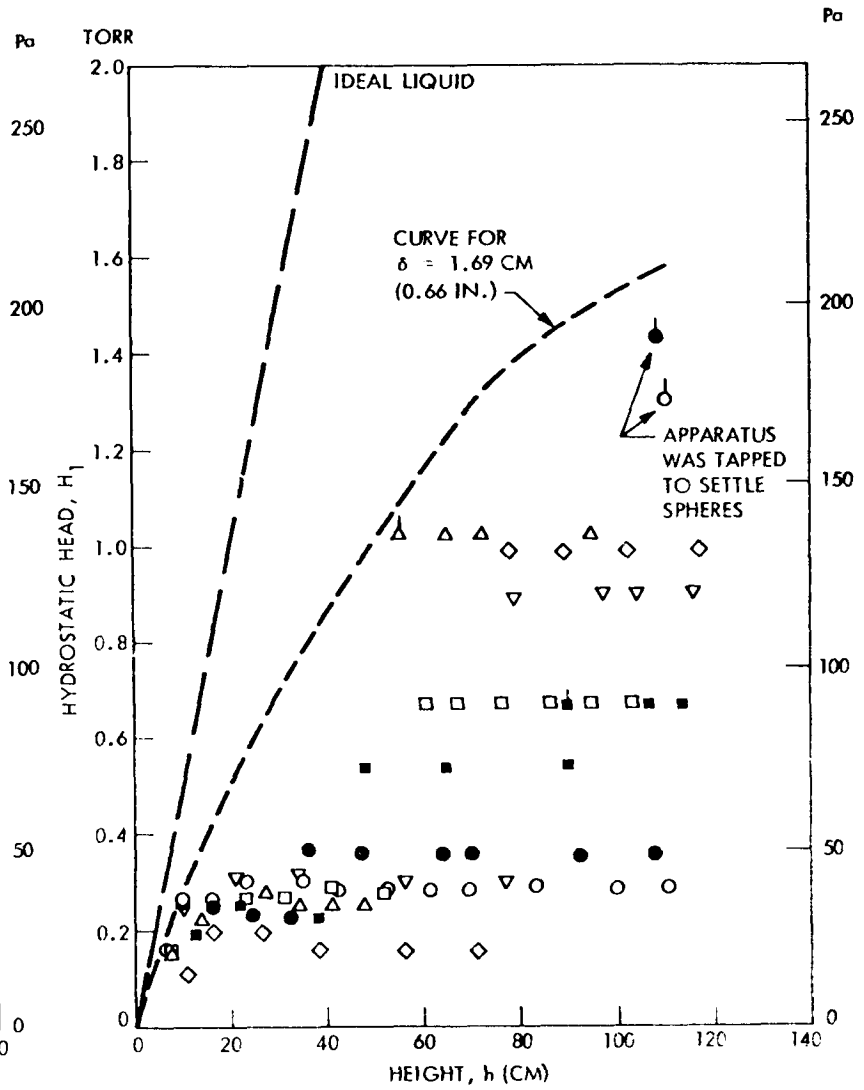


Fig. 6-17 Microsphere Self-Weight [$\delta = 0.98 \text{ cm}$ (0.39 in.)]

bottom jacket pressure sensors. The pressure dropped to less than .013 Pa within minutes following the start of LN₂ fill because of the cryopumping of the residual CO₂ gas. The minimum pressure in the insulation with a 1-atm load on the jacket was .0027 Pa torr at the top and 10⁻⁴ Pa at the bottom of the jacket. These pressures were limited more by the speed of the pumping systems and the low level tank leak rate than the vacuum integrity of the jacket. In fact, no leaks occurred after 13 thermal/pressure cycles in:

- 23.2 m (76 ft) of welded joints
- 4.5 m² (48 ft²) of jacket membrane
- Wedges (including several damaged ones)
- Stiffeners

Leaks did occur in the soldered final closure joint and at the warm ends of the struts.

The jacket expanded and contracted elastically as designed and showed no discernible change in its visual appearance following 13 thermal/pressure cycles.

6.6 DISCUSSION OF TEST RESULTS

An analytical thermal model was developed to predict insulation heat transfer as a function of temperature, compressive load, and interstitial gas pressure. Once the validity and accuracy of this model is established, it provides a tool for thermal design of full-scale cryogen insulation systems.

Methodology of model development is summarized in this section. Also, experimental data from section 6.5 are compared with analytical model thermal performance predictions in terms of boundary temperatures, compressive load, and insulation interstitial gas pressure.

6.6.1 Insulation Thermal Model

The model used to characterize thermal conductivity of microsphere insulation for this program (see section 4.3) is a derivative of an analytical expression developed

under prior LMSC Independent Research programs for heat transfer in packed beds of microspheres. This expression, in turn, is based on results of earlier theoretical and experimental studies (Refs. 6-1 through 6-13) of heat transport in packed beds of spheres. As the basic information leading to its development has appeared in the literature, only the major considerations are discussed here.

Definition of Terms. The terms used in the development of the model follow:

B	=	optical properties of the sphere boundaries, assumed to be gray
d_{gr}	=	microsphere diameter
E	=	compressive modulus
F', F'', F''', F^*	=	packing geometry factors of the bed
H	=	integrated microspheres self-weight
h	=	maximum vertical height of jacket
k	=	effective thermal conductivity
k_c	=	contact thermal conductivity
k_{cg}	=	sum of constriction and gas-phase thermal conductivity
k_g	=	$k_{go}/1 + 2\chi L/\delta_a$
k_{gc}	=	gas-conduction thermal conductivity
k_{go}	=	gas-thermal conductivity at standard conditions
k_{gs}	=	gas-thermal conductivity inside the sphere
k_{gr}	=	$k_s \{ 1 + [2m(1 - \nu)/(2\nu + 1)]/1 - [m(1 - \nu)/(2\nu + 1)] \}$
k_r	=	radiation thermal conductivity
k_s	=	thermal conductivity of glass
K	=	$1 - k_g/k_s$
l	=	insulation thickness
l_c	=	mean free path
m	=	void fraction
n	=	refractive index of microspheres

P	=	external compressive load
P_g	=	gage pressure
Pr	=	Prandtl number
q	=	heat flux
q_r	=	radiation heat flux
r	=	sphere radius
T_g	=	pressure gage temperature
T_H, T_C	=	absolute hot and cold boundary temperatures, respectively
V	=	sphere volume
x	=	thickness
α	=	accommodation coefficient
β	=	extinction coefficient of microspheres
γ	=	specific heat of gas
δ_a	=	$2md_{gr}/3(1 - m)$
ϵ_H, ϵ_C	=	gold coating boundary temperature total hemispherical emittance, metal to vacuum
θ	=	T_C/T_H
μ	=	Poissons ratio
ν	=	k_s/k_g
ρ_s	=	true sphere density
σ	=	Stefan Boltzmann constant
χ	=	$\frac{2}{\gamma + 1} \frac{1}{Pr} \frac{2 - \alpha}{\alpha}$

Analytical Considerations. The major heat-transfer mechanisms in packed spheres under evacuated conditions consist of the surface radiation transfer across the voids and the constricted conduction through the contact surface of packed particles. If a gas is present in the void space between spheres, a second conduction mechanism exists. For a medium with coupled conduction and radiation transport, it has been shown (Ref. 6-14) that the effective (or apparent) thermal conductivity k , defined in the Fourier law

$$q = -k(T) \frac{\partial T}{\partial x} \quad (1)$$

can be well approximated under most conditions as the linear summation of the conduction and radiation contributions

$$k(T) = k_{cg}(T) + k_r(T) \quad (2)$$

where $k_{cg}(T)$ is the additive sum of constriction and gas-phase conduction contributions. In particular, under optically thick conditions such as in most microsphere insulation applications, this summation procedure is an excellent approximation.

For packed solid spheres, the contact conductivity k_c can be expressed as (Ref. 6-9)

$$k_c = Fk_s [(1 - \mu^2)/E]^{1/3} (P)^{1/3} \quad (3)$$

for large compressive loads where P is the compressive pressure, and

$$k_c = F' k_s [(1 - \mu^2)/E]^{1/3} [(\rho_s V(t)/r^3)]^{1/3} \quad (4)$$

for conditions where the contact force is a function of the self-weight of the bed (second bracketed term in the right side of the equation). In the case of thin-walled hollow spheres (wall thickness-to-sphere diameter ratio ≈ 0.01), Eqs. (3) and (4) are modified to $k_c \sim P^{1/2}$ and $k_c \sim t^{1/2}$ (Ref. 6-11), respectively.

When a gas is present in the void volume between spheres, heat is conducted through the gas layer as well as the contact area between spheres. This conduction through the gas is a function not only of the gas thermal conductivity but also the distance between points on the surface of adjacent spheres and the mean-free path of the gas. An apparent thermal conductivity for this mode can be expressed as (Ref. 6-3)

$$k_{gc} \sim F'' k_g f(k_s/k_g) \quad (5)$$

where k_g is the conductivity of the gas at atmospheric pressure modified by the local-spacing/mean-free-path relationship.

The radiative heat flux at any point in an optically thick medium can be expressed as (Ref. 6-15)

$$q_r = \frac{4}{3\beta} \frac{d}{dx} (n^2 \sigma T^4) = \frac{16n^2 \sigma T^3}{3\beta} \frac{dT}{dx} = k_r \frac{dT}{dx} \quad (6)$$

where the extinction coefficient β , which is the sum of absorption and scattering coefficients for the packed sphere medium, is experimentally determined. Coupled with radiation slip boundary conditions, the q_r equation can be solved to give the general expression (not just restricted to the optically thick case) for radiative heat transfer through a plane layer of absorbing and isotropically scattering media:

$$q_r = \frac{n^2 \sigma (T_H^4 - T_C^4)}{3/4 \beta l + (1/\epsilon_H) + (1/\epsilon_C) - 1} \quad (7)$$

For the low emittance metal boundaries, the effective emittance = $n\epsilon$, where n is the effective refractive index of the medium (Ref. 6-16), and ϵ is the metal-to-vacuum emittance.

For comparing with experimental data as well as for engineering applications, it is convenient to define the apparent thermal conductivity as

$$k = ql/(T_H - T_C) \quad (8)$$

The apparent radiation conductivity is

$$k_r = \frac{n^2 \ell \sigma (T_H + T_C) (T_H^2 + T_C^2)}{3/4 \beta \ell + (1/n\epsilon_H) + (1/n\epsilon_C) - 1} \quad (9)$$

and the apparent thermal conductivity can thus be expressed as

$$k = A_1 k_s (T) + k_{gc} (T) + B \ell \sigma T_1^3 (1 + \theta) (1 + \theta^2) \quad (10)$$

where A_1 includes the packing geometry factor and elastic properties of the sphere and the load; $k_s (T)$ is the temperature-dependent thermal conductivity of the sphere material; k_{gc} is the apparent conductivity for the gas phase; B represents the optical properties, assumed to be gray, of the sphere boundaries; and $\theta = T_C/T_H$.

Microsphere Thermal Conductivity Model. The general form given by Eq. (10) is used to define the thermal conductivity of the microsphere insulation as applied to the test article. The first term on the right side of the equation is expressed as

$$F^*(P + H)^{0.5} (a_0 T - a_1 T^2) \quad (11)$$

where F^* is the packing geometry factor; $(P + H)^{0.5}$ represents the contact force resulting from an externally applied compressive load P plus the integrated self-weight of the bed H , and a_0 and a_1 are 6.26×10^{-3} and 7.83×10^{-6} , respectively, as obtained from a fit of the literature data (Ref. 6-17) for the thermal conductivity of horosilicate glass from 20° to 300°K (36° to 540°R). For the case of evacuated microspheres, a thermal conductivity expression is obtained by substitution of the contact conduction and radiation conductivities into Eq. (2).

$$q_x = F^*(P + H)^{0.5} (6.26 \times 10^{-3} T - 7.83 \times 10^{-6} T^2) dT/dx + B \sigma T^3 dT/dx$$

By integrating between 0 and ℓ for x and T_C and T_H for T and multiplying by $\ell/T_H (1 - \theta)$, the resulting equation is

$$k = F^* (P + H)^{0.5} [3.13 \times 10^{-3} T_H^{-3} (1 + \theta) - 2.61 \times 10^{-6} T_H^2 (1 - \theta^3 / 1 - \theta)] + B \sigma \ell T_H^3 (1 + \theta) (1 + \theta^2), \quad (12)$$

assuming B is independent of temperature.

If a gas is present in the void space between spheres, a third term is added to Eq. (12). For hollow spheres having an evacuated or gas-filled interior volume, a form of the gas contribution equation suggested by Kagner (Ref. 6-3) for porous granules was employed for this analysis. This equation relates heat transport to the thermal conductivity of the gas in the voids between granules and the effective conductivity of the granule. The latter conductivity is a function of the conductivity of the gas within the granules and the granule material itself. These properties in the general case are temperature dependent, but the integration of the equation is cumbersome considering temperature dependencies of both thermal conductivity and the gas mean free path. In the solution used in this work, an approximation was made whereby the properties are evaluated as the average temperature between boundaries for the gas phase and by the expression for glass as a function of local temperature in the manner of Eq. (12).

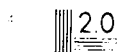
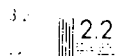
A second consideration in calculation of gas-phase effects is the definition of a local pressure at low pressures as a function of the gage pressure measured remotely from the bed. For Knudsen numbers $(L/\delta_a) \gg 1$, a pressure gradient exists with a temperature gradient in the porous media and one must then include the influence of dP/dx in the rigorous solution. For this analysis, a mean pressure is defined as

$$\bar{P} = \frac{P_g (T_H^{1/2} + T_C^{1/2})}{2 T_g^{1/2}} \quad (13)$$

where P_g is gage pressure and T_g is temperature of the gage. Equation (13) was used to compute the mean free path term for the gas conduction equation.



28 1.25



The equation for the gas conduction contribution to overall thermal conductivity is

$$k_{gc} = k_g \left[\frac{5.8 (1-m)^2}{1 - \frac{k_g}{k_{gr}}} \left(\frac{1}{1 - \frac{k_g}{k_{gr}}} \ln \frac{k_{gr}}{k_g} - 1 - \frac{K}{2} \right) + 1 \right] \quad (14)$$

where k_g is the thermal conductivity of the gas contained within the voids at the pressure of interest, k_{gr} is an effective conductivity of the hollow sphere, and $K = 1 - k_{gs}/k_s \rightarrow 1$ for microspheres at low pressure.

The complete equation used to represent the thermal conductivity of the tank microsphere insulation is then

$$k = k_{sc} + k_{gc} + k_r \quad (15)$$

where for solid conduction

$$k_{sc} = 1.07 \times 10^{-5} (P+H)^{0.535} \left[3.13 \times 10^{-3} T_H (1+\theta) - 2.61 \times 10^{-6} T_H^2 (1-\theta^3/1-\theta) \right]$$

for gas conduction

$$k_{gc} = k_g \left[\frac{5.8 (1-m)^2}{1 - \frac{k_g}{k_{gr}}} \left(\frac{1}{1 - \frac{k_g}{k_{gr}}} \ln \frac{k_{gr}}{k_g} - 1 - \frac{K}{2} \right) + 1 \right]$$

and for radiation

$$k_r = \left(\frac{n^2}{0.75 \beta l + \frac{1}{nc_H} + \frac{1}{nc_C} - 1} \right) \sigma T_H^3 (1+\theta) (1+\theta^2)$$

E-3

The coefficient of the contact conductivity term (1.07×10^{-5}) and the $P + H$ exponent (0.535) were derived from the tank experimental data as discussed in section 6.6.2. The value of H is evaluated from the hydrostatic head test results of section 6.5. β and n in the radiation term were determined experimentally (Ref. 6-12).

6.6.2 Effect of Compressive Loading on Thermal Performance

The experimental data from the compressive load and ground-hold tests were analyzed to evaluate the coefficient and exponent of the contact conduction term of Eq. (15). Total tank heat input data were corrected for heat leaks through supports, LI900 blocks, and springs. This insulation heat input value was then used to calculate an insulation thermal conductivity. Radiation conductivity was computed for each set of boundary temperatures using average emittance values for the jacket and tank based on the data shown earlier in Table 6-3. Temperature dependence of emittance was computed for $\epsilon(T) = aT^{0.5}$ using the data from Ref. 6-5. This radiation conductivity was then subtracted from the total insulation thermal conductivity to give a solid-phase thermal conductivity. The solid-phase thermal conductivity was divided by glass thermal conductivity at equivalent temperatures to obtain a nondimensional conductivity ϕ . Figure 6-18 compares the test article ϕ as a function of compressive load ($P + H$) with those obtained previously using a flat plate calorimeter (FPC) apparatus. The coefficient A_1 and exponent n_1 were calculated using a least-square routine and the result is represented by the dashed line ($A_1 = 1.07 \times 10^{-5}$ and $n_1 = 0.535$). The broken line represents the compressive load behavior observed from FPC data for the initial compression cycle where $n_1 = 0.60$. After the initial cycling, the exponent $n_1 = 0.55$ is the best correlation of the FPC data to 100 cycles. This change in exponent with cycling is attributed to a change in packing geometry, which is evidenced by an observed solid fraction change of 0.60 to 0.64 with the initial loading.

Test tank performance is in good agreement with the FPC data in regards to the load dependence exponent n_1 . However, the coefficient A_1 is less than that derived from the FPC data; consequently, the absolute value of thermal conductivity for the test article is less than that for the FPC as shown by Fig. 6-19. This difference is

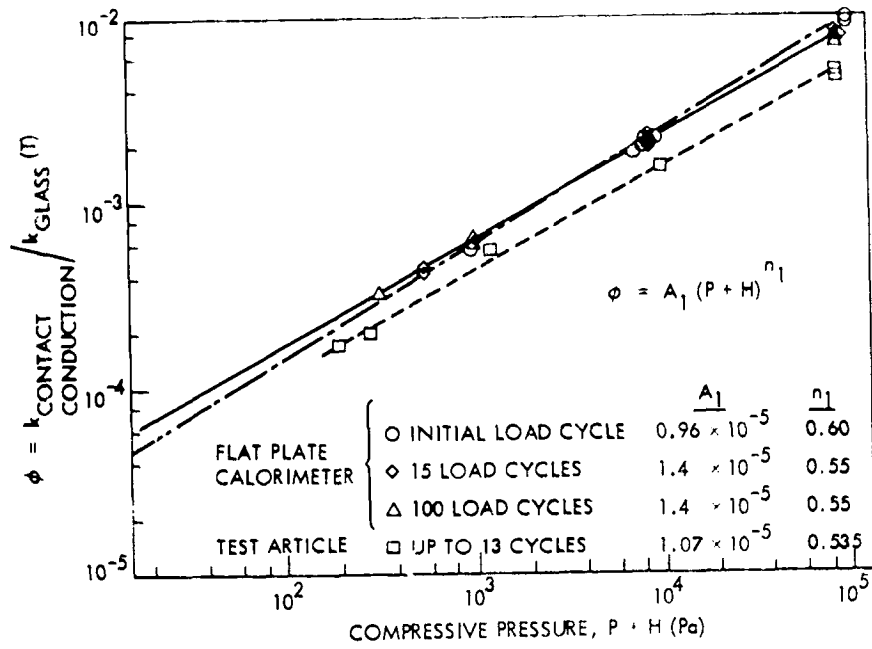


Fig. 6-18 Dimensionless Solid-Phase Thermal Conductivity as a Function of Compressive Pressure

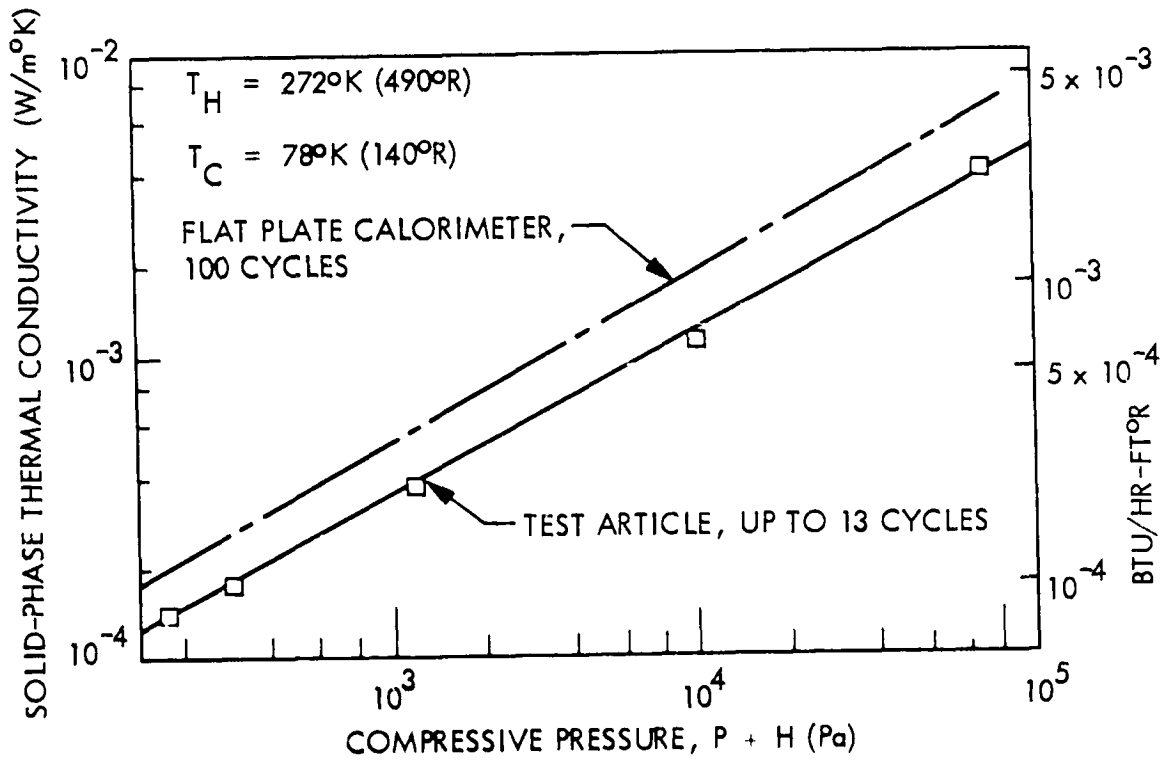


Fig. 6-19 Comparison of Flat Plate and Test Tank Solid-Phase Thermal Conductivity Under a Compressive Load

postulated to be the result of a difference in packing geometry for nearly identical solid fractions. Evidence of this effect has been brought forth in a recent study (Ref. 6-18) of possible contact orientations in a packed bed at a single solid fraction. Figure 6-20 illustrates the range of solid-phase conductivities that can be postulated from a statistical study of packing geometry. Thus, it is seen that solid fraction does not specify a unique packing geometry. In the FPC testing, the packing may be much more uniform than in the test tank because of the differences in the filling method. For the FPC, the insulation is in a horizontal plane and the microspheres are poured carefully to cover uniformly the horizontal area as the bed thickness increases. For the test tank, the microspheres are introduced as a fluidized stream.

6.6.3 Effect of Insulation Gas Pressure on Thermal Performance

The expression in Eq. (15) for prediction of gas-phase thermal conductivity was compared with the nitrogen gas experimental data. The void fraction m , used in the

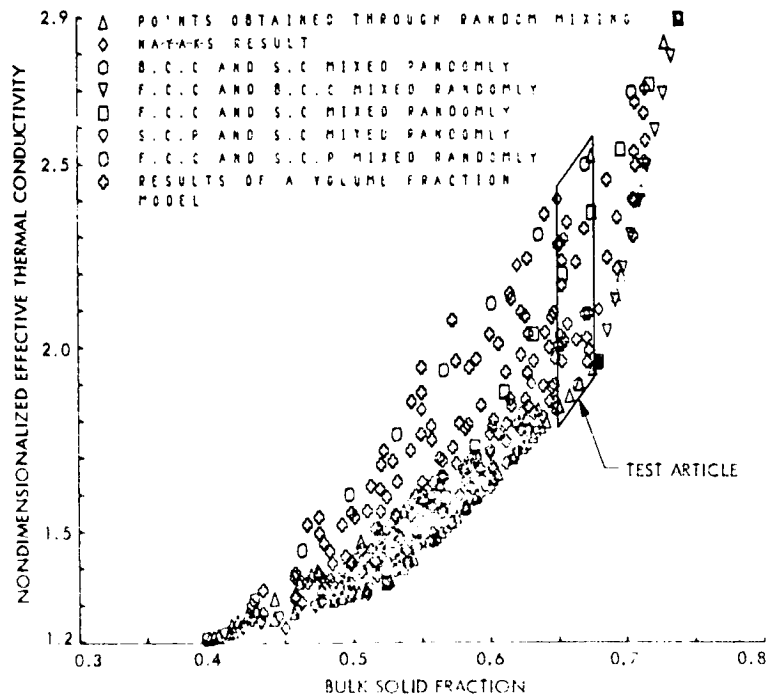


Fig. 6-20 Variation in Solid Conductivity With Packing Geometry

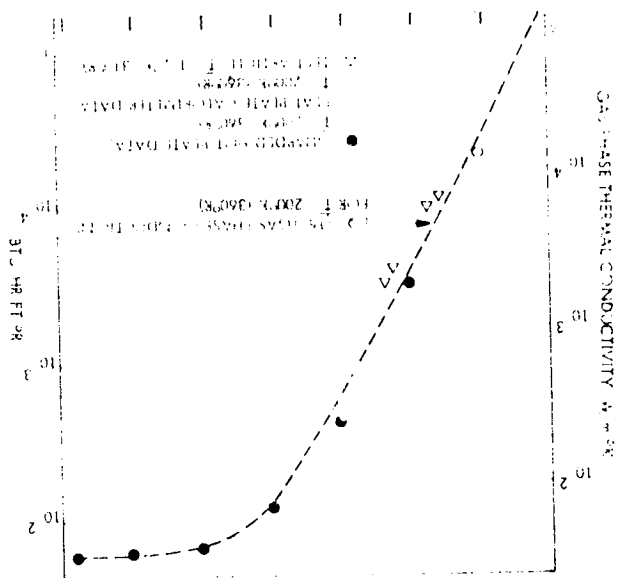
calculations, is 0.36. Sphere thermal conductivity k_{gr} was calculated assuming the pressure within the sphere was .013 Pa of nitrogen gas, and the characteristic void dimension δ_a was based on a mean sphere diameter of 75×10^{-6} m (0.003 in.). Correlation between the conductivity model and earlier experimental data for the microsphere insulation obtained from a guarded hot plate* for helium and nitrogen at two average temperatures is shown in Fig. 6-21. These data for the relatively small temperature difference of 50°K (90°R) between hot and cold boundaries show good agreement was obtained for the temperatures and pressures investigated.

Test article data were analyzed by subtraction of the contact conduction and radiation terms, computed for each test condition, from the total conductivity to obtain the gas-phase apparent conductivity. The test values are compared with the predicted values in Fig. 6-22. The dashed line represents the prediction as a function of pressure. Circles show the earlier data for microspheres and the triangular points are for the test article. The pressures shown are the temperature corrected values of gage pressure, as discussed in section 6.6.1. In all cases of test article data, the experimentally deduced points fall below the prediction. No reason for this deviation is apparent. However, four possible causes can be postulated. First, there is a possibility that the gage pressure is not related directly to the insulation pressure because the pressure data were taken at locations separated from the insulation space by small pore-size screens. Second, the correction applied to the gage pressure may be incorrect, particularly for large temperature differences between boundaries, considering a nonlinear temperature gradient in the insulation. Third, the packing geometry variation suggested from the compressive load data may result in a value of δ_a differing from the assumed value. And finally, the assumption of decoupled heat transport mechanisms may not be adequate for this condition, although it appears reasonably accurate for small ΔT studies.

*ASTM C-177. American Society for Testing and Materials, Philadelphia, Pennsylvania.

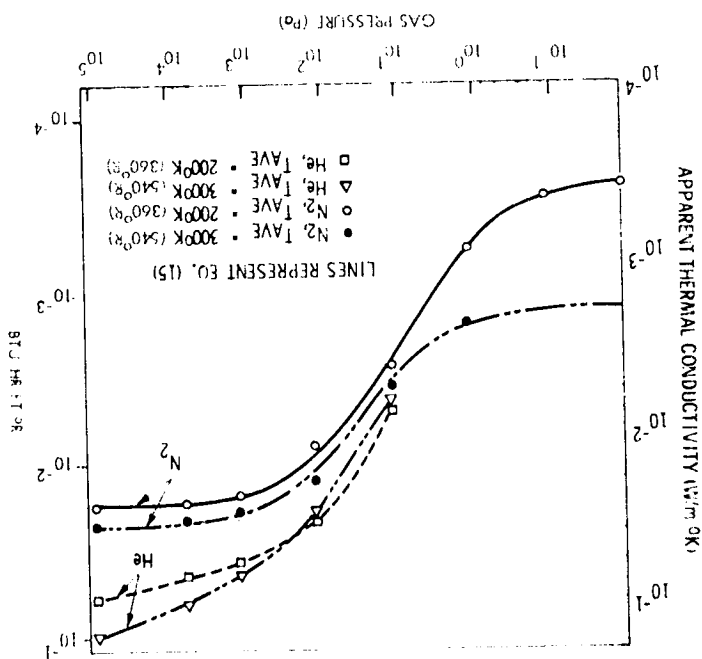
6-12

Fig. 6-22 Predicted Versus Experimental Values of Gas-Phase Thermal Conductivity



REPRODUCIBILITY OF THE ORIGINAL PAGE IS POOR

Fig. 6-21 Apparent Thermal Conductivity of Microsphere Insulation as a Function of Gas Species and Pressure at Two Average Temperatures



6.6.4 Space-Hold Thermal Performance

Thermal conductivity of the microsphere insulation as a function of the warm boundary temperature is shown in Fig. 6-23. The data represented by the open circles are for the initial test, and the triangular and square points are for data obtained after 3 and 7 thermal-pressure cycles, respectively. Considering the initial test and post-third cycle test, the conductivity can be expressed as a function of T_H to the 1.78 power. If all five points are included, the best fit of the data is T_H to the 1.86 power. Except at the limits of pure conduction or radiation, the total conductivity cannot be expressed as a single function of temperature because of the differing temperature dependencies of the conduction and radiation contributions. However, for the space-hold conditions the data should approach the radiation limit - i.e., approximately T^3 .

The calculated thermal conductivity as a function of hot boundary temperature, from Eq. (15), is shown by the dashed line of Fig. 6-23. Over the temperature range shown,

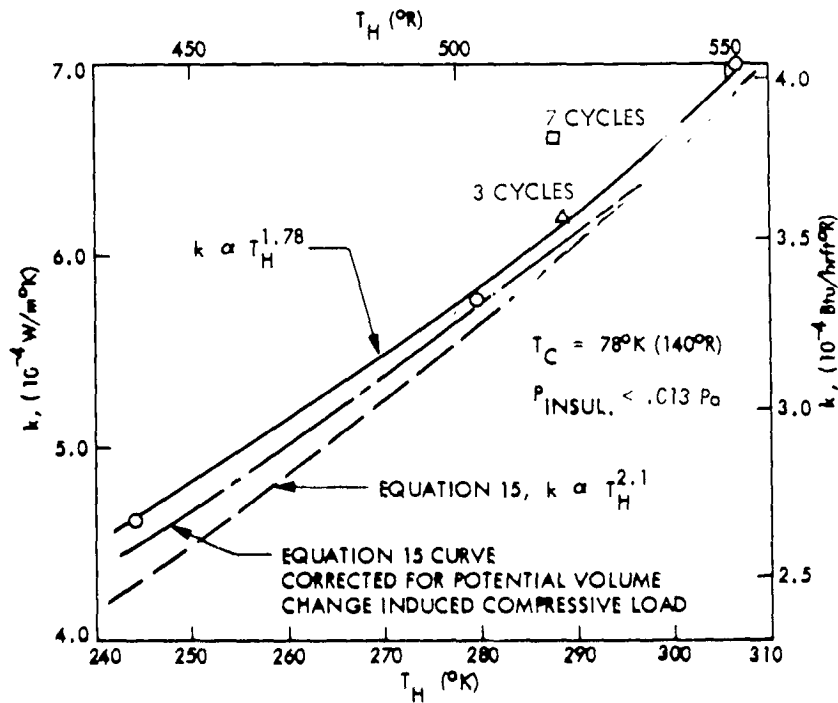


Fig. 6-23 Space-Hold Thermal Conductivity

the calculated conductivity can be approximated as $k \sim T_H^{2.1}$. From flat-plate calorimeter data (Ref. 6-12), $k \sim T_H^{2.7}$ over this range of hot-boundary temperatures. For the FPC data, however, the $(P + H)$ term of Eq. (15) is nearly zero as H is very small and the conduction heat transport is insignificant. In the test article case, H is appreciable (see Figs. 6-16 and 6-17). The conduction term then becomes a significant fraction of the total heat transfer (see section 6.6.6), thereby reducing the temperature dependence exponent to some value less than 2.5.

The displacement calculated from the experimental curve is believed to be the result of a slightly greater conduction component than predicted from the analysis of the compressive load data. An estimate was made of the maximum compressive load that could be exerted on the microspheres due to volume changes and jacket shrinkage at temperatures less than ambient (jacket filling condition). The calculated average load (assuming no jacket support from the springs) is 20 Pa at 280°K (504°R) and 50 Pa at 244°K (439°R). Inclusion of these loads in Eq. (15) increases the thermal conductivity to the values shown by the broken line of Fig. 6-23. (A compressive pressure of 66 Pa would bring the calculated and experimental values into excellent agreement.)

Even without this correction, agreement between calculated and experimentally determined values of thermal conductivity is within 10 percent, on the same order as the uncertainty in the experimental data.

6.6.5 Ground-Hold Thermal Performance

Comparison of predicted versus experimentally evaluated thermal conductivity for the ground-hold conditions is within 10 percent as shown in Fig. 6-24; however, the apparent temperature dependency is vastly different. A $k \sim T_H^{1.87}$ results from the experiment which indicates a radiation-dominant case. Equation (15) yields a temperature dependency of considerably less than unity, corresponding to that of the borosilicate glass — i.e., conduction-dominated. No explanation is presented for this anomaly other than experimental uncertainty. Also, the data are over too limited a range, 25°K (45°R), to provide a reasonable assessment of temperature dependence.

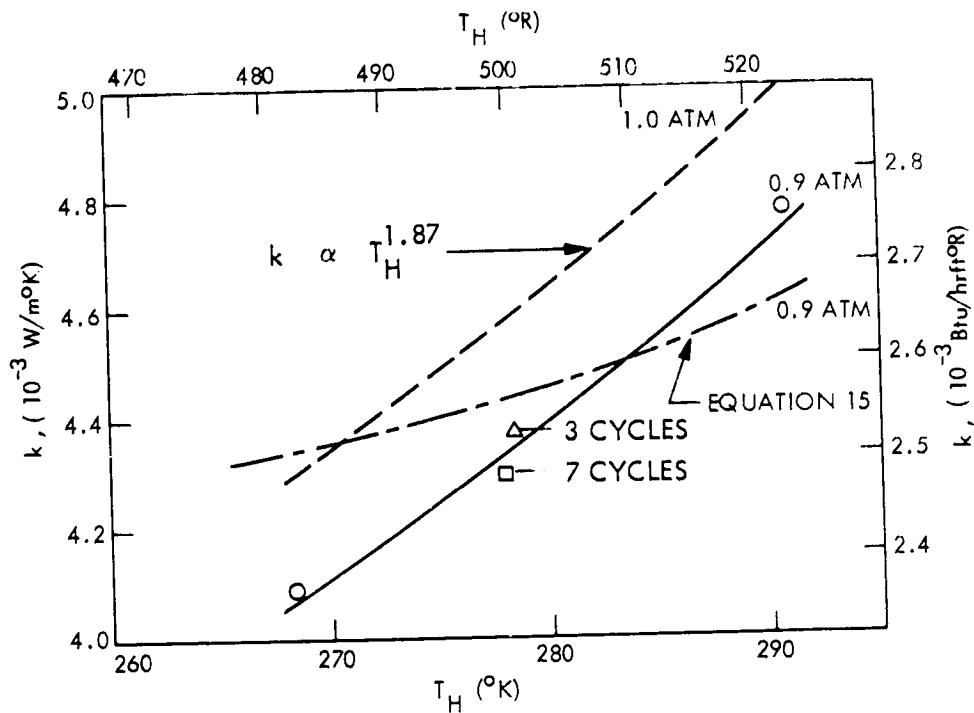


Fig. 6-24 Ground-Hold Thermal Conductivity

6.6.6 Comparison of Calculated and Experimental Test Article Heat Inputs

Table 6-5 presents a comparison of calculated and measured heat inputs to the test article for the different test conditions. Calculated values of conduction, radiation, and insulation penetration heat rates are expressed as percentages of the total calculated heat rate. In general, the agreement between calculated and measured rates are quite good. With the exception of the interstitial gas pressure series, agreement is within 10 percent. For gas pressures in the 1.3 Pa range, the calculated values of heat rate are 19 to 28 percent greater than measured heat rates. At the lower pressures, the calculations are within 10 percent of the measured values.

Table 6-5

CALCULATED VERSUS MEASURED HEAT RATES

Test	Comp. Press., Pa	Gas Press., Pa	T _H , °K (°R)	Microspheres		Spring Assemblies, %	LI900 Blocks, %	Struts, %	Total	
				Conduction, %	Radiation, %				Calculated W (Btu/hr)	Measured, W (Btu/hr)
Ground Hold	9×10^{-4}	<0.013	291(523)	55.2	9.9	1.0	0.7	0.2	329.8(1126)	342(1167)
	9×10^{-4}	<0.013	268(483)	59.7	5.4	1.0	0.7	0.2	279.1(953)	260(885)
Space	<0	<0.013	306(552)	19.2	69.3	6.2	3.9	1.4	58.3(199)	59.6(203)
	↓	↓	280(503)	23.1	63.8	7.1	4.6	1.4	43.7(149)	44.2(151)
	↓	↓	244(439)	29.2	55.9	8.0	5.5	1.4	28.8(98)	29.8(102)
Compressive Load	12.8	<0.013	279(502)	22.8	63.9	7.2	4.7	1.4	42.9(146)	42.6(145)
	102	↓	278(500)	26.9	60.6	6.7	4.5	1.3	44.7(153)	43.8(150)
	986	↓	273(491)	45.0	45.3	5.2	3.4	1.1	55.6(190)	61.4(210)
	9730	↓	264(476)	73.2	21.8	2.7	1.8	0.5	101.5(345)	106.8(365)
Gas Pressure	<0	0.13	268(482)	21.2	9.7	6.8	4.3	1.4	41.5(142)	45.8(156)
	↓	0.65	267(481)	17.7	24.8	5.7	3.7	1.2	40.2(138)	46.6(159)
	↓	1.0	268(483)	16.4	39.3	5.2	3.3	1.1	53.8(184)	48.4(164)
	↓	2.36	260(468)	11.5	52.6	3.8	2.5	0.7	72.0(246)	58.8(201)
	↓	4.05	258(465)	10.4	58.9	3.2	2.2	0.6	80.7(275)	63.8(218)

m. Percentage of total calculated heat rate. T_C = 78°K (110°R).

6.6.7 Experimental Uncertainties

Heat Rate. The uncertainty in the measured value of test tank heat rate is the summation of the individual uncertainties associated with the boiloff measurement and the uncertainty resulting from changes in the sensible heat of the liquid in the tank arising from small ullage pressure changes during the measurement period. This maximum total uncertainty (as opposed to the lower rms uncertainty) may be expressed as

$$\delta q = \delta V + \delta \rho + \delta h_v + \delta Q_{\ell}$$

where δV is the maximum uncertainty in the volumetric measurement of boiloff, considering the individual uncertainties in the flow meter and the measurements of temperature and pressure of the gas; $\delta \rho$ is the uncertainty in gas density derived from the gas temperature and pressure measurements; δh_v is the uncertainty in the latent heat of vaporization which is a function of the liquid purity and the temperature in the tank; and δQ_{ℓ} is the liquid sensible heat term related to time-dependent ullage pressure changes.

The maximum uncertainty in volume measurement δV was calculated to be 1.2 percent for the space-hold tests (lowest heat-rate series) based on the wet-test meter calibration* of ± 0.5 percent and the meter temperature and pressure measurement accuracies. For the ground-hold tests, this maximum uncertainty is 14 percent for the lowest jacket temperature condition decreasing to 9 percent for the highest temperature case (based on the meter calibration accuracy of $\pm 0.4 \text{ m}^3/\text{min}^*$).

The calculated maximum uncertainties for the density $\delta \rho$ and latent heat δh_v are 0.5 and 0.1 percent, respectively. The density uncertainty is based on gas temperature and pressure measurement accuracies of 0.4 and 0.1 percent, respectively, at the

*Calibrated against an NBS traceable meter.

flow meter. The error in latent heat is calculated for a 0.5°K (0.9°R) uncertainty in the liquid temperature. As the liquid purity was greater than 99.998 percent, no error was assumed for any deviation from the latent heat data of Ref. 6-19.

The calculated maximum uncertainties for any test due to the δQ_g term, based on the measured ullage pressure fluctuations, are 1.2 percent for the ground-hold test series and 6.7 percent for the space-hold data.

From these individual uncertainties, the maximum uncertainty in measured tank heat rate is 8.5 percent for the space-hold series of tests. For the ground-hold test series, it ranges from 10.8 to 15.8 percent, the larger value corresponding to the lowest jacket temperature data.

Thermal Conductivity. Uncertainties in the values of microsphere insulation thermal conductivity are a maximum of 19.4 percent for space-hold conditions and 23.3 percent for ground-hold conditions. These values are based on the tank heat rate uncertainties plus those resulting from the insulation mean area and thickness measurements, jacket and tank wall temperature measurements (ΔT), and corrections for heat leaks through the springs, L1900 blocks, and the support struts. Maximum uncertainties assigned to these parameters are:

Area	1%
Thickness	4%
ΔT	2%
Heat Leaks	25% of calculated value (see Table 6-4)

Section 7

DESIGN AND ANALYSIS OF SPACE TUG INSULATION SYSTEM

Using the information developed in this program, the microsphere insulation/flexible jacket system was scaled to the Space Tug design. A preliminary design was performed, weight statements and thermal performance data were generated, a manufacturing plan was prepared, operational requirements were defined, and schedules and costs were laid out. Insulation system weights, thermal performance, and payload performance were then compared with previously established goals. Payload sensitivity analyses were also performed on selected insulation system characteristics.

7.1 INSULATION SYSTEM PRELIMINARY DESIGN

The preliminary design concept shown in Figs. 7-1, 7-2, and 7-3 was evolved using the environmental criteria and Option 2 Space Tug tank designs shown previously in Section 2 as well as the data developed in Sections 3 through 6.

The microsphere insulation consists of hollow, borosilicate glass spheres with a skewed Gaussian-size distribution, a median diameter of approximately 82 μm , and a bulk density of 0.069 g/cc (4.3 lb/ft³).

The characteristics of the LO₂ and LH₂ tank vacuum jackets are summarized in Table 7-1.

The vacuum jacket is spaced off the tank wall by a series of conical, helical, stainless steel springs held in compression by a Kevlar strand (Fig. 7-2, Detail F). The springs and preloaded Kevlar provide uniform jacket spacing off the tank wall in orbit when significant dimensional changes in the tank and jacket can occur (due to pressure and temperature changes). They also provide jacket support under ascent acceleration loads when the atmospheric pressure drops to essentially zero. This design minimizes the heat load and assembly time as compared to the three Kevlar strand design used on the test tank assembly.

Table 7-1

SPACE TUG VACUUM JACKET CHARACTERISTICS

Parameter	LO ₂ Tank	LH ₂ Tank
Material	321 SS	321 SS
Thickness, mm (in.)	0.08 (0.003)	0.08 (0.003)
Unit Weight, kg/m ² (lb/ft ²)	0.62 (0.127)	0.62 (0.127)
Length of Welded Joints, m (ft)	184 (604)	393 (1290)
Number of Circumferential Squares	36	42
Number of Gores at the Equator	12	14
Maximum Wedge Height, cm (in.)	1.16 (0.46)	1.19 (0.47)
Minimum Wedge Height, cm (in.)	0.59 (0.23)	0.62 (0.24)
Wedge Angle (Deg)	30	30
Wedge Spacing at Equator, cm (in.)	32.1 (12.6)	31.2 (12.3)
Number of Spring Attachments	814	1444
Average Spacing off Tank Wall, cm (in.)	2.90 (1.14)	2.02 (0.80)

The formed vacuum jacket uses a pattern of expansion wedges demonstrated on this program that allows the jacket to expand/contract as the tank changes dimensions during cryogenic fill, warmup, or pressurization (Fig. 7-2, Detail C). A stiffening bead pattern is formed in the panel squares to distribute the load at the spring attach points. A special wedge pattern (Fig. 7-2, Detail G) is used to terminate the bi-axially flexing jacket at the rigid tank poles.

Gore panels are joined by an overlap resistance seam-welded joint (Fig. 7-2, Detail D). The final closure joint uses the same concept; flanged holes provide the required access to both sides of this joint during welding. Local flanges act as an assembly aid in pulling the hemispheres together prior to the tack and seam welding of the final closure joint (Fig. 7-2, Detail E).

FOLDOUT FRAME

REPRODUCIBILITY OF THE
ORIGINAL PAGE IS POOR

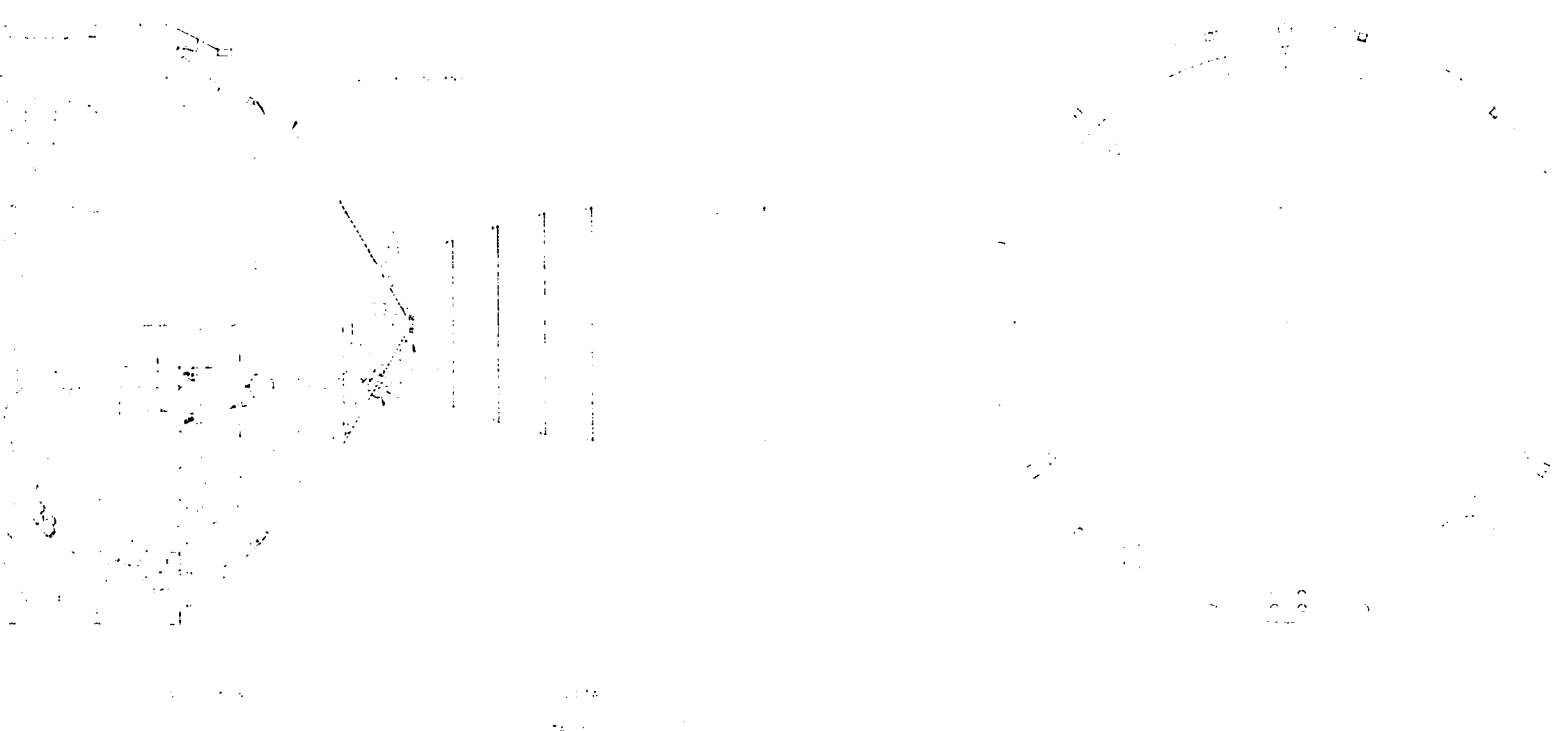
FOLDOUT FRAME



ORIGINAL PAGE 1

2

FOLDOUT FRAME 3



REPRODUCIBILITY OF THE ORIGINAL PAGE IS POOR

Fig. 7-1 Space Tug Insulation System Design

7-3

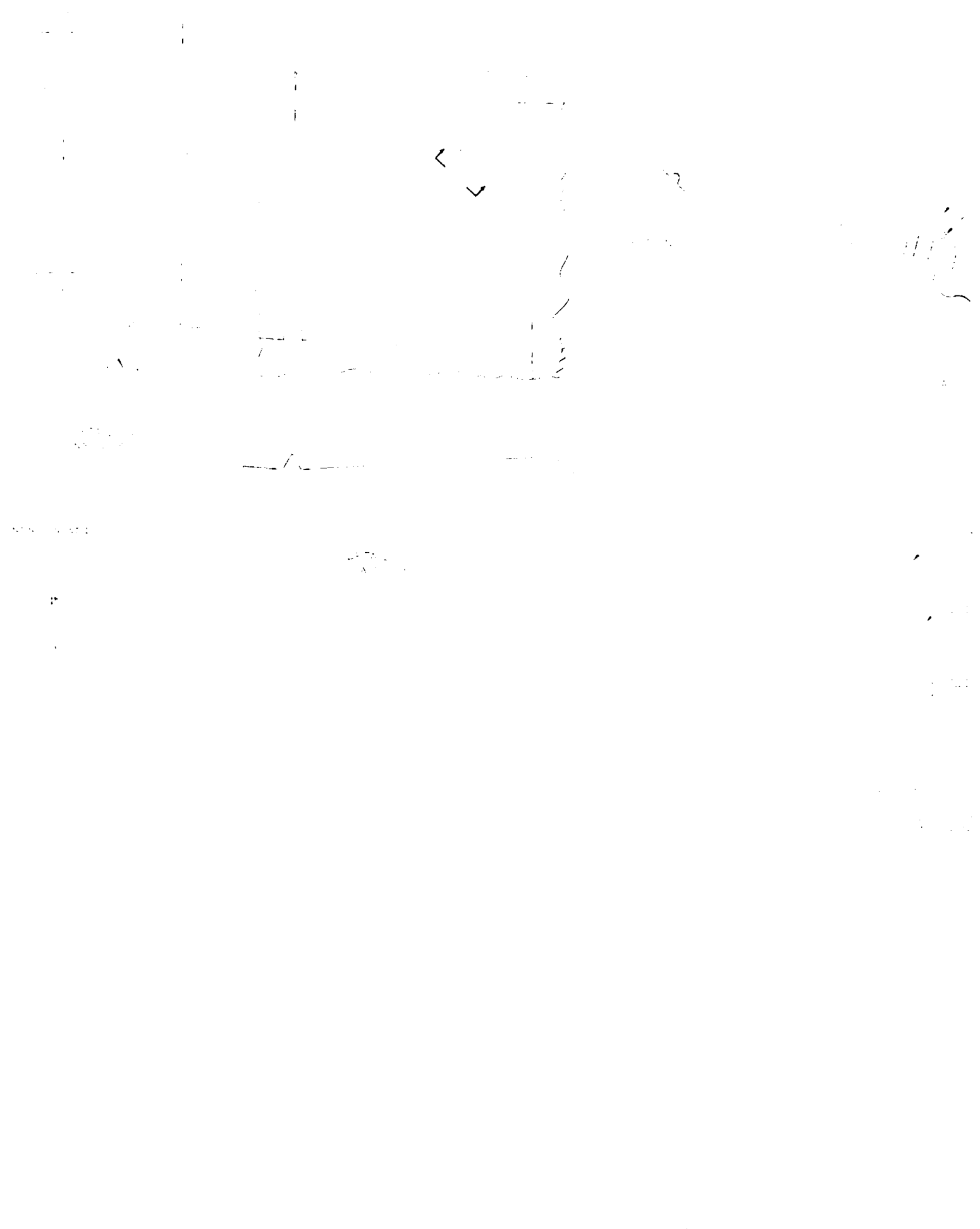
PRECEDING PAGE BLANK NOT FILMED

FOLDOUT FRAME |

REPRODUCIBILITY OF THE
ORIGINAL PAGE IS

FOLDOUT FRAME 2

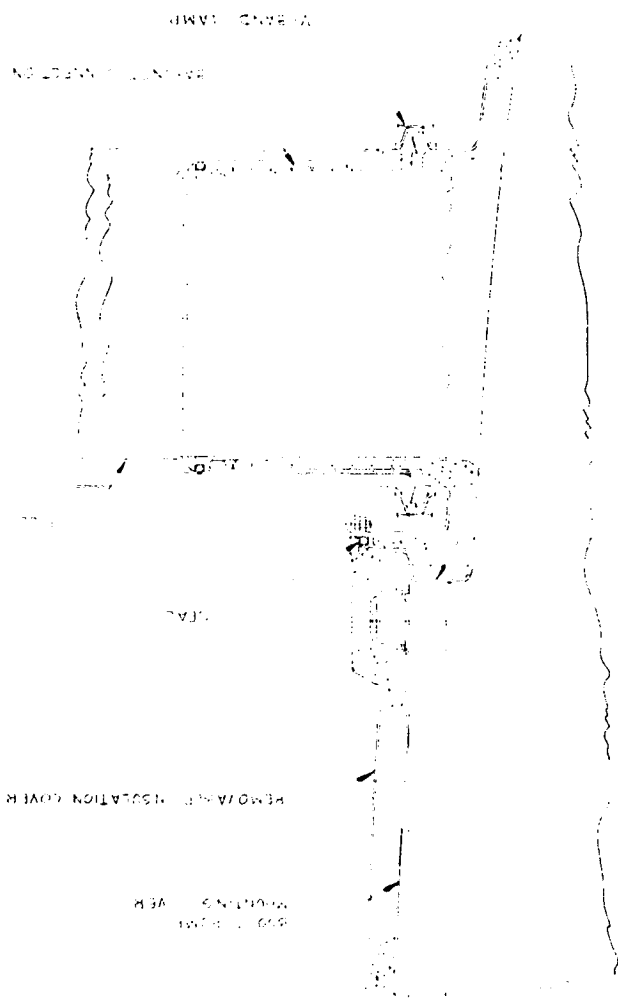
FRAME 1



FOLDOUT FRAME 3



Fig. 7-2 Space Tug Insulation System Design
(Cont.)



DRIVE SHAFT

REAR MOUNTING BRACKET

FRONT MOUNTING BRACKET

SEE DRAWING

LEAF

REAR MOUNTING BRACKET

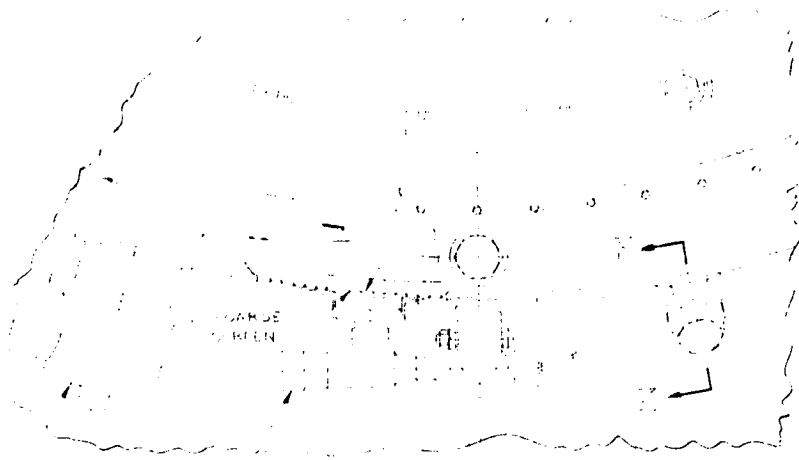
REMOVAL INSULATION COVER

REAR MOUNTING BRACKET

PRECEDING PAGE BLANK NOT FILMED

PHOTOGRAPH

FOLDOUT FRAME 2



SEAL OFF VALVE

FINE SCREEN



WATER PUMP

DETAIL 1
SCALE 1/2"

INSULATION TAP



SECTION 1
SCALE 1/2"

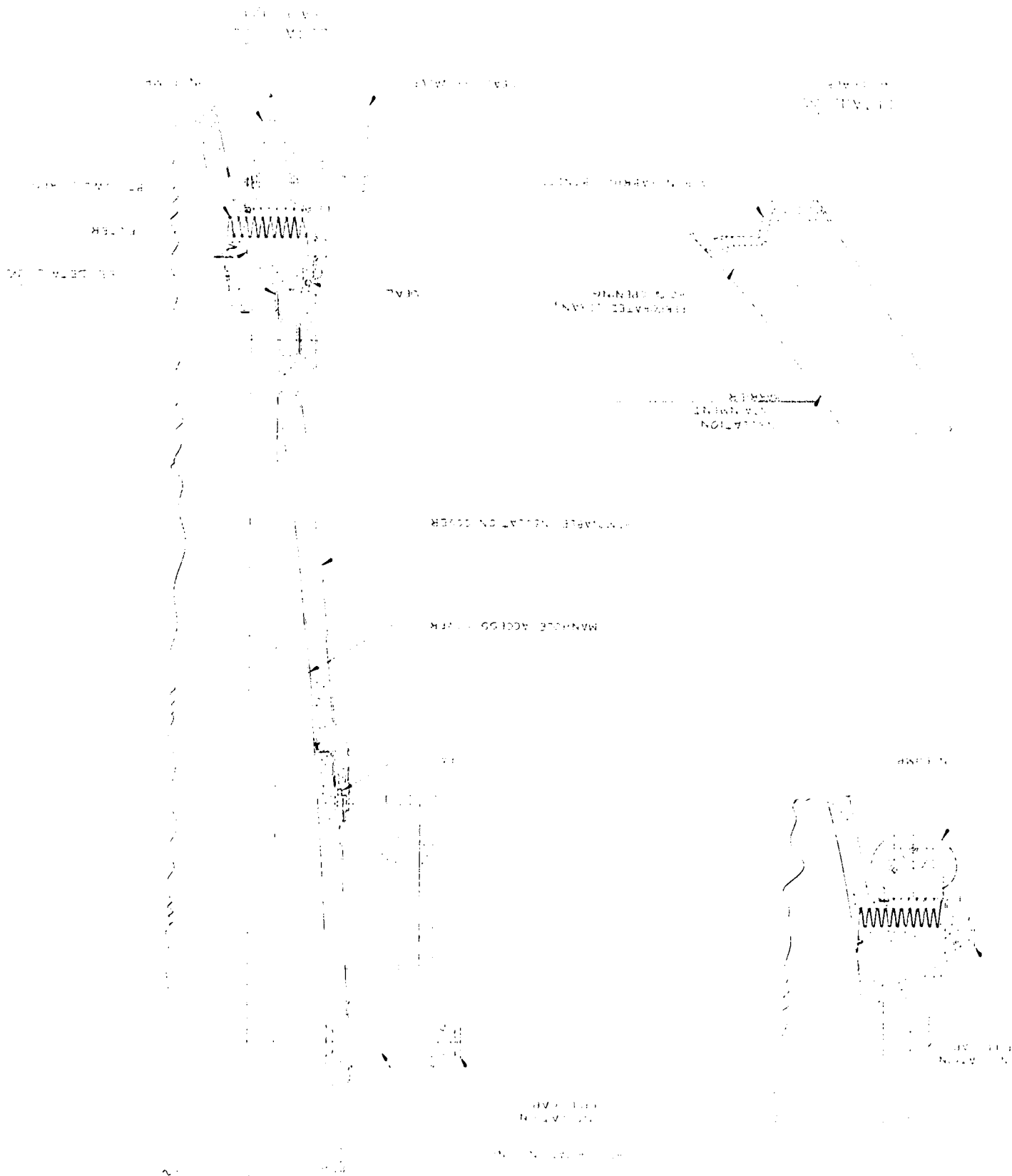
SECTION 2
SCALE 1/2"

SECTION 3
SCALE 1/2"

SECTION 4
SCALE 1/2"

SECTION 5
SCALE 1/2"

Fig. 7-3 Space Tug Insulation System Design (Cont.)



FOLDOUT FRAME 3

FOLDOUT FRAME 2

The vacuum jacket design around the tank support struts (Fig. 7-2, Detail B) uses a corrugated tube to withstand a 1-atmosphere load yet minimize weight. The warm end closeout uses a convoluted design to allow differential movement between the fiberglass strut and the strut cover. The convoluted strut assembly cover provides access to the strut/tank area during final assembly, allows attachment of the struts to the tank, and minimizes the shifting of microspheres during evacuation. A fill port on the cover provides visual verification of the microsphere fill level.

To provide access to the LH₂ tank top manhole cover or LO₂ bottom manhole cover, a removable, doughnut-shaped insulation cover is used (Fig. 7-3, Detail H). The microspheres are contained within a perforated Lexan/Dacron fabric containment barrier on the doughnut that allows evacuation of the total access cover region yet minimizes edge heat leaks. An inner and outer indium sandwich O-ring seal is used on the jacket doughnut section. A similar design is used for the lower LH₂ tank access cover (Fig. 7-3, Detail L). The upper LH₂ access cover and lower LO₂ access cover are sealed off from the main volume of the insulation with stainless steel bellows (to minimize the heat leak) as shown in Fig. 7-3, Detail H. This separation allows the access cover to be opened and closed without affecting the vacuum in the rest of the insulation system. The bellows is ultrasonically welded to the aluminum tank. Polar-cap-type wedges (Fig. 7-3, Detail J) allow differential expansion between the bellows and the tank.

Engine loads are transmitted to the LO₂ tank through a honeycomb structure (Fig. 7-2, Detail P).

The initial vacuum is obtained by evacuating the insulation to 1.3 Pa or less and back-filling with 99.99 percent CO₂ three times. The < .013 Pa pressure is obtained with oil free absorption and turbomolecular pumps. This vacuum level is maintained and monitored by three vacuum ion pumps as well as by the cryopumping action of the LH₂ and LO₂.

Three specially designed relief valves (Fig. 7-3, Detail J; Fig. 7-4; and Fig. 7-5) are used to vent the vacuum jacket in case of gross tank leakage. When alpha particle sensors detect a pressure in the vacuum jacket exceeding the design value, the squib on the relief valve is fired allowing the load release spring to raise the primary spring off the seal seat. The seat is then held in place only by the secondary spring. When the vacuum jacket pressure exceeds the compressive force of the secondary spring, the relief valve vents. Note the relief valve will not allow air back into the system during shuttle reentry into the atmosphere since the seal will reseal due to increasing atmospheric pressure and will not vent again until the ΔP exceeds the secondary spring force. Most of the plumbing penetrations through the vacuum jacket use bayonet-type connections as shown in Fig. 7-3, Detail L. Six insulation fill ports on each jacket, three top and three bottom, plus one on each strut assembly, are provided for blowing microspheres into the annulus after the vacuum jacket has been installed (Fig. 7-3, Detail J). Screens over the evacuation ports prevent microsphere migration into the vacuum pumps.

7.2 INSULATION THICKNESS OPTIMIZATION

The microsphere insulation thermal conductivity was calculated as a function of the warm boundary temperature for the LO_2 and LH_2 tanks. Ground hold (1-atm load) and space conductivities (no external atmospheric load) are shown in Figs. 7-6 and 7-7. The space-hold conductivities were obtained by ratioing the test data to LO_2 or LH_2 cold boundaries with Eq. (15) i.e.,

$$\left(\frac{k_{LH_2}}{k_{LN_2}} \right)_{\text{Eq. 15}} \left(k_{LN_2} \right)_{\text{Test Data}} = \left(k_{LH_2} \right)_{\text{Space-Hold}}$$

The data include the microsphere self-weight contact-conductance term, k_{sc} . In orbit this term theoretically goes to zero; therefore, the conductivities shown in Fig. 7-7 and used in all the subsequent analyses are conservative. Sensitivity analyses in section 7.8 show the space-hold thermal conductivity can potentially drop to less than 1/3 the values shown in Fig. 7-7. Parametric insulation thickness optimizations

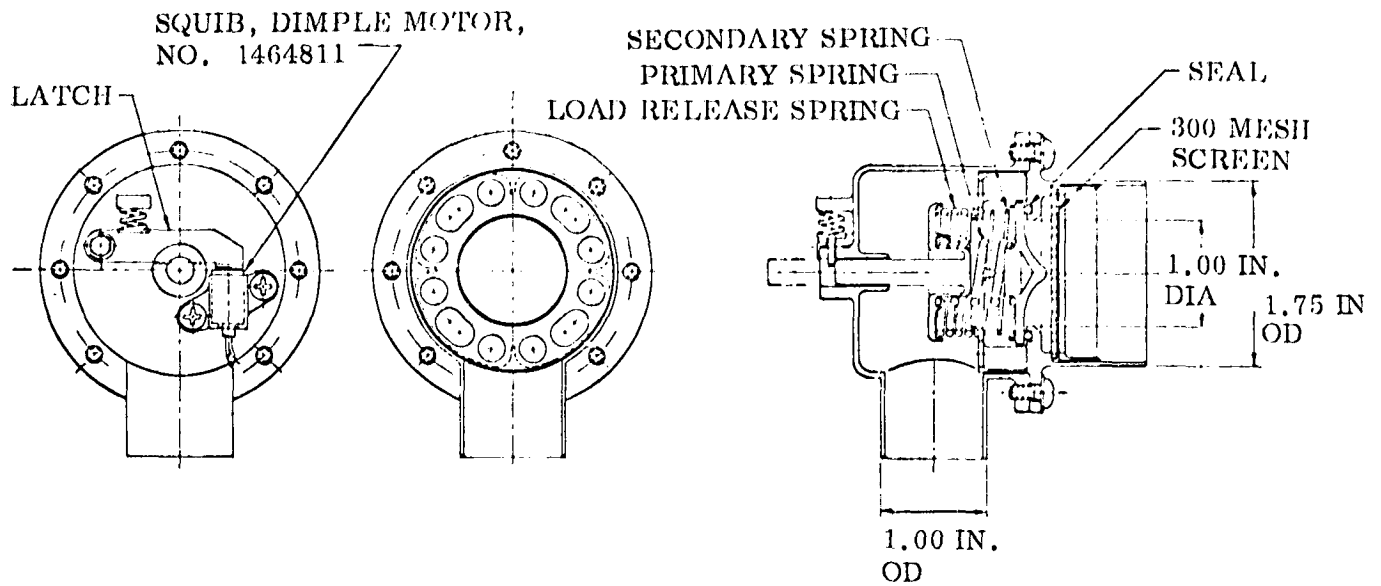
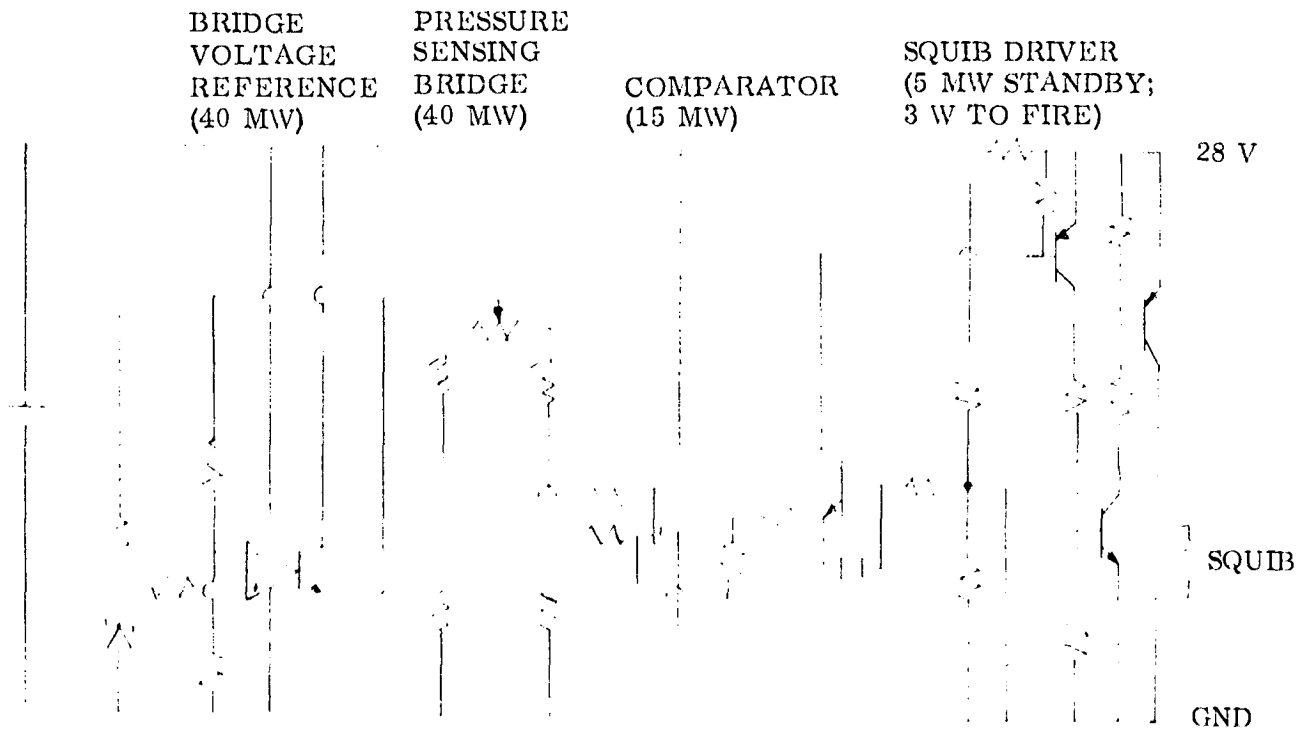


Fig. 7-4 Relief Valve Design



WEIGHT ~ .05 KG STANDBY POWER ~ 100 MW SQUIB FIRE POWER ~ 3 W

Fig. 7-5 Relief Valve Control System Schematic

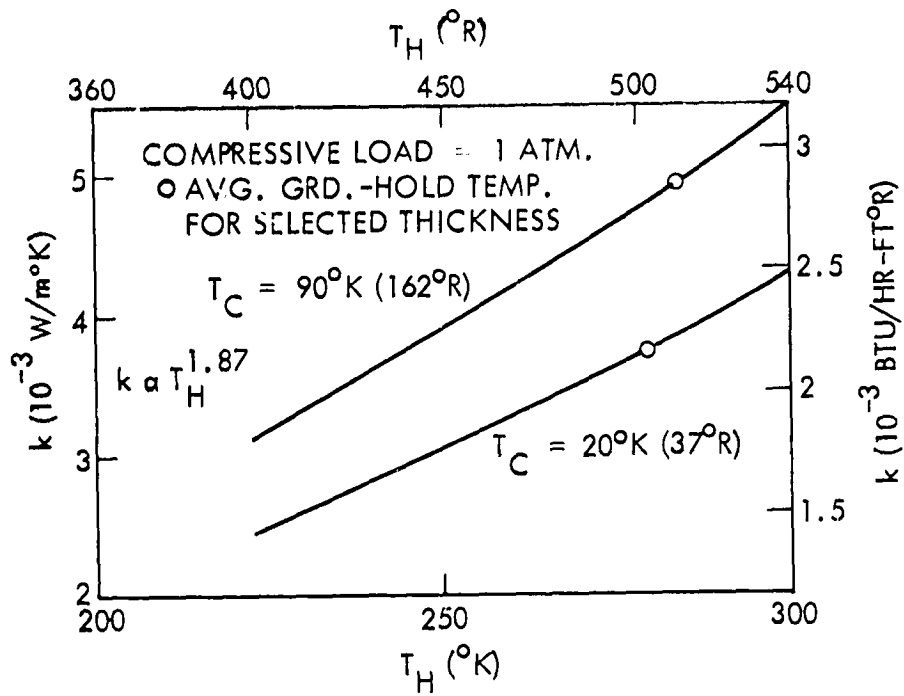


Fig. 7-6 Space Tug Ground-Hold Conductivity

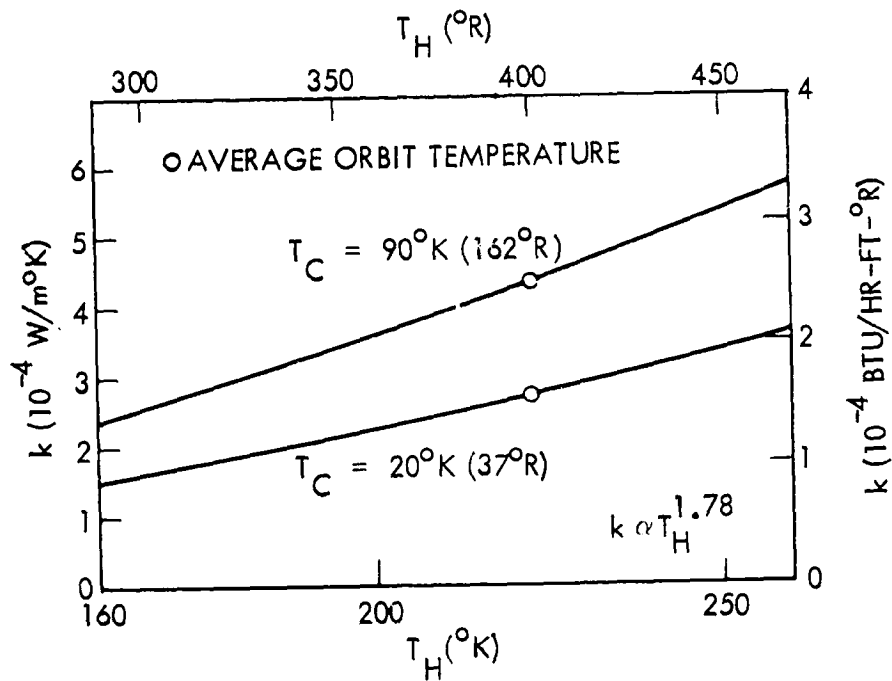


Fig. 7-7 Space Tug Space-Hold Conductivity

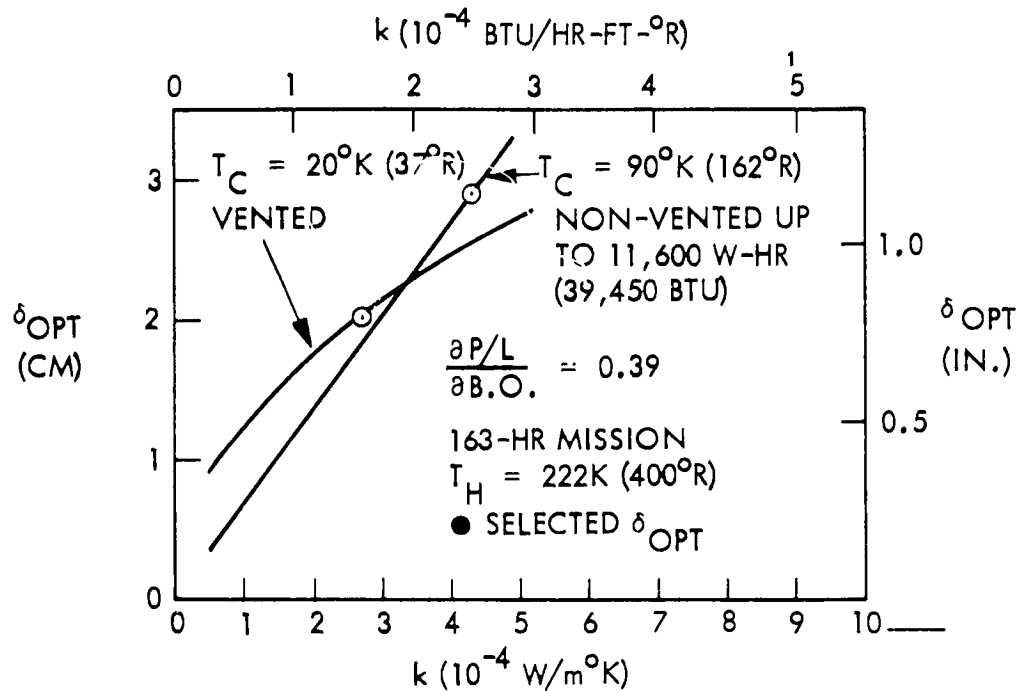


Fig. 7-8 Optimum Insulation Thickness

were performed for the LO₂ and LH₂ tanks as a function of thermal conductivity as shown in Fig. 7-8. Using conductivity data from Fig. 7-7, the optimum thicknesses from Fig. 7-8 are 2.9 cm (1.14 in.) for the LO₂ tank and 2.0 cm (0.80 in.) for the LH₂ tank.

7.3 WEIGHT AND THERMAL PERFORMANCE

A weight statement for the LO₂ and LH₂ microsphere insulation systems is provided in Table 7-2 for the optimized insulation thicknesses. A ground-hold and space-hold heat rate and heat flux summary is provided in Table 7-3.

7.4 MANUFACTURING PLAN

The manufacturing plan is subdivided into seven different areas for purposes of discussion.

Table 7-2

WEIGHT STATEMENT FOR THE SPACE TUG MICROSPIHERE INSULATION SYSTEM

Item		LO ₂ Tank, Lg. (lb)	LH ₂ Tank, Lg. (lb)
1.	Vacuum Jacket	36.29 (80.01)	67.43 (148.65)
1.1	Expansion Wedge Area (includes joints)	21.80 (48.06)	46.51 (103.6)
1.2	Access Cover Area		
	• SS Outer Ring	1.51 (3.33)	1.51 (3.33)
	• Machined Seal and O-Ring	1.73 (3.81)	1.73 (3.81)
	• SS Bellows	0.60 (1.32)	0.60 (1.32)
	• Lexan/Dacron Fabric	0.04 (0.09)	0.04 (0.09)
	• Removable Jacket Doughnut-Shape Cover	2.18 (4.81)	2.18 (4.81)
	• Cover Center and Vent Line	0.11 (0.97)	0.11 (0.97)
	• Screws	0.12 (0.26)	0.12 (0.26)
1.3	Boost-Pump Cover Area		
	• SS Outer Ring	-	1.68 (3.70)
	• Machined Seal and O-Ring	-	0.47 (1.04)
	• Lexan/Dacron Fabric	-	0.03 (0.07)
	• Removable Jacket Doughnut-Shape Cover	-	1.55 (3.42)
	• Cover Center	-	0.36 (0.79)
	• Screws and Nuts	-	0.16 (0.35)
	• Fill/Drain/Abort Bayonet Joint	0.41 (0.90)	0.40 (0.88)
1.4	Strut Sleeves (lower)	3.81 (8.40)	1.70 (3.75)
1.5	Strut Sleeves (upper)	-	1.18 (2.66)
1.6	Vent Line Sleeve	0.13 (0.29)	0.13 (0.29)
1.7	Zero-G Vent Line Sleeve (2 ea.)	0.10 (0.22)	0.10 (0.22)
1.8	Spring Wire Attachments	3.06 (6.76)	5.44 (11.99)
1.9	Epoxy/Gold Coating	0.36 (0.79)	0.77 (1.70)
2.	Microsphere Insulation	76.5 (168.5)	110.40 (243.28)
2.1	Average Thickness	72.0 (158.6)	107.60 (237.1)
2.2	Extra Volume for Top Access Cover	-	0.96 (2.12)
2.3	Extra Volume for Lower Access Cover	0.96 (2.12)	0.30 (0.66)
2.4	Extra Volume for Struts	3.53 (7.78)	1.54 (3.40)
3.	Equipment and Miscellaneous	2.35 (5.18)	2.60 (5.71)
3.1	Microsphere Fill Caps	0.66 (1.46)	0.50 (1.09)
3.2	Seal-Off Valves (3 ea.)	0.15 (0.33)	0.15 (0.33)
3.3	Filters (3 ea.)	0.02 (0.04)	0.02 (0.04)
3.4	Ion Pumps (3 ea.)	0.54 (1.19)	0.54 (1.19)
3.5	Over Pressure Relief Valve (3 ea.)	0.41 (0.90)	0.41 (0.90)
3.6	Over Pressure Relief Valve Control System (3 ea.)	0.14 (0.31)	0.11 (0.31)
3.7	Lines and Tees	0.07 (0.15)	0.07 (0.15)
3.8	Epoxy/Gold Coating on Tank	0.36 (0.79)	0.77 (1.70)
		115 (253.7)	180.4 (397.6)

293-1 (651-3)

Table 7-3
HEAT TRANSFER SUMMARY FOR THE SPACE TUG MICROSHERE
INSULATION SYSTEM

Item	Orbit Heat Leak, W (Btu/hr) $T_H = 222^\circ\text{K} (400^\circ\text{R})$		
	LO ₂ Tank	LH ₂ Tank	
Insulation			
• Microspheres	69.4 (236.8)	207 (707)	
• Spring/Kevlar Attachments	3.2 (11.0)	7.7 (26.5)	
• Lexan/Dacron Edges in Access Cover	0.30 (1.02)	0.62 (2.12)	
• SS Closeoff Bellows	0.67 (2.29)	0.98 (3.34)	
Tank Supports	0.33 (1.13)	0.33 (1.13)	
Plumbing			
• Pressurization Line	0.10 (0.34)	0.15 (0.51)	
• Feed Line Bayonet	0.61 (2.08)	0.89 (3.04)	
• Fill/Drain/Abort Bayonet	1.82 (6.21)	2.65 (9.04)	
• Ground Vent Line	0.61 (2.08)	0.89 (3.04)	
• Space Vent Lines (2 ea.)	0.10 (0.34)	0.15 (0.51)	
Thrust Cone	?	-	
Totals	77.1 (263.3)	221.4 (756.2)	
Space	Heat W/m ² Flux (Btu/hr ft ²)	2.1 (0.68)	2.9 (0.91)
Ground Hold	Heat W/m ² Flux (Btu/hr ft ²)	32 (10)	48 (15)
	T_H (Ground Hold)	283°K (510°R)	280°K (504°R)

7.4.1 Facilities and Tooling

Major facility and tooling requirements for the microsphere insulation system are provided in Table 7-4. The hydropress forming method developed on this program is used as a reference to establish these requirements.

7.4.2 Vacuum Jacket Forming

The hydropress jacket forming method was selected for the test article based on the following rationale:

- The forming method had been demonstrated previously on small panels
- Changes in the jacket tooling dimensions could be made if test results dictated changes
- The maximum size of the gore panel was constrained by the size of the available hydropress
- Assembly costs were not an overriding consideration since only one test article was being fabricated

However, once the basic design has been firmed up, there are other forming procedures such as explosive forming and electroless nickel plating that can be considered for the full-scale Space Tug that simplifies the assembly sequence for multiple assemblies as shown in Fig. 7-9. However, these methods have not been proven and would require additional development before they can be selected.

The explosive forming method consists of stretch forming gores, welding together a hemisphere and then explosively forming the wedges in a one-step operation while immersed under water.

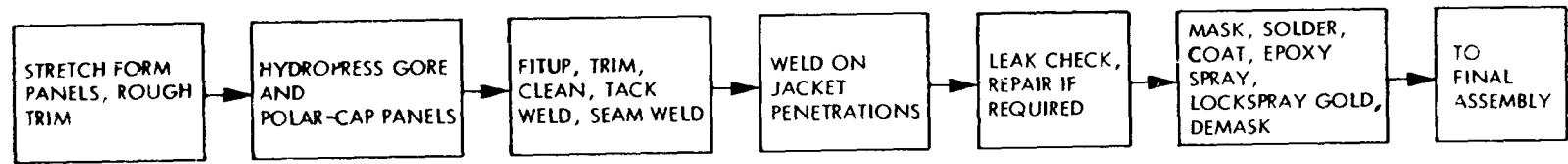
The electroless nickel deposition method deposits a nickel layer inside a rubber female die, shown in Fig. 7-10, allowing a seamless hemisphere to be made. Thickness can be controlled to approximately 10 percent over complex shapes based on small-scale deposition tests.

Table 7-4
 MAJOR FACILITIES AND TOOLING REQUIREMENTS
 (HYDROPRESS FORMING)

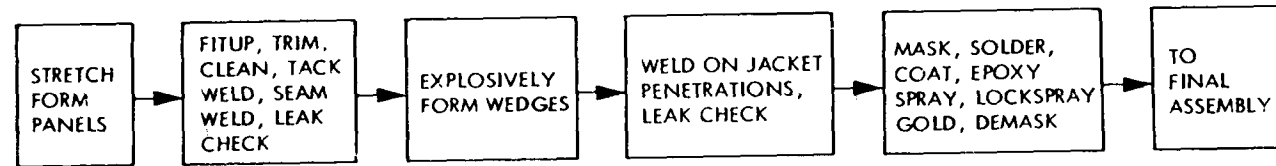
<p>Major Facilities and Equipment</p> <p>LAC3026-030000 Working Area (Good Housekeeping)</p> <p>Large Spray Booth</p> <p>Overhead Cranes</p> <p>Hydropress</p> <p>Stretch Press</p> <p>Resistance Seam Welder</p> <p>He Mass Spectrometer Leak Detector</p> <p>Vacuum Oven</p> <p>Jacket Forming Dies</p> <p>LH₂ Jacket</p> <ul style="list-style-type: none"> ● Two stretch form dies ● Four gore dies ● One polar cap die (includes mating vertical and horizontal gore wedges in pattern) <p>LO₂ Jacket</p> <ul style="list-style-type: none"> ● Three stretch form dies ● Three gore dies ● Two polar cap dies (includes mating vertical and horizontal gore wedges in pattern) 	<p>Jacket Welding and Leak-Checking Fixtures</p> <p>LH₂ Jacket (2 ea.)</p> <p>LO₂ Jacket (2 ea.)</p> <p>Jacket and Tank Handling Fixtures</p> <p>Major LH₂ Jacket Subassemblies (4 ea.)</p> <p>Major LO₂ Jacket Subassemblies (2 ea.)</p> <p>Tank Rotation Fixture (2 ea.)</p> <p>Jacket Storage Fixtures</p> <p>For Small Gores and Polar Cap Panels (200 ea.)</p> <p>For Major Jacket Subassemblies (12 ea.)</p> <p>Microsphere Processing Equipment</p> <p>Air Fractionation</p> <p>Compression</p> <p>Flotation</p> <p>Bakeout</p> <p>Storage</p> <p>Transfer</p>
---	---

7-17

HYDRO-PRESS-JACKET FABRICATION SEQUENCE



EXPLOSIVE-FORM-JACKET FABRICATION SEQUENCE



ELECTROLESS-NICKEL-DEPOSITION-JACKET FABRICATION SEQUENCE

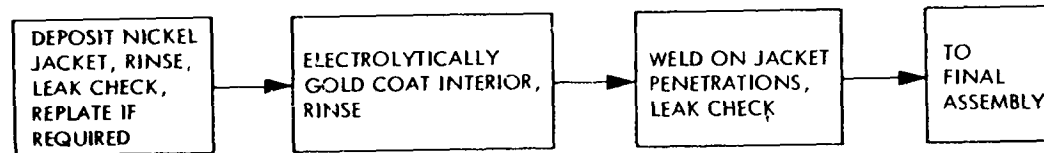


Fig. 7-9 Comparison of Jacket Forming Methods

7-19

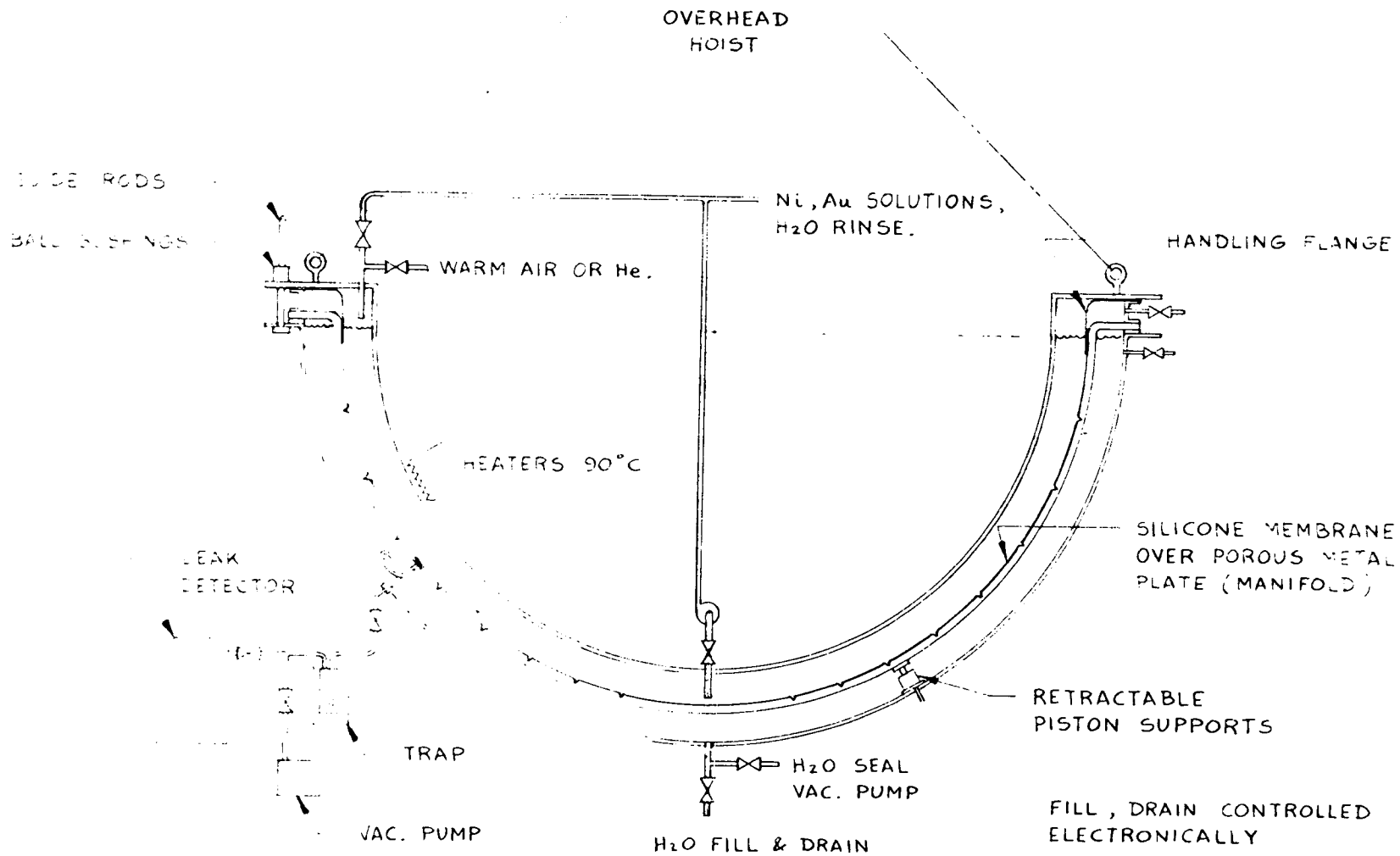


Fig. 7-10 Electroless Nickel Jacket Fabrication Method

Table 7-5 shows the advantages and disadvantages of the two methods as compared with the reference hydropress method. The electroless nickel deposition method appears to offer the greatest potential cost savings by minimizing welded joint lengths, leak checking and repair time, assembly steps, tooling costs, and labor requirements. The nickel coating, however, is slightly heavier than an equivalent stainless steel jacket and may be more brittle. Porosity of nickel coatings have also been a problem in previous work.

7.4.3 Vacuum Jacket Joining

All joints in the vacuum jacket will be resistance seam welded using the methods developed on this program. The location of the final closure joints selected for the LH₂ jacket is pattern 1 in Table 7-6. This pattern minimizes the length of the closure joint over patterns 2 or 3; however, it was judged to be more difficult to install than pattern 3. The final closure joint on the LO₂ tank is located at the equator. Design of the final closure joint was shown previously in Fig. 7-2, Detail E. All strut enclosures and plumbing penetrations are welded into the jacket.

7.4.4 Gold Coating

The epoxy/Lockspray gold coat is applied to the tank using the methods developed on this program. Circular areas for spring attachments need not be masked off; the spring assemblies can be bonded over the coating with good adhesion.

The gold on the inside of the vacuum jacket is deposited in the same manner for hydropress or explosively formed jackets and electrolytically if a nickel jacket is selected. Electrolytic coatings eliminate the need for the spring attachment solder precoat; in addition, there are no joints to be masked off as is the case for the other two forming methods. Electrolytic gold coatings were demonstrated on the strut box interiors in this program.

Table 7-5


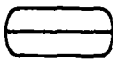
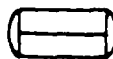
COMPARISON OF FORMING METHODS

Item	Hydropress (Reference)	Explosive Form	Electroless Nickel Deposition
Number of major handling steps which may produce jacket damage after wedges are formed	<ul style="list-style-type: none"> ● Trim panels ● Weld panels ● Leak check ● Remove, install 	<ul style="list-style-type: none"> ● Leak check ● Remove, trim, install 	<ul style="list-style-type: none"> ● Remove, trim, install.
Length of LH ₂ jacket welded joints, (a) m (ft)	393 (1290)	250 (821)	49 (160)
Cost risk if wedge forming produces unacceptable part	Low; lose only one gore	High; lose dome that has been stretch formed, joined, leak checked	Fairly low; lose 2 to 3 days of plating time
ΔP across jacket during leak checking	2.5 cm (1 in.) of H ₂ O; 1 atm over local areas	1 atm	1 atm
Is hard tooling required?	Yes	No	No
Development risk items	—	Forming development, forming over welded joints, part removal	Plating development, nickel properties, part removal
LH ₂ jacket weight differences (%)	0 (Ref.)	-1.0	+ 7.4

(a) Test tank demonstrated on this program has welded joints 23 m (76 ft) long.

Table 7-6

COMPARISON OF FINAL CLOSURE JOINT LOCATIONS FOR THE LH₂ JACKET

Final Joint Pattern	Size of Die(s) m ² (ft ²)	Length of Final Closure Joint m(ft)	Are Special Joining Procedures Required?	Ease of Installation on the Tank
2 parts 1. 	38 (414)	20 (68)	No	2 (cylinder clearance)
2 parts 2. 	38 (414)	25 (85)	Yes, around polar cap wedges and into end caps	2 (strut attach-point clearance)
4 parts 3. 	38 (414)	49 (160)	No	1 ^(a)

(a) Easiest.

7.4.5 Spring Assembly Fabrication

To minimize assembly costs as well as the heat leak, the cylindrical spring assembly with three Kevlar tiedowns used on the program was changed to a conical tapered spring design (Fig. 7-2, Detail F) with a single Kevlar tiedown. Chem-milling of the tapered spring and filament winding of the central Kevlar strand around two end pins needs to be demonstrated.

7.4.6 Microsphere Insulation Processing

The microsphere processing steps developed on this program and recommended for the Space Tug are:

- Sizing by air fractionation
- Compression to 1.33 atm

- Separation of unbroken spheres by flotation
- Vacuum bakeout at 421°C (790°F) at pressures of .0013 Pa for 60 days

7.4.7 Final Assembly

The proposed final assembly sequence for the LH₂ tank shown in Fig. 7-11 is self-explanatory.

The LO₂ tank installation is similar and was demonstrated on the test article (as its final closure joint is also at the equator).

7.5 OPERATIONAL REQUIREMENTS

The following equipment and supplies are required to support the operation of the microsphere insulation system:

- An oil-free ground pumping station consisting of absorption pumps and turbomolecular pumps
- Pumping speed of 500 liters/s
- Ultimate vacuum < .0013 Pa
- A helium mass spectrometer leak detector, special rubber forms for bagging different sections of the jacket, and a helium gas supply
- Crest adhesive and oven
- Pressure gage readouts

Following initial evacuation, the insulation system will require periodic evacuations over its lifetime of approximately 5 years to maintain a pressure below .013 Pa.

Inspection and refurbishment requirements summarized in Table 7-7 are compared with the reference helium purged Superfloc system.

If a jacket leak develops, the helium mass spectrometer is used to pump on the insulation. Areas are bagged using the rubber forms and flooded with helium to pinpoint the leak. The leak is repaired with the flexible low temperature Crest adhesive.

7-24

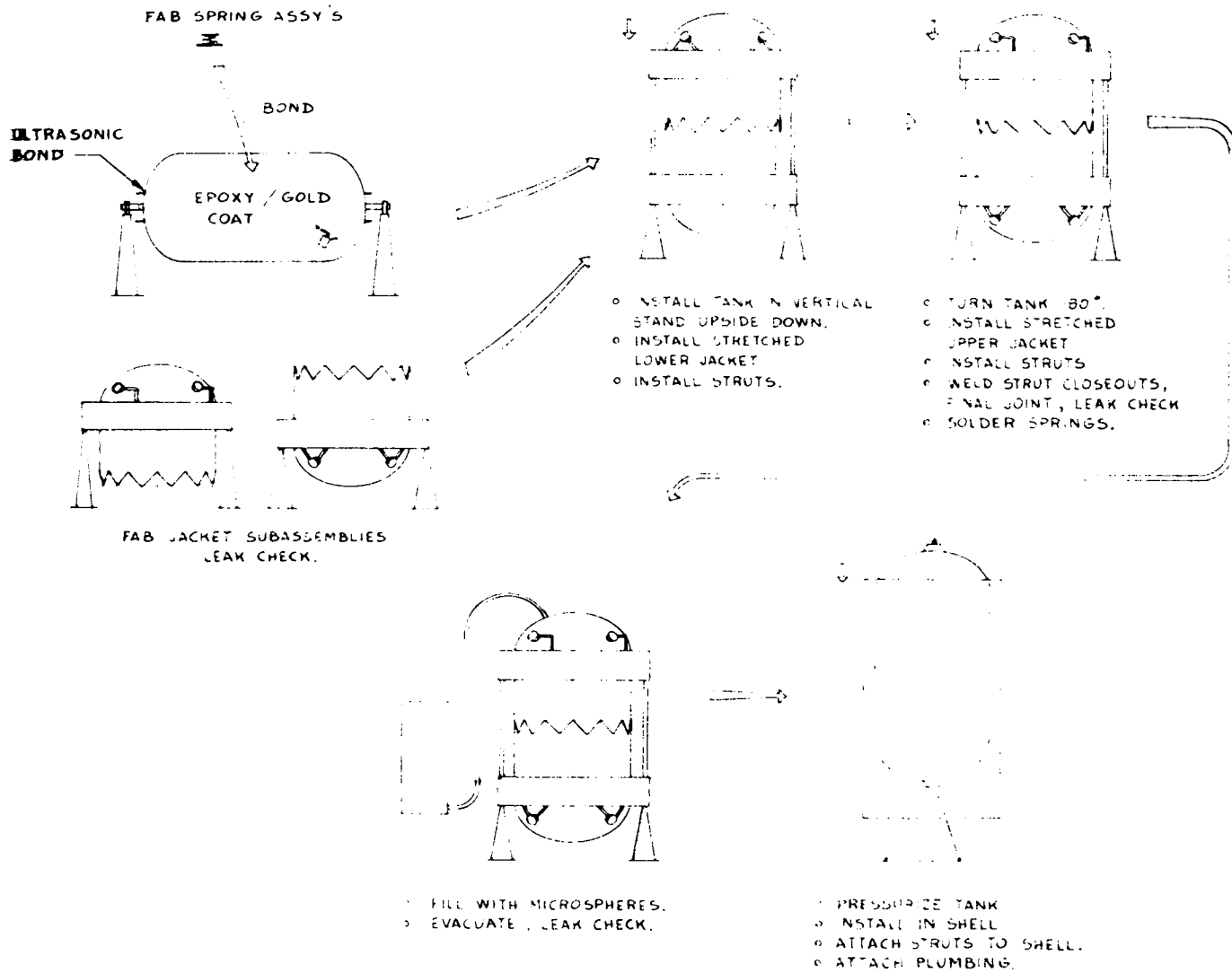


Fig. 7-11 Liquid Hydrogen Tank Final Assembly Sequence

Table 7-7

MICROSPHERE INSULATION SYSTEM INSPECTION
AND REFURBISHMENT REQUIREMENTS

Helium Purged Superfloc Requirements	Microsphere System Requirement
Monitor Boiloff or Pressure Rise During Ground Hold and Orbit	Yes
Visual Inspection of System After Each Flight—	Yes (until experience is gained with system)
Leak Test System After Each Flight	Monitor vacuum jacket pressure during flight and on the ground
Functional Test of System After Each Flight	<ul style="list-style-type: none"> ● Check ion pump operation ● Check jacket overpressure relief system ● Monitor vacuum jacket pressure
No Scheduled Replacements for 20 Flights	<ul style="list-style-type: none"> ● No scheduled replacements for 20 flights ● Ion pumps good for 50 flights (turned on only during flight)
Load Helium for each flight	Periodic re-evacuation may be required or insulation may be vented to space in orbit

7.6 SCHEDULE AND COSTS

The DDT&E schedule for bringing the microsphere/ flexible jacket insulation system to flight qualified status is shown in Fig. 7-12.

Following a development phase, engineering models of both the LO₂ and LH₂ insulated tanks are designed, fabricated, and tested as follows: simulated ground hold and space thermal performance tests, 24 simulated thermal/pressure flight cycles, plus vibration and acoustic tests. A qualification model (where the insulated tanks are installed in a complete Space Tug) is used for a system checkout of the Tug. Following qualification, 17 tugs are fabricated, one every 3.5 months over a 5-year period. This DDT&E schedule could be compressed from 5 to 3.7 years if required.

Cost analyses of the microsphere insulation/flexible jacket system are made using the same manpower categories and costing ground rules given in Ref. 1-3, so direct comparisons with the helium purged Superfloc system can be made. Labor rates used are LMSC averages for the calendar year 1973 and are different from the rates in Ref. 1-3. Fee and GFE furnished cryogenics are not included in the DDT&E costs. Costs for the microsphere processing equipment, spring assembly development, and major tooling are given in Tables 7-8, 7-9, and 7-10. The engineering model costs are provided in Tables 7-11 and 7-12 while the qualification model costs are shown in Tables 7-13 and 7-14.

The total costs for the program (DDT&E, production, and operations) are compared with the helium purged Superfloc system in Table 7-15 and summarized in Table 7-16.

7.7 PERFORMANCE COMPARISON WITH GOALS

A series of weight, thermal performance, and payload performance goals were established in section 2.1, based on data from an analytical study of the Space Tug given in Ref. 1-3. The same company that performed the study demonstrated this insulation concept under another contract (Ref. 1-4) on a 2.23-m (7.3-ft) diameter oblate spheroidal tank. The insulation (Superfloc) ground hold method (helium purge) and mode of operation (reusable) are the same as recommended in the Space Tug study. Therefore, to compare scaled hardware weights from this program against scaled hardware weights for the helium purged Superfloc system, a weight statement was developed as shown in Table 7-17. Note the Superfloc insulation weights, shuttle cargo bay weights, and insulation heat rates (boiloff) were kept identical with the analytical study. The weights of the purge bag, purge distribution hardware, and purge fairing were scaled using a weight/unit area relationship. The penetration panel weights were kept the same as the test panel.

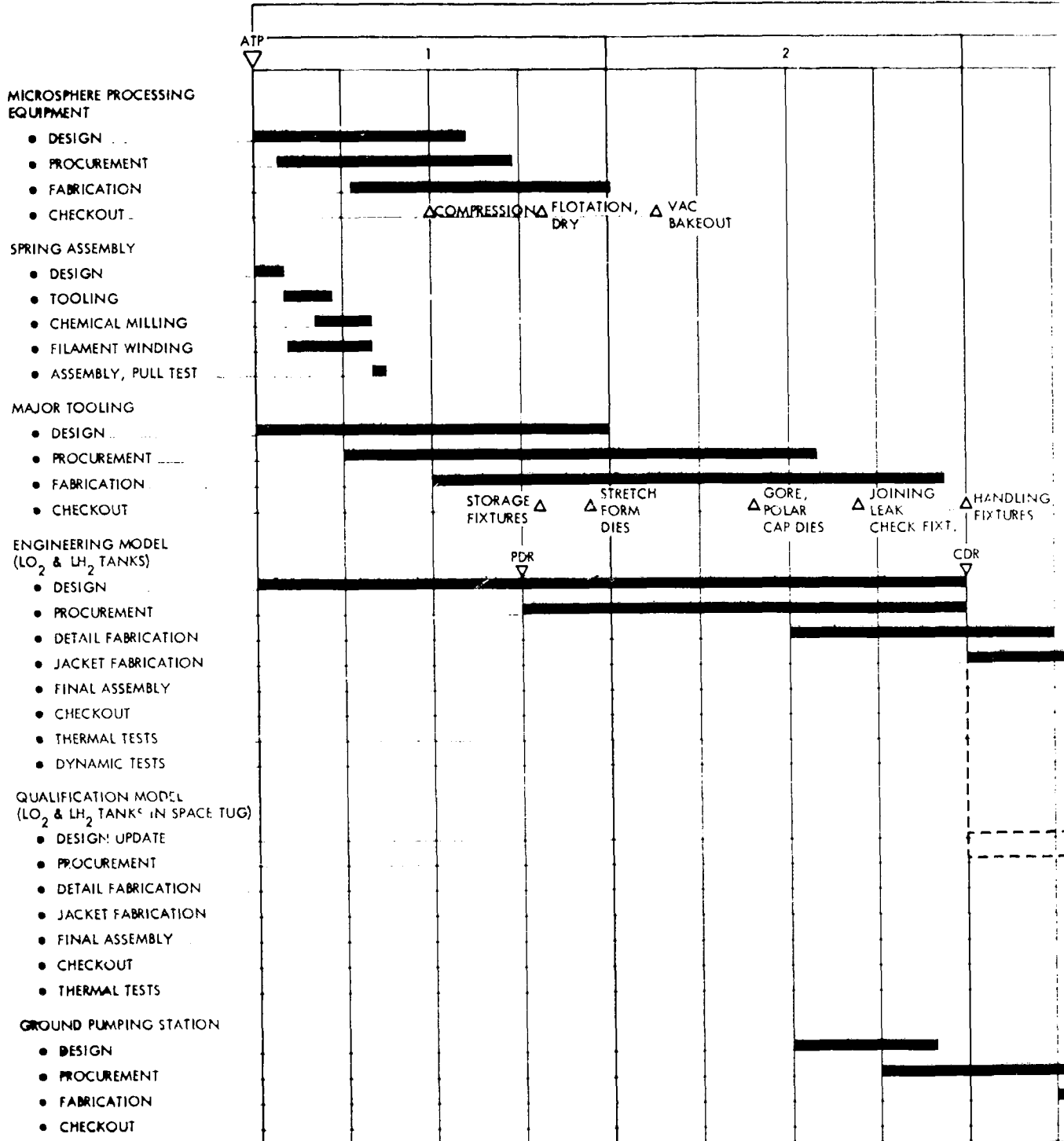
Prorated burnout weight comparisons of the systems in Tables 7-17 and 7-18 for a 163-hour mission show the following:

	kg (lb)	Change (%)
Goal	192.4 (424)	-
Microsphere System	429.8 (948)	+ 124
Superfloc System	559 (1232)	+ 191

7-26

LOCKHEED PALO ALTO RESEARCH LABORATORY
 LOCKHEED MISSILES & SPACE COMPANY, INC.
 A SUBSIDIARY OF LOCKHEED AIRCRAFT CORPORATION

FOLDOUT FRAME 1



FOLDOUT FRAME 2

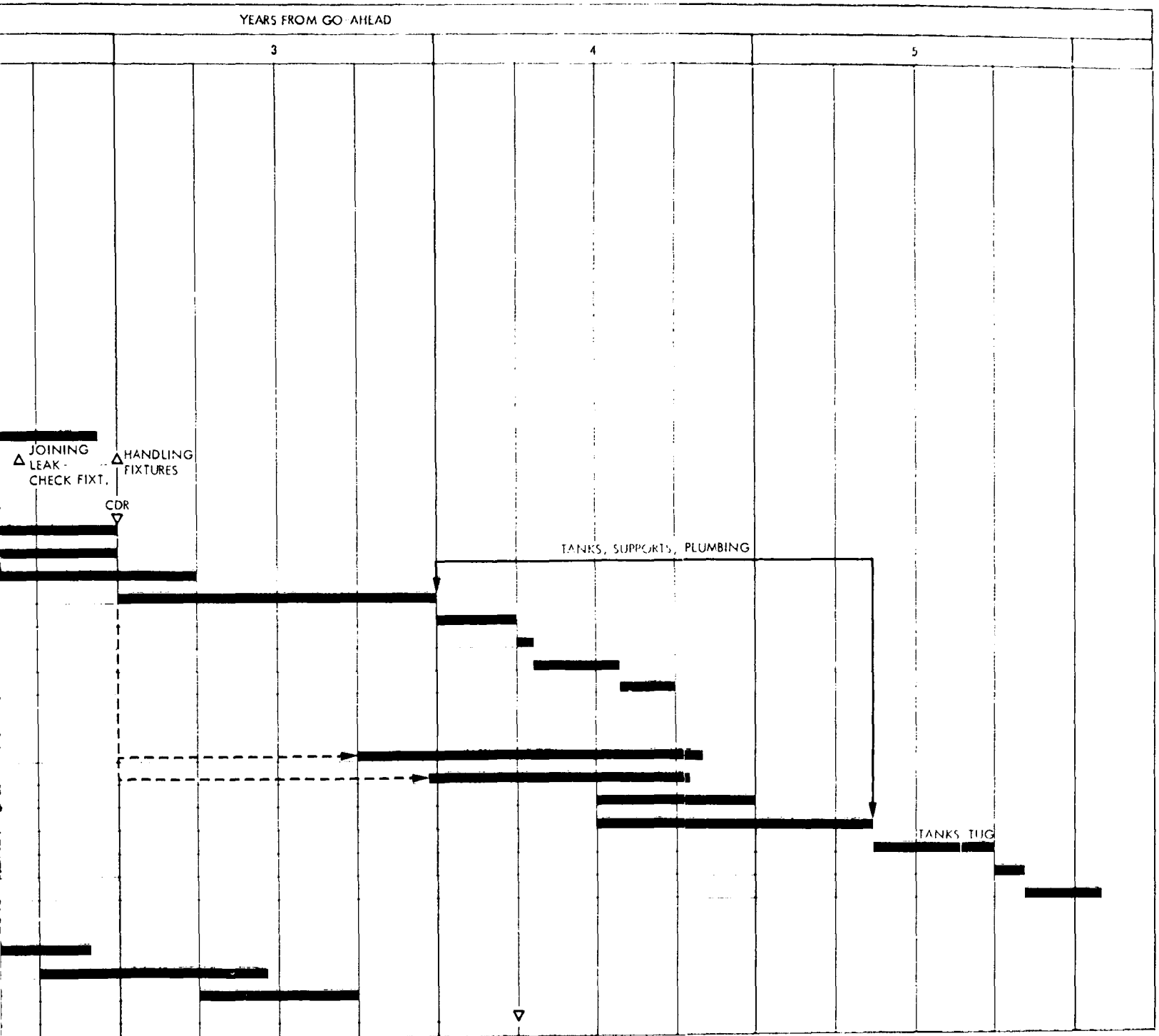


Fig. 7-12 Microsphere Insulation System DDT&E Schedule

Table 7-8
 DDT&E COST BREAKDOWN FOR MICROSPHERE PROCESSING EQUIPMENT
 (HOURS AND 1973 DOLLARS IN THOUSANDS)

	Engineering		Tooling		Test/ Evaluation		Program Management	
	Hr	\$	Hr	\$	Hr	\$	Hr	\$
• Compression	0.2	4	0.3	6	0.3	3		
• Flotation	0.6	12	1.5	30	1.0	17		
• Drying	0.5	10	0.9	18	0.2	3		
• Vacuum Bakeout	0.6	12	1.3	26	0.5	14		
Subtotal	1.9	38	4.0	80	2.2	37	1.2	24

TOTAL

Hr 9.3

\$179

Table 7-9
 DDT&E COST BREAKDOWN FOR SPRING ASSEMBLY DEVELOPMENT
 (HOURS AND 1973 DOLLARS IN THOUSANDS)

	Engineering		Tooling		Test/ Evaluation		Program Management	
	Hr	\$	Hr	\$	Hr	\$	Hr	\$
• End Plate Tooling	0.2	4	0.1	3	0.1	2		
• Spring Chem-Milling	0.4	8	0.4	9	0.4	8		
• Filament Winding and Assembly	0.6	12	0.7	14	0.4	8		
Subtotal	1.2	24	1.2	26	0.9	18	0.5	10

TOTAL

Hr 3.8

\$78

Table 7-10
 DDT&E COST BREAKDOWN FOR JACKET TOOLING AND FIXTURES
 (HOURS AND 1973 DOLLARS IN THOUSANDS)

	Engineering		Tooling		Test/ Evaluation		Program Management	
	Hr	\$	Hr	\$	Hr	\$	Hr	\$
<u>Jacket Tooling</u>								
5 Stretch Form Dies	0.6	12	1.3	28	0.6	12		
7 Gore Form Dies	3.4	69	8.8	178	5.2	105		
3 Polar Cap Dies	1.0	21	2.4	50	1.9	39		
<u>Jacket Welding & Leak- Checking Fixtures</u>								
3 End Closures	2.2	45	11.2	204	6.0	120		
1 Cylindrical Section	0.9	18	3.8	74	2.1	42		
<u>Jacket Storage Fixtures</u>								
200 Small Panels	0.2	4	2.0	39				
12 Major Subassemblies	1.6	32	4.8	95				
<u>Jacket Handling Fixtures</u>								
6 Fixtures	2.8	56	6.0	110	0.4	7		
Subtotal	12.7	257	40.3	778	16.2	325	7.8	155

TOTAL
 Hr 77
 \$1515

Table 7-11

DDT&E ENGINEERING MODEL COST BREAKDOWN (LO₂ INSULATION SYSTEM)
(HOURS AND 1973 DOLLARS IN THOUSANDS)

	Engineering		Test/ Evaluation		Production		Program Management	
	Hr	\$	Hr	\$	Hr	\$	Hr	\$
Design, Documentation	6.0	119						
Microsphere Processing	0.2	4			0.2	10		
Spring Assemblies Fab.	0.2	1			0.4	8		
Jacket Fabrication								
• Form	0.4	8			0.4	10		
• Trim. Join (Including penetrations)	1.0	20			3.8	62		
• Leak Check	1.0	18			1.0	16		
• Solder Coat	0.2	4			0.2	4		
• Gold Coat	0.4	6			0.6	11		
Tank Assembly								
• Gold Coat	0.4	6			0.4	10		
• Bond Springs	0.4	6			0.6	10		
• Assemble Jacket, Struts, Plumbing	1.6	32			2.6	41		
• Leak Check	0.4	8			0.4	8		
• Join Springs	0.4	8			0.6	10		
• Fill With Microspheres	0.8	16			0.8	11		
• Instrument	1.6	32			1.8	30		
Evacuation Tests	0.5	9	0.9	18				
Thermal Performance Tests	3.8	75	11.2	224				
• 24 Thermal/Pressure Flight Cycles	6.0	120	15.0	299				
• Vibration Test	1.0	20	3.0	60				
• Acoustic Test	0.8	16	2.0	40				
Subtotal	27.1	531	32.1	641	13.8	194	6.0	119

TOTAL

Hr 79

\$1455

Table 7-12

DDT&E ENGINEERING MODEL COST BREAKDOWN (LH₂ INSULATION SYSTEM)
(HOURS AND 1973 DOLLARS IN THOUSANDS)

	Engineering		Test/ Evaluation		Production		Program Management	
	Hr	\$	Hr	\$	Hr	\$	Hr	\$
Design, Documentation	7.8	155						
Microsphere Processing	0.2				0.6	18		
Spring Assemblies Fab.	4.2	4			0.6	14		
Jacket Fabrication								
• Form	0.8	16			0.8	18		
• Trim, Join (including penetrations)	2.0	40			7.2	122		
• Leak Check	1.8	36			1.8	30		
• Solder Coat	0.2	4			0.2	4		
• Gold Coat	0.6	12			1.2	24		
Tank Assembly								
• Gold Coat	0.6	12			0.8	18		
• Bond Springs	0.4	8			1.0	16		
• Assemble Jacket, Struts, Plumbing	2.0	40			3.2	54		
• Leak Check	0.6	12			0.6	10		
• Join Springs	0.4	8			1.0	16		
• Fill With Microspheres	1.2	24			1.2	20		
• Instrument	2.0	40			2.2	38		
Evacuation Tests	0.6	12	1.2	24				
Thermal Performance Tests	4.5	90	13.5	269				
• 24 Thermal/Pressure Flight Cycles	6.0	120	15.0	299				
• Vibration Test	1.0	20	3.0	60				
• Acoustic Test	0.8	16	2.0	40				
Subtotal	33.7	673	34.7	692	22.4	402	7.2	143

TOTAL

Hr 98

\$1910

Table 7-13

DDT&E QUALIFICATION MODEL COST BREAKDOWN (LO₂ INSULATION SYSTEM)
(HOURS AND 1973 DOLLARS IN THOUSANDS)

	Engineering		Test/ Evaluation		Production		Quality Control		Program Management	
	Hr	\$	Hr	\$	Hr	\$	Hr	\$	Hr	\$
Microsphere Processing					0.1	5				
Spring Assemblies Fab.					0.2	4				
Jacket Fabrication										
• Form					0.2	1				
• Trim. Join (Including Penetration)	0.3	6			1.6	26				
• Leak Check	0.4	8			0.5	8				
• Solder Coat					0.1	2				
• Gold Coat	0.1	2			0.3	7				
Tank Assembly										
• Gold Coat	0.1	2			0.2	5				
• Bond Springs					0.2	5				
• Assemble Jacket, Struts, Plumbing	0.4	8			1.1	19				
• Leak Check	0.2	4			0.2	4				
• Join Springs	0.2	4			0.3	5				
• Fill With Microspheres	0.3	6			0.3	6				
• Instrument	0.3	6			0.4	8				
Thermal Performance Tests	Included in LH ₂ Costs									
Subtotal	2.3	4.6			5.7	108	3.0	60	4.8	94

TOTAL
Hr 15.8
\$308

7-33

Table 7-14

DDT&E QUALIFICATION MODEL COST BREAKDOWN (LH₂ INSULATION SYSTEM)
(HOURS AND 1973 DOLLARS IN THOUSANDS)

	Engineering		Test/ Evaluation		Production		Quality Control		Program Management	
	Hr	\$	Hr	\$	Hr	\$	Hr	\$	Hr	\$
Microsphere Processing					0.3	9				
Spring Assemblies Fab.					0.3	7				
Jacket Fabrication										
• Form					0.3	7				
• Trim. Join (Including penetrations)	0.5	10			3.0	51				
• Leak Check	0.8	16			0.8	13				
• Solder Coat					0.1	2				
• Gold Coat	0.1	2			0.6	12				
Tank Assembly										
• Gold Coat	0.1	2			0.4	9				
• Bond Springs					0.4	7				
• Assemble Jacket, Struts, Plumbing	0.5	10			1.4	24				
• Leak Check	0.2	4			0.3	5				
• Join Springs					0.4	6				
• Fill With Microspheres	0.4	8			0.4	7				
• Instrument	0.4	8			0.5	10				
Thermal Performance Tests	1.5	30	6.0	119						
Subtotal	4.5	90	6.0	119	9.2	169	6.3	129	12.4	247

TOTAL

Hr 38.4

\$754

7-34

Table 7-15
 INSULATION SYSTEMS COST BREAKDOWN COMPARISON^(a)
 (HOURS AND 1973 DOLLARS IN THOUSANDS)

Insulation System	1973		1973		1973		1973		1973		Total	%
	Hours	\$	Hours	\$	Hours	\$	Hours	\$	Hours	\$		
• Fiberglass Insulation	100	100	100	100	100	100	100	100	100	100	100	100

• Polyurethane Insulation

• Other Insulation

Total

REPRODUCIBILITY OF THE ORIGINAL PAGE IS POOR

Table 7-16

**INSULATION SYSTEMS COST COMPARISON SUMMARY
(MILLIONS OF 1973 DOLLARS)**

	Helium Purged Multilayer System			Microsphere System (Hydropress Formed Jacket)
	Insulation	Controls	Orbiter Purge System	
<u>Nonrecurring Costs</u>	(Includes Qualification Model)			
Eng. & Dev. (DDT&E)		1.3	2.6	8.1 (Includes Engineer- ing and Qualifi- cation Models)
LO ₂ Insulation	0.7			
LH ₂ Insulation	8.5			
Ground Hardware				
LO ₂ Insulation	0.2		0.8	0.2 } Pumping System,
LH ₂ Insulation	0.3			0.2 } Leak Detection System
Subtotal	9.7	1.3	3.4	
Total	14.4			8.5
<u>Recurring Costs</u>				
Production 17 Flights		1.0 (0.14) ^(a)	1.3 (0.837) ^(a)	
LO ₂ Insulation	2.5 (0.226) ^(a)			2.0 (0.189) ^(a)
LH ₂ Insulation	3.8 (0.318) ^(a)			3.3 (0.293) ^(a)
Initial Spares	0	0.2	0.6	0.1
Operations (243 Flights)		1.3	1.9	
LO ₂ Insulation	0.5			0.08
LH ₂ Insulation	0.9			0.08
Subtotal	7.7	3.1	6.8	
Total	17.7			5.6

(a) First Unit.

Table 7-17

HELIUM-PURGED SUPERFLOC INSULATION SYSTEM WEIGHT

	LO ₂ Tank kg	LH ₂ Tank kg	Total Prorated Burnout Weight kg
● Superfloc Multilayers ^(a)	18.6	39.0	57.6
● Purge Bag ^(b)	62.2	129.5	191.7
● Purge Distribution Hardware ^(b)	2.3	5.0	7.3
● Purge Fairing ^(b)	65.2	138.3	203.5
● Penetration Panel ^(b)	28.0	28.0	56.0
● Shuttle Cargo Bay ^(a) Related Weights		38.6	5.8
● Boiloff ^(a)		94.2	36.7
		Total kg (lb)	559 (1232)

(a) Same as goals.

(b) Scaled from hardware weights in Ref. 1-4.

Table 7-18

INSULATION SYSTEM WEIGHT COMPARISON

	Goal		Microsphere System	
	Weight kg	Prorated Burnout Weight kg	Weight kg	Prorated Burnout Weight kg
LO ₂ Insulation System	18.6	18.6	116.8	116.8
LH ₂ Insulation System	39.0	39.0	180.4	180.4
Tug Purge System	92.1	92.1	-	-
Shuttle Cargo Bay Related Weights	38.6	5.8	-	-
Boiloff ^(a)	94.2	36.7	340	132.6
	Totals: kg (lb) = 492.2 (1211)		129.8 (948)	

(a) 163-Hour Mission.

Table 7-19 provides the thermal performance comparison of the systems. In this case, the goal and Superfloc helium-purged system are assumed to be the same. The microsphere system is superior by a factor of 6.2 to 7.3 during ground hold, but the Superfloc system is superior in space by a factor of 2.7 to 4.9 because of the high radiation heat transfer through the uncoated microspheres.

Synchronous equatorial payload performance comparisons for deployment, retrieval, and round trip missions are shown in Table 7-20 and summarized here.

	Change (%)
Goal	-
Microsphere System	- 11.6
Superfloc System	- 26.4
Superfloc System (w/o Purge Fairing)	- 11.7

The Superfloc system and microsphere system are comparable if the purge fairing used to distribute the helium gas beneath the Superfloc layers is eliminated; otherwise, the microsphere system is superior.

7.8 PAYLOAD SENSITIVITY ANALYSES

The effect of changing microsphere bulk density, microsphere conductivity, and boundary emittances on payload performance was calculated.

As can be seen from Fig. 7-13, payload performance improves only slowly as bulk density decreases. On the other hand, decreasing the thermal conductivity using insulation thicknesses optimized for a 163-hour mission provides a more rapid improvement in payload performance as shown in Fig. 7-14. Improving the quality of gold surfaces over that of the test article and assuming the solid conduction goes to 0 in low gravity results in an 8% improvement as shown in Fig. 7-14.

Table 7-19
INSULATION SYSTEM THERMAL PERFORMANCE COMPARISON

	Equivalent Boiloff					
	Ground Hold kg/hr (lb/hr)		Space $T_H = 222^\circ\text{K}$ (400°R) kg/hr (lb/hr)		Integrated Mission, Lift Off to Last Burn at 163 hr kg(lb)	
	LO ₂	LH ₂	LO ₂	LH ₂	LO ₂	LH ₂
Goal	123 (271)	219 (483)	0.48 (1.06)	0.37 (0.83)	29 (64)	65 (144)
Microsphere System	20 (44)	30 (66)	1.3 (3.0)	1.8 (4.0)	16 (103)	294 (648)

Table 7-20
INSULATION SYSTEM SYN-EQ. PAYLOAD PERFORMANCE COMPARISON

	Performance Partial(s) Used		
	$\frac{\partial P/L}{\partial W_{\text{cargo bay}}}$	$\frac{\partial P/L^{(a)}}{\partial W_{\text{inert}}}$	$\frac{\partial P/L}{\partial W_{\text{boiloff}}}$
Deployment	- 0.39	- 2.6	- 0.98
Retrieval	- 0.24	- 1.6	- 0.60
Round Trip	- 0.15	- 1.0	- 0.39 ^(a)

(a) From Ref. 2-1.

Event	Goal kg (lb)	Microsphere System	Payload Performance Change (%)	
			He-Purged Multilayer System	
			With Purge Fairing	Without Purge Fairing
Deployment	≥ 3597 (7930)	- 11.6	- 26.5	- 11.8
Retrieval	≥ 2260 (4982)	- 11.4	- 25.9	- 11.5
Round Trip	≥ 1370 (3020)	- 11.8	- 26.7	- 11.9

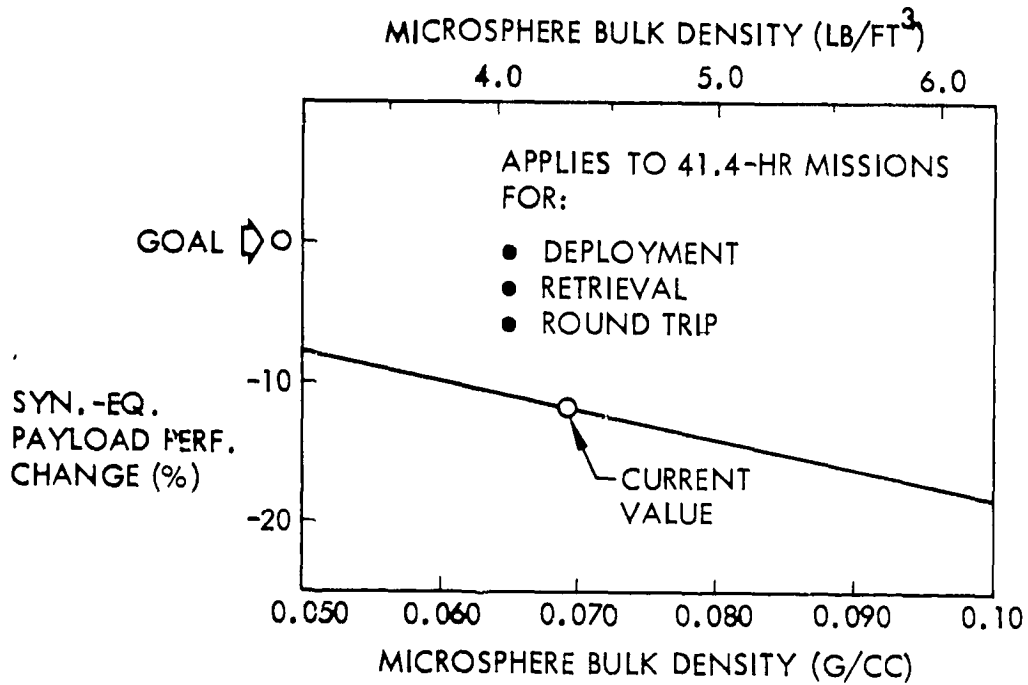


Fig. 7-13 Payload Performance Sensitivity to Microsphere Bulk Density

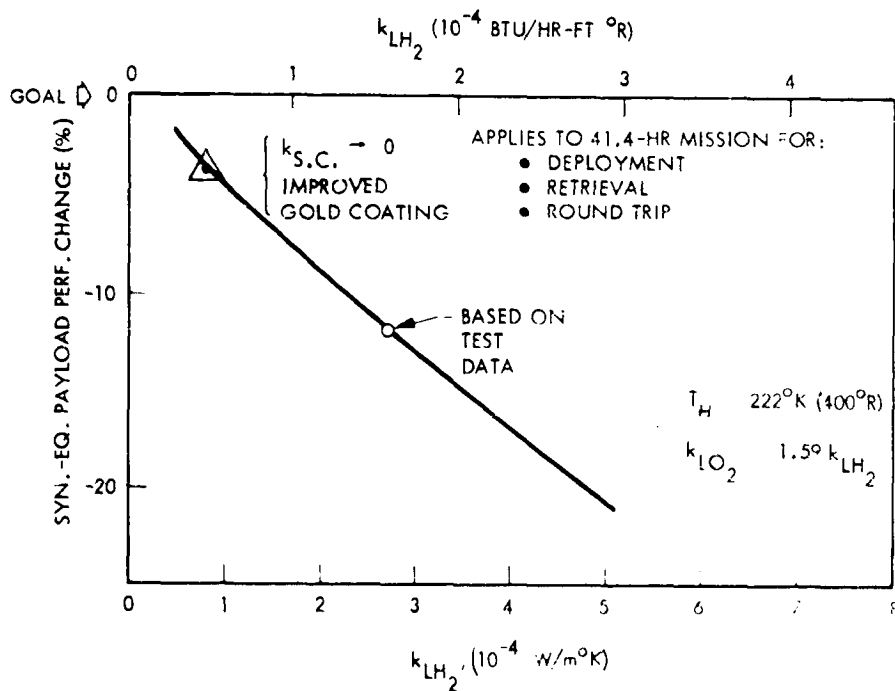


Fig. 7-14 Payload Performance Sensitivity to Microsphere Thermal Conductivity

7-4(i)

Section 8
CONCLUSIONS

Based on the results of this development program, the microsphere/flexible jacket system performed successfully; the required engineering data are now available to scale the system to other tank sizes, shapes and applications. Detailed conclusions from the program follow:

- The spherical vacuum jacket expands and contracts in the elastic range. Design equations quantify the stress/strain curves and elastic limit as a function of wedge dimensions and strain. Uniform radial strain as a function of membrane stress up to the elastic limit for tank shrinkage and expansion is the criterion used for sizing the wedge height.
- The jacket wedges should point inward toward the tank if the system is designed to operate continuously in the atmosphere (does not apply to the Space Tug).
- The above wedge configuration minimizes the chance of accidental wedge damage (if the required insulation thickness is sufficient to permit this design).
- The formed 321 stainless steel jacket expansion wedges, stiffened areas, and 0.08 mm (0.003 in.) thick membrane areas remained vacuum leak-tight for the 13 flight cycles. The jacket area is 4.5 m^2 (48 ft^2).
- The 23.2 m (76 ft) of welded jacket joint remained vacuum leak-tight for the 13 flight cycles.
- The soldered jacket final closure joint was highly unreliable and should be replaced with a new welded joint of the design type shown in the report.
- Vacuum pressure in the 10^{-3} to 10^{-5} Pa range was obtained in the insulation as compared to the required value of 10^{-2} Pa under no load and 1 Pa under 1-atmosphere load. Pumpdown times to 1 Pa from 1 atmosphere required approximately 6 hours; lower pressures were obtained by cryo-pumping action of residual CO_2 in the insulation. Below 1 Pa, the evacuation time was controlled by the filter screens (designed to prevent flow of microspheres into the pumps). Higher flow conductance screens and larger filter areas are needed to reduce pumpdown time in the free molecular regime.

- The fluidizing technique is a rapid, efficient method for filling the jacket with microspheres.
- The interior volume of microspheres can be evacuated using a vacuum bakeout technique.
- The rigid vacuum-jacket, tank support strut covers should be changed to a thin-walled, convoluted, diaphragm-type design to load the microspheres and prevent flow of microspheres under load from the jacket into the strut region. This design would prevent the buckling that occurred in the wedges surrounding the struts (none of the damaged wedges leaked).
- The thermal performance of the insulation under no external load at 1-g is dominated by radiation heat transfer (80% radiation, 20% solid conduction). Future improvements in the insulation for no load applications should concentrate on reducing radiation heat transfer.
- The thermal conductivity of the insulation under 1-atmosphere load remained constant after seven flight cycles on the test tank and after a hundred 1-atmosphere load cycles in flat plate tests. Space Tug conductivity for the LH₂ tank is 3.8×10^{-3} W/m²°K (2.2×10^{-3} Btu/hr-ft-°R), 280 to 20°K.
- The thermal conductivity of the insulation under no load remained constant through seven flight cycles on the test tank (within the accuracy of the test measurement). No change occurred following a hundred 1-atmosphere load cycles in flat plate tests. Space Tug conductivity for the LH₂ tank is 2.7×10^{-4} W/m²°K (1.6×10^{-4} Btu/hr ft °R), 222 to 20°K.
- A thermal model was developed that predicts microsphere thermal conductivity as a function of boundary temperatures and emittance, compressive load, and gas pressure.
- No significant shifting or breakage of the microspheres occurred after 13 flight cycles. Earlier flat plate tests showed the same results following a hundred 1-atmosphere compressive load cycles.
- Space Tug synchronous equatorial payload performance (for deployment, retrieval, and round-trip missions) was compared with a goal established in Task I. A purged multilayer system was compared with this goal as well.

Evacuated Microspheres (Hardware
Weights Scaled From the Test Tank)

- 11.6%
(- 3.2% with
improved gold
coatings and $k_{SC} \rightarrow 0$)

He Purged Multilayers (Hardware
Weights Scaled From Ref. 1-5)

- 26.4%
(-11.7%
w/o purge fairing)

- Advanced lower-cost methods for fabricating the jacket are shown in Section 7 and should be investigated in any future development work.

Section 9
REFERENCES

- 1-1 Lockheed Missiles & Space Company, Inc. Thermal Performance of Multi-Layer Insulations, Contract NAS 3-14377, NASA CR-134477, April 1974.
- 1-2 Goodyear Aerospace Corporation, Flexible Vacuum Jacket Development, Contract NAS 8-11376, Final Report, 22 Jun 1967 -
- 1-3 Linde Division of Union Carbide, Reusable Light Weight Modular Multilayer Insulation for Space Shuttle, Contract NAS 3-14366, CR-121166, Jul 1973
- 1-4 General Dynamics Convair Aerospace Division Reports:
Final Report CASD-NAS 83-033, Vols. I, II, III
Data Dump, Vol. II, Summary Option 2
Data Dump, Vol. 4.0, Mission Accomplishments
Data Dump, Vol. 5.0, System Book 2, Program 2
Data Dump, Vol. 6.0, Operations Book 1, Program 1
Data Dump, Vol. 6.0, Operations Book 2, Program 2
Data Dump, Vol. 7.0, Safety
Data Dump, Vol. 8.0, Programmatic and Cost Book 2, Program 2
- 1-5 General Dynamics Convair, Design and Development of Pressure and Re-pressurization Purge System for Reusable Space Shuttle Multilayer Insulation System
Contract NAS 8-27419, CASD-NAS-74-032, Final Report, Feb 1975
- 4-1 Lockheed Missiles & Space Company, Inc., Effect of Environment on Insulation Materials, Contract NAS 3-14342. Final Report, CR 120978, Feb 1973
- 6-1 J. C. Chen and S. W. Churchill, AIChE J., Vol. 9, No. 1, Jan 1963, p. 35
- 6-2 S. Masamune and J. M. Smith. Ind. Eng Chem Fundamentals, Vol. 2, 1963, p. 136
- 6-3 M. G. Kaganer, Thermal Insulation in Cryogenic Engineering, IPST Press, Jerusalem, 1969, p. 11

- 6-4 G. R. Cunnington and C. L. Tien, Advances in Cryogenic Engineering, Vol. 18, Plenum Press, New York, 1973, p. 103
- 6-5 C. L. Tien and G. R. Cunnington Advances in Heat Transfer, Vol. 9, Academic Press, New York, 1973, p. 349
- 6-6 M. M. Yovanovich and W. W. Kitscha, Prog. in Astro and Aero., Vol. 35, MIT Press, Cambridge, Massachusetts, 1974, p. 293
- 6-7 R. P. Reinker, K. D. Timmerhaus, and R. H. Kropschot, Advances in Cryogenic Engineering, Vol. 20, Plenum Press, New York, 1975, p. 343
- 6-8 C. K. Chan and C. L. Tien, J. Heat Transfer, 96:52, 1974
- 6-9 C. K. Chan and C. L. Tien, J. Heat Transfer, 95:302, 1973
- 6-10 C. K. Chan and C. L. Tien, Proceedings 5th Intern. Heat Transfer Conference, 1:72, 1974
- 6-11 A. L. Nayak and C. L. Tien, Advances in Cryogenic Engineering, Vol. 22, Plenum Press, New York, 1975, p. 251
- 6-12 G. R. Cunnington and C. L. Tien, Advances in Cryogenic Engineering, Vol. 22, Plenum Press, New York, 1975, p. 263
- 6-13 M. M. Yovanovich, "Apparent Conductivity of Glass Microspheres from Atmospheric Pressure to Vacuum," ASME paper 73-HIT-43, presented at ASME-AIChE Heat Conference, Aug 1973
- 6-14 L. S. Wang and C. L. Tien, Inter. J. Heat Transfer, 10:1327, 1967
- 6-15 E. M. Sparrow and R. D. Cess, Radiation Heat Transfer, Brooks-Cole Publishing Co., Belmont, California, 1969
- 6-16 R. P. Caren, J. Heat Transfer, 91:154, 1969
- 6-17 Wright-Patterson Air Force Base, Ohio, Thermophysical Properties of Solid Materials, Vol. III, WADC Technical Report 58-476, 1960, p. 867
- 6-18 C. L. Tien, private communication, Sep 1977
- 6-19 A.G. Furukawa and R.E. McCoskey, NACA TN 2969, 1963